Michel O. Deville · Vincent Couaillier
Jean-Luc Estivalèzes · Vincent Gleize
Thien-Hiep Lê · Marc Terracol
Stéphane Vincent   *Editors*

Turbulence and Interactions

Proceedings of the TI 2015 Conference, November 2–6, 2015, Cargèse, Corsica, France

Springer

Notes on Numerical Fluid Mechanics and Multidisciplinary Design

Volume 135

About this Series

Notes on Numerical Fluid Mechanics and Multidisciplinary Design publishes state-of-art methods (including high performance methods) for numerical fluid mechanics, numerical simulation and multidisciplinary design optimization. The series includes proceedings of specialized conferences and workshops, as well as relevant project reports and monographs.

More information about this series at http://www.springer.com/series/4629

Michel O. Deville · Vincent Couaillier
Jean-Luc Estivalèzes · Vincent Gleize
Thien-Hiep Lê · Marc Terracol
Stéphane Vincent
Editors

Turbulence and Interactions

Proceedings of the TI 2015 Conference,
November 2–6, 2015, Cargèse, Corsica,
France

Springer

Editors
Michel O. Deville
Ecole Polytechnique Fédérale de Lausanne
Lausanne
Switzerland

Vincent Couaillier
ONERA
Châtillon
France

Jean-Luc Estivalèzes
ONERA
Toulouse
France

Vincent Gleize
ONERA
Châtillon
France

Thien-Hiep Lê
ONERA
Châtillon
France

Marc Terracol
ONERA
Châtillon
France

Stéphane Vincent
Université Paris-Est
Marne Valley
France

Preface

The "Turbulence and Interactions 2015" (TI2015) conference was held in Institut d'Etudes Scientifiques de Cargèse on the island of Corsica, France, on November 2nd–6th, 2015. The scientific sponsors of the conference were

- Ecole Polytechnique Fédérale de Lausanne (EPFL)
- ONERA - The French Aerospace Lab

This fourth TI conference was very successful as it attracted 45 researchers from 6 countries. The magnificent venue and the beautiful weather helped the participants to discuss freely and casually, share ideas and projects, and spend very good times all together.

The organizers were fortunate in obtaining the presence of the following invited speakers: J. Derksen (Delft University of Technology), J.-L. Estivalèzes (ONERA), B. Geurts (University of Twente), V. Moureau (Coria), T. Sengupta (Indian Institute of Technology), A. Soldati (University of Udine), and S. Vincent (Université Paris-Est, Marne-La-Vallée).

The topics covered by the 24 contributed papers ranged from experimental results through theory to computations. They represent a snapshot of the state of the art in turbulence research. The papers of the conference went through the usual reviewing process, and the result is given in this book of Proceedings.

In the present volume, the reader will find the keynote lectures followed by the contributed talks given in alphabetical order of the first author.

The organizers of the conference would like to acknowledge the financial support of EPFL and ONERA.

Lausanne, Switzerland   Michel O. Deville
Châtillon, France   Vincent Couaillier
Toulouse, France   Jean-Luc Estivalèzes
Châtillon, France   Vincent Gleize
Châtillon, France   Thien-Hiep Lê
Châtillon, France   Marc Terracol
Marne Valley, France   Stéphane Vincent
March 2017

Contents

Prologue

The Challenge of Turbulence

Turbulence remains one of the major challenges in classical physics to be understood, theorized, and simulated. The fascination of turbulent flows goes back to the early stages of our civilization. We can mention Egyptian and Greek philosophers and scientists, among them, Archimedes. However, a major (more recent) contribution was made by Leonardo da Vinci (1452–1519) who gave us magnificent drawings made with great accuracy and neatness. In Fig. 1, Leonardo studies the eddies produced by a waterfall in a river. The flow is far from laminar; it is in fact turbulent.

Many great fluid mechanists or physicists tackled the problem of turbulence. Without the pretense of being exhaustive, here are a few statements by scientists of the twentieth century.

- "Turbulence is the most important unsolved problem of classical physics." Richard Feynman (1918–1988)
- "One of the best definitions of turbulence is that it is a field of random chaotic vorticity." P.G. Saffman (1931–2008)
- "I am an old man now, and when I die and go to heaven there are two matters on which I hope for enlightenment. One is quantum electrodynamics, and the other is the turbulent motion of fluids. And about the former I am rather optimistic." Horace Lamb (1849–1934) and/or W. Heisenberg (1901–1976)
- "Turbulence is the manifestation of the spatio-temporal chaotic behavior of fluid flows at large Reynolds numbers, i.e., of a strongly nonlinear dissipative system with an extremely large number of degrees of freedom (most probably) described by the Navier-Stokes equations." A. Tsinober

Turbulence is everywhere in nature: in atmospheric turbulence, the planetary boundary layer, clear air turbulence and clouds, bush fires, ocean currents, rivers, the photosphere of the sun, interstellar gas clouds, blood flow, respiratory airways

Fig. 1 Turbulence by L. da
Vinci. Courtesy University of
Montpellier, Department of
Mathematics

in lungs, etc. Figures 2 and 3 show beautiful and spectacular pictures of turbulent
physical phenomena. The solar eruption ejects ionized gaz from the outer crown
of the sun over a distance of several thousands of kilometers. Note the blue spot in
the upper part of the picture that gives the approximate size of the Earth. The Great
Red Spot of Jupiter is produced by an anticyclone in the southern atmosphere of the
planet. It is a system of high pressure that results from the balance between the
strength of the pressure gradient and the Coriolis force. It was observed for the first
time in 1665 by Gian Domenico Cassini.

Turbulence is everywhere in engineering: in aerodynamics: aircraft, wing,
automobiles, ships, train designs; in the processing of liquids/gases: pumps, com-
pressors, pipe lines, etc; in fluid mixing and combustion: fuel and air in engines,

Fig. 2 Breaking wave and cirrus Kelvin–Helmholtz cloud pattern
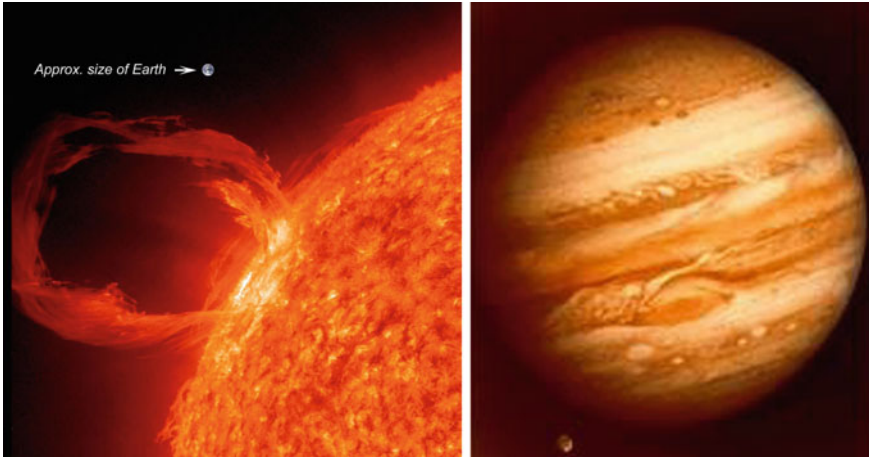
Fig. 3 Solar eruption and the Jupiter Red Spot

boilers, furnaces, chemical reactants; in plumes and turbulent jets, in pollution emission and mixing, etc.

Figure 4 presents the turbulent wake behind a cylinder at two different Reynolds numbers based on the diameter as reference length. The higher the Reynolds number, the more chaotic the wake pattern.

Figure 5 exhibits the flow configuration in the boundary layer on a flat plate obtained by laser-inducedfluorescence. It shows the appearance of coherent structures in the flow.

In the TI 2015 conference, we tackled the Navier–Stokes equations for incompressible or compressible fluids. In some cases, they are coupled with other governing equations related to temperature, concentration, particles, etc. As state-of-the-art problems are intricate and complex, few analytical solutions are available. Numerical methods have become essential tools to examine in detail the flow configuration and the associated dynamics. Experiments constitute also an indispensable way of inspecting carefully the turbulent patterns.
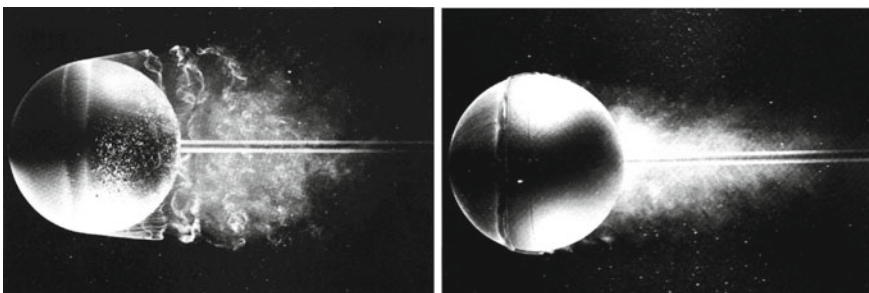
Fig. 4 Wake aft a sphere. Left: Re = 15000. Right: Re = 30000. H. Werlé, ONERA
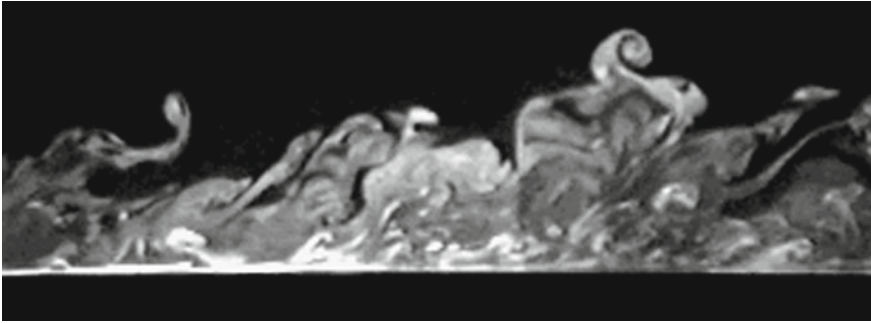
Fig. 5 Turbulent boundary layer on a flat plate

In the sequel, we will summarize the important concepts emerging from the abstracts submitted to the conference.

Space and Time Discretizations

Space Discretization

Most of the numerical methods belong to the FXM methods (Finite X Methods), with X = D for differences, X = E for elements and X = V for volume. Standard schemes are of the second order of accuracy. However, high-order schemes are also used: fourth-order compact schemes, spectral methods (Fourier, Chebyshev), hp, discontinuous Galerkin (DG), etc.

Time Discretization

Explicit and implicit schemes are used with second-order global accuracy. CFL issues constitute a strong difficulty for convection equation. The trend focusses on the use of high-order schemes like Runge–Kutta methods.

Software and Hardware

The goal of the developments of numerical methods and algorithms is directed to the parallelization on dozens of thousands (or even more) of processors to achieve exascale computing. The choice of the programming language is a crucial issue. From the TIOBE 2017 index, Fortran has rank 27. No comment!

Turbulence Modeling and Experiments

Models

Obviously enough, industrial problems are solved using Reynolds averaged Navier–Stokes (RANS) equations with all the bestiary of the various versions: k-ε, RNG, Reynolds stress models, etc. In the framework of large eddy simulations (LES), the taxonomy has grown in DES (detached eddy simulation), DDES (delayed DES), IDDES (improved DDES), ZDES (zonal DES). Hybrid methods couple RANS and LES. In LES, the dynamic Smagorinsky is a frequent choice. Approximate deconvolution method (ADM) is also in favor when more classical approaches fail.

Experiments

In experimental setups, particle image velocimetry (PIV) is the ideal tool. Tomography PIV is a three-dimensional extension of PIV. Laser Doppler anemometry (LDA) and particle tracking (PTV) are also used.

Other Approaches

The proper orthogonal decomposition (POD) is very attractive to resolve the most energetic structures of the turbulent flow. Kinetic theory and lattice Boltzmann method constitute alternatives to mesh-based methods. LES models are developed via tensor representation. The impact of big data on turbulence simulation is of primary concern toward exascale computing.

Suggestions for Improvements

- Need of more computations on transition to better understand the origin and causes of turbulence growth.
- Less emphasis on modeling issues. More focus on numerics.
- High-order space discretization, at least fourth order.
- Domain decomposition and parallelization.
- High-order time discretization, at least fourth order and more stable.

- Focus on advection schemes. CFL issues.
- Dispersion relation and group velocity.
- New tools for the data analysis.
- New tools for visualization.
- What else? (G. Clooney)

EPFL, Lausanne, Switzerland   Michel O. Deville
ONERA, Châtillon, France   Thien-Hiep Lê

Part I
Keynote Lectures

Particle-Resolved Simulations of Solid-Liquid Systems

Jos Derksen

Abstract Solid-liquid flows span a large parameter space, with dimensionless coordinates such as Stokes numbers, the solids volume fraction, the density ratio between the phases, and Reynolds numbers (e.g. associated with the continuous phase flow). We are interested in systems with appreciable inertia effects—i.e. non-zero Stokes and Reynolds numbers—having density ratios of the order of one and solids volume fractions of at least 0.1. In such flows, direct numerical simulations are desired to reveal the relevant interactions. The resolution required for DNS limits the size of the systems that we are able to simulate to the meso-scale. In this paper, examples of direct simulations based on the lattice-Boltzmann method of dense solid-liquid flows are presented, along with suggestions as to how to use their results at the macro-scale.

1 Introduction

Solid-liquid suspensions are abundant in natural and engineered systems. In general, solid-liquid flows span a large parameter space, with dimensionless components such as the Stokes number, the solids volume fraction, the density ratio between the phases, and Reynolds numbers (e.g. associated with the continuous phase flow). Our interest in large-scale industrial multiphase flows implies that we have systems with appreciable inertia effects—i.e. non-zero Stokes and Reynolds numbers—having density ratios of the order of one and solids volume fractions of 0.1 and up. In such suspensions many assumptions that ease the life of the computational researcher do not hold, and direct simulations—including full resolution of the solid-liquid interfaces—are desired to reveal the relevant interactions at the scale of the particles.

This necessarily limits the size of the systems that we are able to simulate; they typically contain up to a thousand particles. In this paper, the scales related to particle size and multi-particle interaction will be termed meso-scales, and our direct simulations are meso-scale simulations. Next to the ambition to fully resolve meso-scale

J. Derksen (✉)
Department of Chemical Engineering, Delft University of Technology,
Delft, The Netherlands
e-mail: j.j.derksen@tudelft.nl

phenomena, we are faced with the issue as to how to incorporate insights gained at the meso-scale in macro-scale modelling approaches (meso-to-macro coupling). In the opposite direction (macro-to-meso), the meso-scale systems need to be agitated (energized) in a manner that realistically represents the energy input that in many practical processes comes from the macro-scale; think of turbulent agitation by impellers, jets, distributor plates, and pumps.

Given the variety of multiple-scale interactions in industrial multiphase flow systems there is, to our knowledge, not a general methodology or framework for establishing the macro-meso coupling. In this paper we present a few examples of meso-scale simulations in the area of liquid-solid suspensions, and also show how their results could be incorporated in macroscopic flow and transport modeling.

The paper is organized in the following manner: First, we give a short overview of our computational methodology which is largely based on the lattice-Boltzmann method for solving the flow of the interstitial liquid. We then briefly describe methods for generating homogeneous, isotropic turbulence as a basic way to excite meso-scale systems. Subsequently two applications will be discussed. They comprise flow-induced forces in agglomerates and fibers, and liquid-solid fluidization.

2 Computational Approach

2.1 Lattice Boltzmann Method

The continuous phase (liquid) flow we solve with the lattice-Boltzmann method (LBM) [11]. For flows in complexly shaped domains and/or with moving boundaries, this method has proven its usefulness (see e.g. the review article by [2]). In the LBM, the computational domain is discretized into a number of lattice nodes residing on a uniform cubic grid. Fluid parcels move from each node to its neighbors according to prescribed rules. It can be proven by means of a Chapman-Enskog expansion that, with the proper grid topology and collision rules, this system obeys, in the low Mach number limit, the incompressible Navier-Stokes equations [2, 21]. The specific implementation used in our simulations has been described by Somers [19]; it is a variant of the widely used Lattice BGK scheme to handle the collision integral (e.g., see [17]). We use the scheme due to Somers, as it manifests a more stable behaviour at low viscosities when compared to LBGK.

2.2 Liquid-Solid Coupling

In the lattice-Boltzmann flow field, spherical (usually monosized) solid particles are suspended. The solid-liquid interfaces are fully resolved. The fluid flow and the motion of the spheres are coupled by demanding that at the surface of each

sphere the fluid velocity matches the local velocity of its surface (that is the sum of the translational velocity $\mathbf{v_p}$ and $\mathbf{\Omega_p} \times (\mathbf{r} - \mathbf{r_p})$ with $\mathbf{\Omega_p}$ the angular velocity of the sphere, $\mathbf{r_p}$ the center position of the sphere, and $\mathbf{r}$ a point on its surface). In the forcing scheme (aka immersed boundary method; [7, 9, 16]) that is applied here this is accomplished by imposing additional forces on the fluid at the surface of the solid sphere (which are then distributed to the lattice nodes in the vicinity of the particle surface). The details of the implementation can be found elsewhere [4, 10, 22]. The collection of forces acting on the fluid at the sphere's surface and its interior is subsequently used to determine the hydrodynamic force and torque acting on the sphere ($action = -reaction$) [6].

In our simulations, the radius of each spherical particle is specified and input radius refers to this radius scaled by the lattice spacing. In the LBM simulations, as the spherical particle is represented by forces that are confined to a cubic grid, the input radius does not reflect the actual radius of the particle. A calibration procedure to estimate the effective radius of this object (commonly referred to as the hydrodynamic radius) was introduced by Ladd [14]. We apply his scheme to estimate the hydrodynamic radius of the particles. The hydrodynamic radius is recognized as a and is given in lattice units. In our work radii in the range $a = 6 - 12$ are used. Typically the input radius turns out to be some 10% smaller than the hydrodynamic radius [22].

In multiple-sphere systems when two particles are at close proximity, with their separation being of the order of or less than the lattice spacing, the hydrodynamic interaction between them will not be properly resolved by the lattice. Therefore, we explicitly impose lubrication forces on the particles, in addition to the hydrodynamic forces stemming from the LBM. We use the procedure developed by Nguyen and Ladd [15] to smoothly make the transition between resolved and unresolved hydrodynamic interactions.

In addition to interactions via the liquid, spherical particles undergo direct interactions, mostly hard-sphere. If the motion of the spheres is constrained (such as with fibers built of strings of spheres) we—for reasons of computational efficiency—apply soft-sphere interactions.

2.3 Homogeneous, Isotropic Turbulence

A typical way to agitate our meso-scale systems is by generating turbulence in fully periodic, three-dimensional domains. Adding particles to the domains allows us to study the (two-way) coupling of solid and liquid motion. So far mainly homogeneous isotropic turbulence (HIT) has been considered in our work. HIT is e.g. characterized by its root-mean-square velocity u_{rms} and a Kolmogorov length scale $\eta_K = \left(\frac{\nu^3}{\bar{\varepsilon}}\right)^{1/4}$ with $\bar{\varepsilon}$ the volume and time averaged dissipation rate (which in steady state in a fully periodic domain equals energy input) and ν the kinematic viscosity of the liquid. If solids are added, the relevant dimensionless numbers are then based on the radius

of the spherical particles involved: $\frac{a}{\eta_K}$ and (if $\frac{a}{\eta_K} \geq 1$ so that the turbulence scales interfere with the sphere size) $\mathrm{Re}_{rms} = \frac{u_{rms}a}{\nu}$.

We have been using two different strategies to make HIT. One is based on random forcing and was introduced by Alvelius [1] in the context of spectral methods, later adapted for the lattice-Boltzmann method by [23]. This strategy has the advantages that the power input can be controlled accurately, and that it allows for more general forms of turbulence, including anisotropy. The second strategy is linear forcing, where turbulence is sustained by a force that is proportional to the local velocity [18]. This method has the elegance of simplicity and (as a result) computational efficiency at the cost of being less general than random forcing.

3 Case Studies

3.1 Flow-Induced Forces in Agglomerates and Fibers

In many processes involving solid particle formation or solids handling, particles have a tendency to stick together. Sometimes agglomeration is a wanted phenomenon to effectively grow particles making separation easier. It also is a mechanism that potentially destroys a narrow particle size distribution, and as a result could deteriorate product quality. Much effort goes into preventing or promoting agglomeration, and much effort goes into repairing the harm agglomeration has done. Regardless of whether agglomeration is wanted or unwanted, it is relevant to assess the stability and the integrity of the bond holding the primary particles together. Agglomerates can break as a result of a variety of mechanisms, one of them being the flow of fluid surrounding the agglomerate: velocity gradients induce forces on and in agglomerates that could break them.

Understanding and modeling agglomerate breakage as a result of fluid flow is largely based on relatively simple concepts involving estimating shear rates and semi-empirical correlations for breakage statistics. As described in recent papers on the broader subject of population balance modeling of colloidal dispersions [20], the physics of breakage due to flow date back quite some time [3, 13], and are prone to refinement in terms of getting the (statistics of the) hydrodynamic environment of agglomerates right, and in terms of estimating the actual hydrodynamic forces in agglomerates immersed in complex flow.

As a starting point we here assess the role of some of the non-ideal factors in the flow-induced forces in agglomerates. For this we have chosen to consider the virtually simplest agglomerate possible: two equally sized spheres (radius a), rigidly constrained together at their (single) point of contact. The two spheres are touching, they have zero separation.

We release a single doublet in homogeneous, isotropic turbulence (generated through linear forcing) and monitor the forces and torques at the point of contact needed to keep the two spheres attached. The time series are highly erratic (see the
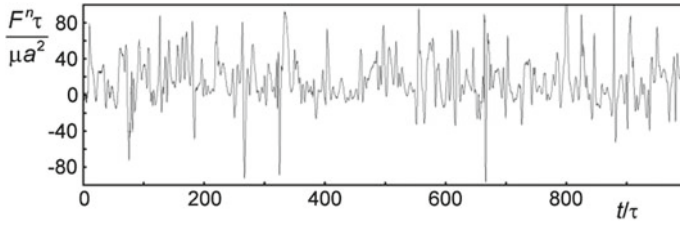
Fig. 1 Time series of the flow-induced normal force at the point of contact of a sphere doublet. Time has been normalized with the Kolmogorov time scale τ

Fig. 2 Root-mean-square $F^{n\prime}$ normal force in the sphere doublet at various turbulence conditions, characterized by the ratio a/η_K along with a trend line
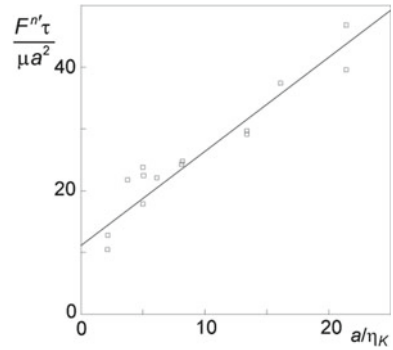
example in Fig. 1), with the fluctuation levels usually much higher than the averages. Running a number of simulations with $\frac{a}{\eta_K}$ as the main variable shows an interesting scaling of the force fluctuation levels. As $\frac{a}{\eta_K}$ increases, the flow around the agglomerate gets more inhomogeneous which adds to the fluctuations, see Fig. 2. More details and results can be found in one of our papers [5].

An extension of the above work is to consider (flexible) fibers in turbulent flow. If the fibers have a finite bending stiffness, we expect an interesting competition between turbulence bending the fibers, and stiffness trying to keep the fibers stretched. The fibers are modelled as equally sized spheres connected through rods and hinges, see Fig. 3. The bending stiffness enters through a (restoring) torque that is proportional to the vector product of the vectors defining the two rods connected by the joint (see the right panel of Fig. 3): $\mathbf{T_{jm}} = -\gamma \frac{\mathbf{j_m} \times \mathbf{j_{m+1}}}{j^2}$ with γ the stiffness parameter. Some preliminary results are given in Fig. 4 in terms of snapshots of the fibers bending in turbulent flow, and Fig. 5 in terms of time series of the fiber-averaged bending angle. Obviously, the stiffer the fiber, the more it stays stretched in turbulent flow.

As for the sphere doublets, we also keep track of the forces and torques required to retain the integrity of the fibers. The torque obviously increases with increasing fiber stiffness; the force is quite independent of the stiffness of the fibers, as is evident from Fig. 6.
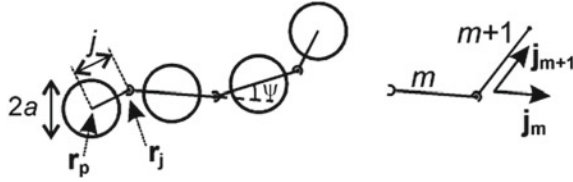
Fig. 3 Definition of fibers as *spheres* connected through joints. *Right* definition of the rod vectors $\mathbf{j_m}$
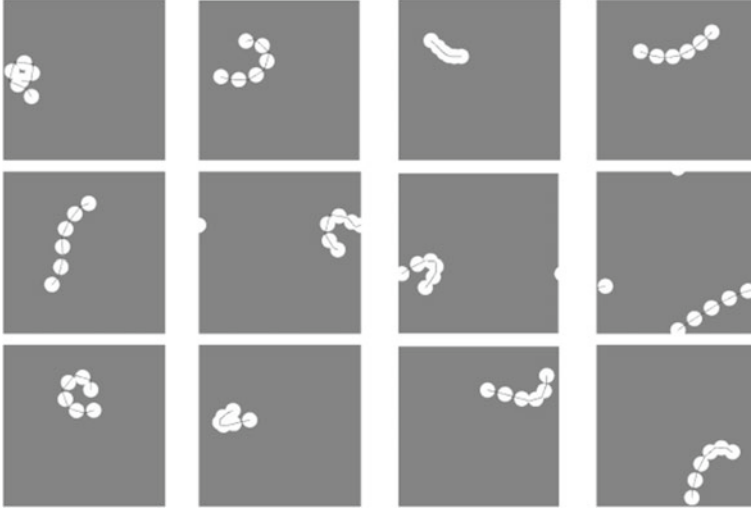
Fig. 4 Side views of fibers in the 128^3 periodic domain, three snapshots per case. From *left* to *right* increasing bending stiffness $\gamma . \gamma / \left(12\pi \nu \rho a^2 u_{rms} \right) = 0, 1.78, 14.2, 56.8$

3.2 Direct Simulations of Solid-Liquid Fluidization

Our numerical work of liquid-solid fluidization is inspired by the experimental work due to Duru et al. [8]. They carried out an extensive study of the onset and characteristics of planar waves in relatively narrow liquid fluidized beds. Their experimental variables were the ratio of particle and fluid densities, the particle size, the fluid viscosity, the size ratio (particle diameter divided by tube diameter) and the average particle volume fraction (which was controlled by the superficial velocity of the fluidizing liquid). Figure 7 shows a typical experimental result obtained by them: a space-time plot of the solids volume fraction. Clearly visible are regions of low particle volume fraction ("voids") that travel with a well-defined speed in the vertical (z) direction.

Here we directly simulate one-dimensional travelling waves such as those shown in Fig. 7. The specific experiments that we selected from Duru et al. [8] had particles with $a = 342$ μm and a density ratio $\rho_s / \rho_f = 4.1$. In order to keep the computa-
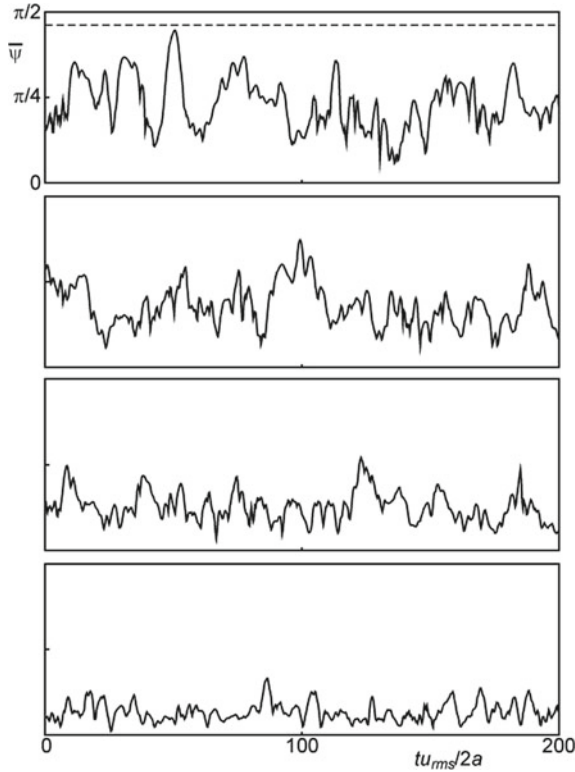
Fig. 5 Time series of the fiber-averaged angle $\bar{\psi}$ with from *top* to *bottom* increasing bending stiffness $\gamma/(12\pi\nu\rho a^2 u_{rms}) = 0$, 1.78, 14.2, 56.8. The *dashed line* in the *upper panel* represents ψ_{max}, i.e. the fiber-averaged angle of a fully curled up fiber

tions affordable, we restricted our simulations to a fully-periodic three-dimensional domain. Since we wish to simulate one-dimensional travelling waves, we suppress the onset of secondary instabilities by choosing the lateral dimensions to be small (typically $12a$).

A homogeneous bed was first created by placing a set of non-overlapping spheres randomly in space in the periodic domain. At the start of the simulation, the velocities of the particles and the fluid were set to zero. At $t=0$, gravity and the body force on the fluid were switched on. As the lateral dimensions of the domain are small, there is very little opportunity for any persistent lateral structure to evolve, but one can readily see non-uniform structures that travel in the direction of the mean fluid flow. This is illustrated in Fig. 8, which shows a series of snapshots taken at an arbitrary vertical cross section of the periodic domain. The system develops a wave structure in a time span of the order of a^2/ν. A region of lower particle volume fraction, henceforth referred to as "void", travels in the direction opposite to gravity (i.e. the positive z-direction). Outside the void, the particle volume fraction is significantly
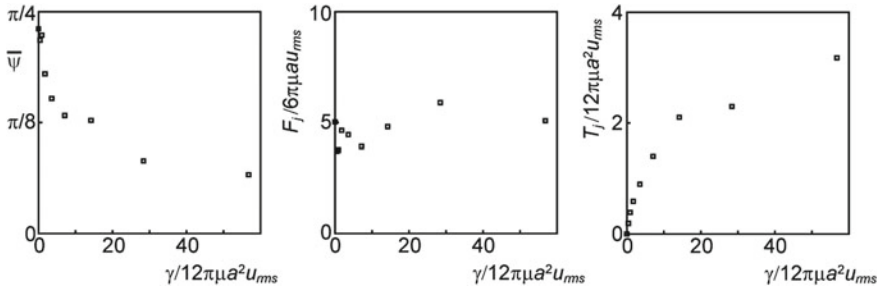
Fig. 6 Time-averaged, fiber-averaged angle, absolute joint force, and absolute joint torque (from *left* to *right*) as a function of the fibers' bending stiffness γ

Fig. 7 Experimental space-time plot of the solids volume fraction at an average solids volume fraction of $\bar{\phi} = 0.540$. The wave speed c can be deduced from the slope of the light *lines* representing the void regions. Reprinted from Duru et al. [8]
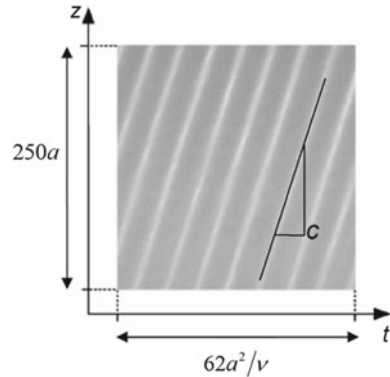
Fig. 8 Cross section through the simulated liquid-solid field with $\bar{\phi} = 0.505$ at various moments in time. Colors indicate liquid velocity magnitude
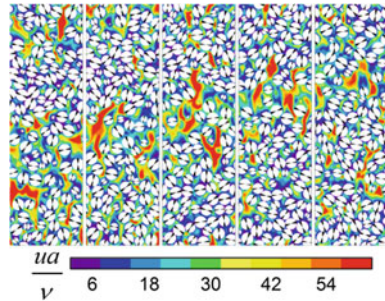
higher than the average value $\bar{\phi}$. Above the void, particles detach from the dense region, then "rain" through the void, and subsequently collect on the dense region below the void.

The simulated wave was averaged over the horizontal directions (x and y), and represented in a space-time plot similar to the experimental ones, as an example at $\bar{\phi} = 0.488$ see Fig. 9. The dimensionless wave speed $\tilde{c} = \frac{ca}{\nu}$ (with c being the dimensional wave speed) extracted from Fig. 9 is 16.6. The error margin in determining $\tilde{c}$
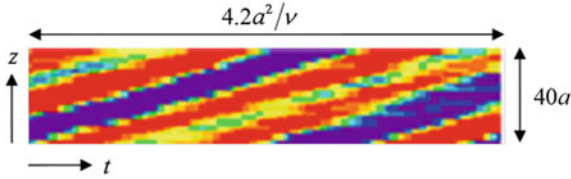
Fig. 9 Space (*vertical*) versus time plot of the solids volume fraction for a simulation at $\bar{\phi} = 0.488$
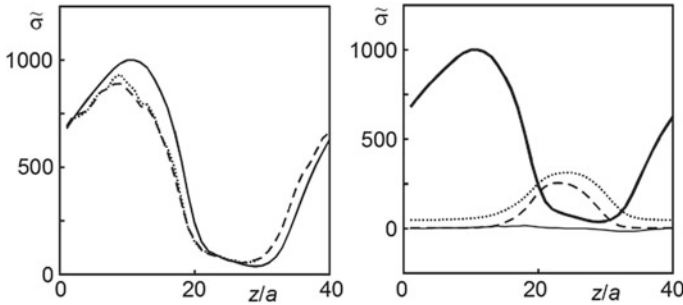
Fig. 10 Dimensionless stress $\tilde{\sigma} = \sigma a^2/(\rho_f v^2)$ as a function of height for $\bar{\phi} = 0.505$. *Left* the three components of the collisional normal stress with the drawn *line* the *zz* component. *Right thick*, *drawn line* collisional stress; *thin drawn line* stress due to lubrication; *dotted line* fluid streaming stress; *dashed line* particle streaming stress. The *center* of the voidage wave is located at $z/a \approx 24$, it is some 16a wide

from the simulation results was estimated as ± 1. For the comparable experimental system Duru et al. [8] measured a dimensionless wave speed of $14\,(\pm 1)$.

The liquid-particle system transfers momentum through a variety of mechanisms: particle and fluid streaming motion (streaming stresses), particle-particle collisions (collisional stress), particle-particle interaction through lubrication forces, and fluid-phase viscous stresses. The wave clearly induces anisotropy. As an example, we show in Fig. 10 (left panel) the three components of the collisional normal stress. As expected, the two lateral components (*xx* and *yy*) are approximately equal to one another, and the axial component (*zz*) differs appreciably from the other two. The effects of particle volume fraction are clearly visible in the stress profiles. The collisional stress is much lower in the void region than in the dense plug.

The most important *zz*-stresses are presented in Fig. 10 (right panel). Collisions are largely responsible for the particle phase stress in the parts of the flow that have a high particle volume fraction. In the void, fluid and particle streaming stress are significant and of comparable magnitude. Lubrication only plays a modest role. The fluid-phase viscous normal stresses (not shown in Fig. 10) are negligible.

The results have been further analyzed in terms of the solids phase bulk and shear viscosity [6]. Given the expansion and compression of the solids phase in the

Fig. 11 Particle-phase
viscosity as a function of
solids volume fraction. The
squares (*triangles*) denote
the shear viscosity in the
compaction (dilation)
branch. The plusses are bulk
viscosity estimates
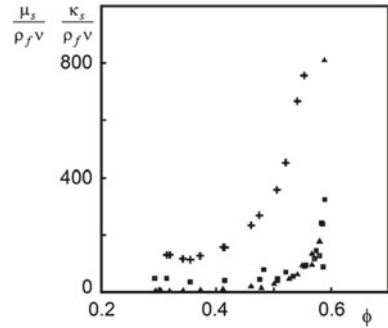
wave, and the significant stresses related to the compaction part, the bulk viscosity
is significant and in general is higher than the shear viscosity, see Fig. 11.

Analysis of its results towards two-fluid closure of multiphase flow is a primary
motivation for performing direct simulations as described above. Two-fluid closure
requires expressions that relate e.g. solids-phase viscosity with the properties of the
granular system (such as local solids volume fraction and granular temperature). Our
mesoscale simulations can directly assess the quality of such expressions given the
availability of both the input and the output parameters in the simulations. Next to
solids phase stress closure (as touched upon here in terms of solids phase viscosities),
also closures for inter-phase momentum transfer (drag as a function of solids volume
fraction and potentially fluctuating quantities) have been considered [6].

4 Summary

This paper presents a few case studies of mesoscopic modelling of solid-liquid flows,
with underlying topics such as momentum transfer, and flow-induced forces in and on
agglomerates. Except for lubrication modelling, the simulations are direct, meaning
that no (empirical) closures or empirical correlations for e.g. forces on particles enter
the simulations.

From an industrial standpoint the flow systems studied are (still) very simple:
monosized spherical, solid particles in Newtonian carrier fluids. The choice for
monodispersed systems is not fundamental; the simulation strategy easily allows
for size distributions. The extension towards non-spherical particles would be much
less straightforward [12, 24]. Specifically in dense systems, handling collisions of
non-spherical particles would get (computationally) more complicated.

In retrospect, the reason for the relative simplicity at the mesoscale was to keep
the parameter space limited. Adding complications (at the mesoscale) strongly adds
to the dimensionality of the parameter space (then size distributions, particle shape
characterization, and rheological parameters would enter). It would be useful though
to add complexity to the mesoscale, the challenge being to directly mimic the inter-

actions there and for instance see how particle shape impacts momentum transfer in dense suspensions. The price to pay for this is getting less general (i.e. work towards more and more specific applications); results only apply to the specific systems of choice; the (general) link to the macro-scale would be harder to establish.

Relating with real processes and industry in this respect is essential. Zooming in on practical systems and making choices regarding the physics to be incorporated there only pays off if it helps in solving practical problems with economic and environmental impact.

From a computational perspective there is significant opportunity for increasing the size and/or complexity of the meso-scale simulations through parallelization. The results presented above are almost exclusively based on sequential (i.e. one-cpu) computations with memory requirements per simulation in the range of 100 Mbyte to 5 Gbyte. The simulations run on Linux clusters with standard (PC) processors.

Parallelization of the lattice-Boltzmann part of the computational procedure is straightforward given the local nature (only nearest neighbor interaction) of its operations. Parallelization of the solid particle dynamics and its coupling with LBM is more complicated with the particles extending over of the order of 10 grid spacings and thus requiring more communication between cpu's in parallel runs.

References

1. Alvelius K (1999) Random forcing of three-dimensional homogeneous turbulence. Phys Fluids 11:1880–1889
2. Chen S, Doolen GD (1998) Lattice Boltzmann method for fluid flows. Annu Rev Fluid Mech 30:329–364
3. Delichatsios MA, Probstein RF (1976) The effect of coalescence on the average drop size in liquid-liquid dispersions. Ind Eng Chem Fund 14:134–138
4. Derksen J, Van den Akker HEA (1999) Large-eddy simulations on the flow driven by a Rushton turbine. AIChE J 45:209–221
5. Derksen JJ (2008) Flow induced forces in sphere doublets. J Fluid Mech 608:337–356
6. Derksen JJ, Sundaresan S (2007) Direct numerical simulations of dense suspensions: wave instabilities in liquid-fluidized beds. J Fluid Mech 587:303–336
7. De Rosis A, Falcucci G, Ubertini S, Ubertini F, Succi S (2013) Lattice Boltzmann analysis of fluid-structure interaction with moving boundaries. Comm Comput Phys 13:823–834
8. Duru P, Nicolas M, Hinch J, Guazelli E (2002) Constitutive laws in liquid-fluidized beds. J Fluid Mech 452:371–404
9. Feng Z-G, Michaelides E (2004) The immersed boundary-lattice Boltzmann method for solving fluid-particles interaction problems. J Comput Phys 195:602–628
10. Goldstein D, Handler R, Sirovich L (1993) Modeling a no-slip flow boundary with an external force field. J Comput Phys 105:354–366
11. Higuera FJ, Succi S, Benzi R (1989) Lattice gas dynamics with enhanced collisions. Europhys Lett 9:345–349
12. Krueger T, Frijters S, Guenther F, Kaoui B, Harting J (2013) Numerical simulations of complex fluid-fluid interface dynamics. Eur Phys J Spec Top 222:177–198
13. Kusters KA (1991) The influence of turbulence on aggregation of small particles in agitated vessel. PhD, Eindhoven University of Technology, Netherlands
14. Ladd AJC (1994) Numerical simulations of particle suspensions via a discretized Boltzmann equation. Part 2. Numerical results. J Fluid Mech 271:311–339

15. Nguyen N-Q, Ladd AJC (2002) Lubrication corrections for lattice-Boltzmann simulations of particle suspensions. Phys Rev E 66:046708
16. Niu X, Shu C, Chew YT, Peng Y (2006) A momentum exchange-based immersed boundary-lattice Boltzmann method for simulating incompressible viscous flows. Phys Lett A 354:173–182
17. Qian YH, d'Humieres D, Lallemand P (1992) Lattice BGK for the Navier-Stokes equations. Europhys Lett 17:479–484
18. Rosales C, Meneveau C (2005) Linear forcing in numerical simulations of isotropic turbulence: physical space implementations and convergence properties. Phys Fluids 17:095106
19. Somers JA (1993) Direct simulation of fluid flow with cellular automata and the lattice-Boltzmann equation. Appl Sci Res 51:127–133
20. Soos M, Sefcik J, Morbidelli M (2006) Investigation of aggregation, breakage and restructuring kinetics of colloidal dispersions in turbulent flows by population balance modeling and static light scattering. Chem Eng Sci 61:2349–2363
21. Succi S (2001) The lattice Boltzmann equation for fluid dynamics and beyond. Clarondon Press, Oxford
22. Ten Cate A, Nieuwstad CH, Derksen JJ, Van den Akker HEA (2002) PIV experiments and lattice-Boltzmann simulations on a single sphere settling under gravity. Phys Fluids 14:4012–4025
23. Ten Cate A, Van Vliet E, Derksen JJ, Van den Akker HEA (2006) Application of spectral forcing in lattice-Boltzmann simulations of homogeneous turbulence. Comput Fluids 35:1239–1251
24. Zhang J, Johnson PC, Popel AS (2007) An immersed boundary lattice Boltzmann approach to simulate deformable liquid capsules and its application to microscopic blood flows. Phys Biol 4:285–295

Modeling and Analysis of the Interactions of Coherent Structures with a Spray Flame in a Swirl Burner

L. Guedot, G. Lartigue and V. Moureau

Abstract With the constant increase in super-computing power, Large-Eddy Simulation (LES) has become an important tool for the modeling and the understanding of flame dynamics in complex burners. A fine description of the reaction layers in such devices requires fine meshes and the resolution of a broad range of turbulent scales. Unfortunately, extracting the large-scale features is not trivial. To this aim, implicit high-order filters that are based on simple low-order finite-volume operators have been proposed. These filters are applied in the LES of the MERCATO burner in order to study the complex interactions of the Precessing-Vortex Core, a large vortex typical of swirl burners, and a spray flame. High-order filters conveniently enable the analysis of the flame anchoring and its dynamics in the wake of the PVC.

1 Background and Motivation

1.1 Main Features of Swirling Flows

Swirling jet flows are widely used in combustion devices for the stabilization of premixed or partially premixed flames. This stabilization is made possible by the vortex breakdown that occurs when the geometric swirl number, which measures the ratio of tangential over axial momentum flux, is sufficient. The swirl generates a pressure decrease near the axis that leads to the formation of an axial recirculation zone. In such flows, incoming gases are slowed down by the recirculation zone that acts as an aerodynamic blockage, and the reaction zone is fed with recirculating hot gases

L. Guedot · G. Lartigue · V. Moureau (✉)
CORIA - CNRS UMR 6614, Normandie Université, Université et INSA de Rouen,
Saint Etienne du Rouvray, France
e-mail: vincent.moureau@coria.fr

ensuring the stability of the flame [13, 17]. In some conditions, the vortex breakdown may also lead to the formation of coherent structures such as the Precessing Vortex Core (PVC) [13, 23], which consists of single or multiple helical vortices.

The PVC plays an important role in the dynamics of the flow, and this instability has been widely studied, as reveals the extensive literature addressing this issue. Based on modal analysis of experimental data, some authors showed that the PVC may be responsible for local extinction of the flame or auto-ignition, and strongly interacts with the flow [1, 22]. The PVC may also wrinkle the premixed flame front creating isolated flame pockets [23]. The wrinkling and stretching of the flame surface leads to periodic fluctuations of the heat release rate, that might affect the acoustic behavior of the chamber. Some recent studies [21] showed that the PVC can either amplify or damp acoustic instabilities, according to the respective position of the PVC and the flame, highlighting the complexity of the phenomenon. In the same perspective, Caux-Brisebois et al. developed an advanced post-processing method of experimental data to study the coupling between acoustic instabilities and the PVC, and predict the burner stability [2].

In the case of spray flames, the PVC also influences the distribution of fuel mass fraction as it leads to preferential segregation of fuel droplets [18, 20]. Some recent work [10] showed that the high level of turbulence due to the PVC close to the fuel injection helps the atomization process and the development of small droplets, improving the efficiency of the device. The influence of the PVC in two-phase reacting flows results in complex coupling mechanisms. The analysis of this large-scale feature is mandatory to improve the understanding of the dynamics of swirling flows.

Guedot et al. [7] recently proposed high-order implicit filters for the extraction of large scales in complex geometries. These filters were successfully applied to the identification of large vortices in the isothermal flow in a complex swirl burner. The aim of the present paper is to apply the same methodology to all the available data found in high-fidelity Large-Eddy Simulations in order to identify the dominant interactions in a semi-industrial spray burner.
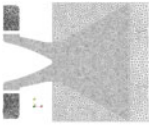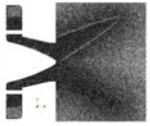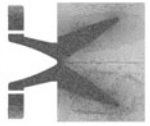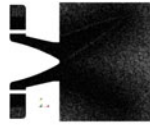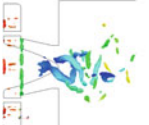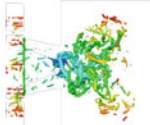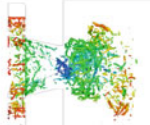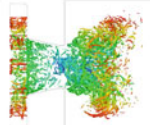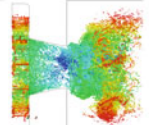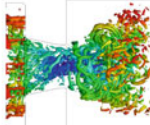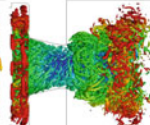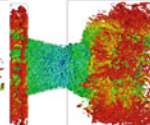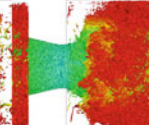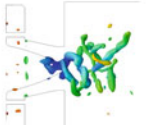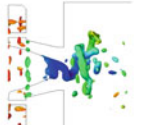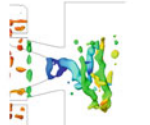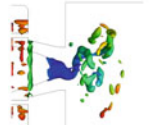
1.2 Extraction of Large-Scale Structures in High-Fidelity Simulations

Large-Eddy Simulation is a powerful tool for the analysis of coherent structures in turbulent flows. The steady increase in computational power leads to finer and finer mesh resolutions, which enables an accurate prediction of all flow features. As a result, large scale simulations with meshes up to several billion cells are currently performed on massively parallel machines using thousands of processors. The analysis of these billion-cell simulations is very challenging because it requires to handle a large amount of data, and traditional data processing tools have to be redesigned to post-process and analyze large scale simulation. In particular, the extraction of large scale structures becomes very challenging when dealing with highly refined

meshes. High-fidelity simulations provide solutions that contain a wide range of length-scales, ensuring a good description of the physics, but making it difficult to extract relevant information among the large amount of data it generates.

A convenient tool for the visualization of coherent vortices is the Q-criterion, which is the second invariant of the deformation tensor [9]. The Q-criterion is related to the Laplacian of the pressure field in incompressible flows [4]. For homogeneous isotropic turbulence, the scaling power of the Q-criterion with the wave number k is larger than unity [16]. The Q-criterion exhibits larger values for small vortices than for big vortices, because the smallest vortices have a greater velocity gradient. This issue is particularly annoying in well refined simulations that feature a large range of turbulent scales. In these simulations, the small vortices completely mask the large vortices when looking at Q-criterion iso-values as shown with the iso-surfaces of unfiltered Q-criterion in Table 1). This problem is illustrated here in the simulation of a semi-industrial swirl burner operated in the PRECCINSTA European project.

Table 1 Extraction of the PVC with unfiltered and filtered Q-criterion in the LES of the PREC-CINSTA burner at various mesh resolutions from 3 million to 878 million tetrahedral elements. The vortices are colored by the axis distance

	3 M	14 M	41 M	110 M	878 M
Mesh					
Q-criterion					
	$Q = 0.32 \times 10^8$	$Q = 0.8 \times 10^8$	$Q = 1.5 \times 10^8$	$Q = 2 \times 10^8$	$Q = 5 \times 10^8$
Q-criterion					
		$Q = 0.32 \times 10^8$	$Q = 0.32 \times 10^8$	$Q = 0.32 \times 10^8$	$Q = 0.32 \times 10^8$
Filtered Q-criterion					
		$\overline{Q} = 0.32 \times 10^8$	$\overline{Q} = 0.32 \times 10^8$	$\overline{Q} = 0.32 \times 10^8$	$\overline{Q} = 0.32 \times 10^8$

The Q-criterion has already been used to visualize the PVC on coarse grids in this configuration [14, 19] but an issue appears for highly refined simulations. This issue is illustrated in Table 1. A Q-criterion iso-surface is used to visualize the PVC, on 5 meshes from 3 million to 878 million tetrahedral cells. The method performs well on the coarse grid but appears to be inefficient on refined grids. A low Q-criterion threshold must be chosen to capture the PVC since it is a large scale vortex compared to the smaller resolved scales. But since the Q-criterion of the smallest vortices is larger than the one of the large coherent structures, the PVC is masked by small-scale surrounding turbulence. When choosing a higher threshold, only the smaller vortices can be observed. The Q-criterion is a good candidate for vortices extraction but it is limited to the visualization of vortices of characteristic length-scale close the smallest scales resolved on the mesh.

To circumvent the Q-criterion scaling issue, it is mandatory to develop numerical techniques able to perform scale separation of the different coherent structures, such as spatial low-pass filters. This filtering operation is challenging as it requires to extract features from a large amount of data distributed across a large number of processors. This operation necessitates a good selectivity in order to leave the large scales unaffected while damping all the smallest scales. To this aim, high-order filters were implemented in the Large-Eddy Simulation (LES) solver YALES2 [15], and applied in an aeronautical swirl burner as depicted in Fig. 1 [7]. This figure shows that the PVC is successfully extracted from these highly refined simulations when filtering the Q-criterion at a high order.

2   Application to a Realistic Swirling Two-Phase Flow in Reactive Conditions

2.1   Operating Conditions

In this section, the MERCATO test-rig [11] is simulated in reactive operating conditions. First, the simulation is initiated with purely gaseous flow. Fresh gases are injected at the inlet at 293 K. Then particles are injected, and combustion is initiated with a heat source. Once steady state is reached, statistics are accumulated over 150 ms. Axial velocity measurements are available for the liquid and the gaseous phase in planar sections located at 10, 26, 56 and 116 mm of the injection plane. The operating conditions are summarized in Table 2. Under these conditions, the Reynolds number based on the diameter of the swirler exit and the bulk velocity is approximately $Re = 54\,000$ and the swirl number $Sw = 0.7$.

Table 2 Operating conditions

T_{air} (K)	T_{fuel} (K)	$\dot{m}_{air}$ (g/s)	$\dot{m}_{fuel}$ (g/s)	P (Pa)
293	300	35	2.25	101 300

2.2 Numerical Setup

A two-step chemical scheme was used to describe the kinetics of reaction [5]. To take into account the flame/turbulence interaction, the TFLES model was chosen [3, 12]. It artificially thickens the flame front according to a dynamic flame sensor based on a progress variable source term, which is the sum of the species mass fractions of CO, CO_2 and H_2O.

2.3 Mean Flow Statistics

Mean gaseous and liquid velocities extracted in the sections given by Fig. 1 are represented in Figs. 2 and 3 and compared to those obtained experimentally and with LES by [8]. The flow is characteristic of swirl burners with a large central recirculation. The global flow topology and the amplitude of the mean and RMS velocity profiles are well reproduced. The size of the central recirculation zone is over-estimated in the two first planes, but in good agreement with the simulations of Hannebique [8]. The profiles at 56 and 116 mm from the injection plane are in excellent agreement with the experiments.

2.4 Flame Anchoring Dynamics

The flow dynamics in the swirl burner is dominated by a periodic motion that appears close to the injection plane. Figure 4 shows temperature and mixture fraction fields in the mid-plane at successive times. The anchoring point in the central recirculation zone periodically oscillates from top to bottom in the mid-plane. The period of this fluctuation is approximately 0.9 ms, which is in good agreement with the PVC frequency, measured experimentally at 1050 Hz [11]. The flame anchoring is a key parameter for the stability of the combustor. To track the location of this point over several PVC periods, high-order filtering was used to extract the most backward axial position in the burnt gases within the injection area. The extraction algorithm,

Fig. 1 Axial position of the profiles in the burner

Experiment   □
AVBP   —·—·—
YALES2 MS   - - - - -
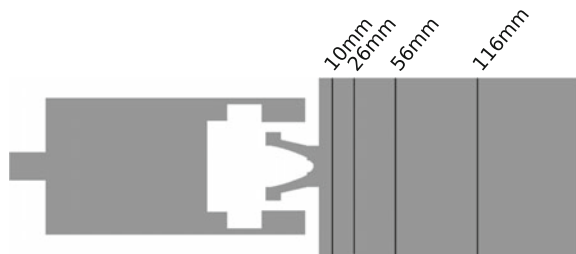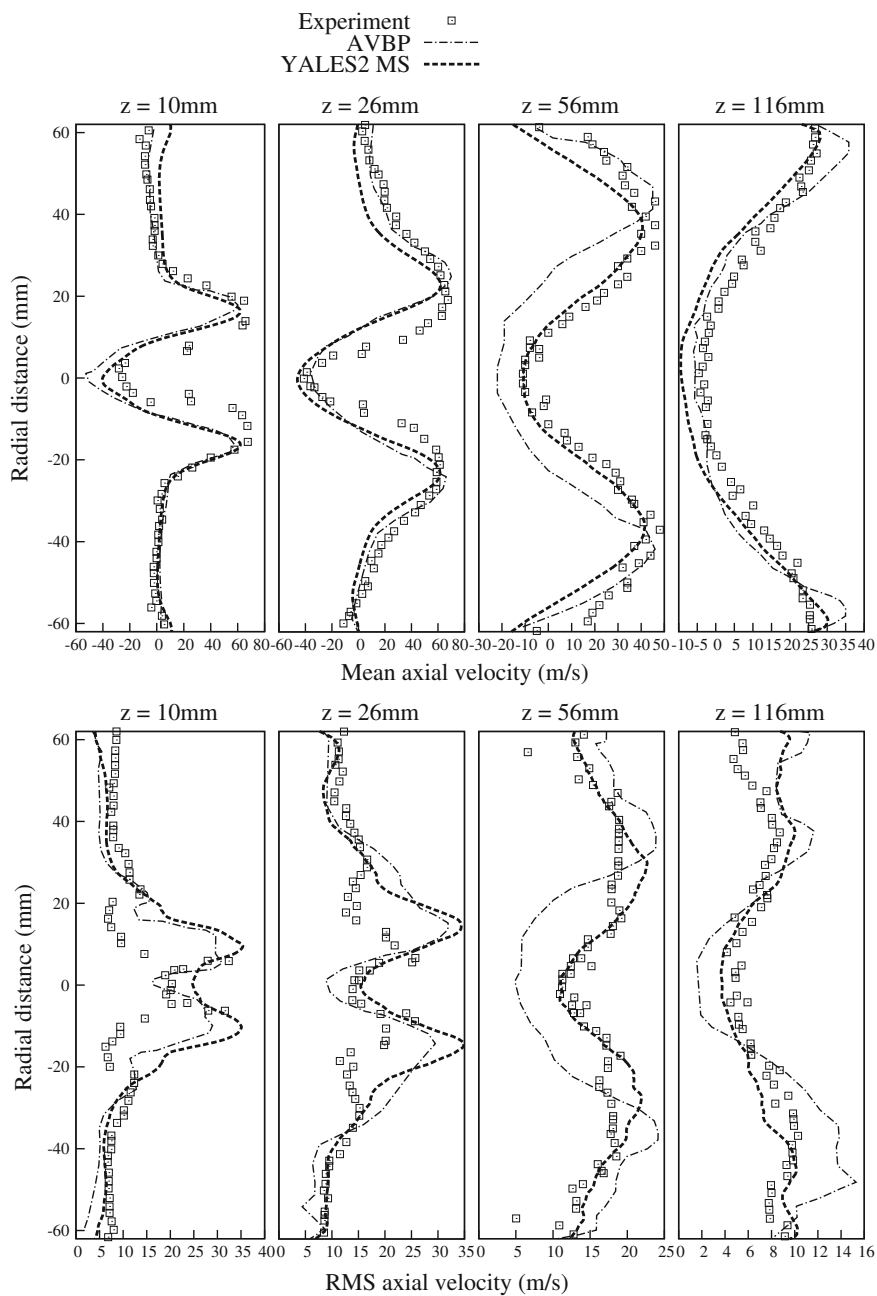
Fig. 2 Mean gaseous velocity profiles
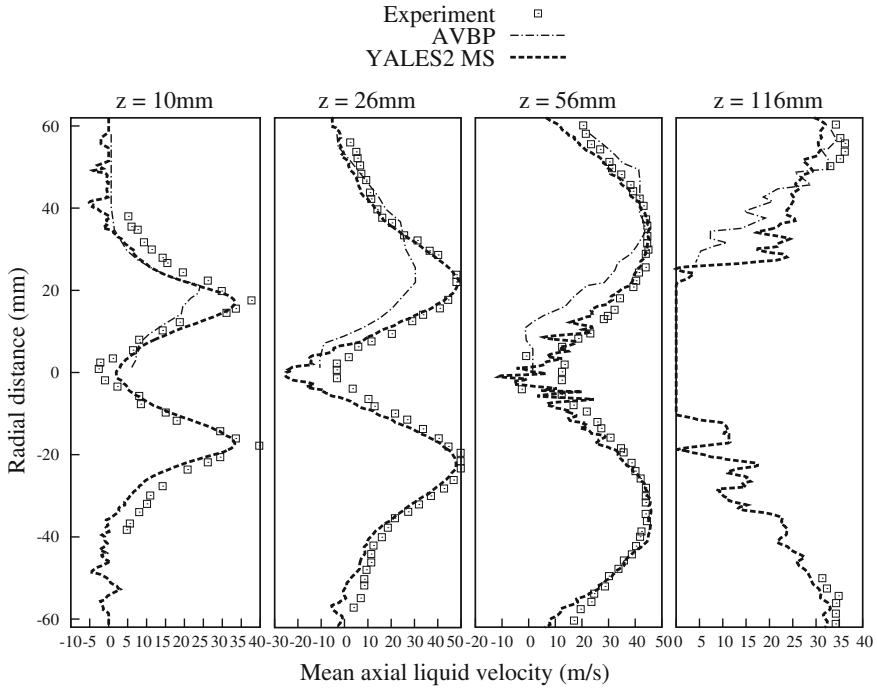
Fig. 3 Mean liquid velocity profiles
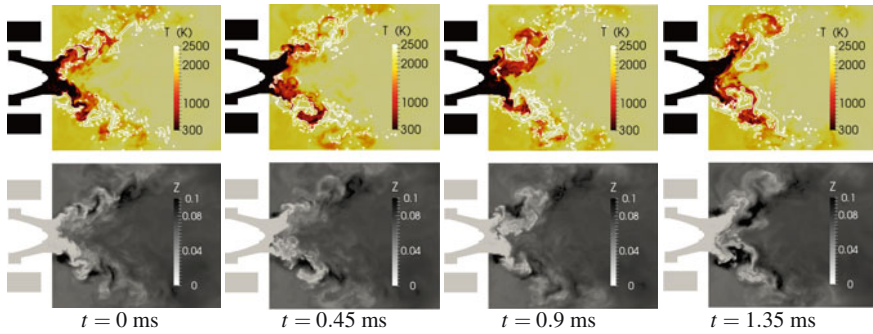
Fig. 4 Mixture fraction and temperature for four successive instants. The view is limited axially to $Z = 150$ mm. The central recirculation zone anchoring has a periodic motion inside the swirler

illustrated in Fig. 5 consists of filtering the temperature, and segmenting the image based on the $\overline{T} = 1100$ K iso-surface. The anchoring point is defined as the mesh point of the filtered iso-surface with the most backward axial coordinate. The research area is narrowed to a small volume from the injection plane to two exit diameters downstream, and within a radial distance smaller than the exit diameter.
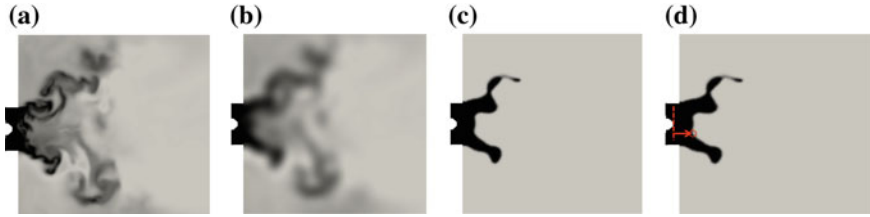
Fig. 5 **a** Temperature, **b** high-order filtered temperature, **c** segmentation based on the filtered temperature iso-surface $\overline{T} = 1100\,\text{K}$, and **d** determination method of the anchoring point. The view is limited axially to $Z = 130\,\text{mm}$
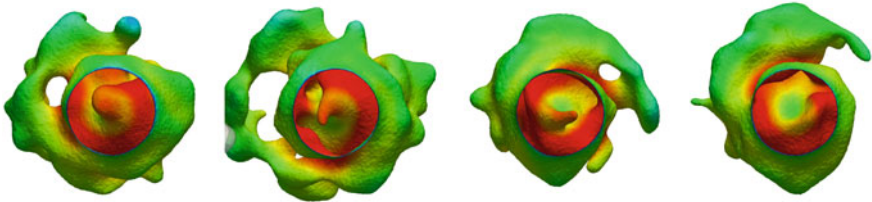
Fig. 6 Rotation of the anchoring point, visualized by iso-surfaces of filtered temperature. Snapshots are taken every 0.22 ms

The filtered flame surface is represented in Fig. 6, where its rotation is clearly visible. The rotation direction matches the one of the precessing movement of the PVC, and of the swirl motion in the burner. The flame surface however wraps around the central recirculation in the opposite rotation direction. It was verified (not shown here) that over more 10 PVC periods, the anchoring point follows an almost perfect circle. All the collected points are gathered around 6mm from the rotation axis, and at 10 mm from the combustor head, with small fluctuations in the axial direction.

2.5 Spray-PVC-Flame Interactions

In this section, the interactions of the PVC with the spray flame are analyzed more in details. The objective is to show that high-order filters enable to gain a deeper insight into the large-scale dynamics of the spray flame. This analysis complements the study of [6], who investigated the dynamics of swirling propage/air flames. They found that the flame stabilization point follows a helicoidal trajectory, which is phase-shifted with the PVC. The present study aims at extending this analysis to spray flames. High-order filters were used at order 8 and with a filter size of $\Delta = 12\,\text{mm}$ to filter all the available data such as Q-criterion, temperature, kerosene mass fraction, evaporation rate, reaction rate and velocity.
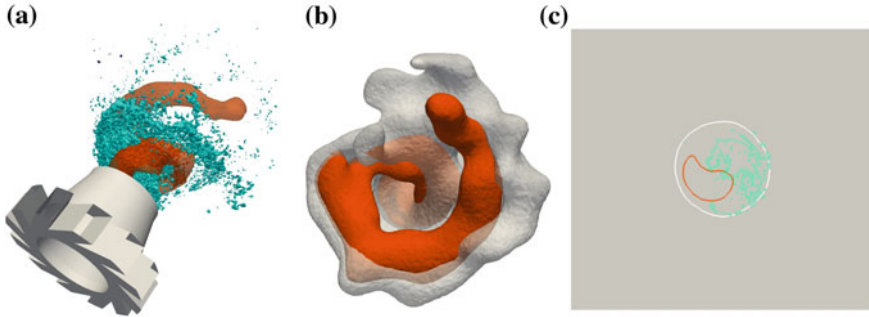
Fig. 7 Filtered temperature iso-surface to represent the flame (*white*), filtered Q-criterion iso-surface to show the PVC (*orange*), and spray droplets (*blue*) inside the burner (**a**), (**b**), and in a planar section at 6 mm of the combustor head (**c**)

Figure 7 shows iso-surfaces of filtered Q-criterion and temperature to materialize the PVC and the flame surface, respectively. The latter follows the helical shape of the PVC. This phenomenon is responsible for the periodic release of hot pockets convected to the outlet, and the periodic heat release observed experimentally in this type of burner. The Fig. 7a, c show that the presence of the PVC breaks the initial symmetry of the spray. At 6 mm from the injection plane, the spray is swept away by the PVC, and particles are concentrated in the azimuthal portion of the plane opposite to the PVC. This phenomenon, combined with the precessing movement of the PVC generates a precession of the spray that follows the PVC, and gives a helical shape to the spray droplets.

Iso-surfaces of all filtered variables are displayed in Fig. 8 in order to highlight the complex interactions between the PVC and the spray flame. As explained earlier, the spray is asymmetric and droplets are gathered away from the rotation axis of the swirler due to the PVC motion. Fuel droplets start evaporating as soon as they encounter hot burnt gases in the inner and outer recirculation zones. Because of the segregation of the fuel droplets due to the PVC, local rich pockets of gaseous fuel are generated when the droplets evaporate. The dynamics of these rich fuel pockets is the same as the one of the fuel droplets: the spatial distribution of the evaporated kerosene is helically shaped and follows the PVC with a phase shift. The fuel released in these rich pockets starts burning in a diffusion regime. This combustion regime was assessed by plotting the Takeno flame index (not shown here). The remaining fuel is then mixed by turbulence and burns in a premixed regime further downstream. Larger particles, with higher evaporation time-scales, disappear further away in the burnt gases, generating small isolated reaction zones.

Fig. 8 Iso-contours of filtered Q-criterion (*dark pink*), of filtered axial velocity (*orange*), of filtered temperature (*light blue*), of filtered kerosene mass fraction $\overline{Y}_{kero} = 0.01$ (*yellow*), filtered fuel evaporation rate $\overline{\dot{\omega}}_{kero,evap}$ (*transparent green*), filtered enthalpy source term $\overline{\dot{\omega}}_T$ (*dark blue*) and spray droplets (*green*) for the same snapshot in the vicinity of the injector
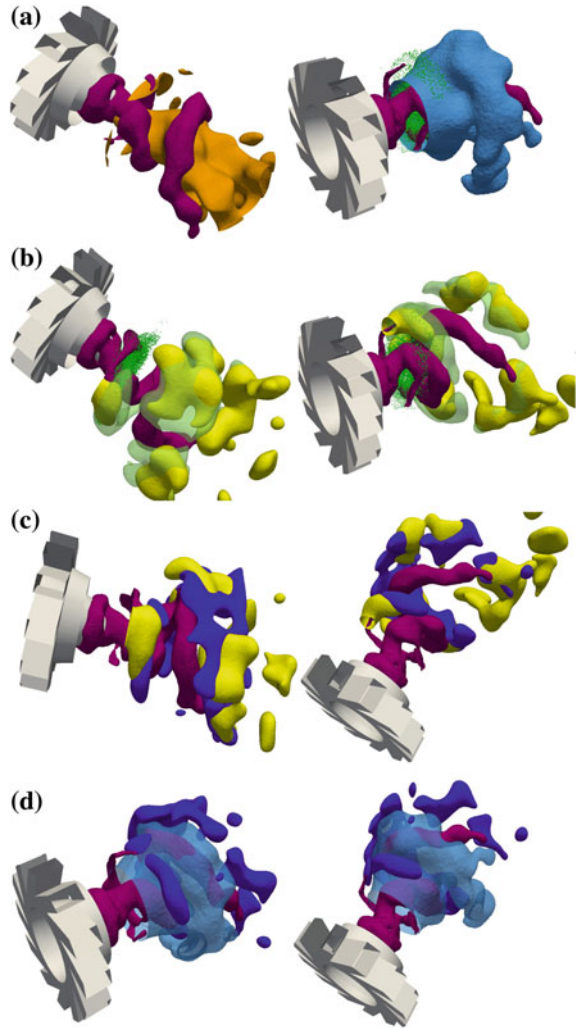
To ease the understanding of the complex PVC/spray flame interactions, a sketch based on the observation of all the filtered variables at several chosen instants is shown in Fig. 9. The sketch represents the interlacing of the important zones of the flow: the PVC, the fuel droplets, the evaporated fuel pockets and the heat release fronts. This figure again highlights the strong impact of the PVC on the dynamics of the flow.
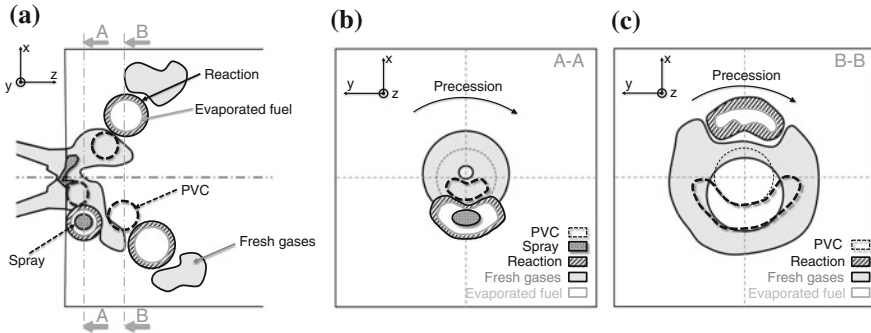
Fig. 9 Illustration of the PVC/spray flame interactions. **a** side view, **b** and **c** view of planes that are orthogonal to the burner axis

3 Conclusions

Simulations of the MERCATO burner were carried out in reactive flow conditions with liquid fuel injection. These simulations were validated against experimental and numerical data obtained by another group. The objective of the paper was to demonstrate the potential of implicit high-order filters to extract the large-scale dynamics of the flow even for complex burners. In particular, the flow in the MERCATO burner exhibits a strong Precessing Vortex Core, which imposes its dynamics to the spray and the flame. This leads to periodic fluctuations of the flame anchoring and of the heat release in the burner at the PVC frequency.

In this paper, a single set of operating conditions was investigated. The analysis, which was carried out may be different if the droplet diameter distribution changes. Indeed, the segregation effect of the PVC on the fuel droplets is directly related to the diameter distribution. Changing the PVC related Stokes number may reduce the segregation of the fuel droplets and reduce the interactions. Studying other sets of operating conditions would also be interesting to know if the PVC has a positive or negative impact on the global performances of the burner: compactness of the flame, lean blow-out limits, pollutant emissions.

References

1. Boxx I, Stöhr M, Carter C, Meier W (2010) Temporally resolved planar measurements of transient phenomena in a partially pre-mixed swirl flame in a gas turbine model combustor. Combust Flame 157(8):1510–1525

2. Caux-Brisebois V, Steinberg AM, Arndt CM, Meier W (2014) Thermo-acoustic velocity coupling in a swirl stabilized gas turbine model combustor. Combust Flame 161(12):3166–3180

3. Colin O, Ducros F, Veynante D, Poinsot T (2000) A thickened flame model for large eddy simulations of turbulent premixed combustion. Phys Fluids (1994-present) 12(7):1843–1863

4. Dubief Y, Delcayre F (2000) On coherent-vortex identification in turbulence. J Turbul (1)

5. Franzelli B, Riber E, Sanjose M, Poinsot T (2010) A two-step chemical scheme for kerosene-air premixed flames. Combust Flame 157(7):1364–1373

6. Galley D, Ducruix S, Lacas F, Veynante D (2011) Mixing and stabilization study of a partially premixed swirling flame using laser induced fluorescence. Combust Flame 158(1):155–171

7. Guedot L, Lartigue G, Moureau V (2015) Design of implicit high-order filters on unstructured grids for the identification of large-scale features in large-eddy simulation and application to a swirl burner. Phys Fluids (1994-present) 27(4):045107

8. Hannebique G (2013) Etude de la structure des flammes diphasiques dans les brûleurs aéronautiques. PhD thesis

9. Hunt JCR, Wray AA, Moin P (1988) Eddies, streams, and convergence zones in turbulent flows, pp 193–208

10. Jones W, Lettieri C, Marquis AJ, Navarro-Martinez S (2012) Large eddy simulation of the two-phase flow in an experimental swirl-stabilized burner. Int J Heat Fluid Flow 38:145–158

11. Lecourt R, Linassier G, Lavergne G (2011) Detailed characterisation of a swirled air/kerosene spray in reactive and non-reactive conditions downstream from an actual turbojet injection system. In: ASME 2011 turbo expo: turbine technical conference and exposition. American Society of Mechanical Engineers, pp 185–194

12. Légier J, Poinsot T, Veynante D (2000) Dynamically thickened flame les model for premixed and non-premixed turbulent combustion. In: Proceedings of the summer program. Citeseer, pp 157–168

13. Lucca-Negro O, O'doherty T (2001) Vortex breakdown: a review. Prog Energy Combust Sci 27(4):431–481

14. Moureau V, Bérat C, Pitsch H (2007) An efficient semi-implicit compressible solver for large-eddy simulations. J Comput Phys 226(2):1256–1270

15. Moureau V, Domingo P, Vervisch L (2011) Design of a massively parallel cfd code for complex geometries. Comptes Rendus Mécanique 339(2–3):141–148. http://dx.doi.org/10.1016/j.crme.2010.12.001

16. Nabil T, Kareem WA, Izawa S, Fukunishi Y (2000) Extraction of coherent vortices from homogeneous turbulence using curvelets and total variation filtering methods. J Turbul 57:76–86

17. Poinsot T, Veynante D (2011) Theoretical and numerical combustion

18. Providakis T, Zimmer L, Scouflaire P, Ducruix S (2013) Characterization of the coherent structures in swirling flames stabilized in a two-staged multi-injection burner: Influence of the staging factor. C R Mécanique 341(1):4–14

19. Roux S, Lartigue G, Poinsot T, Meier U, Bérat C (2005) Studies of mean and unsteady flow in a swirled combustor using experiments, acoustic analysis, and large eddy simulations. Combust Flame 141(1–2):40–54

20. Sanjosé M, Senoner J, Jaegle F, Cuenot B, Moreau S, Poinsot T (2011) Fuel injection model for euler-euler and euler-lagrange large-eddy simulations of an evaporating spray inside an aeronautical combustor. Int J Multiph Flow 37(5):514–529

21. Steinberg AM, Boxx I, Stöhr M, Meier W, Carter CD (2012) Effects of flow structure dynamics on thermoacoustic instabilities in swirl-stabilized combustion. AIAA J 50(4):952–967

22. Stöhr M, Boxx I, Carter C, Meier W (2011) Dynamics of lean blowout of a swirl-stabilized flame in a gas turbine model combustor. Proc Combust Inst 33(2):2953–2960

23. Syred N (2006) A review of oscillation mechanisms and the role of the precessing vortex core (PVC) in swirl combustion systems. Prog Energy Combust Sci 32(2):93–161

DNS and LES of the Flow Over Periodic Hills Based on a Discontinuous Galerkin Approach

Marta de la Llave Plata, Vincent Couaillier and Marie-Claire le Pape

Abstract A high-order discontinuous Galerkin (DG) approach is used for the DNS and LES of the flow over periodically arranged hills. In order to assess the capacity of the DG method to capture the Reynolds-number dependent features of the flow, four Reynolds numbers are considered: 2800, 10 595, 19 000, and 37 000. The DG solutions are compared with the reference data available in the literature. For $Re_b = 10\,595$ the no-model and the WALE LES approaches are compared. The hp-convergence analyses performed for the DNS demonstrate the superior performance of increasing the polynomial order as compared to refining the mesh. It appears from this study that the use of a subgrid modelling approach together with an appropriate level of local hp-refinement could greatly improve the solution without penalising the computational cost of the simulation.

1 Introduction

The study of turbulence has been an area of active research for over a century. The numerous industrial applications in which turbulence is present justify the great effort devoted to understanding the complex physics of turbulent flows.

The accurate and efficient simulation of turbulent flows imposes two main requirements on the discretization scheme. First, it must be able to provide very low levels of dissipation and dispersion, so that the finest scales of turbulence are accurately resolved over long integration periods. Second, it must be highly parallelizable so that we can achieve high performance on many-core architectures.

M. de la Llave Plata (✉) · V. Couaillier · M.-C. le Pape
ONERA, 92322 Châtillon, France
e-mail: marta.de_la_llave_plata@onera.fr

V. Couaillier
e-mail: vincent.couaillier@onera.fr

M.-C. le Pape
e-mail: marie-claire.le_pape@onera.fr

The high-order DG method meets these two requirements, i.e. high-order accuracy and excellent parallel capabilities. This is the reason why the scientific community is currently working on the industrialization of this type of approach [5].

The DG method is based on the variational projection of the Navier-Stokes (N-S) equations onto a hierarchy of polynomial basis functions. It is characterised by being locally conservative and by providing high-order spectral accuracy on irregular meshes. The resulting numerical scheme is compact which makes them particularly well suited to the implementation of highly-parallel algorithms. DG approximations also provide a natural framework for the implementation of adaptive schemes, not only based on local mesh h-refinement, but also on p-refinement. The overall flexibility provided by the DG approach therefore makes this type of discretization a very appealing tool for the simulation of inhomogeneous high-Reynolds-number flows.

In this work we will focus on the use of a modal DG approach for the simulation of a detached flow configuration, the flow over a 2D periodic hill. This test case is of interest for the evaluation of high-order methods in the context of DNS and LES, due to the periodic boundary conditions and the 2D character of the geometry which significantly reduces the computational cost. A number of DG simulations of this configuration at $Re_b = 2800$ and $10\,595$ have been reported in the recent literature (see e.g. [6, 7]). Here, we extend the study by considering also the higher Reynolds numbers $Re_b = 19\,000$ and $37\,000$. An hp-convergence analysis is carried out for the DNS at $Re_b = 2800$. As regards the LES simulations at $Re_b = 10\,595$ the no-model and the WALE model [4] approaches are tested. For the higher Reynolds numbers $Re_b = 19\,000$ and $37\,000$ only the WALE approach is considered. The DG solutions are compared with the reference CFD data provided by Breuer et al. [1] and Manhart et al. [2], and the experimental data from Rapp [3].

2   The Discontinuous Galerkin Method

The simulation results presented here have been performed using the DG unstructured solver *Aghora* [8, 9] developed at ONERA. This solver is designed to solve the full set of compressible N-S equations, namely,

$$\mathbf{U}_t + \nabla \cdot (\mathbf{f_c} - \mathbf{f_v}) = \mathbf{S} \tag{1}$$

where $\mathbf{U} = (\rho, \rho\mathbf{V}, \rho E)^T$ is the vector of conservative variables. The vectors $\mathbf{f_c}$, and $\mathbf{f_v}$ are the convective and viscous fluxes, respectively, and $\mathbf{S}$ is a source term.

The DG discretization implemented into *Aghora* is based on a modal approach that relies on the use of a hierarchy of orthogonal polynomial functions as basis for the Galerkin projection. The modal basis used is that proposed in [10] by Bassi et al. The discrete orthogonal polynomial spaces are directly computed in physical space. The methodology consists in defining a starting set of monomial basis functions in each (arbitrarily shaped) element and applying a modified Gram-Schmidt orthogonalization procedure. This ensures the orthogonality of the basis, and thereby the

diagonality of the mass matrix. Numerical integration on general-shaped elements is efficiently performed by means of a Gaussian quadrature. The time integration is performed using an explicit third-order accurate Runge-Kutta method [11]. The DG method used in this work is briefly outlined below.

We start by defining a shape-regular partition of the domain Ω, into N non-overlapping and non-empty cells κ of characteristic size h. We also define the sets $\mathscr{E}_i$ and $\mathscr{E}_b$ of interior and boundary faces in Ω_h, such that $\mathscr{E}_h = \mathscr{E}_i \cup \mathscr{E}_b$.

Let $\mathscr{V}_h^p = \{\phi \in L^2(\Omega_h) : \phi|_\kappa \in \mathscr{P}^p(\kappa), \ \forall \kappa \in \Omega_h\}$ be the functional space of piecewise polynomials of degree at most p, and $(\phi_\kappa^1, \ldots, \phi_\kappa^{N_p}) \in \mathscr{P}^p(\kappa)$ a hierarchical and orthonormal modal basis of $\mathscr{V}_h^p$, of dimension N_p, confined to κ. The solution in each element is thus expressed as

$$\mathbf{u}_h(\mathbf{x}, t) = \sum_{l=1}^{N_p} \phi_\kappa^l(\mathbf{x})\mathbf{U}_\kappa^l(t), \quad \forall \mathbf{x} \in \kappa, \ \kappa \in \Omega_h, \ \forall t \geq 0, \tag{2}$$

in which the polynomial coefficients $(\mathbf{U}_\kappa^l)_{1 \leq l \leq N_p}$ represent the degrees of freedom (DOF) of the discrete problem in element κ. The semi-discrete variational form of system of Eq. (1) thus reads: find $\mathbf{u}_h$ in $\mathscr{V}_h^p$ such that $\forall \phi_h \in \mathscr{V}_h^p$ we have

$$\int_{\Omega_h} \phi_h \partial_t \mathbf{u}_h dV + \mathscr{L}_c(\mathbf{u}_h, \phi_h) + \mathscr{L}_v(\mathbf{u}_h, \phi_h) = \int_{\Omega_h} \phi_h \mathbf{S}_h \tag{3}$$

In Eq. (3) $\mathscr{L}_c$ and $\mathscr{L}_v$ represent the weak form of the convective and viscous terms, respectively. The right-hand-side of Eq. (3) is the variational projection of the source term $\mathbf{S}$ onto $\mathscr{V}_h^p$.

We now introduce the following notation: for a given interface e in $\mathscr{E}_i$ we define the average operator $\{u\} = (u^+ + u^-)/2$ and the jump operator $[\![\mathbf{u}]\!] = \mathbf{u}^+ \otimes \mathbf{n} - \mathbf{u}^- \otimes \mathbf{n}$, where u^+ and u^- are the traces of the variable u at the interface between elements κ^+ and κ^-. The DG discretization of the convective terms then reads

$$\mathscr{L}_c(\mathbf{u}_h, \phi_h) = -\int_{\Omega_h} \mathbf{f}_c(\mathbf{u}_h) \cdot \nabla_h \phi_h dV$$
$$+ \int_{\mathscr{E}_i} [\![\phi_h]\!]\mathbf{h}_c(\mathbf{u}_h^+, \mathbf{u}_h^-, \mathbf{n})dS + \int_{\mathscr{E}_b} \phi_h^+ \mathbf{f}_c(\mathbf{u}_b) \cdot \mathbf{n}dS \tag{4}$$

where the boundary values $\mathbf{u}_b = \mathbf{u}_b(\mathbf{u}_h^+, \mathbf{u}_{ext}, \mathbf{n})$, with $\mathbf{u}_{ext}$ a reference external state, are computed so that the boundary conditions are satisfied on $\mathscr{E}_b$. The numerical flux $\mathbf{h}_c$ is chosen so that it is consistent and compact. For the simulations presented in this paper the local Lax-Friedrichs (LLF) flux has been employed. The discretization of the viscous terms is performed using the *symmetric interior penalty* (SIP) method [12],

$$\mathcal{L}_v(\mathbf{u}_h, \phi_h) = \int_{\Omega_h} \mathbf{f}_v(\mathbf{u}_h, \nabla_h \mathbf{u}_h) \cdot \nabla_h \phi_h \, dV$$

$$- \int_{\mathcal{E}_i} [\![\phi_h]\!] \{\mathbf{f}_v(\mathbf{u}_h, \nabla_h \mathbf{u}_h)\} \cdot \mathbf{n} \, dS - \int_{\mathcal{E}_b} \phi_h^+ \mathbf{f}_v(\mathbf{u}_b, \nabla \mathbf{u}_b) \cdot \mathbf{n} \, dS$$

$$- \int_{\mathcal{E}_i} [\![\mathbf{u}_h]\!] \{\mathbf{G}^T(\mathbf{u}_h) \nabla_h \phi_h\} \cdot \mathbf{n} \, dS - \int_{\mathcal{E}_b} (\mathbf{u}_h^+ - \mathbf{u}_b) \{\mathbf{G}^T(\mathbf{u}_b) \nabla_h \phi_h^+)\} \cdot \mathbf{n} \, dS$$

$$+ \int_{\mathcal{E}_i} \eta_{IP} [\![\mathbf{u}_h]\!][\![\phi_h]\!] \, dS + \int_{\mathcal{E}_b} \eta_{IP} (\mathbf{u}_h^+ - \mathbf{u}_b) \phi_h^+ \, dS \qquad (5)$$

where $\mathbf{G} = \partial \mathbf{f}_v / \partial (\nabla_h \mathbf{u}_h)$ is the so-called homogeneity tensor. The penalty parameter η_{IP} has to be chosen sufficiently large to ensure the coercivity of the bilinear form and thus the numerical stability of the simulation [12].

3 The 2D Periodic Hill Configuration: Numerical Results

The flow configuration considered here represents a fully developed turbulent flow over periodically arranged hills, exhibiting separation from the curved surface, reattachment, and post-reattachment recovery. A detailed description of this configuration can be found in [13]. The flow is driven by a spatially constant mean pressure gradient in the streamwise direction. This pressure gradient is designed to ensure a target mass flow rate according to the specified Reynolds number Re_b, based on the hill height h and the bulk velocity u_b above the crest. Periodicity of the flow is assumed in the streamwise and spanwise directions, and isothermal no-slip boundary conditions are imposed on the lower and upper walls. The Mach number is set to $M_0 = 0.1$ so that the flow regime is quasi-incompressible. Two levels of mesh refinement have been used in this study, shown in Fig. 1. A coarse fourth-order mesh composed of 8 192 elements and a twice finer version of this mesh composed of 65 536 elements. Both meshes were generated using the 3D FE mesh generator Gmsh [14]. The details of the high-order grids used for the DG simulations as well as those used in the reference finite volume (FV) computations in [1] (LESOCC code) and [2] (MGLET code) are provided in Table 1. The polynomial degree of the

(a) Coarse mesh $32 \times 16 \times 16$ (b) Fine mesh $64 \times 32 \times 32$
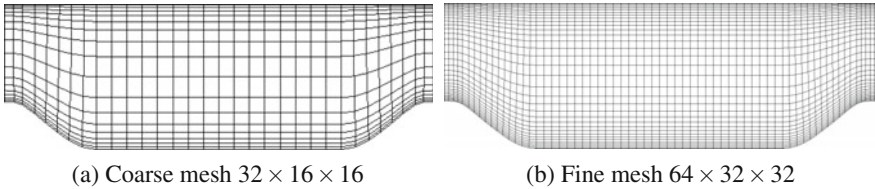
Fig. 1 Fourth-order meshes used in the DG simulations

Table 1 Grid resolutions used for the DNS and LES computations

	Grid resolution	# Elements	Grid order
FV LESOCC	–	12.4 M	1
FV MGLET	$216 \times 168 \times 104$	3.77 M	1
DG Coarse mesh	$32 \times 16 \times 16$	8192	4
DG Fine mesh	$64 \times 32 \times 32$	65 536	4

simulations is set to $p = 3$, 4 up to 5 for the DNS simulations on the coarse grid, and $p = 3$ and 4 for all other simulations. The computational results presented in the following sections have been obtained using a pure MPI approach on the Cines machine Occigen (project dsn7441). The coarse mesh computations were carried out using 264 cores, whereas the fine mesh computations are performed on 2208 cores.

The normalised time step used in the different computations is of the order of 10^{-4}. The solution is advanced in time until a statistically steady state is reached. From this point, the flow statistics are gathered over a sufficient number of convective times $t_c = 9h/u_b$. The time-averaged data is also averaged in the spanwise direction to achieve more rapidly statistical convergence.

For each computation, the resolution at the wall is evaluated in terms of the normalised values of $y^+ = \Delta y_c u_\tau / \nu$, where Δy_c denotes the height of the first cell at the wall, ν is the kinematic viscosity, and $u_\tau = \sqrt{\tau_w/\rho}$ is the friction velocity, being τ_w the wall-shear stress and ρ the density at the wall. These values are measured at the point of maximum wall-shear stress, which is located on the windward side of the hill. They are compiled in Table 2. Note that in the DG approach, an estimate of the effective y^+ can be obtained by dividing the cell height by the number of DOF within the element, i.e. for a polynomial approximation of degree p we have $y^+ = \Delta y_c^+/(p + 1)$. We can see from Table 2 that for the higher Reynolds numbers the values of y^+ are above the recommended value ($y^+ < 2$), although in line with the values reported in [2]. As pointed out by the author, the distance over which the maximum wall stress is acting on the flow is very short (≈ 0.5 h), and thus at all other positions the wall resolution can be considered as sufficient.

The results from the different DG simulations are analysed in detailed in the following sections. To this end, the profiles of mean streamwise velocity U, as well

Table 2 Wall resolution Δy_{max}^+ at point of maximum wall-shear stress for the DG simulations

Re_b	LES approach	Simulation	# DOFs	$\Delta y_{max}^+/(p + 1)$
2800	–	DG-p4, fine mesh	1.02 M	1.7
10 595	No-model	DG-p3, fine mesh	4.19 M	5.7
10 595	WALE	DG-p3, fine mesh	4.19 M	5.6
19 000	WALE	DG-p3, fine mesh	4.19 M	9.0
37 000	WALE	DG-p3, fine mesh	4.19 M	14.3

as the turbulent Reynolds stresses $\langle u'v' \rangle$ are compared against the available reference data. We pay particular attention to stations $x/h = 0.5$ and $x/h = 4$. The first $x/h = 0.5$ corresponds to a position located right after the separation region and intersects the strong shear layer generating from the detachment point. The second station $x/h = 4$ is placed at the end of the recirculation bubble (close to the reattachment point for the lower Reynolds numbers).

3.1 Comparison of DG Solutions at $Re_b = 2800$ up to $37\,000$

The streamlines of the time-averaged velocity field for $Re_b = 2800$ up to $37\,000$ are depicted in Fig. 2. As expected, the reattachment point moves upstream with increasing Reynolds number, reducing the size of the recirculation bubble. The position of the reattachment point at the lowest Reynolds number is $x_R/h \approx 5.4$ which is in agreement with the value reported in [1]. For $Re_b = 10\,595$ the reattachment point is located at $x_R/h \approx 3.9$, which is slightly different from the experimental value ($x_R/h \approx 4.21$) [18] and from the reference LESOCC simulation ($x_R/h \approx 4.69$). Finally, for the highest Reynolds number $Re_b = 37\,000$ the reattachment point is located at $x_R/h \approx 3.2$ not far from the value of $x_R/h \approx 3.68$ reported by Chaouat and Schiestel [19] in their hybrid RANS/LES simulation on a grid composed of 10^6 points.

The profiles of time-averaged wall-shear stress at the bottom wall for $Re_b = 2800$ are depicted in Fig. 3a. We observe that all discretizations, except for the $DG - p3$ simulation on the coarse mesh, are able to reproduce the peak of maximum wall-shear stress located on the windward side of the hill. The strong oscillations near the separation point exhibited by the $DG - p3$ and $DG - p4$ coarse mesh simulations

(a) $Re_b = 2800$

(b) $Re_b = 10\,595$

(b) $Re_b = 19\,000$

(c) $Re_b = 37\,000$
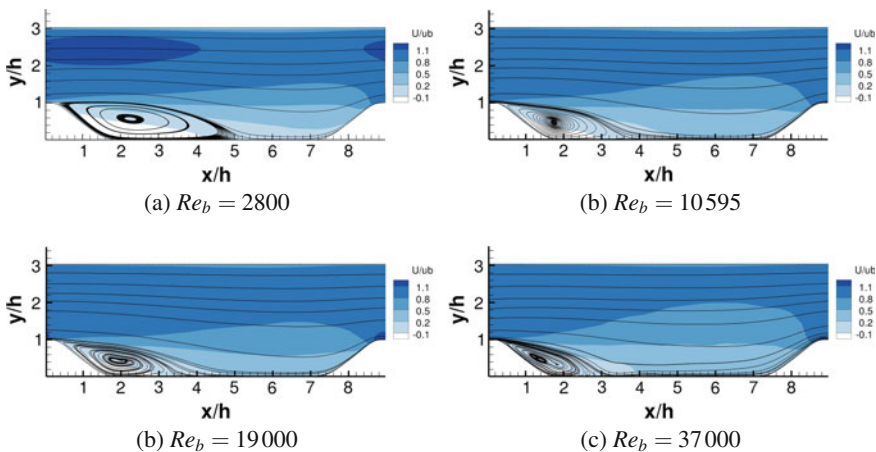
Fig. 2 Streamlines of the time-averaged streamwise velocity field U/u_b from DG simulations

(a) Wall-shear stress $Re_b = 2800$ (b) Wall-shear stress $Re_b = 2800$ up to $Re_b = 37\,000$
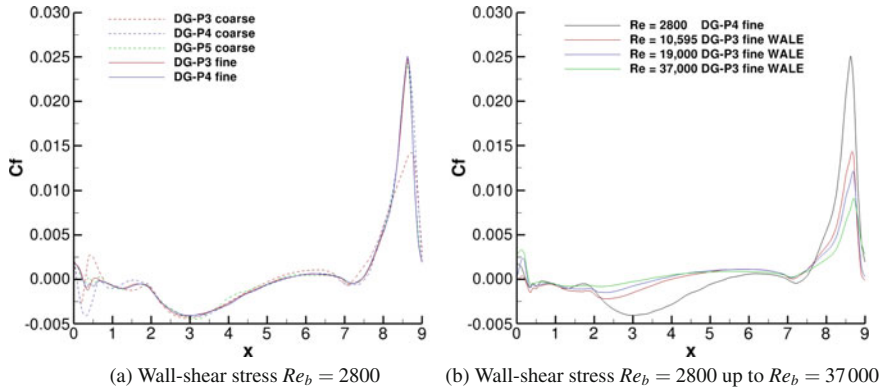
Fig. 3 Profiles of wall-shear stress at bottom wall for the DG simulations

are clearly due to a lack of resolution in this area. Indeed, this oscillating behaviour disappears when the polynomial degree is increased. This is shown by the results obtained from the $DG - p5$ coarse mesh simulation, which closely match the data obtained from the best resolved simulations for a reduced number of degrees of freedom (1.77 M in the $DG - p5$ with respect to 4.19 M and 8.19 M in the $DG - p3$ and $DG - p4$ fine mesh simulations, respectively). This outcome emphasises the greater advantage of using local hp-adaptation for flow configurations featuring highly localised phenomena.

In Fig. 3b we compare the profiles of wall-shear stress for all four Reynolds numbers. The trends are in agreement with the results reported in [1].

3.2 DNS Results at $Re_b = 2800$

Figure 4 shows the profiles of averaged streamwise velocity and Reynolds stresses obtained from the DG DNS at the different levels of resolution considered. They are compared to the DNS data from the LESOCC code. The computational cost per convective time of the DG simulations performed are compiled in Table 3. These values have been normalised by the cost of the coarsest simulation which is considered as 1.

It can be observed that all DG simulations are able to reproduce the main features of the flow. Naturally, the best match with the reference DNS is obtained for the $DG - p4$ simulation on the fine grid (8.19 M DOF), as we reach numerical convergence when the number of DOF increases. However, if we look carefully at the solution from the $DG - p5$ coarse mesh simulation, we observe that the match with the $DG - p4$ fine mesh simulation and the reference data is remarkably good. This is taking into account the great reduction in the number of DOF with respect to the two other simulations (8.19 M and 13.1 M, respectively). It is also worth noting that the

Mean streamwise velocity U/u_b at $x = 0.5h$ (left) and $x = 4h$ (right)

Shear stresses $\langle u'v' \rangle / u_b^2$ at $x = 0.5h$ (left) and $x = 4h$ (right)
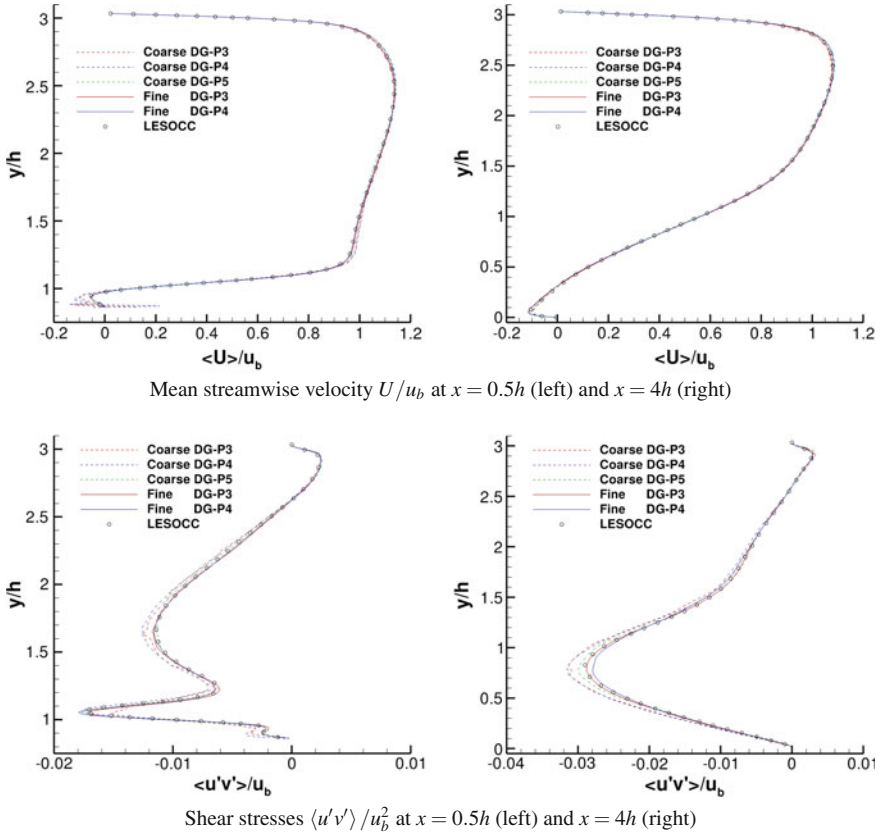
Fig. 4 DNS at $Re_b = 2800$. Comparison of DG simulations with reference LESOCC simulation at station **x = 0.5 h** (*left panels*) and **x = 4 h** (*right panels*). ∘ : LESOCC 2nd-order (13.1 M DOF); - - - : $DG - p3$ on coarse mesh (0.52 M DOF); - - - : $DG - p4$ on coarse mesh (1.02 M DOF); - - - : $DG - p5$ on coarse mesh (1.77 M DOF); —— : $DG - p3$ on fine mesh (4.19 M DOF); —— : $DG - p4$ on fine mesh (8.19 M DOF)

Table 3 Computational cost of DG-DNS at $Re_b = 2800$

Simulation	#DOFs	Δt	#Cores	CPU time/tc
DG-p3 coarse	0.52 M	$2.5 \cdot 10^{-4}$	264	1.0
DG-p4 coarse	1.02 M	$2.5 \cdot 10^{-4}$	264	2.8
DG-p5 coarse	1.77 M	$1.7 \cdot 10^{-4}$	264	13.1
DG-p3 fine	4.19 M	$1.8 \cdot 10^{-4}$	2208	10.8
DG-p4 fine	8.19 M	$1.4 \cdot 10^{-4}$	2208	39.9

Mean streamwise velocity U/u_b at $x = 0.5h$ (*left*) and $x = 4h$ (*right*)

Shear stresses $\langle u'v' \rangle /u_b^2$ at $x = 0.5h$ (*left*) and $x = 4h$ (*right*)
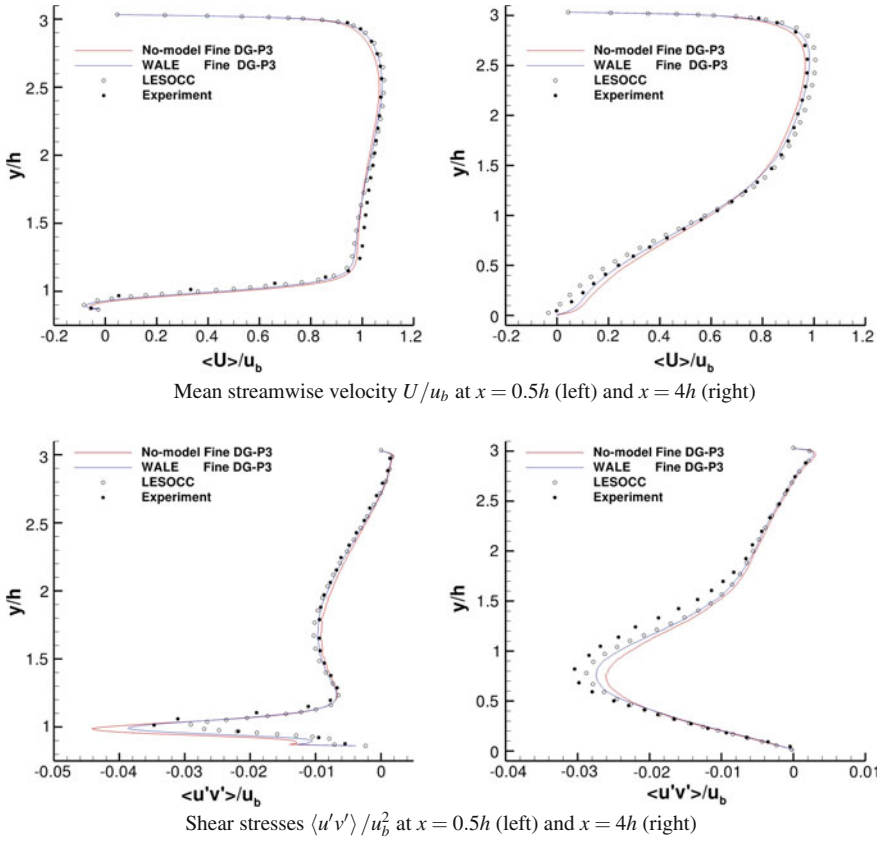
Fig. 5 **LES at $Re_b = 10\,595$.** Comparison of DG simulations with reference LESOCC simulation and experimental data at station **x = 0.5 h** (*left panels*) and **x = 4 h** (*right panels*). ● : Experiment; ○: LESOCC 2nd-order (13.1 M DOF); ——— : No-model $DG - p3$ simulation on fine mesh (4.19 M DOF); ——— : WALE $DG - p3$ simulation on fine mesh (4.19 M DOF); $---$: WALE $DG - p4$ simulation on coarse mesh (1.02 M DOF)

computational cost of the $DG - p5$ is significantly lower than that of the $DG - p4$ simulation and only slightly higher than that of the $DG - p3$ simulation on the fine mesh, as seen from Table 3.

As already discussed in the previous section, the $DG - p3$ and $DG - p4$ coarse mesh simulations exhibit an oscillatory behaviour in the vicinity of the separation point (see left upper panel in Fig. 4). These oscillations disappear when the polynomial order is increased to $p = 5$.

We can conclude from this analysis that an optimal performance of the DG method could be obtained by appropriate local hp-adaptation. This would allow us to greatly reduce the cost of the simulation while keeping the same level of accuracy as that provided by uniform h or p-refinement.

Mean streamwise velocity U/u_b at $x = 0.5h$ (left) and $x = 4h$ (right)

Shear stresses $\langle u'v' \rangle /u_b^2$ at $x = 0.5h$ (left) and $x = 4h$ (right)
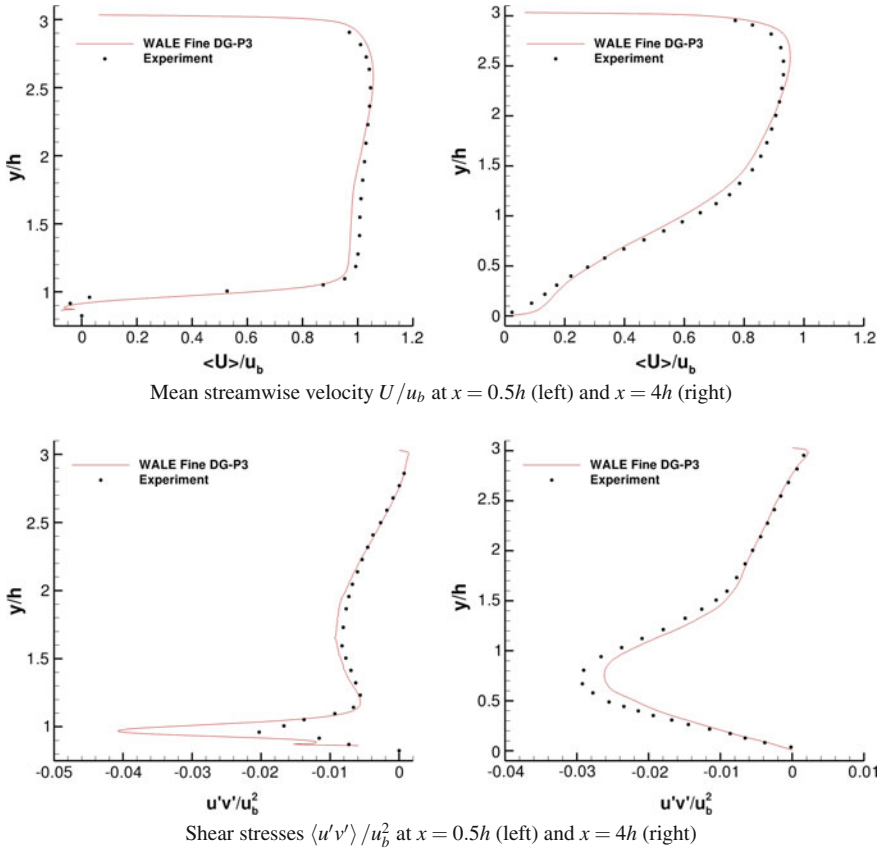
Fig. 6 LES at $Re = 19\,000$. Comparison of DG simulations with experimental data at station **x = 0.5h** (left panels) and **x = 4h** (right panels). • : Experiment; —— : WALE $DG - p3$ simulation on fine mesh (4.19 M DOF)

3.3 LES Results at $Re_b = 10\,595$

Figure 5 shows the profiles of mean velocity and turbulent stresses obtained from the $DG - p3$ fine mesh simulations using the no-model and the WALE approaches. They are compared to the LES data produced by the LESOCC code as well as to the experimental data from Rapp [3].

It can be seen from these plots that at this moderate Reynolds number the results yielded by the no-model and the WALE approaches are not fundamentally different. The WALE approach, however, seems to provide slightly better results, specially in the region behind the separation point ($x = 0.5$ h).

Mean streamwise velocity U/u_b at $x = 0.5h$ (left) and $x = 4h$ (right)

Shear stresses $\langle u'v' \rangle /u_b^2$ at $x = 0.5h$ (left) and $x = 4h$ (right)
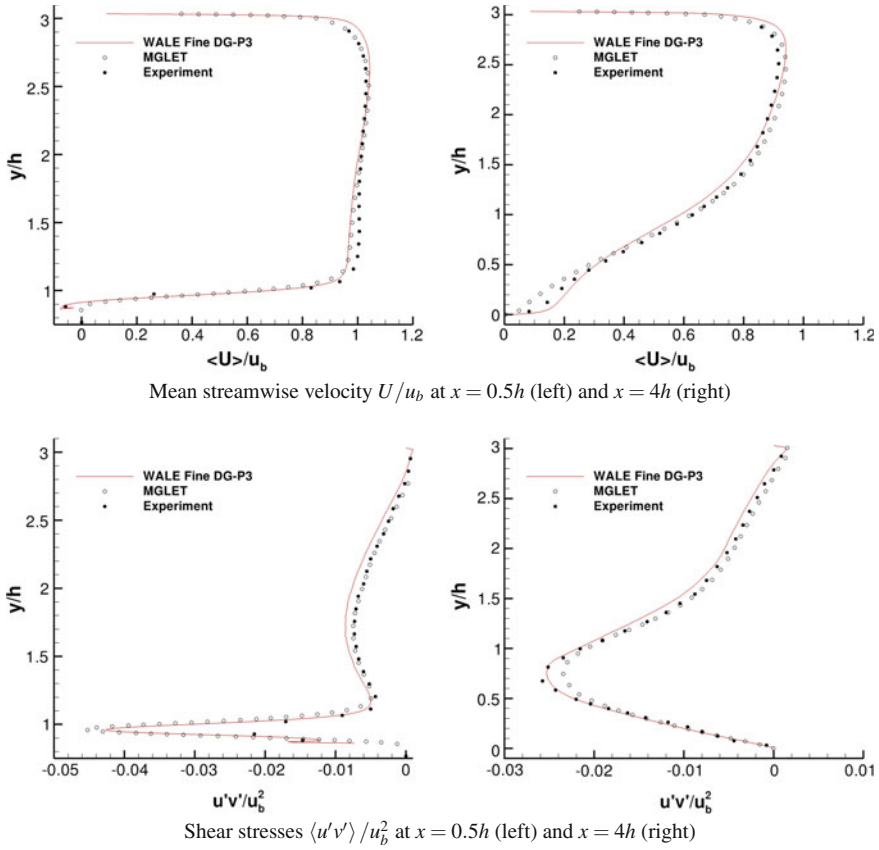
Fig. 7 LES at $Re = 37\,000$. Comparison of DG simulations with reference MGLET simulation and experimental data at station **x = 0.5h** (left panels) and **x = 4h** (right panels). ● : Experiment; ○ : MGLET 2nd-order (4.1 M DOF); —— : WALE $DG - p3$ simulation on fine mesh (4.19 M DOF)

3.4 LES Results at $Re_b = 19\,000$

In Fig. 6 the profiles of mean velocity and Reynolds stresses obtained from the $DG -$ $p3$ fine mesh simulation are compared with the experimental data from Rapp [3]. We note that at this higher Reynolds number the DG scheme employed ($p = 3$ and LLF numerical flux) did not provide a sufficient amount of numerical dissipation to achieve a stable simulation. This was also the case for $Re_b = 37\,000$.

An overall good agreement is found with the experimental data. The main differences are found in the vicinity of the separation point. At this location the profiles of $\langle u'v' \rangle$ from the DG simulation present a strong overshoot near the wall, which might suggest a need to improve the resolution in this area. It is difficult to discern, however, whether the discrepancies observed at some stations in the channel are due to

numerical artifacts, or to measurement uncertainties during the experiment. Further DG simulations at this higher Reynolds number, ideally using a locally hp-adapted grid, could help understand the nature of these differences.

4 LES Results at $Re_b = 37\,000$

Figure 7 shows the profiles of mean velocity and Reynolds stresses obtained from the $DG - p3$ fine mesh simulation using the WALE approach. They are compared to the LES data produced by the MGLET code [2] as well as to the experimental data from Rapp [3].

An overall good agreement is found between the mean streamwise velocity profiles and the reference data. Note that the overshoot exhibited by the shear stress $\langle u'v' \rangle / u_b^2$ near the bottom wall at $x = 0.5h$ is also observed in the MGLET profiles as well as in the numerical results reported by Chaouat and Schiestel [19].

5 Conclusions

The capacity of a modal DG approach to capture the Reynolds-number dependent features in a detached flow configuration has been assessed for Reynolds numbers ranging from $Re_b = 2800$ up to $37\,000$.

For the DNS at $Re_b = 2800$, the hp-convergence studies demonstrate the superior performance of increasing the polynomial order as compared to refining the mesh. A very good agreement with the reference simulation of Breuer et al. [1] is actually obtained by considering a sixth-order discretization ($p = 5$) on a very coarse mesh, involving only 1.77M DOF with respect to the 13.1M DOF used in the reference FV computation.

For $Re_b = 10\,595$, $19\,000$, and $37\,000$ fourth-order LES simulations ($p = 3$) based on the WALE approach have been carried out on a grid composed of 65\,536 elements, which leads to 4.19M DOF. All simulations are able to capture the main features of the flow. In particular, a good agreement with the reference data is found for $Re_b = 10\,595$ and $Re_b = 19\,000$. The discrepancies found for $Re_b = 37\,000$ between the DG simulation and the experiment are in line with those reported in [2] using the MGLET FV code on a mesh composed of 4.1M points and in [19] using a hybrid RANS/LES approach on a 1M point grid. An additional no-model LES (or under-resolved DNS) simulation has been performed at $Re_b = 10\,595$. The solutions from the no-model and the WALE approaches do not appear to be fundamentally different. The WALE approach, however, seems to provide slightly more accurate results, specially in the vicinity of the separation point and in the recirculation area. Note that for $Re_b = 19\,000$ and $37\,000$ the no-model approach did not yield stable simulations, which is a manifestation of the very low dissipation level provided by the DG scheme.

In view of these results, we can conclude that the use of a subgrid modelling approach together with an appropriate level of local *hp*-refinement could greatly improve the accuracy of the LES solutions. Furthermore, in order to reduce the computational cost associated with the use of high polynomial degrees it would be advantageous to use a hybrid MPI/openMP approach. This is the subject of current research in the framework of the Aghora project.

References

1. Breuer M, Peller N, Rapp Ch, Manhart M (2009) Flow over periodic hills—numerical and experimental study in a wide range of Re. Comput Fluids 38:433–457
2. Manhart M, Rapp Ch, Peller N, Breuer M, Aybay O, Denev J, Falconi CJ (2011) Assessment of eddy resolving techniques for the flow over periodically arranged hills up to $Re = 37,000$. In: Salvetti MV, Geurts B, Meyers J, Sagaut P (eds) Quality and reliability of LES II, ERCOFTAC Series 16. Springer, pp 361–37
3. Rapp Ch (2009) Experimentelle Studie der turbulenten Strömung über periodische Hügel, PhD Thesis, Technische Universität München, Germany
4. Nicoud F, Ducros F (1999) Subgrid-scale stress modelling based on the square of the velocity gradient tensor, flow. Turb Comb 62:183–200
5. Kroll N, Hirsch C, Bassi F, Johnston C, Hillewaert K (2015) IDIHOM: industrialization of high-order methods—a top-down approach, notes on numerical fluid mechanics and multidisciplinary design series, 128. Springer
6. Diosady L, Murman S (2014) DNS of flows over periodic hills using a discontinuous galerkin spectral-element method. In: AIAA Paper 2014, p 2784
7. Beck AD, Bolemann T, Flad D, Frank H, Gassner G, Hindenlang F, Munz C-D (2014) High order discontinuous Galerkin spectral element methods for transitional and turbulent flow simulations. Int J Numer Methods Fluids 76:522–548
8. Renac F, de la Llave Plata M, Martin E, Chapelier JB, Couaillier C (2015) Aghora: a high-order dg solver for turbulent flow simulations. In: IDIHOM: industrialisation of high-order methods—a top down approach, notes on numerical fluid mechanics and multidisciplinary design, 128. Springer, pp 315–335
9. Chapelier JB, de la Llave Plata M, Renac F, Lamballais E (2014) Evaluation of a high-order DG method for the DNS of turbulent flows. Comput Fluids, 95, pp 206–226
10. Bassi F, Botti L, Colombo A, Di Pietro DA, Tesini P (2012) On the flexibility of agglomeration based physical space DG discretizations. J Comput Phys 231:45–65
11. Gottlieb S, Shu CW, Tadmor E (2001) Strong stability-preserving high-order time discretization methods. SIAM Rev 43:89–112
12. Arnold DN, Brezzi F, Cockburn B, Marini LD (2001) Unified analysis of discontinuous Galerkin methods for elliptic problems. SIAM J Numer Anal 39:1749–1779
13. Rodi W, Bonnin JC, Buchal T (eds) (1995) ERCOFTAC workshop on data bases and testing of calculation methods for turbulent flows, University of Karlsruhe
14. Geuzaine C, Remacle J-F (2009) Gmsh: a three-dimensional finite element mesh generator with built-in pre- and post-processing facilities. Int J Numer Meth Eng 79:1309–1331
15. Chapelier JB (2013) Développement et évaluation de la méthode de Galerkin discontinue pour la simulation des grandes échelles des écoulements turbulents, PhD Thesis, Université de Bordeaux

16. Ducros F, Comte P, Lesieur M (1995) LES of a spatially growing boundary layer over an adiabatic flat plate at low mach number. Int J Heat Fluid Flow 16:341–348
17. Lesieur M, Métais O, Comte P (2005) Large-eddy simulations of turbulence. Cambridge University Press, Cambridge
18. Rapp CR, Manhart C (2011) Flow over periodic hills—an experimental study. Exp Fluids 51:247–269
19. Chaouat B, Schiestel R (2013) Hybrid RANS-LES simulations of the turbulent flow over periodic hills at high reynolds number. Comput Fluids 84:279–300

DNS of Turbulence from Receptivity Stage: Role of Spatio-Temporal Wave Front

Tapan K. Sengupta

Abstract Turbulence is ubiquitous phenomenon and remains as one of the last few challenges of classical physics. Instead of dwelling on the question of whether this is deterministic or stochastic, here we focus upon some recent successes reported in the literature by Sengupta and Bhaumik (Phys Rev Lett 107:154501, 2011), Bhaumik and Sengupta (Phys Rev E 89:043018, 2014) while computing and matching the corresponding experiment with deterministically excited transition to turbulence of flow over a flat plate. One of the key features of these studies, is the central role played by spatio-temporal wave front (STWF) in causing transition to turbulence. In the present study, we further emphasize the roles of STWF in the external flow. We also comment upon the correspondence between such instability modes with POD modes.

1 Introduction

Transition to turbulence for flow over a flat plate remained an unsolved problem till very recently. It is however understood that the process of transition to turbulence onset is via flow instability. While flow instability has been studied theoretically [5, 14] to show the presence of Tollmien-Schlichting "wave", its experimental validation took longer, till quiet wind tunnel was designed and a ribbon was vibrated at a single frequency, deep inside the boundary layer of a flat plate [13]. While this experiment established the 2D "waves", corresponding 3D "waves" were shown much later [8, 9]. It has been established [2, 17] that these are wave-packets and will be noted here as wave-packet. Experimentally reproducible turbulence encourages one to follow

T.K. Sengupta (✉)
High Performance Computing Laboratory, Department of Aerospace Engineering,
Indian Institute of Technology, Kanpur 208016, India
e-mail: tksen@iitk.ac.in

the same route computationally via deterministic excitation. This has been reported successfully for 2D [17] and 3D routes [2] of transition over a zero pressure gradient boundary layer.

A striking feature of these simulations is the presence of STWF, which actually triggers secondary and nonlinear instabilities leading to formation of turbulent spots and merge together, leading to fully developed turbulent flow. This segregation of STWF from Tollmien-Schlichting wave-packet is noted for moderate to high frequency of monochromatic excitation at the wall. Presence of STWF was noted first, while investigating spatially stable boundary layer [23, 24] from the Bormwich contour integration of Orr-Sommerfeld equation and numerical solution of Navier-Stokes equation. While the solution of Orr-Sommerfeld equation is obtained by delta function excitation, solution of Navier-Stokes equation requires a finite width exciter [17, 23].

The sighting of STWF has been reported by other authors who noted that *due to the fact that for the simulations the disturbances are introduced for $t > 0$ into a flow that was, prior to that, steady and undisturbed, the propagating, time-periodic Tollmien-Schlichting waves are preceded by a wave-front that is essentially a wave packet. Of course, the nonlinear behaviour of the leading wave packet would be very different from that of pure Tollmien-Schlichting waves. The more complicated developments in this leading wave packet are not considered here, but will be the subject of another detailed investigation* [7]. However, such an investigation has not been reported since. But, such a result has been shown theoretically by solving Orr-Sommerfeld equation first in [24] as a linear effect and later its linear and nonlinear evolution has been shown from the solution of Navier-Stokes equation, that also requires high accuracy filters (see [15]), in [2, 17]. Thus the solution of Orr-Sommerfeld and Navier-Stokes equations require very high accuracy methods to tackle stiffness and dispersion relation preservation of these equations. Better dissipation and dispersion error controls were aided by identifying the sources in [21]. Original theoretical study of Orr-Sommerfeld equation was developed in [16] by a spatio-temporal approach, integrating along Bromwich contours in complex wavenumber and circular frequency planes.

Two-dimensional Tollmien-Schlichting wave-packets were reported in [13], by electromagnetically vibrating a full-span ribbon in wall-normal direction, which was placed at a small constant height from the flat plate in a wind tunnel. In [8], a similar vibrating ribbon was restrained from vibrating at locations along the spanwise direction periodically, thereby enforcing spanwise periodic three-dimensionality.

2 Governing Equations

The incompressible 2D zero pressure gradient flow is solved using stream function-vorticity formulation of Navier-Stokes equation given by,

$$\frac{\partial^2 \psi}{\partial x^2} + \frac{\partial^2 \psi}{\partial y^2} = -\omega \tag{1}$$

$$\frac{\partial \omega}{\partial t} + u \frac{\partial \omega}{\partial x} + v \frac{\partial \omega}{\partial y} = \frac{1}{Re}\left(\frac{\partial^2 \omega}{\partial x^2} + \frac{\partial^2 \omega}{\partial y^2}\right) \tag{2}$$

where $u = \frac{\partial \psi}{\partial y}$ and $v = -\frac{\partial \psi}{\partial x}$ and Re is the Reynolds number based on a scale (L). We note that the unsteady Navier-Stokes equation has been used here [14, 17], which is quite unlike the variants of Navier-Stokes equation used in [4, 28], while using (ψ, ω)-formulation by adding hypo- and hyper-viscosity terms, in addition to temporal damping and assorted forcing terms composed of Gaussian and white noises. We also note in passing that in many primitive variable formulations either periodicity is imposed [27] or erroneous implicit-explicit (IMEX) time integration method has been used [11].

The reason that earlier published works using derived or primitive variables could not show the STWF, can be traced to the domain size used in the simulations. In Fig. 1, we indicate the domains used by different researchers and this is shown with respect to the neutral curve. In [6, 11] the domain does not even cover the region where the flow is found to be unstable by spatial theory. In contrast, the successful computation efforts in [2, 17], the domain is significantly larger and is able to capture STWF from onset, for very low amplitude of excitation. For the 2D case, the domain used is given by $-0.05L \leq x \leq 120L$ and $0 \leq y \leq 1.5L$, where Reynolds number based on L is 10^5, with 12000 points in the x-direction and 1000 points in y-direction. The time step chosen is 8×10^{-5} for these simulations [22].
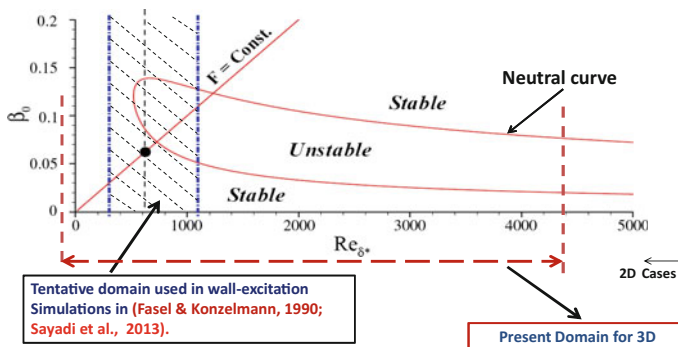
Fig. 1 Computational domain used by different authors shown in $(Re_{\delta*}, \omega_0)$ -plane along with the neutral curve

For the reported 3D case, the domain is given by $-0.05L_1 \leq x \leq 50L_1$, $0 \leq y \leq L_1$ and $-0.5L_1 \leq z \leq 0.5L_1$, with $L_1 = 26\delta*_{out}$ and $\delta*_{out}$ is the displacement thickness at the outflow of the computational domain. The grid is generated such that the points are clustered near the leading edge of the plate and uniform after $x = 5L_1$. The grid points are also clustered near the wall of the plate to accurately resolve the boundary layer. Clustering in both the streamwise and wall-normal directions is performed using tangent hyperbolic function, as it produces minimum aliasing error during computation. We have used uniformly spaced grid-points along the spanwise direction, which is taken as periodic.

Imposed wall-normal velocity for the 2D exciter is given by, $v_{wall}(x,t) = \alpha_1 A_m(x) H(t)e^{i\omega_0 t}$, where α_1 and ω_0 denote the amplitude and the frequency of excitation. Here, $H(t)$ is the Heaviside function needed for the impulsive start of excitation. The variation of amplitude function, $A_m(x)$ with streamwise distance is given by a simultaneous blowing suction strip as in [6, 19]. For the circular patch of radius r_{max} excitation amplitude in 3D case is given by, $A_m(x,z) = \frac{1}{2}\left[1 + cos\left(\frac{\pi r}{r_{max}}\right)\right]$, where $r = \sqrt{x^2 + z^2}$; for $r \leq r_{max}$ and is zero elsewhere. For the frequency f in Hz, the circular frequency is $\omega_0 = 2\pi f$. One defines a non-dimensional frequency given by, $F = 2\pi \nu f / U_\infty^2$. The governing Navier-Stokes equation in velocity-vorticity formulation for 3D disturbance field are given in [2, 3] and of the three formulations described, the rotational form is chosen due to its higher accuracy, which is given by

$$\frac{\partial \boldsymbol{\omega}}{\partial t} + \nabla \times \mathbf{H} = 0 \tag{3}$$

where $\mathbf{H} = \boldsymbol{\omega} \times \mathbf{V} + \frac{1}{Re_L}\nabla \times \boldsymbol{\omega}$, with $\boldsymbol{\omega}$ and $\mathbf{V}$ are the vorticity and velocity vectors. Two components of velocity vector are obtained from

$$\nabla^2 \mathbf{V} = -- \nabla \times \boldsymbol{\omega} \tag{4}$$

and the third component of velocity is obtained by ensuring solenoidality of velocity vector numerically at each node, i.e., from $\nabla \cdot \mathbf{V} = 0$. Detailed numerical methods and implementations are described in [2, 3]. Spanwise periodic conditions imply existence of such exciter at a periodic interval of z_{max}.

It has been shown for atmospheric dynamics [10] and in an engineering flow [19] that 2D dynamics predominate and accounts for more than 98% of total kinetic energy. One of the aims of the present study is also to show similar mechanism of transition for 2D and 3D disturbance field, hence we begin by showing the results for 2D transition by solving NSE for very small level of excitation ($\alpha_1 = 0.002$).

3 Two-Dimensional Spatio-Temporal Wave Front Over Flat Plate

As noted above that the route of transition is qualitatively same for 2D and 3D routes, we first focus on the former, as that allows higher resolution in studying the phenomenon. In all the simulations, a computational domain is taken as shown in Fig. 2. This shows the simultaneous blowing suction strip exciter [6, 19] near the leading edge of the flat plate with sharp leading edge; an inflow which is ahead of the plate; a far-field and outflow boundary segments.

The equilibrium flow is first computed in this domain by solving Navier-Stokes equation. Once this is established, the exciter is turned on and a typical result is shown in Fig. 3, for $F = 10^{-4}$. In this case the Tollmien-Schlichting wave-packet and STWF shows the typical behaviour termed as Class-C [19]. Both these structures propagate in space, the stability property of Tollmien-Schlichting waves attenuates the amplitude with respect to space, causing the wave-packet to form. In contrast, STWF is a spatio-temporal entity convecting and growing in space and time. This is demonstrated by Bromwich contour integral of Orr-Sommerfeld equation [16, 23]. As a consequence, the Tollmien-Schlichting wave-packet appears rooted at same spatial location, while the STWF shows rapid growth and shows nonlinear stage in the last frame of Fig. 3. For these flow parameters, the transition to turbulence is entirely due to STWF and Tollmien-Schlichting wave-packet remains passive.

There are also other features of the disturbance field during transition shown in Fig. 4. The first and foremost is the behaviour of the disturbance field once the nonlinearity sets in. In frame (b), one notices the significant distortion of the original STWF which amplifies and disperses very strongly and as a consequence, spawns a secondary STWF, marked as B in the figure. In subsequent frames, this structure (B) also grows nonlinearly and spawns another packet upstream of it, marked as C. This is a self-sustaining regeneration of STWF and shows the irreversibility of turbulence generation. Such upstream regeneration of STWFs cannot be explained by parabolized stability equation.
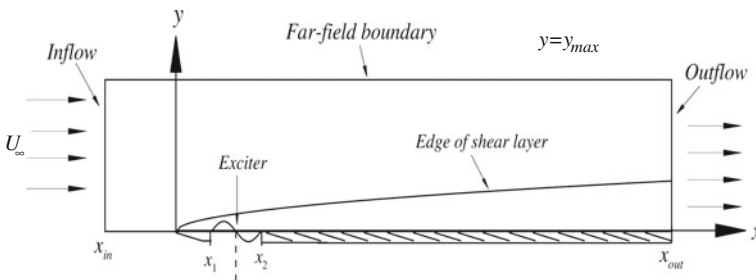
Fig. 2 Present computational domain in the physical plane, including the leading edge of the plate for 2D transition
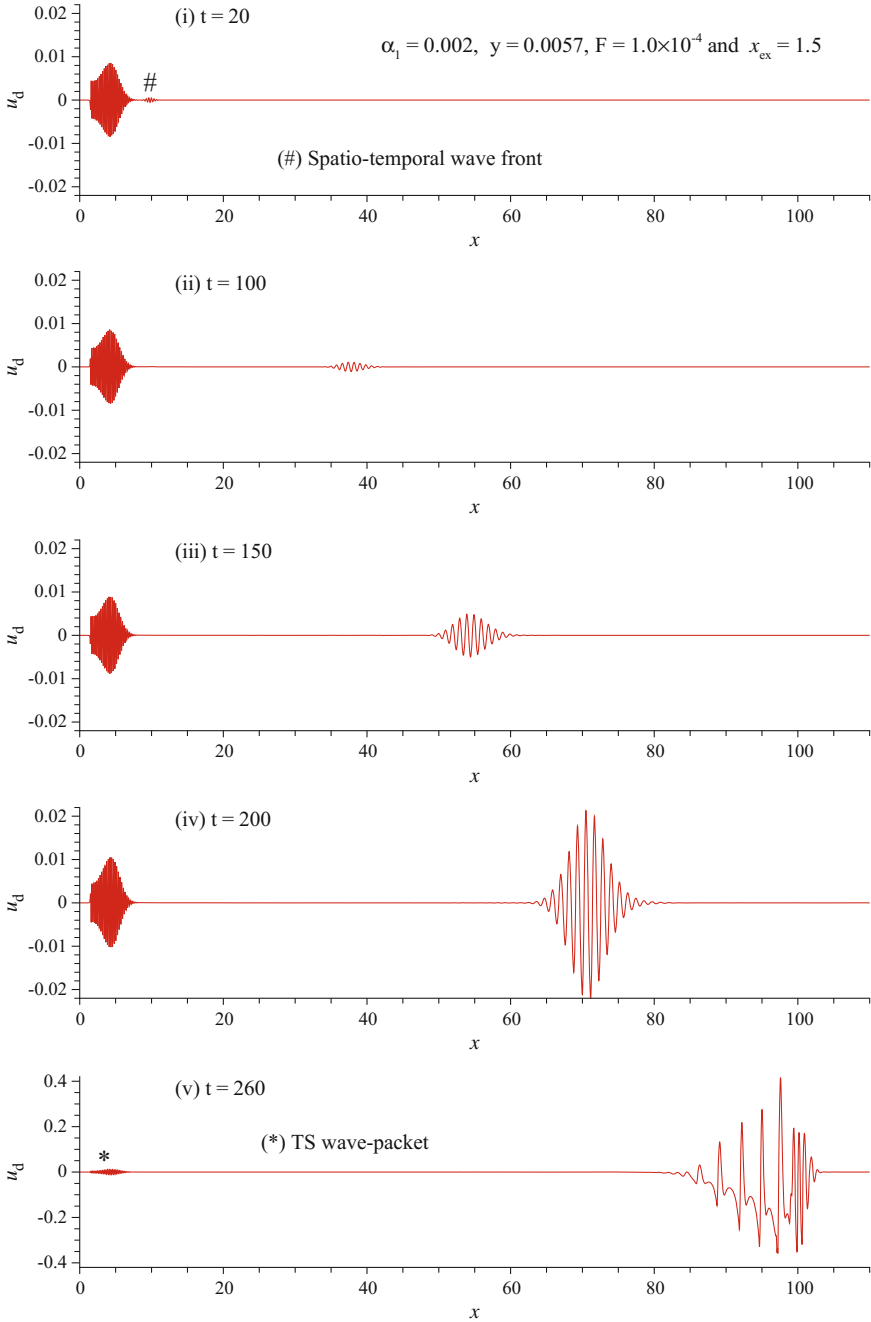
Fig. 3 Streamwise disturbance velocity (u_d) variation at $y = 0.0057$ with x at indicated times, for the parameters: $\alpha_1 = 0.002$, $F = 1.0 \times 10^{-4}$, with exciter located at $x_{ex} = 1.5$. STWF and Tollmien-Schlichting wave-packet are shown as marked
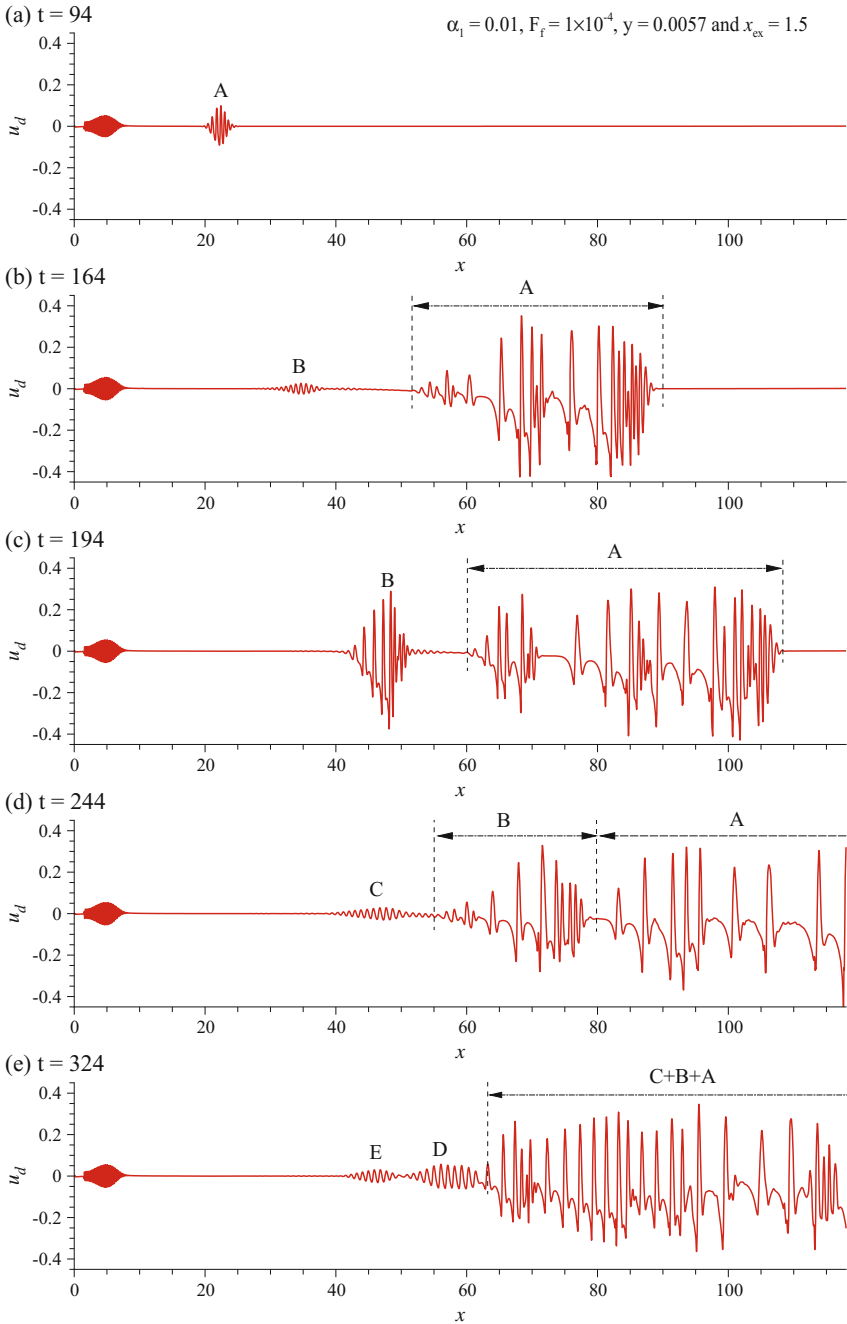
Fig. 4 Nonlinear evolution of u_d for the case of Fig. 3. Upstream induction of higher order instabilities invalidates parabolized stability equation (PSE) approaches
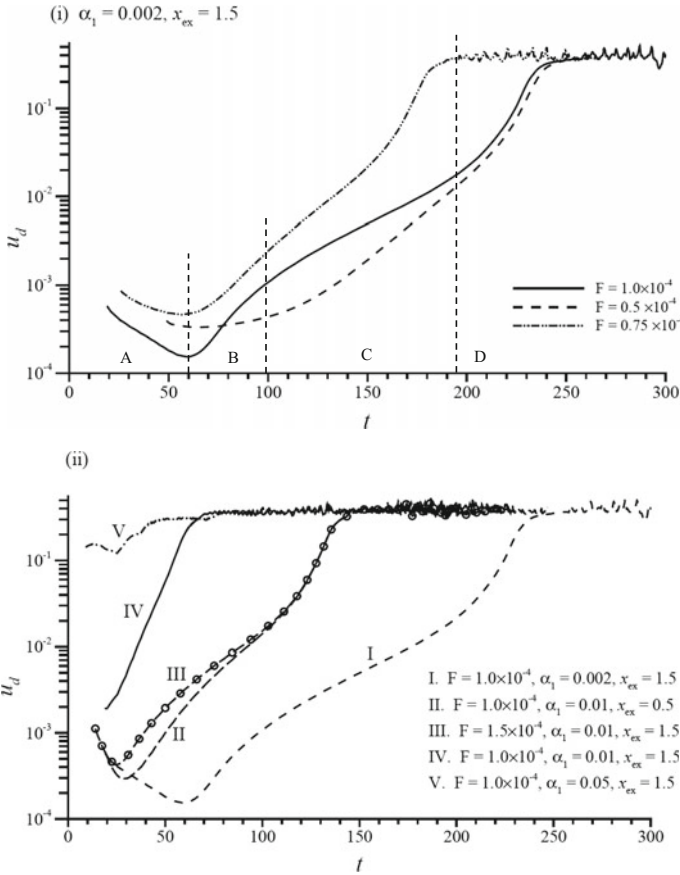
Fig. 5 Effects of amplitude, frequency and location of exciter for 2D transition

In Fig. 5, effects of frequency and amplitude of exciter is shown by displaying maximum peak-to-peak amplitude variation with time. The following are noted: During phase A, receptivity to excitation along with dispersion is shown for the Tollmien-Schlichting wave-packet despite the fact that the excitation is monochromatic. In phase B, the maximum amplitude correspond to the maximum amplitude of STWF. This is followed by secondary and nonlinear growth stage of STWF in stage C. Once the maximum amplitude saturates to about $0.4U_\infty$, we achieve a turbulent stage.

The above scenario in Figs. 4 and 5 show different route to turbulence, yet the terminal stage appears as same. In Fig. 6, different routes are classified. In Class-A, created STWF after detaching from Tollmien-Schlichting wave-packet grows transiently for a short stretch, after which it decays. This happens due to the close location of the exciter with respect to the leading edge of the plate. Figure 4 exhibits the Class-C route and we have identified the stages of transition in Fig. 5. In Classes-
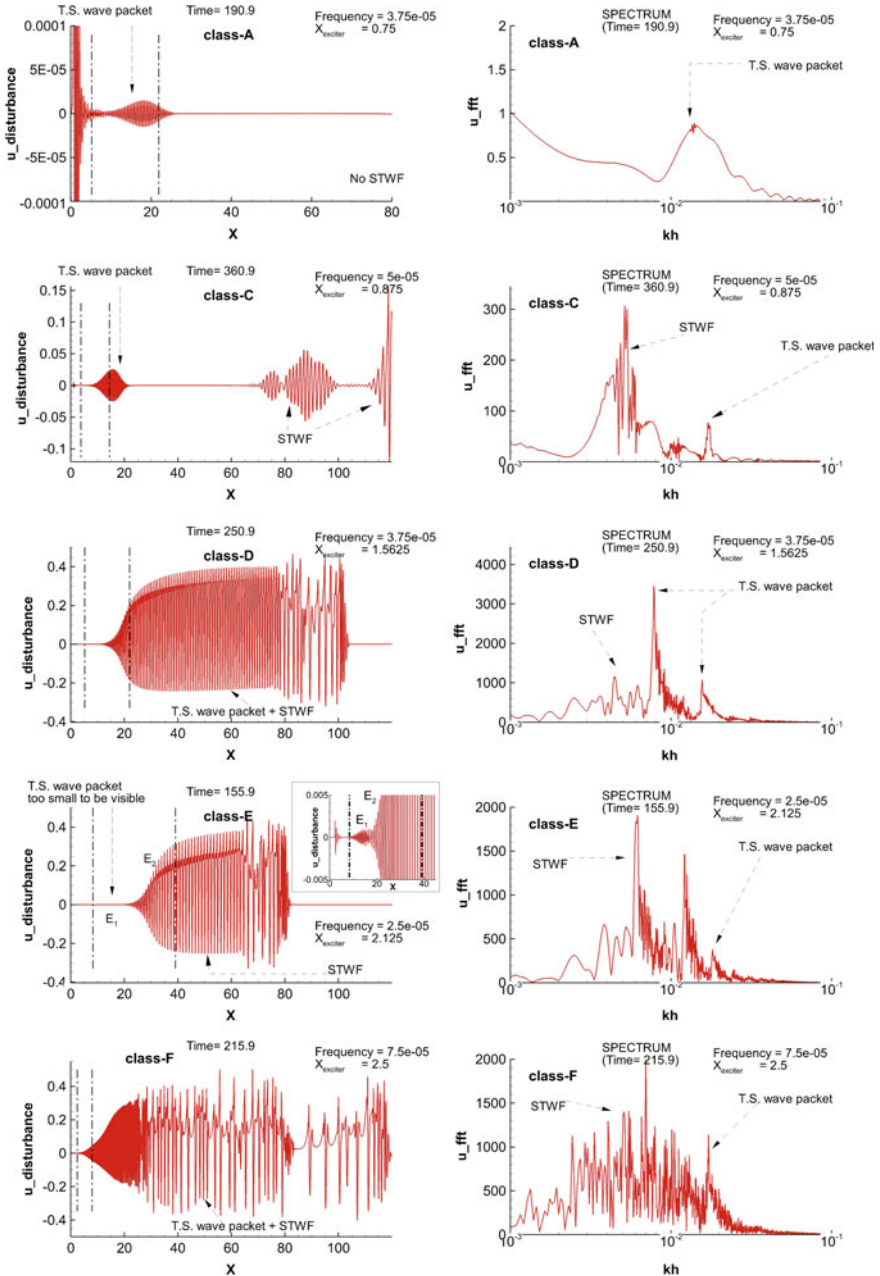
Fig. 6 Routes of 2D disturbance growth shown in physical and spectral planes (*right*). Class-A represents damped case and classes-D, -E and -F show interactions between STWF and Tollmien-Schlichting wave-packet
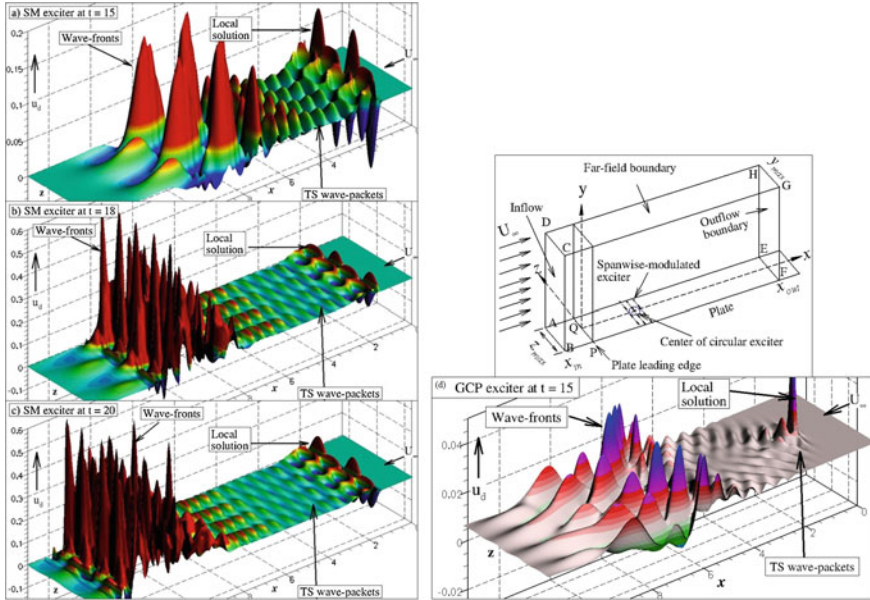
Fig. 7 3D route of transition, created by a Gaussian circular patch and spanwise-modulated exciter on the wall. Presence of STWF is noted in these routes. Domain is shown in *top right*

D, E and F, the frequency of excitation and amplitude combination are such that Tollmien-Schlichting wave-packet and STWF joins together. The spectrum shown on the right column helps us understand the transitional flow better, as the peaks associated with Tollmien-Schlichting wave-packet and STWF are marked in these figures.

4   Three-Dimensional Spatio-Temporal Wave Front Over Flat Plate

For 3D transition route we have already defined the Gaussian circular patch (GCP) excitation. For spanwise modulated (SM) excitation, the amplitude of wall excitation is given by, $A_m(x, z) = A_{mx} \sin(\pi z / z_{max})$, with A_{mx} being the same that is used for 2D excitation field, as given in [6]. Results of these two types of excitations are shown in Fig. 7. For the case of Gaussian circular patch excitation, we have used 5001 points in the streamwise direction, 301 points in the wall normal direction and 101 points in the spanwise direction. In comparison, for the spanwise modulated excitation case, we have used $5001 \times 301 \times 51$ points for the simulations. The parallel simulations were done using 500 cores of the system of CMMACS Bangalore and the numerical methods are given in details in [1, 3]. As in 2D transition routes,
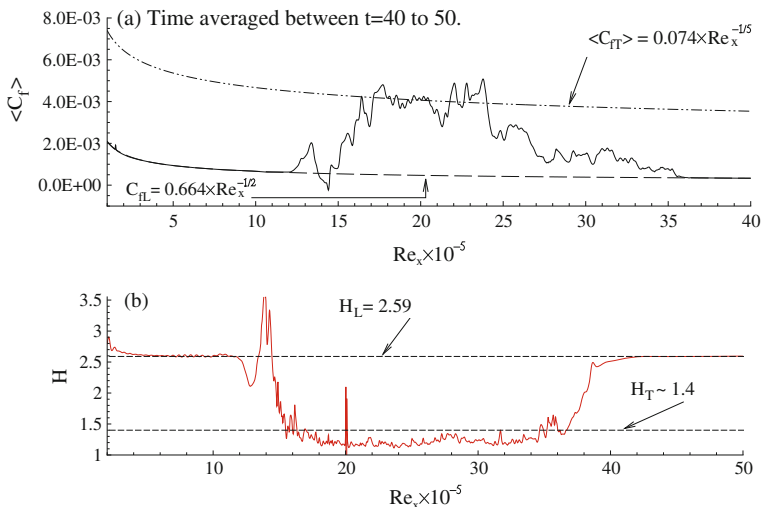
Fig. 8 Time averaged skin friction (*top*) and shape factor for the transitional flow shown with respect to laminar and turbulent empirical correlations

one notices a local solution, which is near the exciter and that is followed by the asymptotic solution. These asymptotic solutions are similar to Tollmien-Schlichting wave-packet, in wedge-form for circular patch excitation and parallel crests and troughs for the spanwise modulation excitation cases. The most remarkable feature of the displayed solutions is the presence of STWF which breaks down to turbulence beyond the nonlinear growth stage of transitional flow. As in 2D transition, here also one notices various stages traversed by the transitional flow to fully developed stage and this is irrespective of spanwise period of the domain. More details of 3D routes are described in [1, 2]. It has been shown that these three essential elements are present for both 2D and 3D routes. However, the vortical structures formed over the plate differs for the Klebanoff-type transition and H-type routes, as explained in [2]. Unlike the results presented in [11, 29], we see the presence of Tollmien-Schlichting wave-packet for both low and high frequency cases.

In Fig. 8, the time averaged skin friction (during $40 \leq t \leq 50$) and shape factors are shown, along with empirical correlation obtained from [12]. It is readily evident that the flow follows laminar values for small Re_x and in the turbulent patch, it closely meanders around the time-averaged turbulent properties. Ahead of the turbulent patch, the flow relaxes back to laminar state.

One of the way to understand the structure of the evolving flow is obtained by POD [18, 20, 25]. For flow past the flat plate, POD is performed during the time interval, $0 \leq t \leq 80$, and shown in Fig. 9, obtained following the method of snapshot [26]. POD modes are further sub-classified [25] in terms of regular and anomalous modes. A further sub-class identified which represents STWF was noted in [25], as shown for modes 15–18 in Fig. 9.
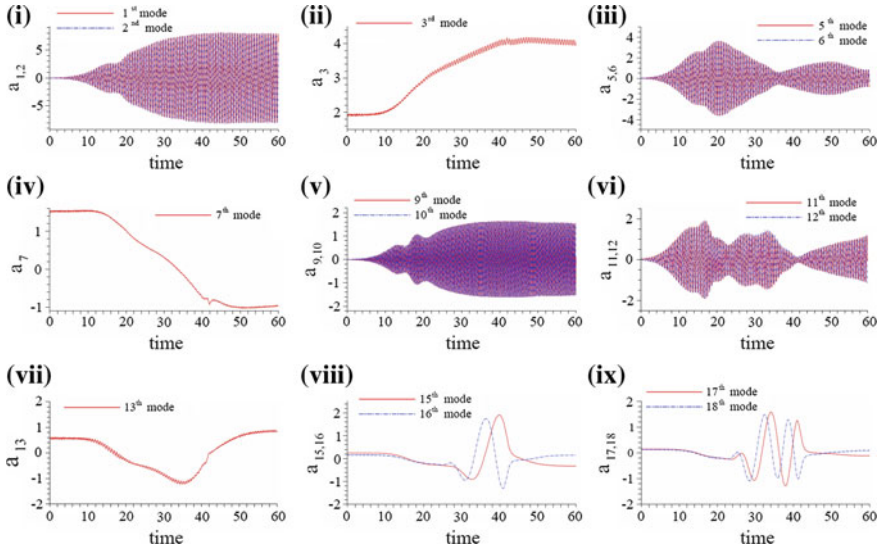
Fig. 9 Amplitude functions of POD modes for 2D transition showing up to 18th mode. Note the STWF in modes 15–18 [1]

5 Summary and Conclusions

In the presented work here, we once again establish the centrality of STWF as the precursor of turbulence, as opposed to the conventional view-point that Tollmien-Schlichting wave-packet is responsible for transition. This is achieved here by solving Navier-Stokes equation for flow over a flat plate, as excited in the corresponding experiments. It is shown that STWF is responsible for both 2D and 3D routes of transition over a flat plate. This helps in demonstrating that STWF is the main element of transition to turbulence for this external wall bounded flows.

References

1. Bhaumik S (2013) Direct numerical simulation of transition to turbulent over zero pressure gradient boundary layer. PhD thesis, Department of Aerospace Engineering, IIT Kanpur
2. Bhaumik S, Sengupta TK (2014) Precursor of transition to turbulence: spatiotemporal wave front. Phys Rev E 89:043016
3. Bhaumik S, Sengupta TK (2015) A new velocity-vorticity formulation for direct numerical simulation of 3D transitional and turbulent flows. J Comput Phys 284:230–260
4. Bracco A, McWilliams JC (2010) Reynolds-number dependency in homogeneous, stationary two-dimensional turbulence. J Fluid Mech 646:517–526
5. Drazin PG, Reid WH (1981) Hydrodynamic stability. Cambridge University Press, UK
6. Fasel H, Konzelmann U (1990) Non-parallel stability of a flat plate boundary layer using the complete Navier-Stokes equation. J Fluid Mech 221:331–347

7. Fasel HF, Rist U, Konzelmann U (1990) Numerical investigation of the three-dimensionaldevelopment in boundary-layer transition. AIAA J 28(1):29–37
8. Kachanov YS, Levchenko VY (1984) Resonant interactions of disturbances in transition to turbulence in a boundary layer. J Fluid Mech 138:209
9. Klebanoff PS, Tidstrom KD, Sargent LM (1962) The three-dimensional nature of boundary-layer instability. J Fluid Mech 12:1–34
10. Nastrom GD, Gage KS, Jasperson WH (1984) Kinetic energy spectrum of large-scale and mesoscale atmospheric processes. Nature 310:36–38
11. Sayadi T, Hamman CW, Moin P (2013) Direct numerical simulation of complete H-type and K-type transitions with implications for the dynamics of turbulent boundary layers. J Fluid Mech 724:480–509
12. Schlichting H (1979) Boundary layer theory, 7th edn. McGraw Hill, New York
13. Schubauer GB, Skramstad HK (1947) Laminar boundary layer oscillations and the stability of laminar flow. J Aero Sci 14(2):69–78
14. Sengupta TK (2012) Instabilities of flows and transition to turbulence. CRC Press, Taylor & Francis Group, Florida
15. Sengupta TK (2013) High accuracy computing methods: fluid flows and wave phenomenon. Cambridge University Press, USA
16. Sengupta TK, Ballav M, Nijhawan S (1994) Generation of Tollmien-Schlichting waves by harmonic excitation. Phys Fluids 6(3):1213–1222
17. Sengupta TK, Bhaumik S (2011) Onset of turbulence from the receptivity stage of fluid flows. Phys Rev Lett 107:154501
18. Sengupta TK, Bhaumik S, Bhumkar YG (2011) Nonlinear receptivity and instability studies by POD 6th. In: AIAA theoretical fluid mechanics conference, Honululu, Hawaii, USA, pp 27–30
19. Sengupta TK, Bhaumik S, Bhumkar YG (2012) Direct numerical simulation of two-dimensional wall bounded turbulent flow from receptivity stage. Phys Rev E 85(2):026308
20. Sengupta TK, Dey S (2004) Proper orthogonal decomposition of direct numerical simulation data of bypass transition. Comput Struct 82:2693–2703
21. Sengupta TK, Dipankar A, Sagaut P (2007) Error dynamics: beyond von Neumann analysis. J Comput Phys 226:1211–1218
22. Sengupta TK, Sathyanarayanan VK, Sriramakrishnan M, Mulloth A (2015) Role of time integration in computing transitional flows caused by wall excitation. J Sci Comput 65:224–248
23. Sengupta TK, Rao AK, Venkatasubbaiah K (2006a) Spatio-temporal growing wave fronts in spatially stable boundary layers. Phys Rev Lett 996(22):224504
24. Sengupta TK, Rao AK, Venkatasubbaiah K (2006b) Spatio-temporal growth of disturbances in a boundary layer and energy based receptivity analysis. Phys Fluids 18: 094101–1–4
25. Sengupta TK, Vijay VVSN, Singh Neelu (2011) Universal instability modes in internal and external flows. Comput Fluids 40(1):221–235
26. Sirovich L (1987) Turbulence and the dynamics of coherent structures. part I: coherent structures. Q Appl Math 45(3):561–571
27. Skote M, Haritonidis JH, Henningson DS (2002) Varicose instabilities in turbulent boundary layers. Phys Fluids 14:2309–2323
28. Smith LM, Yakhot V (1994) Finite-size effects in forced two-dimensional turbulence. J Fluid Mech 274:115–138
29. Wu X, Moin P (2009) Direct numerical simulation of turbulence in a nominally zero-pressure-gradient flat-plate boundary layer. J Fluid Mech 630:5–41

Turbulent Motion and Clustering of Buoyant and Swimming Plancton in Free Surface Flows

Alfredo Soldati, Francesco Zonta and Salvatore Lovecchio

Abstract In this paper we will use Direct Numerical Simulations of turbulence and Lagrangian Particle Tracking to elucidate the physics of the motion of inertial particles in different turbulence instances and we will provide insight for modelling and simulating turbulent dispersed flows important in industrial, environmental and geophysical applications.

1 Introduction

Turbulent fluids and small particles, droplets or bubbles are common to a number of key processes in energy production, product industry and environmental phenomena. In modeling these processes, the dispersed phase is usually assumed uniformly distributed. Indeed, it is not. Dispersed phases can be focused by turbulence structures and can have a time-space distribution that barely resembles prediction of simplified averaged modeling. Preferential distribution controls the rate at which sedimentation and re-entrainment occur, reaction rates in burners or reactors and can also determine raindrop formation and, through plankton, bubble and droplet dynamics, the rate of oxygen-carbon dioxide exchange at the ocean-atmosphere interface.

In this paper, we will review a number of physical phenomena in which particle segregation in turbulence is a crucial effect describing the physics by means of

A. Soldati (✉) · F. Zonta
Institute of Fluid Mechanics and Heat Transfer,
Vienna University of Technology, Vienna, Austria
e-mail: alfredo.soldati@tuwien.ac.at

F. Zonta
e-mail: francesco.zonta@tuwien.ac.at

S. Lovecchio
Institut de Mecanique des Fluides, Universite de Toulouse, Toulouse, France
e-mail: lovecchio.salvatore@imft.fr

Direct Numerical Simulation of turbulence. We will elucidate concepts and modeling ideas derived from a systematic numerical study of the turbulent flow field coupled with Lagrangian tracking of particles under different modeling assumptions. We will underline the presence of the strong shear which flavors wall turbulence with a unique multiscale aspect and adds intricacy to the role of inertia, gravity and buoyancy in influencing particle motion. We will describe the role of free surface turbulence in dispersing and clustering the light particles such as plancton and the role of the distribution of dissipation in non-homogeneous turbulence to control breakage rates of brittle and ductile aggregates. Through a number of physical examples of practical interest such as boundary layers, free-surface and stratified flows, we will show that a sound rendering of turbulence mechanisms is required to produce a physical understanding of particle trapping, segregation and ultimately macroscopic flows such as surfacing, settling and re-entrainment.

2 Methodology

The physical problem considered in this study is the dispersion of the small particles in channel turbulence ($x-$, $y-$ and $z-$axis point in the streamwise, spanwise and wall-normal directions). The flow can have a free surface and can be subject to thermal stratification (through the imposition of a constant heat flux at the top and an adiabatic condition at the bottom boundary). Note that periodicity is applied in x and y for both velocity and temperature. The size of the channel is $2\pi h \times \pi h \times h$ in x, y and z, with h the channel height. When surface heating is accounted for, there is a negative temperature difference between the bottom and the top layers of the channel which causes a stable buoyancy effect (the gravitational acceleration g acting downward along the wall-normal direction). In dimensionless form the conservation of mass, momentum and energy of the fluid is described by the following set of three-dimensional time-dependent equations:

$$\nabla \cdot \mathbf{u} = 0 \,, \tag{1}$$

$$\frac{\partial \mathbf{u}}{\partial t} + \mathbf{u} \cdot \nabla \mathbf{u} = \frac{1}{Re_\tau}\nabla^2\mathbf{u} - \nabla p + \frac{Gr}{Re_\tau^2}\theta\delta_g + \delta_p, \tag{2}$$

$$\frac{\partial \theta}{\partial t} + \mathbf{u} \cdot \nabla \theta = \frac{1}{Re_\tau Pr}\nabla^2\theta - \beta_T, \tag{3}$$

where $\mathbf{u} = (u_x, u_y, u_z)$ is velocity, p is the fluctuating kinematic pressure, $\delta_p = (1, 0, 0)$ is the mean pressure gradient that drives the flow in the streamwise direction, θ is temperature and $\delta_g = (0, 0, 1)$ is used to compute the buoyancy term only in the wall-normal direction. The dimensionless Reynolds, Grashof and Prandtl number are defined as

$$Re_\tau = \frac{u_\tau h}{\nu}, \qquad Gr = \frac{g\beta h^3}{\nu^2} \frac{\partial \theta}{\partial z}\Big|_s, \qquad Pr = \frac{\mu c_p}{\lambda}. \qquad (4)$$

where μ and ν are the dynamic and the kinematic viscosity, β is the thermal expansion coefficient, c_p is the specific heat and λ is the thermal conductivity. In the definition of Re_τ and Gr, $u_\tau = (h|\delta_p|/\rho)^{1/2}$ is the shear velocity (ρ being the fluid density) whereas $\partial\theta/\partial z|_s$ is the imposed free-surface heating. Note that for unstratified flows, $Gr = 0$. Note that an open channel flow with a constant surface heating, $\beta_T = 1/(Re_\tau Pr)$ in Eq. 3. Equations 1–3 are discretized using a Fourier-Chebychev pseudo-spectral method. Time integration is realized through a two-level explicit Adams-Bashfort scheme for the non-linear terms and an implicit Crank-Nicolson method for the viscous terms. Further details can be found in [1, 2].

The dynamics of small passive floaters (i.e. particles lighter than water) is described by a set of ordinary differential equations for the position, x_p, and the velocity, v_p, of the floaters. In a vector form:

$$\frac{d\mathbf{x}_p}{dt} = \mathbf{v}_p, \qquad (5)$$

$$\frac{d\mathbf{v}_p}{dt} = \left(1 - \frac{1}{S}\right)\mathbf{g} + \frac{(\mathbf{u}_{@p} - \mathbf{v}_p)}{\tau_p}(1 + 0.15\, Re_p^{0.687}), \qquad (6)$$

where $\mathbf{u}_{@p}$ is the fluid velocity at the position of the floater, interpolated with 6th-order Lagrange polynomials, whereas $\tau_p = \rho_p d_p^2/18\rho\nu$ is the relaxation time of the floater based on the density ρ_p and the diameter d_p of the floater. The parameter $S = \rho_p/\rho_f$ is the specific density of the floater. The Stokes drag coefficient is computed using a standard non-linear correction when the Reynolds number of the floater $Re_p = |\mathbf{u}_{@p} - \mathbf{v}_p|d_p/\nu > 0.2$. For the base configuration (passive light particles), particles are considered pointwise non-rotating rigid spheres (point-particle approach) and are injected into the flow at a concentration low enough to consider dilute system conditions (one-way coupling approach). The case of active particles (swimmers) dispersed in turbulence will be presented and discussed below. Periodic boundary conditions are imposed on particles moving outside the computational domain in the homogeneous directions. In the wall-normal direction, the floaters reaching the free surface still obey the buoyancy force balance, whereas elastic rebound is enforced at the walls. When free-slip conditions are used, the particles reaching the free surface still obey the buoyancy force balance. Integration in time of Eqs. 5–6 is realized through a 4th-order Runge-Kutta scheme (assuming a random initial position of particles).

3 Results

It is well-known that a single particle interacts with vortices of different sizes depending on its inertia. In a turbulent boundary layer, where vortices of different sizes are present (coherent and turbulent structures), this interaction induces particle sedimentation and reentrainment [3]. A picture elucidating this concepts is presented in Fig. 1. However, turbulence features change according with the geometric features of the flow. Some significant environmental problems are relative to free surface turbulence. The free surface turbulence, albeit constrained onto a two-dimensional space, exhibits features that barely resemble predictions of simplified two-dimensional modeling. In particular, in a three dimensional open channel flow, surface turbulence is characterized by upscale energy transfer that controls the long term evolution of the larger scales. This can be demonstrated by associating (see Fig. 2) downscale and upscale energy transfer (Π^{Δ}) at the surface with the trace of the velocity gradient tensor (∇_{2D}). The presence of the inverse energy cascade at the free-surface is crucial in determining the pattern evolution of floaters and passive planctonic species [4]. In particular it is possible to demonstrate that particle buoyancy induces clusters (Fig. 3) that evolve towards a long-term fractal distribution in a time much longer than the Lagrangian integral fluid time scale, indicating that such clusters overlive the surface turbulent structures which produced them [5].

The results discussed above concern the case of unstratified flows ($Gr = 0$). When the flow is thermally stratified ($Gr \neq 0$), the dynamics of floaters is strongly influenced by the interaction of turbulence structures with the thermal stratification [1, 2]. In the bulk of the flow, turbulence modulation by thermal stratification strongly influences the rising velocity of floaters. At the surface, stratification acts to hinder floaters segregation (Fig. 4). For unstratified turbulence (Fig. 4a–b), floaters organize into clusters that are stretched by the fluid and form filaments (which correlate well with the behavior of ∇_{2D}). The situation changes for increasing stratification (Fig. 4e–f). In this case, upwellings/downwellings at the free surface are less intense and the filamentary structures less evident, with floaters being almost homogeneously distributed.

Fig. 1 Vortices and inertial particles in a boundary layer. Different *color* for the vortices indicate clockwise or counter-clockwise rotation in the streamwise direction. *Blue particles* are directed away from the wall; *Purple particles* are directed towards the wall
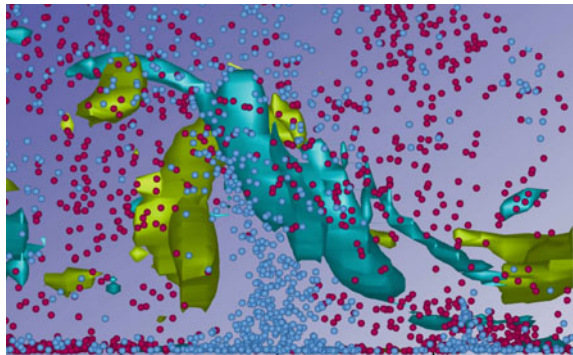
Fig. 2 Contour maps of the
energy flux (**panel a**) and of
the two-dimensional surface
divergence (**panel b**)
computed at the free surface
for Re = 509
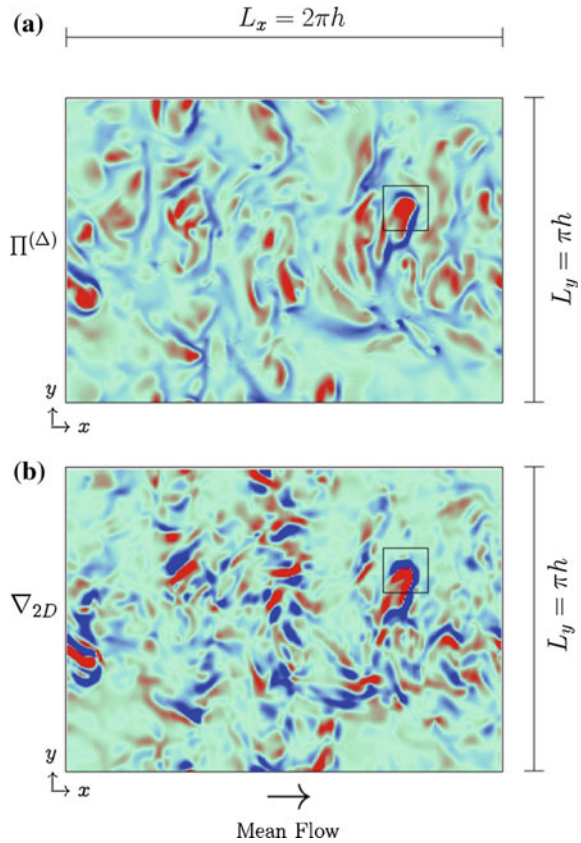
When motile planctonic species are considered, the interaction between turbulence, thermal stratification and plancton dynamics is even more complex, due to the particle anisotropy (heavy bottom inducing gyrotaxis) and self-propulsion. To analyze this situation, we consider a swarm of swimming micro-organisms. Each micro-swimmmer is modeled as a spheroidal particle (see Fig. 5a) whose position evolves as:

$$\frac{d\mathbf{x}}{dt} = \mathbf{u}(\mathbf{x}) + v_s \mathbf{p}, \tag{7}$$

where v_s is the mean cell swimming speed, $\mathbf{u}(\mathbf{x})$ is the fluid velocity at the position of the swimmer and $\mathbf{p}$ is the particle orientation unit vector. The orientation of each swimmer evolves in response to the biasing torques acting upon it. Under the assumptions that the micro-swimmers have a spheroidal geometry, the reorientation rate of the organisms is defined by the following force balance:

$$\frac{d\mathbf{p}}{dt} = \frac{1}{2B}\left[\mathbf{k} - (\mathbf{k}\cdot\mathbf{p})\mathbf{p}\right] + \frac{1}{2}\boldsymbol{\omega}\wedge\mathbf{p} \tag{8}$$
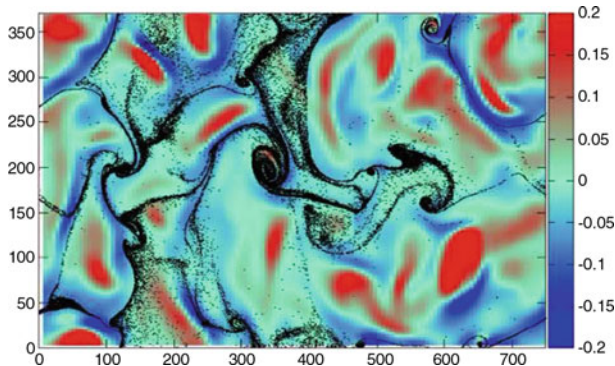
Fig. 3 Light particles (floaters) moving on a flat shear-free surface of a turbulent open water. This configuration mimics the motion of buoyant matter (e.g. phytoplankton, pollutants or nutrients). Correlation between floater clusters and surface divergence ∇_{2D}. Floaters segregation $\nabla_{2D} < 0$ regions (in *blue*, footprint of sub-surface downwellings) avoiding footprint of sub-surface upwellings). Particle buoyancy induces clusters that evolve towards a long-term fractal distribution in a time much longer than the Lagrangian integral fluid time scale, indicating that such clusters over-live the surface turbulent structures which produced them [5]

where $\mathbf{k} = [0; 0; 1]$ is a unit vector pointing upward in the vertical direction, ω is the fluid vorticity and B is the gyrotactic reorientation time (namely the characteristic time a perturbed cell takes to re-align with the vertical direction when $\omega = 0$). A dimensionless reorientation time can be introduced, $\Psi = \frac{1}{2B} \frac{v}{u_\tau^2}$. The first term on the right hand side of Eq. 8 describes the tendency of a cell to remain aligned along the vertical direction due to bottom-heaviness while the second term represents the tendency of vorticity to overturn a cell by imposing a viscous torque on it. The reorientation timescale generally spans the range $0.1 < B < 10$ s and phytoplankton's swimming velocities are usually in the range $10 < v_s < 1000\,\mu m/s$. In our simulations we used $B = 0.1, 1$ and 10 s, whereas $v_s = 100\,\mu m/s$ (corresponding to the swimming velocity of Chlamydomonas augustae, a particular phytoplankton species with gyrotactic timescale equal to 3.4 s). The corresponding dimensionless values in wall units are $B^+ = 1.13, 0.113, 0.0113$ and $v_s^+ = 0.048$. Preliminar results on these issues indicate that phytoplancton align with the mean shear and may be trapped within the thermocline (the region near the water surface characterized by a large temperature gradient). This represents a further obstacle to the process of plancton surfacing, as shown in Fig. 5b.

4   Conclusions and Future Developments

In this paper, we have considered the dynamics of passive and active (light) particles in free surface turbulence. We have shown that light particles segregate at the free surface into filaments and large scale structures. For thermally stratified flow condition,
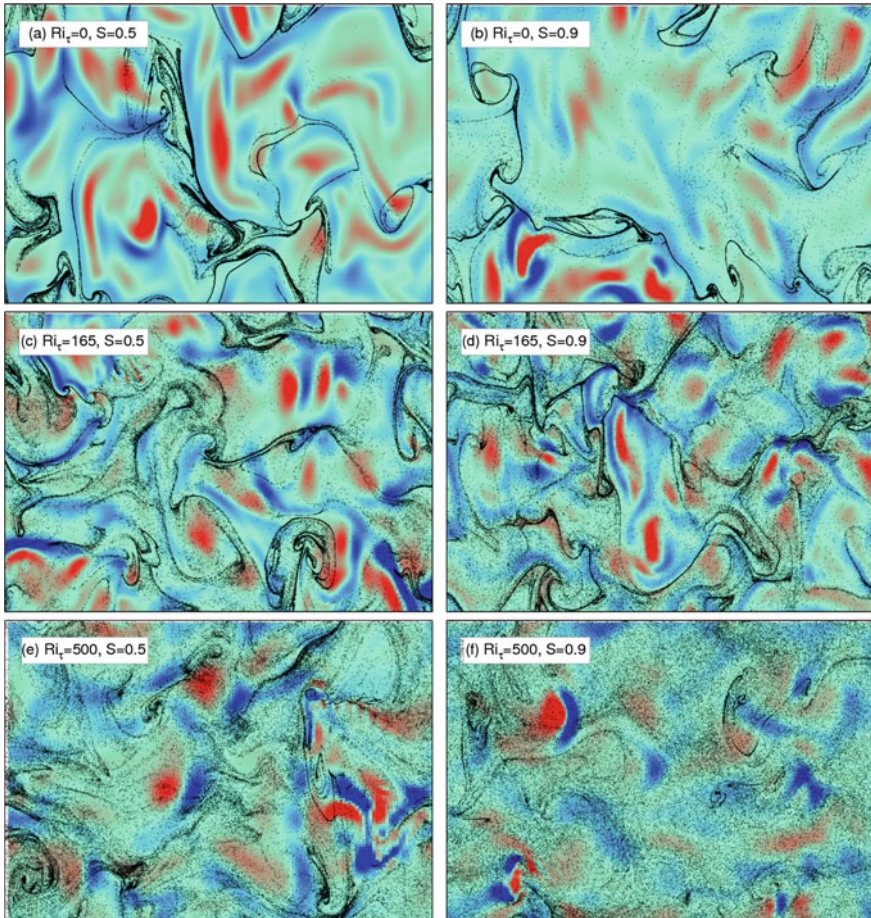
Fig. 4 Correlation between floater clusters and surface divergence ∇_{2D} for $Ri_\tau = 0,\ 165$ and 500 and for floater specific density $S = 0.5$ and $S = 0.9$. Panels: **a** $Ri_\tau = 0$ and $S = 0.5$; **b** $Ri_\tau = 0$ and $S = 0.9$; **c** $Ri_\tau = 165$ and $S = 0.5$; **d** $Ri_\tau = 165$ and $S = 0.9$; **e** $Ri_\tau = 500$ and $S = 0.5$; **f** $Ri_\tau = 500$ and $S = 0.9$. Note that for increasing stratification (increasing Ri_τ) the filamentary structure observed for unstratified turbulence ($Ri_\tau = 0$, **panels a–b**) progressively tends to an homogeneous distribution ($Ri_\tau = 500$, panels e–f)

turbulence is damped and floaters segregation at the free surface reduced. When particles are motile (motile planctonic species and swimmers), they tend to align with the mean shear and can be trapped into regions characterized by strong temperature gradients (thermocline). Future developments of the present work will include the analysis of the local shearing effect induced by turbulence on the rupture of aggregates (see Fig. 6 for a conceptual sketch of this process). Brittle and ductile aggregates will be examined and physics and statistical features of the rupture will be discussed [6, 7].
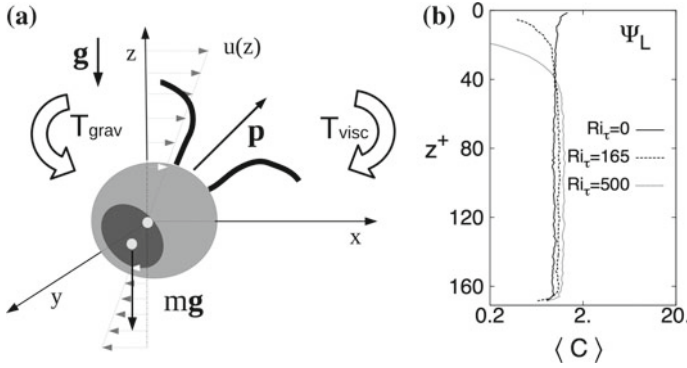
Fig. 5 Panel a Sketch of a gyrotactic microorganism (active motile plancton) swimming with velocity V_s along the orientation vector p given by the torque balance. The torque due to the cell asymmetry (*bottom* heaviness: T_{grav}) tends to align the cell to its preferential orientation along the vertical direction k whereas the torque due to the fluid viscosity (T_{visc}) tends to rotate the cell according to the flow streamlines. **Panel b** Averaged concentration $\langle C \rangle$ of motile plancton cells with smaller reorientation time (Ψ_L, which indicates that these cells adapt slowly to flow changes) along the vertical direction z^+ for different levels of stratification (i.e. different Ri_τ). Note that for increasing Ri_τ plancton cells hardly reach the flow surface (located at $z^+ = 0$)
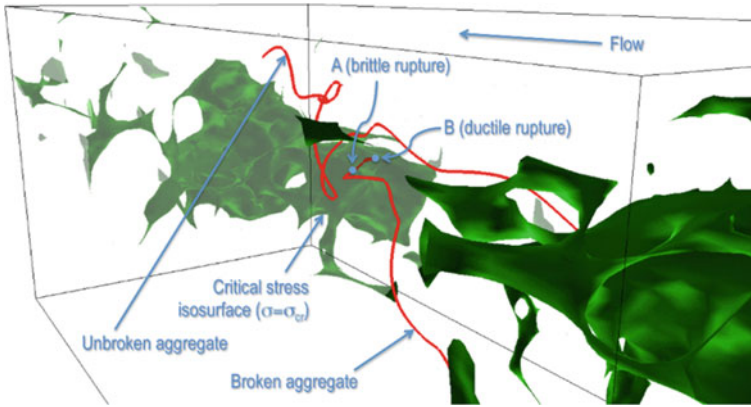
Fig. 6 Rendering of brittle and ductile rupture in turbulent flow. The trajectory of two different aggregates is shown, superimposed onto the isosurface of the critical stress $\sigma = \sigma_{cr}$ required to produce brittle rupture or activate ductile rupture. The broken aggregate trespasses the σ_{cr} isosurface at point A (potential brittle rupture) and undergoes ductile rupture at point B (where the breakage condition $E > E_{cr}$ is met). The unbroken aggregate avoids all regions where $\sigma > \sigma_{cr}$ and does not break within the time window considered in this figure. Critical stress isosurface is taken at the time of ductile rupture. Aggregate trajectories are tracked several time steps backward from this time

References

1. Zonta F, Onorato M, Soldati A (2012) Turbulence and internal waves in stably-stratified channel flow with temperature-dependent fluid properties. J Fluid Mech 697:175–203
2. Lovecchio S, Zonta F, Soldati A (2014) Influence of thermal stratification on the surfacing and clustering of floaters in free surface turbulence. Adv Water Resour 72:22–31
3. Marchioli C, Soldati A (2002) Mechanisms for particle transfer and segregation in turbulent boundary layer. J Fluid Mech 468:283–315
4. Lovecchio S, Zonta F, Soldati A (2015) Upscale energy transfer and flow topology in free surface turbulence. Phys Rev E 91:033010
5. Lovecchio S, Marchioli C, Soldati A (2013) Time persistence of floating particle clusters in free-surface turbulence. Phys Rev E 88:033003
6. Babler M, Biferale L, Brandt L, Feudel U, Guseva K, Lanotte AS, Marchioli C, Picano F, Sardina G, Soldati A, Toschi F (2015) Numerical simulations of aggregate breakup in bounded and unbounded turbulent flows. J Fluid Mech 766:104–128
7. Marchioli C, Soldati A (2015) Turbulent breakage of ductile aggregates. Phys Rev E 91:053003

An Improved Multiscale Eulerian-Lagrangian Method for Simulation of Atomization Process

J.L. Estivalèzes, D. Zuzio and B. DiPierro

Abstract The physics of atomization process involves many spatial scales, generating a wide variety of liquid inclusions of different sizes with large density and viscosity ratios between liquid and gas phases. To correctly capture the dynamics of these phenomena, each scale should be resolved with an appropriate method to ensure the conservation of physical quantities (mass, momentum) as well as the jump conditions across the liquid-gas interface. To address these problems, an original multi-scale methodology has been developed. It consists of a core coupled Level set/Volume of Fluid method (CLSVOF) for accurate capture of primary atomization, an adaptive mesh refinement technique (oct-tree AMR) to dynamically optimize the structured Cartesian mesh and a particle tracking algorithm to capture droplet dynamics. An improved Eulerian-Lagrangian coupling has been developed to assure a smooth transition between the Eulerian and the Lagrangian modelling of the droplets, where both methods approach their design limits. Results show its ability to reproduce the whole atomization process, from large scale instabilities to small droplet dynamics.

1 Introduction

The physics of atomization involves a wide range of phenomena and a strongly multi-scale dynamics, where many order of magnitude span between larger and smaller structures. Very different topologies such as drop, ligament, liquid sheet, may appear due to the many instabilities arising [1–3]. The most common approach used in

J.L. Estivalèzes (✉) · D. Zuzio
ONERA/DMAE, 2 Ave E. Belin, 31055 Toulouse, France
e-mail: jean-luc.estivalezes@onera.fr

D. Zuzio
e-mail: davide.zuzio@onera.fr

B. DiPierro
Université Lyon 1, 69100 Villeurbanne, France
e-mail: bastien.di-pierro@univ-lyon1.fr

industrial oriented Large Eddy Simulations of reacting flows is to directly inject the spray with assumed characteristics, given by semi-empirical correlations. The liquid being modelled by a dispersed phase approach, no atomization is resolved within the simulation. Examples can be found in [4]. In more research-oriented simulations, focused on the atomization mechanisms, many numerical methods allow the Direct Numerical Simulation of these complex two phase flows, usually in much more simplified and small scale configurations.

As the detailed simulation of all the spatial scales remains very expensive, the particle tracking method appear interesting for the smallest particles. Following this idea, the problem can be numerically split in two "moments" following the two stages of atomization, in order to adapt the local two-phase modelling. A separated phases model as the VOF or Level-Set could describe the primary atomization, where the two phases are clearly distinguished and the interface in subject to low frequency instabilities, while the dispersed phase model would be better adapted to describe the evolution of the sprays in terms of secondary atomization, transport and eventually evaporation. In [5] (by extension of [6] with a Level Set method), [7, 8] the coupled DNS and Lagrangian method technique has been successfully applied to the atomization of jets in cross-flow configuration. In [9] (coupled to a VOF method [10]) and in [11] a similar approach involving VOF and CLSVOF methods were developed to resolve assisted atomization. Both of them tracked point particle liquid particles with a drag force to couple Eulerian and Lagrangian quantities, this methodology seeming accurate enough to capture both large and small inclusion. In other approaches, the generation of the spray is not direct but it is instead treated by a more statistical approach, as in [12, 13], in order to avoid the use of cell sizes small enough to resolve the smallest drops. However, in most of those approaches the transition from Eulerian to Lagrangian formulation is still controversial as well as the treatment of inclusions exceeding the grid size.

Indeed, if one consider a medium liquid drop, i.e. a quasi-spherical inclusion whose radius is equivalent to a few mesh cell, the Eulerian formulation is not able to correctly predict the dynamics. Actually, between 6 and 10 grid points per radius are needed to described the evolution of such drop in order to avoid disappearance of liquid inclusion due numerical diffusion of level-set method, or less accurate interface representation of the piecewise linear reconstruction of VOF method. Moreover, the Lagrangian tracking could not be applied, the assumption of dispersed phase is not fulfilled any more. Hence, a third modelling scale have to be introduced so that the spatial gap between the two models is filled. In order to lessen these problems, the present work proposes an approach to model this third scale between pure Eulerian and Lagrangian representations: medium drops are supposed to have a rigid spherical shape, and they are followed by rigid translation while their mass and momentum properties are projected on the Eulerian field.

2 Numerical Method

The numerical methodology proposed here aims to solve two-phase flows under the incompressibility hypothesis. Hence in each phase we consider the Navier-Stokes equations under free divergence velocity field constraint. Interface tracking between both phases is performed thanks to a CLSVOF (Coupled Level-Set Volume Of fluid) method [14] with some further improvements described in [15]. Surface tension forces are taken into account by a ghost-fluid method (GFM) as well as viscous jump [16]. Five order accurate WENO schemes are used to discretize convective terms. AMR (Adaptive Mesh Refinement) is used to refine the grid near the interface. It is bases on the Paramesh library [17]. Finally pressure Poisson equation is solved by a Krylov BiCG-Stab precondionned by a multilevel algorithm built on the AMR tree. Detailed informations on the full algorithm can be found elsewhere [15, 18].

3 Multi-scale Approach

The approach proposed in this paper proposes the separate treatment of the liquid inclusions in two main scenarios, depending on the to-be-converted particle size:

1. the droplet size is lesser than the local mesh cell size. This kind of droplet will be called "small inclusion" within this paper;
2. the droplet size is greater than the local mesh size. This kind of droplet will be called "medium inclusion" within this paper.

In the first case, the dispersed phase approach hypothesis are considered as satisfied, so that a classical treatment is done, either in one or two ways coupling[1]; in the second, a kind of penalty method has been developed to allow the more complex interaction of the medium droplets and the underlying flow. The proposed multi-scale approach includes the Lagrangian to Eulerian inverse conversion. This allows in the primary atomization process the droplets to collide and merge with a resolved liquid body. The collision is handled differently for the small and medium particles.

3.1 Treatment of Medium Droplets

Handling the medium droplets involves three main items: their detection and subsequent conversion to Lagrangian droplets, their advection and their potential liquid collision.

---

[1]In the application foreseen in this paper, the one way approach is considered as sufficient, even if the small droplets can in practice have almost the size of the cell.

3.1.1 Detection and Transformation

The first step of the multi-scale algorithm is to detect the liquid inclusion to be transformed. A tag-propagation algorithm is employed. As illustrated on Fig. 1, each liquid inclusion is detected by propagation of a tag over each liquid-cell, i.e. a cell where the volume fraction $C_i > 0.5$. At first, each liquid-cell is tagged with an unique number. Then, the smallest tag is iteratively propagated among each neighbouring liquid-cell. When the tag is entirely propagated among all liquid cells which constitute the liquid inclusion, the tag is then extended to all surrounding cells where $0 < C_i < 0.5$. Considering a liquid inclusion l, one can evaluate the volume of this inclusion v_l, its center of mass $\mathbf{x}_l$ and average velocity $\mathbf{v}_l$ over all cells i_l which contains the liquid inclusion through the VOF function:

$$v_l = V_{cell} \sum_{i \in i_l} C_i \quad \mathbf{x}_l = V_{cell} \frac{1}{v_l} \sum_{i \in i_l} \mathbf{x}_i C_i \quad \mathbf{v}_l = V_{cell} \frac{1}{v_l} \sum_{i \in i_l} \mathbf{v}_i C_i \tag{1}$$

where $\mathbf{v}_i$ is the eulerian velocity interpolated at the center of cell i and V_{cell} the volume of the cell.

As it is quite difficult to determine a physical parameter (like Weber number) to determine the stability of any drop and allow the transition between Eulerian and Lagrangian resolution, a possible transition is determined here based on geometrical considerations. Let N_l be the total number of cell contained in a liquid inclusion l. For very small inclusions where $N_l < 2^m$, with m the dimension of the considered problem ($m = 2$ for bidimensional problems, $m = 3$ for three dimensional cases),
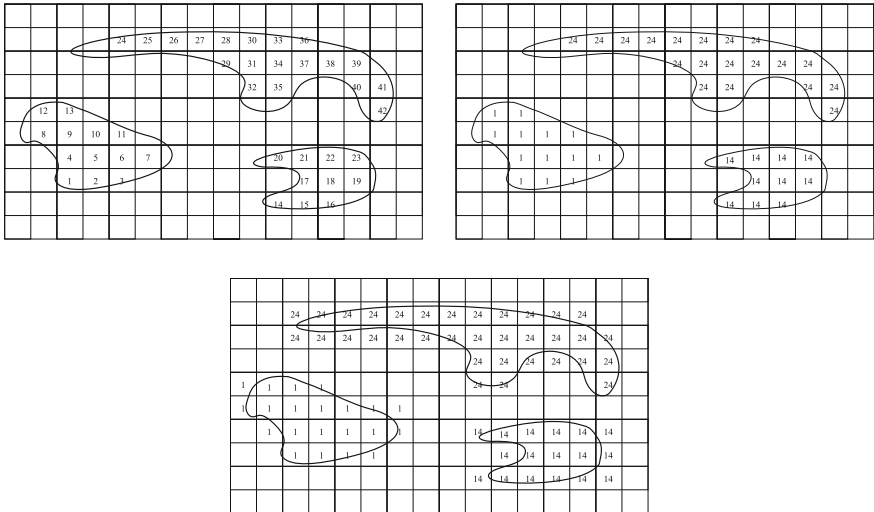
Fig. 1 Illustration of liquid inclusion detection

Fig. 2 Sphericity criterion for medium inclusion
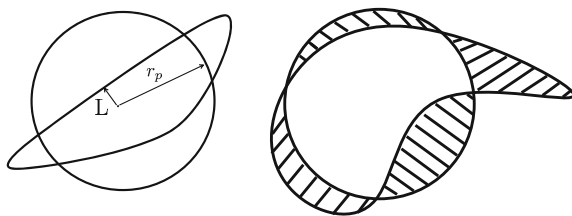
the inclusion is automatically treated in a Lagrangian point particle way, without any other arguments. For medium inclusion $2^m \leq N_l \leq 6^m$, a sphericity criterion is used, as illustrated on Fig. 2.

To this way, a sphere of equivalent volume is superimposed on the center of mass of the liquid inclusion, for which the radius is

$$r_p = \left(\frac{v_l}{\pi}\right)^{1/m} \left(\frac{3}{4}\right)^{(m-2)/m} \tag{2}$$

and the difference of characteristic length δ_l and volume δ_V (dashed part on the right of Fig. 2 are computed:

$$\begin{cases} \delta_l = r_p - L \\ \delta_V = V_{cell} \sum_{i \in i_l} |C_i - \chi_i| \end{cases} \tag{3}$$

where $\chi_i = 1$ if $||\mathbf{x}_i - \mathbf{x}_l|| \leq r_p$, 0 otherwise and L is the smallest length between the center of mass and the interface, i.e. $L = \phi(\mathbf{x}_l)$. The inclusion is assumed as quasi-spherical if

$$\frac{\delta_l}{r_p} < \alpha \quad \frac{\delta_V}{v_l} < \beta. \tag{4}$$

After some numerical test, α and β have been set between 0.5 and 1 (these values can be increased to force more conversions). If those two criteria are satisfied, the inclusion becomes a Lagrangian particle of volume v_l, radius r_p and initial velocity $\mathbf{v}_p = \mathbf{v}_l$ at the location $\mathbf{x}_p = \mathbf{x}_l$. If they are not satisfied, the inclusion is still treated by the Eulerian CLSVOF resolution until a possible stabilization or fragmentation occurs.

An original tracking method has been developed for the medium drop, in a way of a penalty method. Indeed, the idea of this method is to project the mass and momentum particle on the Eulerian field. Hence, for a given particle:

$$(\rho^{n+1}, \mu^{n+1}, \mathbf{u}^n)_i = \begin{cases} (\rho_l, \mu_l, \mathbf{v}_p) & \text{if} \quad ||\mathbf{x}_i - \mathbf{x}_p|| \leq r_p \\ (\rho_g, \mu_g, \mathbf{u}_i^n) & \text{otherwise} \end{cases} \tag{5}$$

Then, the velocity prediction equation is solved on the Eulerian grid with the new values of density, viscosity and velocity updated with respect to particle positions. The pressure inside the drops is corrected by Laplace relation:

$$p_i^{n+1} \rightarrow p_i^{n+1} + \frac{\sigma}{r_p} \quad \text{if} \quad ||\mathbf{x_i} - \mathbf{x_p}|| \le r_p \tag{6}$$

Afterwards, the pressure correction equation is solved with the corrected pressure. Then, the new particle velocity is obtained by averaging the Eulerian velocity inside the considered drop

$$\mathbf{v}_p = \frac{1}{v_p} \sum_i V_{cell,i} C_i \mathbf{u}_i^{n+1} \quad \text{if} \quad |\mathbf{x_i} - \mathbf{x_p}| \le r_p \tag{7}$$

and finally Eq. 13 is solved with this new particle velocity. This formulation take implicitly into account the drag force on the particle and lead to a more conservative form than the method presented into previous section, while allowing the de-refinement process as the particle moves away from the interface.

3.1.2 Drop-Interface Collision

In the present work, a re-impact algorithm is implemented to take into account of a possible collision between particles and the liquid-gas interface. The re-impact is allowed if a given particle is moving throw the interface and if this particle is sufficiently closed to it:

$$\mathbf{v}_p \cdot \nabla \phi > 0, |\phi_p| < r_p + \Delta_{x,min} \tag{8}$$

where ϕ_p is the interpolation of ϕ at a location $\mathbf{x} = \mathbf{x}_p$ and $\Delta_{x,min}$ the grid size. If those criterion are satisfied, both Level Set and VOF functions are reconstruct inside the drop:

$$\phi_i^n = r_p - ||\mathbf{x}_p - \mathbf{x}_i||, C_i^n = 1 \tag{9}$$

for all cells i inside the drop (i.e. $||\mathbf{x}_p - \mathbf{x}_i|| < r_p$). To the drop periphery, the Level Set function is fixed to 0 and the difference between the drop volume and the VOF newly added is equally distributed to the VOF function on all cells at the drop periphery, to ensure mass conservation. Afterwards, the velocity inside de drop is imposed on the Eulerian field with momentum conservation consideration:

$$\mathbf{u}_i^n \rightarrow \frac{C_i^n \rho_l \mathbf{v}_p + (1 - C_i^n)\rho_g u_i^n}{C_i^n \rho_l + (1 - C_i^n)\rho_g} \tag{10}$$

which is exactly equal to $\mathbf{v}_p$ for full cells (i.e. $C_i^n = 1$) and is a mass weighted for mixed cells or small droplet ($r_p \le \Delta_{x,min}$). Finally, the redistance algorithm is used to regularize the function ϕ^n into the gas phase.

3.2 Treament of Small Droplets

The detection of droplets smaller than the finest mesh size is performed by detecting any cells characterized by a value of VOF $0 < C_i < 0.5$ not attached to any larger structure, i.e. surrounded by cells with $0 < C_i < 0.5$. In this case the Level-Set function does not see any liquid mass, so that for the CLSVOF this liquid would be effectively lost. For these small Lagrangian droplet (i.e. $r_p \leq \Delta_{x,min}$), a classical drag coefficient for spherical point particle is used, from Schiller and Neumann:

$$C_D(R_{e,p}) = \begin{cases} 24R_{e,p}^{-1}(1 + 0.15R_{e,p}^{0.687}) & \text{if} \quad R_{e,p} < 1000 \\ 0.424 & \text{otherwise} \end{cases} \tag{11}$$

with $R_{e,p} = 2r_p\rho_g||\mathbf{v}_p - \mathbf{v}_{p,e}||/\mu_g$ and where $v_{p,e}$ the Eulerian velocity interpolated at the particle location. These values give a relaxation time in the form $\tau_p = 8\rho_l r_p/(3\rho_g C_D||\mathbf{v}_p - \mathbf{v}_{p,e}||)$. Then, the particle velocity and position follow the equations

$$\frac{d\mathbf{v}_p}{dt} = \tau_p^{-1}||\mathbf{v}_p - \mathbf{v}_{p,e}|| \tag{12}$$

and its position

$$\frac{d\mathbf{x}_p}{dt} = \mathbf{v}_p \tag{13}$$

Equations 12 and 13 are integrated using a classical second order Runge-Kutta scheme. The potential collision of these droplets with an interface can happen in two different ways. In the first case, the droplet is considered as small even on the finest mesh, so that its mass and momentum can be directly injected into the local cell. In the second, the particle approaching the interface crosses one or more mesh refinement jumps: once its size exceeds the cell size, it is detected by the medium droplets search algorithm and switches in this category, so that it is projected on the Eulerian field before the actual impact (see Sect. 3.1.2). Medium droplets entering a coarse enough region are transferred to this category too.

4 Validation and Results

4.1 Medium Droplet Validation

In this first example, a three dimensional liquid drop at rest ($\rho_l = 2\,\text{kg.m}^{-3}$, $\mu_l = 0.001\,\text{kg.m}^{-1}.\text{s}^{-1}$) is immersed into an uniform gas stream ($\rho_g = 1\,\text{kg.m}^{-3}$, $\mu_g = 0.001\,\text{kg.m}^{-1}.\text{s}^{-1}$) with constant velocity in the x direction $\mathbf{u}(t = 0) = [U_0, 0, 0]^T$ with $U_0 = 0.1\,m.s^{-1}$ and a surface tension $\sigma = 0.001\,Nm^{-1}$. The computational domain consists of a square box of size $L = 0.5\,\text{m}$ with slip conditions on the walls

tangent to the gas stream and respectively uniform inlet and outlet on the two walls orthogonal to the stream. This lead to following non dimensional numbers, based on the drop radius $R = 0.05$ m:

$$W_e = \frac{\rho_l U_0^2 R}{\sigma} = 1, \qquad R_e = \frac{\rho_l U_0 R}{\mu_l} = 10 \qquad (14)$$

The test consists into a study of the acceleration of the droplet up to a physical time of $t_{end} = 2\ s$ done with the CLSVOF with increasing refined meshes. The coarsest mesh is composed by 32×32 (M32) cells, which correspond to 7 cells per droplet diameter. The droplet can still be considered (but barely) as resolved. The more refined meshes are given by 64×64 and 128×128 cells (M64 and M128). The most refined mesh (M 128) is considered as the reference for medium Lagrangian droplet validation. Actually, with the choosen parameters for this validation, the Weber number of the particule is $We = 1$, and M 128 mesh gives 25 grid point per diameter which is enough for a good resolution. The medium Lagrangian droplet computation is performed on the coarsest (M32) of the meshes. The particle is initialized as in the pure Eulerian case, but the multi-scale algorithm is allowed to detect and transform at the very first time-step: the Level-Set and VOF liquid fields are removed and a Lagrangian medium particle is added with the radius equal to $R = 0.05\ m$. Figure 3 shows a direct comparison between the mesh converging Eulerian results and the Lagrange medium droplet formulation. The visualization clearly shows that the final position of the droplet ($x(t = t_{end})$ is shifted forward when a more accurate resolution is performed. The M32 mesh droplet is clearly late in comparison with the reference result of the M128 mesh. Conversely, the Lagrangian result (on M32 mesh) shows a good agreement with the most accurate M64 and M128 meshes. The velocity field obtained with the mixed formulation is close to the one obtained with the Eulerian, whereas a classical Lagrangian drag-force model fails to correctly reproduced the flow topology.

The position and velocity of the droplet have been measured, their values plotted against time in Fig. 4. For the CLSVOF computation, the position of the center of
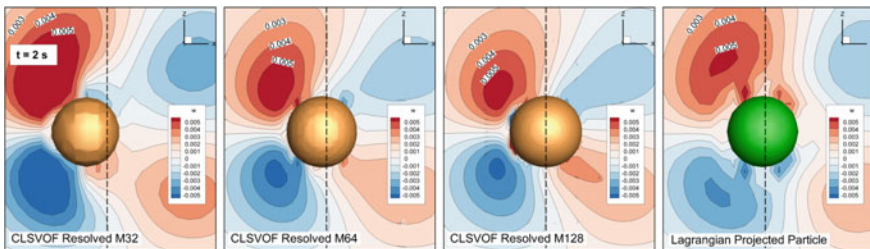
Fig. 3 Advection of the liquid droplet at $t_{end} = 2\ s$. From *left* to *right*, three CLSVOF results with increasing mesh refinement (M32, M64, M128) and the result of the multi-scale computation. The *colour* field is the z component of the velocity **u**. The *vertical dotted white line* represents the x position of the droplet center of mass, as calculated with the CLSVOF M128 (the finest) mesh
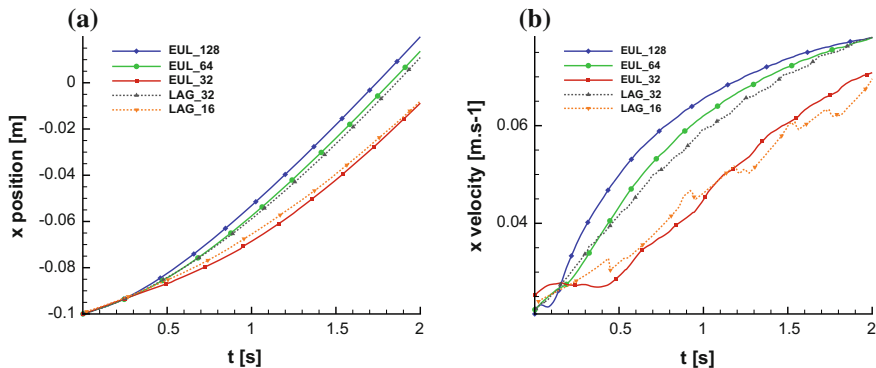
Fig. 4 **a** $x(t = t_{end})$ position of the droplet **b** x velocity component of the droplet versus time. *Continuous lines* Eulerian computation, *dotted lines* Eulerian/Lagrangian

mass and resulting velocity of the droplet have been evaluated as

$$
\mathbf{x}_{drop} = \frac{\int_{\Omega_l} \mathbf{x} \, dv}{\int_{\Omega_l} dv} = \frac{\sum_i C_i \mathbf{x}_i}{\sum_i C_i} \qquad \mathbf{v}_{drop} = \frac{\int_{\Omega_l} \mathbf{u} \, dv}{\int_{\Omega_l} dv} = \frac{\sum_i C_i \mathbf{u}_i}{\sum_i C_i} \qquad (15)
$$

A Lagrangian computation with a very coarse mesh (M16) has been plotted as well. The plots clearly show how the Lagrangian medium droplet modelling is able to reach almost the same accuracy as the Eulerian modelling with a mesh size twice as refined. It is also visible how the inaccurate prediction of the increasing velocity for the M32 CLSVOF solution is affected by an initial plateau between $t = 0\,s$ and $t = 0.5\,s$: the initial acceleration being delayed, the following evolution is shifted towards lower values.

4.2 Assisted Atomization of a Liquid Sheet

The whole multi-scale algorithm has been applied to the simulation of the primary atomization of a liquid sheet sheared by two parallel air streams. The considered numerical configuration aims to reproduce a simple atomization device as the one experimentally investigated in [19]. The injector, depicted in Fig. 5a, consists of a NACA-shaped injector immersed into a channel gas flow, discharging the liquid by a rectangular fence 300 μ m thick (visible in the middle of the device nozzle). Different geometrical configurations as well as liquid and gas flow regimes are considered by the authors. The parameters are summarized in Table 1.

The simulation domain, with reference to Fig. 5b, is a rectangular box of $L_x = 40.96$ mm, $L_y = 10.24$ mm, $L_z = 5.12$ mm. AMR blocks of $16 \times 16 \times 8$ cells have been used; a total of 5 levels of refinement give an equivalent fine mesh of 1024 ×

Fig. 5 **a** Actual liquid sheet injector device. **b** Numerical computation set-up
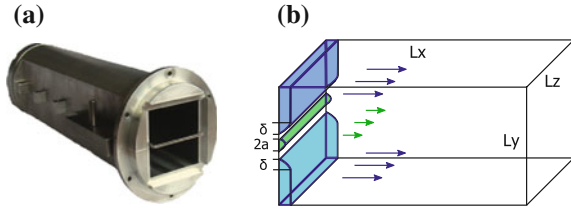
Table 1 Dimensionless parameters of the 3D atomization simulation

Gas reynolds	$Re_g = \frac{\rho_g u_g \delta}{\mu_g}$	1115
Liquid reynolds	$Re_l = \frac{\rho_l u_l a}{\mu_l}$	104
Weber	$We = \frac{\rho_g (u_g - u_l)^2 a}{\sigma}$	17.42
Momentum ratio	$M = \frac{\rho_g u_g^2}{\rho_l u_l^2}$	0.91

256×128, which means $\Delta x = 40\,\mu$ m. Inflow condition are imposed on the left face, slip conditions on the horizontal and vertical faces and outflow on the right face. The droplet detection algorithm is capped at a maximum droplet size of seven δx, giving a possible diameter range of $[0 : 280]\,\mu$ m.

A comparison of some large scale features of the atomization process has been made with respect to the experimental results found in [19]. A comparative visualization of the behaviour of the sheet is given in Fig. 6. The simulation correctly captures the growing longitudinal instability of the sheet, as well as the transversal modulation. The thin ligaments formed by the primary atomization at the break-up point are fully captured by the CLSVOF eulerian solution. A first wave of droplets is formed at this location. The liquid detached from the main sheet body undergoes further deformation and break-up into a fully three-dimensional flow: it can be seen in both images that large liquid parcels coexist with smaller stable droplets.

A preliminary analysis has been performed on the droplet spray, the results compared to the experience by laser diffraction system allowing measurement of spray droplet size distributions. The statistics involve the droplets in the whole numerical domain; their characteristics are averaged in time, the samplings taken with a frequency corresponding to an average convection time in order to avoid repeated registrations of the same droplet. The particles of diameter inferior to the finest mesh cell ($40\,\mu$ m) have been discarded, as no physics is involved in their creation.

A total of 18457 droplets ($40 < D < 320\,\mu$ m) have been registered. Figure 7 shows the corresponding distribution in volume. The simulation seems able to capture the predominant diameters around 255 microns, but no information has been extracted from structures larger than 320 microns in diameter, so that the distribution is truncated after this value. Actually, the distribution is only estimated on Lagrangian particles (both medium and point ones). It would seem that the evolution of the distribution with decreasing diameters is underestimated, a possible conse-
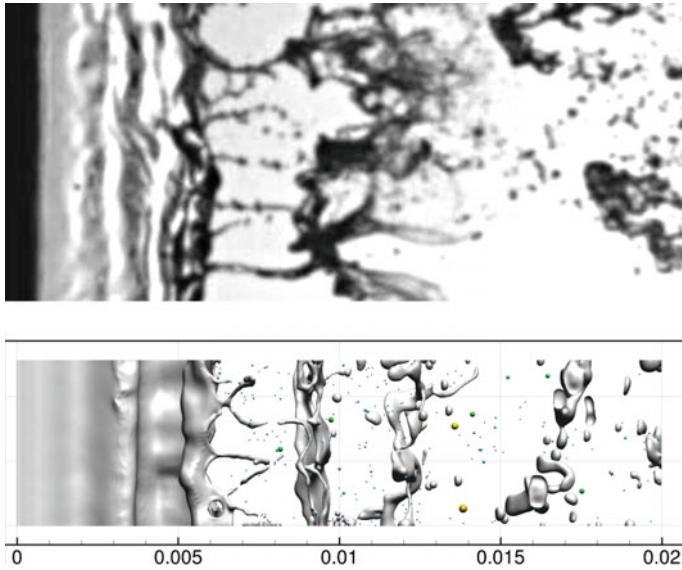
Fig. 6 Snapshots of both experimental visualization and simulation, arbitrary time step
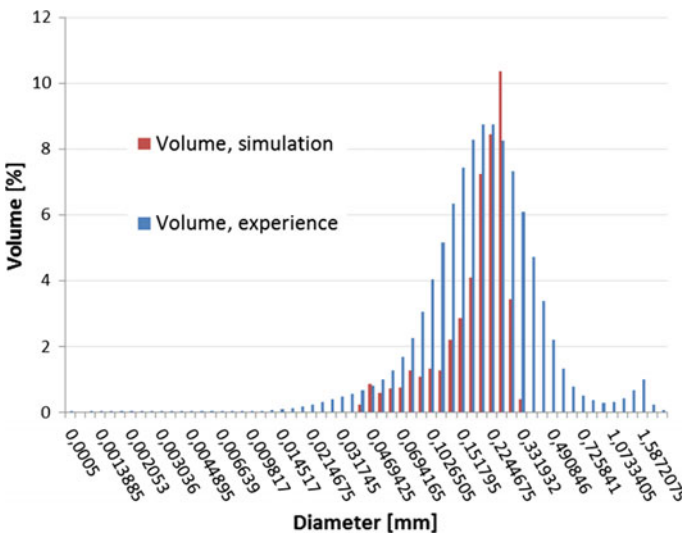
Fig. 7 Droplet volume distribution obtained from the simulation dispersed phase, comparison with the experience

quence of the considered volume of interest close to the injector and the absence of a secondary atomization model. The numerical diameter is $D_{32} = 158\,\mu$ m, where the experimental one is $D_{32} = 165\,\mu$ m showing a pretty good agreement.

5 Conclusion

An innovative multi-scale methodology for the direct numerical simulation of atomization has been presented. It consists of three main items. The first is a coupled Level Set/Volume of Fluid method (CLSVOF) for accurate capture of the primary atomization process. The second an adaptive mesh refinement technique (oct-tree AMR) to dynamically optimize the structured Cartesian mesh. The third consists of a particle tracking algorithm to capture droplet dynamics. An improved Eulerian-Lagrangian coupling has been developed to assure a smooth transition between the Eulerian and the Lagrangian modelling of the droplets, where both models approach their design limits. Results show its ability to reproduce the whole atomization process, from large scale instabilities to small droplet dynamics. A preliminary statistical spray analysis is performed as well, showing a realistic distribution of droplet sizes and average droplet diameter.

References

1. Stapper B, Sowa W, Samuelsen G (1992) An experimental study of the effects of liquid properties on the breakup of a two-dimensional liquid sheet. J Eng Gas Turb Power 114:32–39
2. Mansour A, Chigier N (1990) Disintegration of liquid sheets. Phys Fluids 2:706–719
3. Fernandez VG (2009) Experimental study of a liquid sheet disintegration in a high pressure environment. Ph.D. thesis, ISAE
4. Jaegle F, Senoner J-M, Garcia M, Bismes F, Lecourt R, Cuenot B, Poinsot T (2011) Eulerian and lagrangian spray simulations of an aeronautical multipoint injector. In: Proceedings of the combustion institute. doi:10.1016/j.proci.2010.07.027
5. Herrmann M (2010) A parallel eulerian interface tracking/lagrangian point particle multi-scale coupling procedure. J Comput Phys 229:745–759
6. Herrmann M (2008) A balanced force refinement level sel grid method for two-phase flows on unstructured flow solver grid. J Comput Phys 227:2674–2706
7. Herrmann M (2010) Detailed numerical simulations of the primary atomization of a turbulent liquid jet in crossflow. J Eng Gas Turbines Power 132(6):451–466. doi: 10.1115/1.4000148, http://link.aip.org/link/?GTP/132/061506/1
8. Li X, Arienti M, Soteriou M, Sussman M (2010) Towards an efficient, high-fidelity methodology for liquid jet atomization computations. In: AIAA, 2010-210 48th AIAA Aerospace Sciences Meeting 2010
9. Tomar G, Fuster D, Zaleski S, Popinet S (2010) Multiscale simulations of primary atomization using gerris. Comput Fluids 39(10):1864–1874. http://gfs.sf.net/papers/tomar2010.pdf
10. Fuster D, Bague A, Boeck T, LeMoyne L, Leboissetier A, Popinet S, Ray P, Scardovelli R, Zaleski S (2009) Simulation of primary atomization with an octree adaptive mesh refinement and VOF method. Int J Multiph Flow 35:550–565
11. Arienti M, Li X, Soteriou C, Eckett C, Sussman M, Jensen R (2013) Coupled level-set/volume-of-fluid method for simualtaion of injector atomization. J Propul Power 29:147–157

12. Apte S, Gorokhovski M, Moin P (2003) Les of atomizing spray with stochastic modeling of secondary break-up. Int J Multiph Flow 29:1503–1522
13. Gorokhovski MA, Saveliev VL (2003) Analyses of kolmogorov's model of breakup and its application into lagrangian computation of liquid sprays under air-blast atomization. J Phys Fluids 15(1):184–192. doi:10.1063/1.1527914
14. Sussman M, Puckett E (2000) A coupled level set and volume of fluid method for computing 3d and axisymmetric incompressible two-phase flow. J Comput Phys 162:301–337
15. Sarthou A, Zuzio D, Estivalezes J-L (2013) Multiscale euler-lagrange method for parallel simulation of atomization induced by air-blast planar injectors. In: 21st AIAA computational fluid dynamics conference
16. Kang M, Fedkiw R, Liu XD (2000) A boundary condition capturing method for multiphase incompressible flow. J Sci Comput 15:323–360
17. MacNeice P, Olson KM, Mobarry C, deFainchtein R, Packer C (2000) Paramesh: a parallel adaptive mesh refinement community toolkit. Comput Phys Commun 126
18. Zuzio D, Estivalezes J-L (2011) An efficient block parallel amr method for two phase flow simulations. Comput Fluids 44:339–357
19. Déjean B, Berthoumieu P, Gajan P (2016) Experimental study on the influence of liquid and air boundary conditions on a planar air-blasted liquid sheet, part i: liquid and air thicknesses. Int J Multiph Flow 79:202–213

Part II
Regular Papers

Effects of Free Stream Turbulence on a Three-Dimensional Transitional Flow

Pramodkumar Bagade and Tapan K. Sengupta

Abstract In the present research we investigate the effects of free stream turbulence (FST) on transitional flow in a square duct. The computed flows at sub-critical Reynolds number (Re = 800) is studied for effects of FST. A FST model is developed based on existing wind tunnel data by matching the statistics of the synthesized FST data up to fourth order statistics of wind tunnel data. Finally, receptivity of the flow in the square duct is reported for this Re flow in the square duct.

1 Introduction

Flow through a 3D square duct represents geometrical symmetry in flow structure, even when the flow is turbulent [6, 8]. This flow is different from turbulent plane Poiseuille flows because of the secondary motions, identified and known as Prandtl's secondary motion of second kind. However, the experimental evidence [3] demarcate the possibility of transition for Re greater than equal to about 1000. Our interest is on effects of FST of transitional flow, we first attempt to compute equilibrium flows in the square duct for Re = 800 and 1100. Here, Re is defined in terms of the half width of the duct as the length scale and inflow velocity of the duct as the velocity scale. The receptivity of the equilibrium flow for Re = 800 is reported for a Gaussian circular patch excitation at the wall and is shown to display no receptivity to this type of wall excitation [11]. It is also noted that the flow for Re = 1100 does not exhibit any computational equilibrium state, implying the strong receptivity to existing numerical noise and the response to small background noise in the form

P. Bagade (✉)
Department of Aerospace Engineering, IIT Kanpur, Kanpur, India
e-mail: pramodbagade@gmail.com

T. Sengupta
HPCL, IIT Kanpur, Kanpur 208016, India
e-mail: tksen@iitk.ac.in

of spatio-temporal wave fronts [11]. This approach of studying receptivity for 2D channel flow has been reported [4], but no details exist in literature for 3D channel flow or flow in a square duct.

Effects of FST on flow has been reported [15] via a dynamical system approach, which showed the flows past a cylinder for Re = 53 to be different for different diameter cylinder and different flow speeds, due to difference in FST in the same tunnel at different speeds. The FST model has been developed in [12, 13] and furthermore refined for application in low Reynolds number aerodynamics [1].

2 Free-Stream Turbulence Modeling

In the moving average model of FST used here, the histogram or probability distribution function for the central moments are obtained first from the data for different flow speeds. Thereafter a synthetic time series is generated using a standard first order moving average model, with the help of second and fourth moments. Hence in this model the FST quantity is obtained from, $x_t = e_t + \alpha_{fst} e_{t-1}$ where e_t is defined by a normal distribution with zero mean and standard deviation defined as σ. To include effects of skewness (third moment) in this model, low wavenumber (k) FST component is added, taken from the experimental facility (from wind tunnel or flight data). The large-scale anisotropy of incoming flow is retained by this model. The first four central moments of e_t are given by $\mu_1(e_t) = 0$; $\mu_2(e_t) = \sigma^2$; $\mu_3(e_t) = 0$ and $\mu_4(e_t) = 3\sigma^4$ and with this one can obtain the central moments of the moving time average model, as (at every instant, e_t and e_{t-1} are uncorrelated) from the following $\mu_1(x_t) = 0$; $\mu_2(x_t) = \sigma^2(1 + \alpha_{fst}^2)$; $\mu_3(x_t) = 0$ and $\mu_4(x_t) = 3\sigma^4(1 + \alpha_{fst}^4)$. Note that the coefficient of skewness and kurtosis are given by $\gamma_1 = \mu_3/\mu_2^{3/2}$ and $\gamma_2 = \mu_4/\mu_2^2 - 3$. The first four moments of the time series x_t are matched with the four central moments from the experimental histogram to obtain σ and α_{fst}. Skewness is a measure of convection and vortex stretching and hence cannot be neglected. Thus, large scale anisotropy of incoming flow is retained up to low k range. This is also related to space-time correlation of FST, i.e., the dispersion relation of the convective dynamics. Generated synthetic FST data is obtained for two tunnel data, as compared in Fig. 1 for the streamwise component. Using the correlation among the three components of channel experimental data [9] one can create not only the three velocity components, but also the corresponding vorticity components. The comprehensive match between the tunnel and synthetis data assures one that such a FST model can be used in DNS and LES for computing FST effects by using the model data at the inflow of a computational domain.
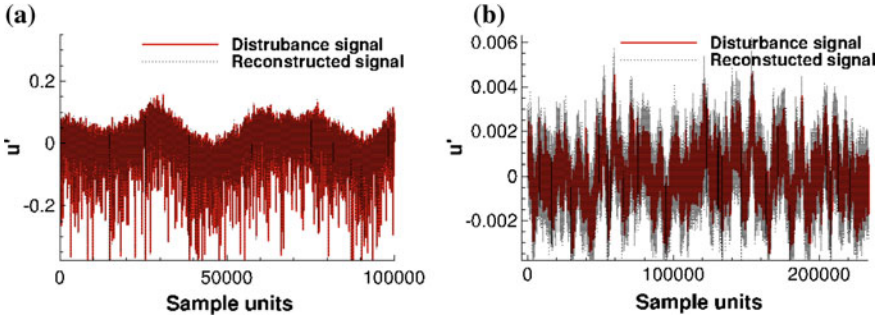
Fig. 1 Comparison of FST model with empty tunnel noise data from two wind tunnels. On the *left* is the NWTF tunnel, IIT Kanpur data and on the *right* is the low speed tunnel data from Ecole Polytechnique, Montreal
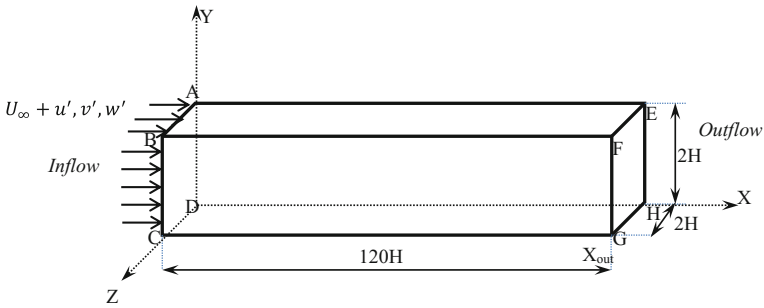
Fig. 2 The schematic and domain of the computational flow in the square duct

3 Effects of FST on Square Duct Flow

Above FST model can be used for flow in a square duct by imposing it along with the uniform velocity at the inflow. The schematic of the computational domain is shown in Fig. 2, which shows the cross-section given by $(2H \times 2H)$, while the streamwise length of the domain is taken as $120H$ for the reported results. For this incompressible flow, the velocity-vorticity rotational formulation [2, 10] is used for all the simulations. The no-slip side walls help obtain the wall vorticity values and the prescribed velocity and vorticity components are as obtained from the FST model at the inflow. At the outflow, Sommerfeld boundary condition is used for all the three vorticity components with identical convection speed ($U_c = 1$).

The imposed FST is shown in Fig. 3, at an instant by using the model for each and every point in the inflow plane. Note the difference in the scales of the velocity components in the streamwise and cross flow planes.
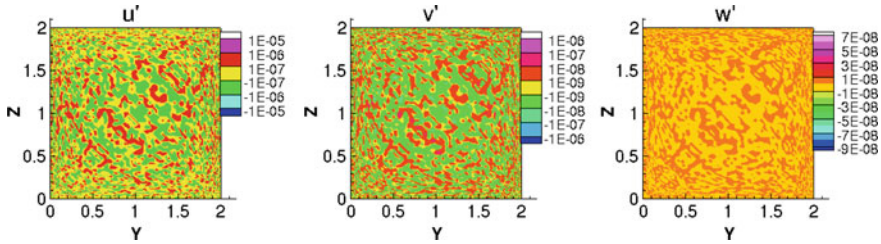
Fig. 3 Snapshot of velocity components developed by the FST model at the inflow of the duct

4 Results and Discussion

It was noted [11] that for Re = 800, one could obtain an equilibrium flow by $t = 200$, and the receptivity of FST on this sub-critical flow is studied here. The results are shown for the streamwise vorticity contours in cross flow planes at the indicated stations of Fig. 4. The results shown on the top row is immediately after switching on the FST model and one can notice not only the symmetry of the computed equilibrium flow, but also the secondary flow of second kind characterized by flow from the corners towards the center along the diagonals. This flow shows multi-cellular structures disturbed by the FST. The effects of the FST becomes very prominent at $t = 225$, with rapid changes downstream. Streamwise streaky vortex structures are noted along the center, prominently visible in the first two stations. With time and distance, such streaky structures diminish in size and at $t = 300$, one can notice the vortices of same sign merge together. This flow is strongly 3D and such inverse cascade is highly unexpected!

In the literature, inverse energy cascade has been thought to be the signature of 2D dynamics [7] and its presence here provokes one to investigate the contribution to total energy by various physical processes. This is seen best by the enstrophy transport equation (ETE) [14]. This equation was developed specifically to explain the appearance of small scales, irrespective of whether the flow is 2D or 3D for inhomogeneous flow.

In Fig. 5, we use this diagnostic tool of ETE to characterize the creation of rotationality by diffusion in the flow field. Various terms of ETE [14] is shown in perspective plots showing the minimum and maximum values of the quantity displayed for $t = 300$. At this time, the flow field shows mild time variation, as is evident from the range of variation of local acceleration term. In contrast, the convective acceleration term is orders of magnitude higher, as notes in the second frame from the top. However, the most interesting for this 3D flow is the contribution provided by the stretching term, which is more than hundred times smaller than the convective acceleration term. Even more striking is the contribution of diffusion and dissipation terms in transporting enstrophy, which are about ten times larger than convective acceleration terms. While dissipative term is necessarily only positive, the diffusion
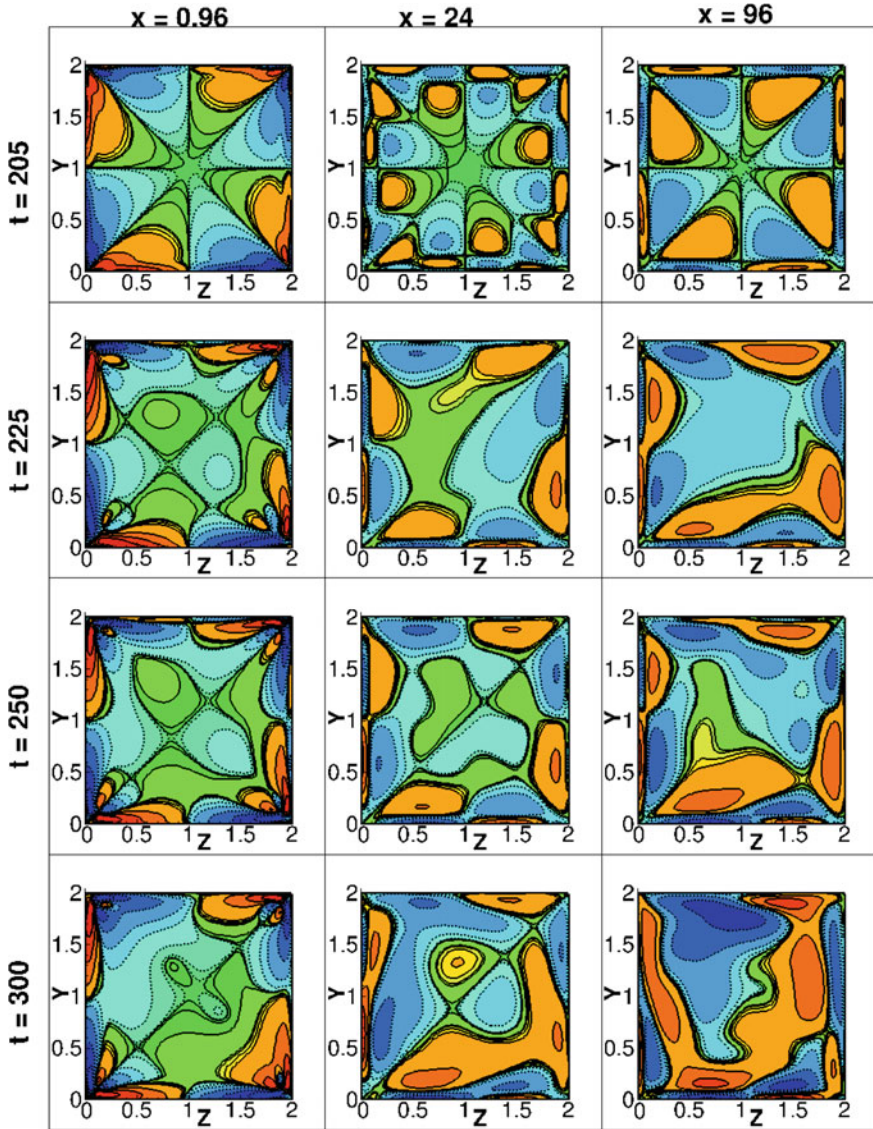
Fig. 4 Contours of streamwise vorticity component at representative cross flow planes at the indicated times

term for inhomogeneous flow can act as a source of rotationality, when this term has negative contribution, once again highlighting the important contribution made by the developed ETE [14].
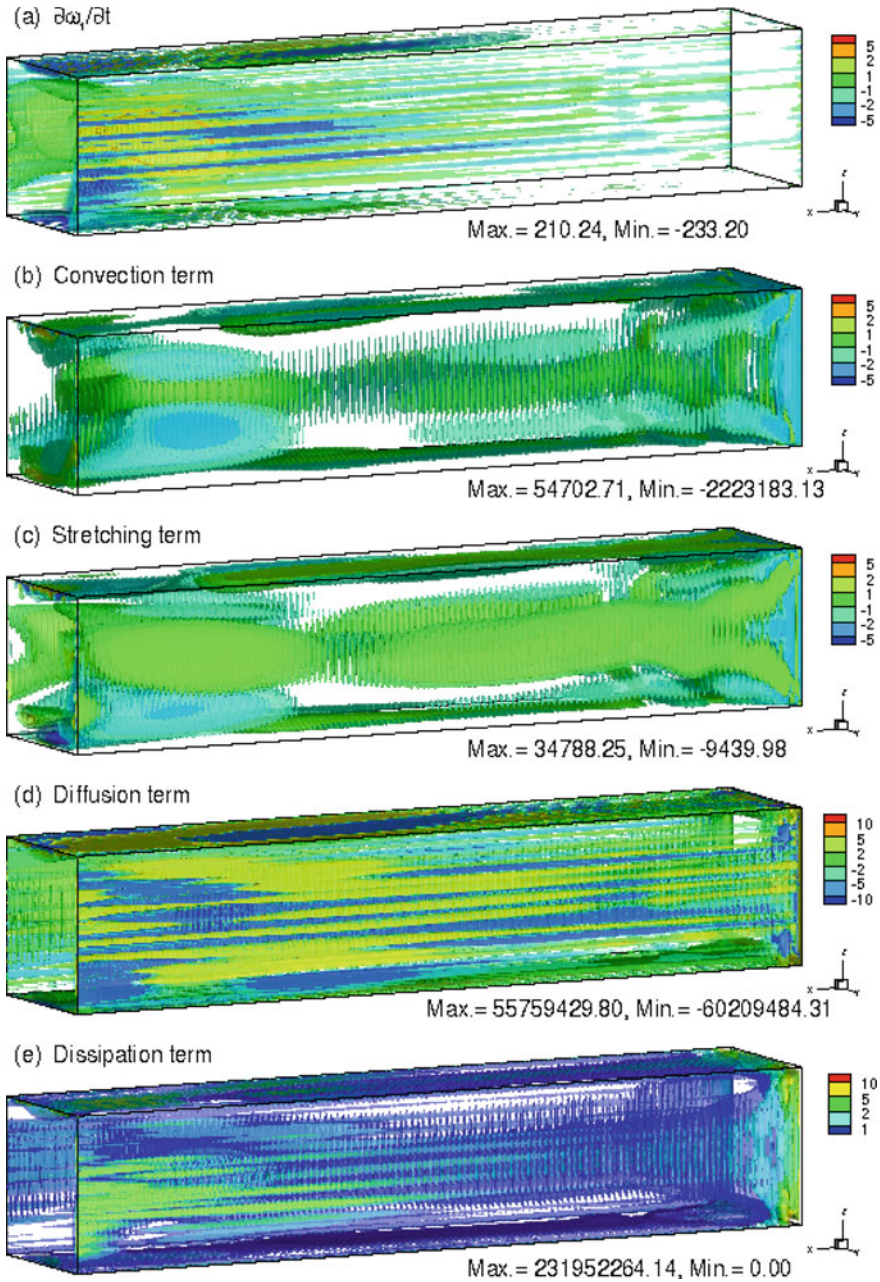
Fig. 5 Contributions of various terms contributing to the enstrophy transport equation

5 Summary and Conclusion

Based on past studies of wall excitation for sub-critical $Re = 800$ flow [11], here the effects of FST imposed through the inflow is studied for the same. Significant effects of FST is found and typical results are presented. However, the main emphasis of this study is to demonstrate the advantage of the developed FST model for DNS and LES for any realistic flows. For this favourable pressure gradient flow, it is noted that the flow is receptive to disturbances imposed near the center. Despite the flow being highly 3D, merger of small scale vortices created by FST into larger scale shows the lesser role for vortex stretching and more for inverse cascade in this flow. This study also highlights the importance of enstrophy transport equation in deciding scale selection for inhomogeneous flows.

References

1. Bagade PM, Krishnan SB, Sengupta TK (2015) DNS of low Reynolds number aerodynamics in the presence of free stream turbulence. J Aerosp Eng 4(1):20–34
2. Bhaumik S, Sengupta TK (2015) A new velocity-vorticity formulation for direct numerical simulation of 3D transitional and turbulent flows. J Comput Phys 284:230–260
3. Davies SJ, White CM (1928) An experimental study of the flow of water in pipes of rectangular section. Proc R Soc Lond Ser A 119:92
4. Dipankar A, Sengupta TK (2006) Symmetrized compact scheme for receptivity study of 2D transitional channel flow. J Comput Phys 215:245–273
5. Drazin PG, Reid WH (1981) Hydrodynamic stability. Cambridge University Press, UK
6. Gavrilakis S (1992) Numerical simulation of low-Reynolds-number turbulent flow through a straight square duct. J Fluid Mech 244:101–129
7. Kraichnan RH, Montgomery D (1980) Two-dimensional turbulence. Rep Prog Phys 43:547–615
8. Nikuradse J (1926) Untersuchungen *ü*ber die geschwindigkeitsverteilung in turbulenten str*ö*mungen. PhD Thesis G*ö*ttingen VDI Forsch
9. Schlichting H (1979) Boundary layer theory, 7th edn. McGraw Hill, New York
10. Sengupta TK (2013) High accuracy computing methods: fluid flows and wave phenomenon. Cambridge University Press, USA
11. Sengupta TK (2017) DNS of turbulence from receptivity stage: Role of spatio-temporal wave front. In: Deville M, Le TH (eds) Proceedings Turbulence and Interaction, TI-2015, Springer Verlag
12. Sengupta TK, Das D, Mohanamuraly P, Suman VK, Biswas A (2009) Modeling free-stream turbulence based on wind tunnel and flight data for instability studies. Int J Emerg Multidiscip Fluid Sci 1(3):181–199
13. Sengupta TK, De S, Gupta K (2001) Effect of free-stream turbulence on flow over aerofoil section at high incidence. J Fluids Struct 15:671–690
14. Sengupta TK, Singh H, Bhaumik S, Chowdhury RR (2013) DIffusion in inhomogeneous flows: Unique equilibrium state in an internal flow. Comput Fluids 88:440–451
15. Sengupta TK, Singh N, Suman VK (2010) Dynamical system approach to instability of flow past a circular cylinder. J Fluid Mech 656:82–115

Turbulent Non-axial Flow in Rod Bundles

U. Bieder, A. Scoliege and Q. Feng

Abstract CFD studies were performed to evaluate the flow field, the turbulent statistics and pressure losses in rod bundles in cross flow with slope angle of 90°, 45° and 30° between main flow and the axis of the rods. Due to the presence of non-isotropic turbulence in rod bundles, Large Eddy Simulations (LES) are used. This approach is first justified by mesh convergence studies of a single rod in cross flow, simulated by two popular linear eddy viscosity turbulence models. Then the LES approach is validated by comparing the calculations of 90° cross flow to results known from the literature: the well-known experiment of Simonin et al. (1986) for a triangular rod arrangement and the very fine calculations of Iacovides et al. (2014) for inline rod arrangements. Comparison to the CEA experimental program EOLE is discussed which was performed with inclined rod bundles. The calculated pressure losses for 90°, 45° and 30° slope angles and two Reynolds numbers where compared to the experiments. Mean velocity profiles and turbulent statistics are presented.

1   Introduction

Heterogeneities in the coolant flow map in Pressurized Water Reactor (PWR) cores are one of the mechanisms involved in fuel assembly deformation which has sometimes been detected after core unloading [1]. The cross flow within fuel assemblies generate lateral hydraulic forces on the fuel rods which are strongly influenced by the core inflow and outflow conditions. In this context, the pressure forces acting on the rods are assumed to be the dominant hydro-mechanical force under high mass flow conditions.

U. Bieder (✉) · A. Scoliege · Q. Feng
Commissariat Lnergie atomique et aux nergies alternatives CEA
DEN/DANS/DM2S/STMF/LMSF, 91191 Gif-sur-Yvette, France
e-mail: ulrich.bieder@cea.fr

For a given assembly geometry, intra assembly pressure drops depend on both the mass flow and the slope angle between the main flow direction and the fuel bundle axis. Usually, empirical correlations were used to estimate the pressure drop coefficient in rod bundles for axial flow and 90° cross flow A nuclear reactor specific experimental program in rod bundles called EOLE has been performed at CEA by Peybernes [1] under non-axial flow conditions to evaluate the pressure drop coefficient as a function of the slope angle.

The EOLE experiments have been analyzed by detailed CFD calculations with the CEA in-house code TrioCFD [2] by applying the Large Eddy Simulation (LES) turbulence modelling method. The objective of these calculations was to better understand the turbulent flow field in the inclined rod bundles and to enrich the existing experimental data base (mainly pressure drop measurements) by detailed mean velocity and turbulence statistics information.

The single rod preparatory study in Sect. 2 shows that linear eddy viscosity models fail to predict turbulence effects in unsteady flow with vortex shedding. This conclusion is not new but often ignored in engineering CFD analysis [3]. The used LES method is tested in Sect. 3 for triangular rod arrangement against experimental data and fine LES calculations [4] and for inline rod arrangement against the detailed numerical analysis of Iacovides [5]. The EOLE experiment is analysed in Sect. 4. Pressure losses, mean velocity distribution and turbulence statistics are presented for various slope angles and two Reynolds numbers.

2   Turbulent Flow Around a Single Rod

More and more publications exist in the engineering literature where unsteady flow as e.g. the flow around singles rods is analyzed with Reynolds Averaged Navier-Stokes (RANS) turbulence modelling based on the linear eddy viscosity concept. The dependency of vortex shedding frequency and velocity amplitudes on the turbulence model is often analyzed; however, their dependency on the mesh refinement is not always tested until mesh convergence [3].

For the 2D test case presented by Rahman [3], this dependency on the meshing is shown in Fig. 1 for two popular RANS turbulence models; "realizable k-epsilon" and "k-ω SST". The vortex shedding for three mesh refinements was analyzed: "coarse" with 17,000 elements, "normal" with 33,000 elements and "fine" with 100,000 elements. The coarse mesh confirms the shedding frequency and velocity amplitude reported by Rahman [3]. Refining the mesh however leads to significant variations of both shedding frequency and velocity amplitude as can be seen from Fig. 1. The strong sensitivity of the shedding frequency and the velocity amplitudes on the mesh refinement has excluded RANS methods with linear eddy viscosity turbulence modelling for the analysis of the flow in rod bundles (although only 2D calculations have been performed). Hence, the analysis of the non-axial turbulent flow in rod bundles has been made with Large Eddy Simulations.
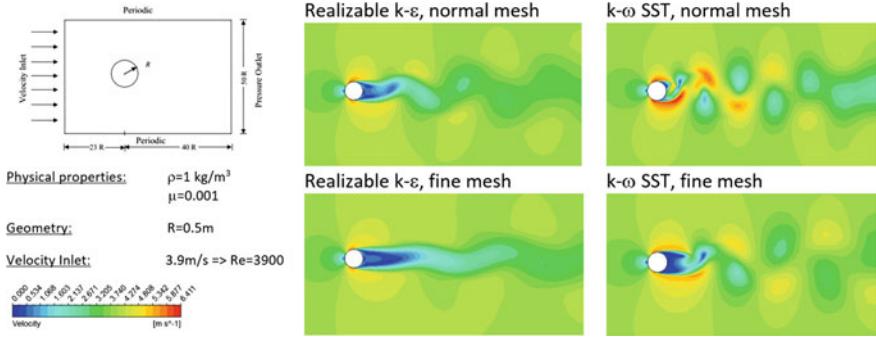
Fig. 1 Dependency of shedding frequency and velocity amplitude on mesh refinement

3 The TrioCFD Code

All LES calculations were made with the CEA in-house code TrioCFD [2] by using the numerical scheme shown in Table 1. This scheme has been used successfully in the analysis of turbulent flow in nuclear fuel assemblies with mixing grids [6].

A hybrid Finite Volume Element discretization method on tetrahedral grids is implemented in TrioCFD. This method approximates a continuous problem by a discrete solution in the space of the finite elements by maintaining the balance notation of finite volumes. In TrioCFD, the main unknowns as velocity and temperature are located in the center of the faces of the tetrahedral element leading to a P1 non-conforming discretization (P1NC) [7]. The pressure is discretized in both the center (P0) and the vertices (P1) of an element. The resulting staggred mesh arrangement improves the velocity/pressure coupling. The SOLA velocity projection method is used to assure the mass conservation [8].

Table 1 Numerical scheme for LES

Meshing	Element	Tetrahedra
	Discretization	P0+P1 for P
		P1NC for U
Time scheme	Adams bashforth	2nd order explicit
Discretization in space	Convection	2nd order centred
	Diffusion	2nd order centred
	Pressure solver	PETSc conjugated gradient solver
	Wall law	Reichhardt
Turbulence	LES	WALE

4 Upright Rod Bundles in Turbulent Cross Flow

Before simulting turbulent flow in inclined rod bundles with only limited experimental data available, the modelling is validated for 90° cross flow in triangular—(Sect. 4.1) and inline (Sect. 4.2) rod arrangement.

4.1 Rod Bundles with Triagonal Arrangement

Benhamadouche [4] has analyzed with detailed LES calculations the experiment of Simonin [9]. The same experiment is used here to test the LES approach and to compare two implementations of the wall law of Reichardt; a standard Dirichlet type [6] and a mixed Robin type implementation [7].

A 2-D representation of the geometry and of 1/4 of the meshing is shown on top of Fig. 2. Two hydraulic diameters in z-direction are included in the model leading to a mesh of about 5 Million control volumes. Selected turbulence statistics after convergence are given in Fig. 2 for the line x = 0. The Robin type implementation of the wall law gives globally better agreements to the experiment and the LES reference calculation of [4]. This implementation is forthcoming recommended in TrioCFD for LES.

4.2 Rod Bundles with Inline Arrangement

Inline rod bundles are characterized geometrically by the relationship of rod to rod pitch P to rod diameter D. Iacovides et al. [5] have extensively analyzed the flow in inline rod bundles by using different turbulence modelling approaches. All their simulations were conducted at the Reynolds number 41,000 based on the rod diameter and the bulk gap velocity. A hydraulic instability was detected for $1.4 < P/D < 2$. The result for P/d = 1.6 is used to further test the numerical model for LES of TrioCFD given in Table 1. Reichardt's wall law with a maximum y^+ of 13 is used for this analysis. The calculation domain and the velocity vectors in the central cut plane (temporal mean values) are shown in Fig. 3. In agreement to Iacovides et al. [5], a deflection of the recirculation bubble of about 22° was detected.

The lift coefficient calculated with Reichardt's wall function (Robin type implementation) is compared in Fig. 3 to the wall resolved result of Iacovides et al. [5]. As expected, the wall function calculation reproduces azimuthal course and phase shift of the wall resolved lift coefficient generally correct, however, both absolute value of the lift coefficient and phase shift at 270° are under-predicted.
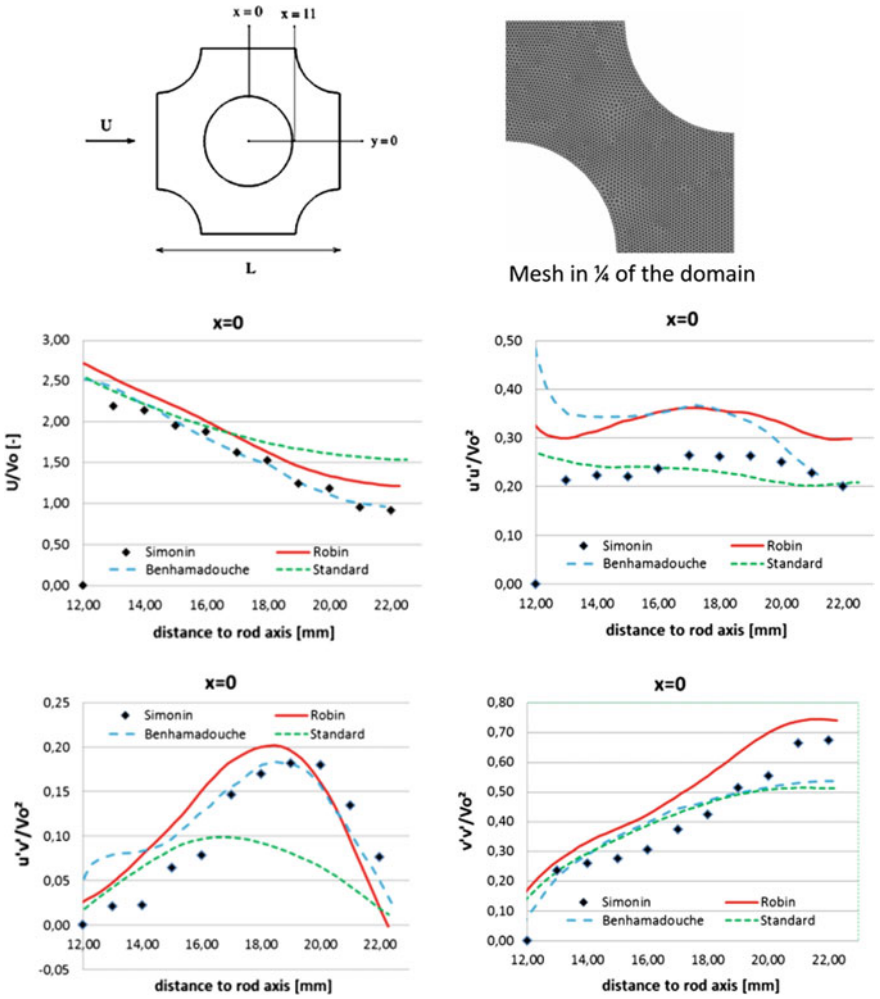
Fig. 2 Geometry, mesh refinement and normalized velocity profiles for x = 0
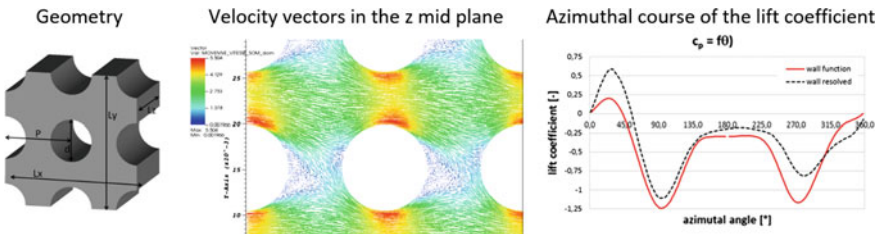
Fig. 3 Calculation domain, temporal mean velocity and lift coefficient

5   Inclined Rod Bundles in Cross Flow

The numerical model is first validated in Sect. 5.1 for inclined rod bundles placed in the EOLE test section. Then, in Sect. 5.2 the validated model is applied to more realistic nuclear reactor geometry.

5.1   Rod Bundles Placed in the EOLE Test Section

The former validated LES method for 90° cross flow in rod bundles (Sect. 4) is compared to results of the CEA experimental program EOLE [1]. The test facility with a rod bundle of 30° slope angle, placed in the quadratic test channel made of plexiglas, is shown on the left of Fig. 4.

The following experimental procedure has been used to predict the pressure loss of one row of rods: Subtracting the measured total pressure loss in flow direction of 6 rows from that of 8 rows give the pressure loss of two rows. Using this procedure, bundle inflow and outflow effects are expected to be eliminated from the results [1]. On the right hand side of Fig. 4, a horizontal cut through the calculation domain for the EOLE setup is given and the used boundary conditions are added to the figure. This calculation procedure is extremely CPU time intensive. The test section was discretized in up to 80 million control volumes to respect the requirements of LES and up to 300.000 CPU hours on 2000 processor cores of OCCIGEN [10] were needed to converge the statistics for one rod arrangement (6 calculations were performed for 3 inclination angles). Thus a cheaper method was developed by defining axially periodic calculation domains. For the inclined tube bundles, two periodic domains can be defined as shown in Fig. 5; a parallelepipedic one and an inclined one.

Two components of the temporal mean velocity are shown in Fig. 5 for the two periodic domains. In fact, the temporal mean velocity in x-direction (Ux) is given for the central vertical cut-plane and the temporal mean velocity in z-direction (Uz) is given in the central horizontal cut plane. No significant differences are detected for the distribution of the temporal mean velocities Ux and Uz. For Ux, the acceleration between the rods is good visible. The increase of Ux in the bundle near the bottom channel wall and its decrease near the top wall is also easily detectable. For Uz, Fig. 5 shows that the flow ascents (Uz > 0) in the wake of the inclined rods; for mass conserving considerations the flow descents (Uz < 0) in the crosswise gap

Fig. 4   EOLE test section with an 8 row rod bundle in place (30° slope angle); calculation domain
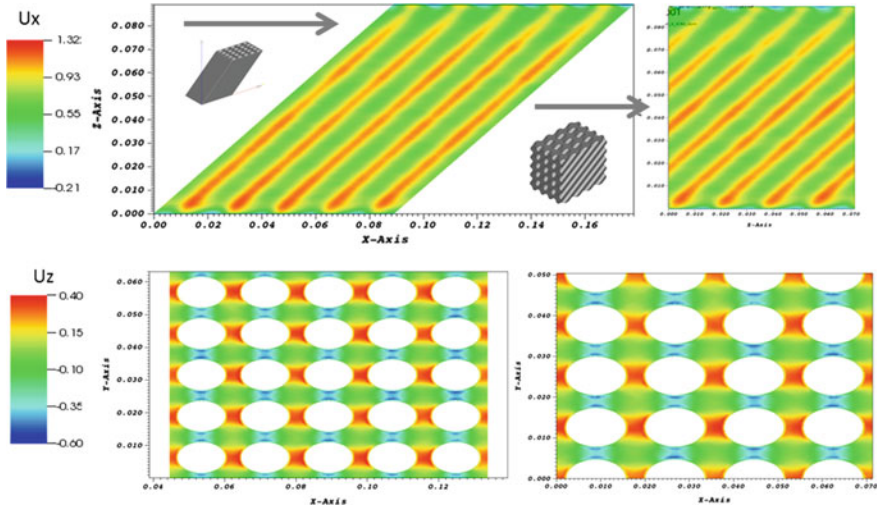
Fig. 5 Mean velocity in x and y direction in a central vertical and horizontal cut plane: *Left*, inclined domain; *Right*, parallelepipedic domain

Table 2 Calculated and measured pressure loss per row [Pa]

Reynolds number	12350			32300		
Slope angle [°]	90	45	30	90	45	30
EOLE experiment	239	133	93	1446	834	512
EOLE setup	200	107	78	–	–	–
Periodic parallelepipedic	206	120	89	1416	754	512
Periodic inclined	–	126	91	–	791	425

between rods. The upward mass flux balances the downward mass flux leading to a zero net mass flux in the whole cut plane. The calculated pressure losses per row of rods for 90°, 45° and 30° slope angles and two Reynolds numbers where compared in Table 2 to the experiment. The EOLE setup as well as the two periodic domains underestimate slightly the experimental values with the largest difference detected for the non-periodic full experiment calculations. An insufficient mesh refinement is most probably responsible for the discrepancy, although up to 80 Million control volumes have been used to discretize the experiment. Inclined and parallelepipedic domains give results of similar quality what underlines the consistency of the periodic modelling approaches.
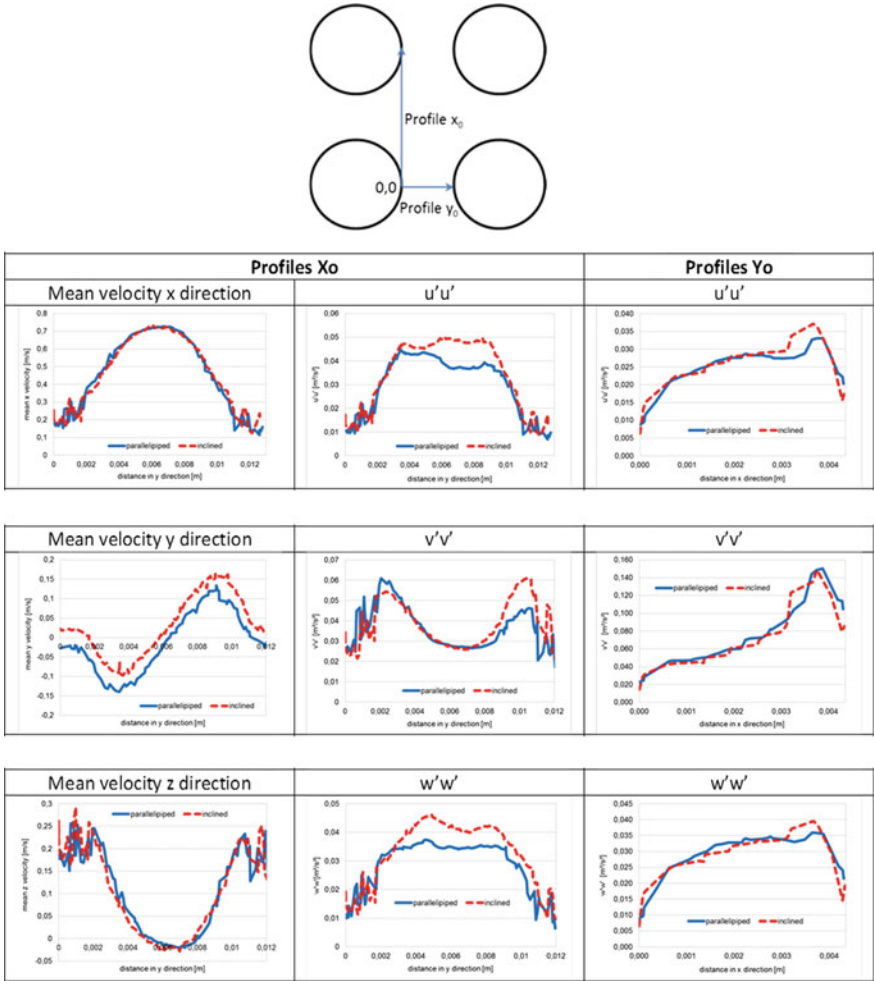
Fig. 6 Profiles of turbulence statistics along two lines; parallelepipedic and inclined domain

The turbulence statistics u′u′, v′v′ and w′w′ are visualized in Fig. 6 for the example of the two profiles Xo and Yo also given in Fig. 6. The point (0, 0) is located vertically in the center of the domain, downwind of the central rod. The courses of the shown correlations show strong differences in the local values what indicates the anisotropy of the turbulence. The profiles along Xo are slightly shifted out of the center. This might be an indicator that an azimuthal shift of the flow is present in the case of inclined tubes for P/d = 1.33 without forming a recirculation bubble as detected for upright rods between P/d = 1.4 and P/d = 2.

5.2   *Rod Bundles Placed in a Nuclear Reactor Core*

Figure 7 shows schematically the two calculation domains and the associated boundary conditions placed in a fuel assembly of a nuclear reactor core. The main flow direction is given by the arrow. The walls of the plexiglas channel of the EOLE test section do not represent realistically the flow in the reactor core; the solid walls inhibit any flow alignment to the rods axis over a longer axial distance. As shown in Fig. 5, the global mass flux across a cut plane placed horizontally in an inclined rod bundle is zero. Thus, to better represent the open, unbounded character of the flow in the reactor core, the vertical boundary condition has been changed from "wall" in the EOLE case to "periodic" in the REACTOR case. The side condition "global mass flux=0" is added. The norm of the velocity for the two cases is shown in Fig. 7 for a vertical cut plane between the rods.

The REACTOR case shows a vertically homogeneous distribution of the velocity field with acceleration between the rods and de-acceleration in the sub-channels. The mean velocity in the EOLE case accelerates near the bottom - and decelerates near the top channel wall as already shown in Fig. 5. Hence, the EOLE experiments cannot account for open, unbounded flow typically present in the reactor core.

The resulting pressure drop per row of rods is given in Table 3. The EOLE and REACTOR cases are compared to the experimental values. The modified boundary condition for the REACTOR case increases the pressure loss per row up to a
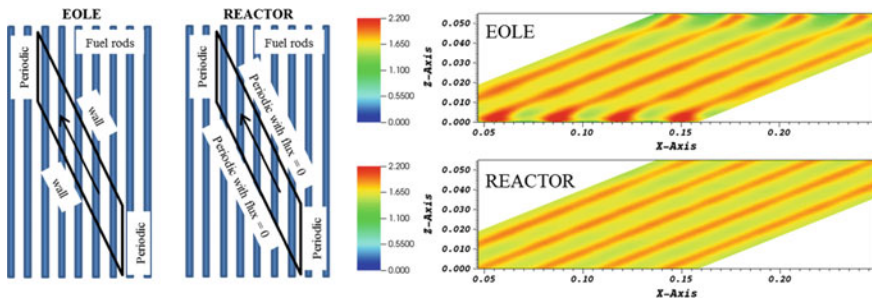
Fig. 7   Boundary conditions and flow field for an enclosed and open rod bundle

Table 3   Pressure loss per row [Pa] as a function of the calculation case

Reynolds number	12350		32300	
Slope angle [°]	45	30	45	30
EOLE experiment	133	93	834	512
EOLE case	126	91	791	425
REACTOR case	195	164	1305	1013
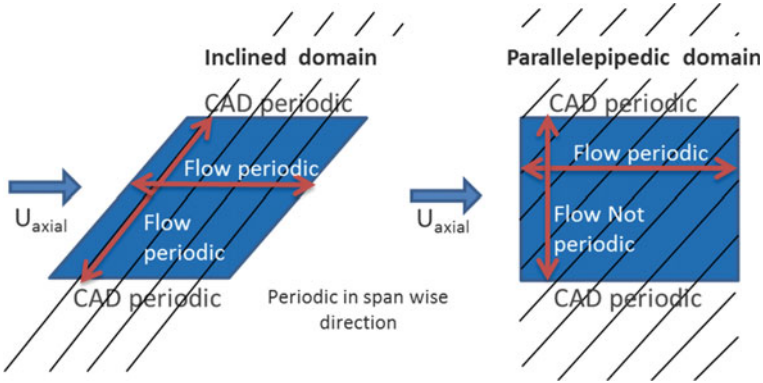
Fig. 8 Periodicity in the parallelepipedic and inclined domain

Table 4 Pressure loss per row [Pa/row] as a function of the calculation domain

Reynolds number	12350		32300	
Slope angle [°]	45	30	45	30
EOLE experiment	133	93	834	512
Inclined	195	164	1305	1013
Parallelepiped	113	78	725	454

factor two. This result might put the pressure loss correlations derived from simple experiments as EOLE into question regarding their application to the nuclear reactor core.

Finally, it is tested if the pressure loss for the REACTOR case is independent of the geometry of the calculation domain. As already mentioned and shown in Fig. 8, the CAD model of inclined and parallelepiped domain is periodic in all directions. The vertical (z-direction) periodicity of the inclined domain simulates an infinitely long rod. The flow in the wake of a certain rod leaving the domain at the top arrives in the wake of the same rod at the bottom of the domain. The physical meaning of the vertical periodicity of the parallelepipedic domain is not so evident. The flow leaving the domain at the top in the wake of a rod arrives in the wake of another rod at the bottom of the domain. Hence, the parallelepipedic domain seems not to simulate an infinitely long rod.

The resulting pressure drop per row of rods for the two periodic domains and the comparison to the EOLE experiment are given in Table 4 for two Reynolds numbers. The measured pressure loss per row is overestimated by the inclined domain by up to 100% and underestimated by the parallelepipedic domain by up to 20%. The parallelepipedic domain with vertical periodicity underestimates the pressure loss calculated for the same domain but with walls (Table 2), probably due to the missing friction on the channel walls. It is not surprising that inclined and parallelepipedic domains lead to different pressure losses per row as these domains seem to simulate

different physical phenomena. However, it is not evident which modelling approach represents better the cross flow in a nuclear reactor core. New experiments seem necessary to answer this question.

6   Conclusion

Anisotropic turbulent flow in upward and inclined rod bundles was analysed. The dependency of shedding frequency and velocity amplitude on mesh refinement was first shown for two popular linear eddy viscosity RANS models. As a consequence of this sensibility, LES turbulence modelling was used in this study.

The LES modelling (numerical scheme and mesh refinement) was then validated for 90° crossflow by analyzing the experiment of Simonin [9] in triangular rod arrangement and repeating the fine calculations of Iaconides et al. [5] for inline rod arrangement.

Then the EOLE experiments of the CEA [1] were analysed for two Reynolds numbers and three inclination angles (90°, 45° and 30°). The LES calculations helped to extend the data basis of the experiments from mainly pressure losses in inclined rod bundles to complete fields of velocity mean values and turbulence statistics. Three calculation domains have been tested for simulating the EOLE experiments; a full channel description with the tube bank inside and two domains which are periodic in flow direction; a parallelepipedic one and an inclined one. All domains give similar results for mean velocities, turbulence statistics and pressure losses.

When simulating cross flow in the core of a nuclear reactor, the selection of the calculation domain is very important as an inclined domain overestimates the EOLE experiment by up to 100%, whereas a parallelepipedic domain underestimates the EOLE experiment by up to 20%.

References

1. Peybernes J (2004) Evaluation of the forces generated by cross-flow on PWR Fuel assembly. In: Structural behavior of fuel assemblies for water cooled reactors, Proceedings of a technical meeting held in Cadarache, France, 2226 November 2004, IAEA-TECDOC-1454
2. Angeli P-E, Bieder U, Fauchet G (2015) Overview of the Trio_U code: main features, V&V procedures and typical applications to engineering, NURETH-16, Chicago, USA
3. Rahman M, Karim M, Alim A (2007) Numerical investigation of unsteady flow past a circular cylinder using 2-D finite volume method. J Nav Archit Mar Eng
4. Benhamadouche S, Laurence D (2003) LES, coarse LES, and transient RANS comparisons on the flow across a tube bundle. Int J Heat Fluid Flow 24:470479
5. Iacovides H, Launder B, West A (2014) A comparison and assessment of approaches for modelling flow over in-line tube banks Int. J Heat Fluid Flow 49:6979

6. Bieder U, Falk F, Fauchet G (2015) CFD analysis of the flow in the near wake of a generic PWR mixing grid. Ann Nucl Energy 169–178
7. Pironneau O (1988) Finit element methods for fluids, Wiley
8. Hirt CV, Nichols BD, Romero NC (1975) SOLA-A numerical solution algorithm for transient flow. Los Alamos National Lab., Report LA-5852
9. Simonin O, Barcouda M (1986) Measurements of fully developed turbulent flow across tube bundle. In: 3eme Conference Internationale sur les Applications de l'Anemometrie Laser a la Mecanique des Fluides
10. OCCIGEN. http://www.cines.fr

A New Strategy for Analysis and Visualization of Massively Parallel Computations of Turbulent and Transitional Flows

A. Cadiou, M. Buffat, B. Di Pierro, L. Le Penven and C. Pera

Abstract Massively parallel simulations generate increasing volumes of large data, whose exploitation requires large storage resources, efficient network and increasingly large post-processing facilities. In the coming era of exascale computations, there is an emerging need for new data analysis and visualization strategies. In order to meet these challenges, an original solution based on Python and open-source libraries has been developed. It is shown to make it possible to embed analysis and visualization into the code and efficiently shorten the exploitation of massively parallel computations. Applications are given for direct numerical simulations of turbulent and transitional flows.

1 Introduction

Over the past few decades, considerable effort has been made to get benefit of the massively parallel platforms and implement accurate numerical methods for the simulations of transitional and turbulent flows. Solvers have now reached a mature stage and most of them are ready for exascale computations. However, the increasing volumes of large data generated by the simulations raise new challenges to keep pace for the data analysis and visualization [13].

Data manipulation, during the simulation and after, considerably slows down the analysis process, that becomes the bottleneck of high performance computing. The traditional usage consists in performing the simulations in order to write output data on disk. When dealing with three-dimensional, time-dependent problems computed on thousands of cores, the volume of data generated is big and highly partitioned. As

A. Cadiou (✉) · M. Buffat · B. Di Pierro · L. Penven · L. Pera
Laboratoire de Mécanique des Fluides et d'Acoustique,
Université Claude-Bernard Lyon 1/ CNRS/ École centrale de Lyon/ INSA de Lyon,
43, bd du 11 novembre 1918, 69622 Villeurbanne, France
e-mail: anne.cadiou@ec-lyon.fr

a consequence, it is often necessary to reduce the space or time resolution in order to perform the post-processing on local platforms, which have less ressources than the computational machine. Another solution consists in coupling the analysis with the solver in the simulations, so that both are performed simultaneously, thereby preserving the accuracy of the numerical method.

Following this idea, an original methodology for in-situ analysis, adapted for massively parallel time-evolving computations has been developed and applied to the simulation of turbulent and transitional flows. The method is described in Sect. 2 and examples of applications are given in Sect. 3.

2 Embedded Analysis

Fundamental aspects of turbulent and transitional flows are since the 70's studied with high-order numerical methods (see e.g. [11, 12, 14]). For such applications, high-resolution direct numerical simulations take continuously part of the computational challenges (see e.g. [17]). Simulations nowadays often consist in multiple runs in batch mode on remote multi-cores massively parallel supercomputers. This traditional workflow results in the production of data files, that are written on disks and transferred on a local data server. In this context, we have developed an accurate spectral code to solve the incompressible Navier-Stokes equations (`NadiaSpectral` [3]) and made it ready for large simulations of turbulent and transitional flows on ten thousands of cores [9]. The efficient parallel kernel is encapsulated in a C/C++ library used by the solver. It is now possible to make direct numerical simulations of highly resolved flows on a large amount of cores. To be consistent with these efforts, spectral approximation should be preserved when data processing is performed. The resolution being kept as such, this means that the post-processing calculations must be parallel, but on a smaller scale than the one used for the computational efficiency of the solver, because this step is often performed on a smaller platform than the supercomputers where the simulations where ran. The results consist in a big data set (made of several tens of To of large and highly partitioned files) whose frequent transfer from one machine to another is not an option. The solution is to remotely access the data from a local cluster (either by NFS of by a client/server system) and to steer the post-processing with a virtualGL client if needed. This traditional workflow (see Fig. 1) has been used with `NadiaSpectral` and was effective when a large amount of data is generated [1, 4, 6].

To minimize the volume of raw data, a part of the analysis is done in the simulation. It is traditionally calculated in the iterative loop of the main numerical solver. in a tightly coupled manner. This has two major drawbacks: the analysis shares the resources with the solver, thereby reducing its overall efficiency, and must be defined in the code before running the simulation. Consequently, if an unforeseen event occurs, the simulation must be stopped to amend the analysis accordingly in the code. The new strategy presented here circumvents them by embedding the analysis in the code in an asynchronous way. Two communicators are defined in the new version of

Fig. 1 Traditional usage
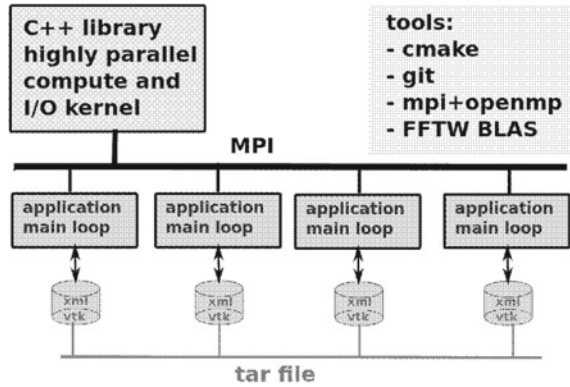
Fig. 2 Embedded analysis
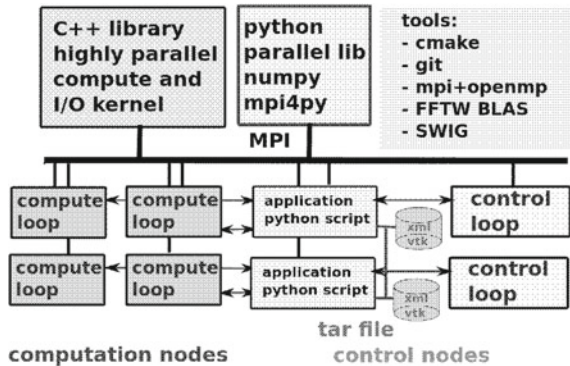
the code, one is dedicated to the solver resolution, the other one to the analysis (see Fig. 2). The simulation is thus run on a large number of MPI processes for the solver and a smaller one for the analysis, on two distinct sets of nodes, if needed. Both parts communicate via MPI but there is no need to write the data on disks nor to duplicate them on the memory. Moreover, this has been implemented using an original use of the Python language, in which interpreters are launched by the code and can be modified in-the-fly. This creates a new possibility to steer the simulation on demand, thereby getting closer to a numerical experiment, where the control of physical and numerical settings are driven by the analysis. The developments make use of open-source libraries such a Numpy, Matplotlib, MPI4py and allow to preserve the spectral accuracy of the code by sharing the C/C++ library of the solver via SWIG.

3 Examples of Application

3.1 Asynchronous I/O

The simplest application of the embedded analysis method consists in performing asynchronous I/O with the time-iterative solver, when writing data on disks. Comparisons between the traditional usage and the present workflow are given on a plane channel configuration of size $L_x/h \times L_y/h \times L_z/h = 75 \times 2 \times 6.4$ with $5760 \times 192 \times 512$ modes ($\sim$566 millions of modes), that corresponds to the simulation of the boundary layer instabilities at the entrance of the channel (h being the channel half-width). Each velocity field occupies $\sim$13 Go. With the traditional usage, If the solver runs on 2048 cores with 4 threads per MPI tasks, each of the 512 processes write its own partition on disk. In the present method, it is possible to devote only 16 MPI tasks to the analysis. Each velocity field is partitioned in only 16 parts and is written asynchronously to the solver. For this configuration, the time spent in writing one velocity field is not very large as it takes less than 30% of the time spent per solver iteration. Writing the data asynchronously to the execution of the iterative time step does not strongly modify here the global restitution time of the simulation. However, for larger configurations or when variables that are different from the velocity field directly computed by the solver have to be written into output files, asynchronous I/O reduce the time lost in writing files. Although the new approach is beneficial in that specific case, the fact remains that the files still are written to disks. To avoid the generation of a huge amount of data, the calculation of additional variables and the extraction of the pertinent criterion for the analysis must also be performed asynchronously to the iterative solver. For example, this has been applied to the visualization of the Λ_2 criterion to follow the spatio-temporal development of the transitional and turbulent flow structures [16]. The evaluation of this criterion needs the calculation of the eigenvalues of the pressure Hessian [8], which implies to compute second-order derivatives by Fast Fourier Transforms (global operations) in order to preserve the spectral accuracy. Moreover, it is needed to interpolate the field on a regular grid for the visualization of isovalues surfaces, as most visualization softwares (here VisIt [15]) make a linear interpolation on the grid points, The output data is made of images, written at each analysis step. If the solver is computed on 2048 cores for 512 MPI partitions and 512 additional cores are devoted to the co-processing using 64 MPI partitions, the generation of the image takes about 20 iterations of the solver to be performed. The computational time step is based on the stability condition of the scheme and is much smaller than the physical time scale of the convection of the turbulent structures, so that the analysis is done every 50 iterations only. With this procedure, is has been possible to let the structures evolve over more than 3000 instants [2, 5]. To perform it with the traditional usage, it would have been needed to write, transfer and process more than 84 To (Figs. 3 and 4).

Fig. 3 Visualization of the modification of the time-evolving three-dimensional flow structures under the control of a physical parameter
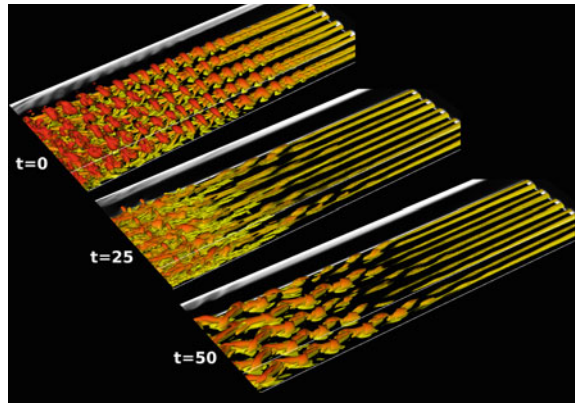
Fig. 4 Budgets in the fully developed region compared to a periodic turbulent channel flow (MKM $Re_\tau = 590$) [10]
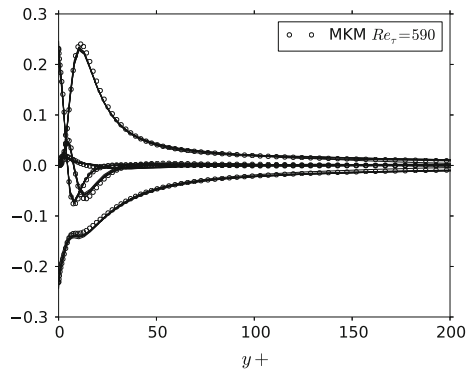
3.2 Evaluation of Statistics

The configuration consists in a very elongated plane channel in which a laminar flow enters. The flow is perturbed so that the transition to turbulence occurs in the boundary layers quite close to the entry and then, the flow evolves slowly towards the fully developed channel (statistically invariant in the downstream direction). The statistics of the turbulent boundary layers and the channel flow are compared and their budgets are analyzed in the region in-between, where the turbulence is spatially developing. The domain is given by $L_x/h \times L_y/h \times L_z/h = 280 \times 2 \times 6.4$ with $23040 \times 128 \times 512$ modes ($\sim$1.5 billions of modes) [7]. Each velocity field occupies $\sim$36 Go. For checkpoint-restart, 688 Go are stored for the evaluation of three-dimensional time-averaged statistics, including the budget of the second-order correlations of the fluctuating velocity. Statistics are calculated after an initial transient time, once the flow is established into the whole channel length. They are evaluated every 250 iterations, which corresponds to the eddy turnover-time of the fully developed turbulent channel flow. As the evaluation of the budgets involves the calculation of spatial derivatives, the time spent in the evaluation of the statistics costs

2.5 times the time spent per iteration. This does not affect the solver efficiency when performed asynchronously by the analysis step. Moreover, the additional variables needed for the statistics evaluation are created also in the analysis step, so that the solver code is not modified by the analysis.

As the flow evolves in space, the convergence rate of the statistics is slower than in a periodic channel flow (only the transverse spatial direction can be included in the samples). The convergence of the time-averaged quantities has been followed in the analysis step of the simulation and modifications of the statistics are easily implemented during the computations. Indeed, as long as the new variables required for the evaluation of the statistics are created in-the-fly in the analysis part of the computations, the new analysis strategy allows to increase flexibility. As a consequence, this facilitates the development of the code, the solver being affected as less as possible by the analysis.

4 Conclusion

This is shown that the use of libraries such as Numpy, Maplotlib, MPI4py and SWIG make it possible to implement a Python-based embedded analysis and visualization of direct numerical simulations of turbulent and transitional flows. Being asynchronously connected to the Navier-Stokes solver, it does not affect the code efficiency. It brings along more flexibility in the analysis and provides promising features to gain interactivity and control onto the simulation.

References

1. Buffat M, Cadiou A, Le Penven L (2014) Bypass transition at the entrance of a plane channel. In: EFMC10 conference, Copenhague, Danemark, 14–18 Sept 2014
2. Buffat M, Cadiou A, Le Penven L, Pera Ch. (2015) In-situ analysis and visualization of massively parallel computations. Int J High Perf Comput Appl 1–15
3. Buffat M, Le Penven L, Cadiou A (2011) An efficient spectral method based on an orthogonal decomposition of the velocity for transition analysis in wall bounded flow. Comput Fluids 42:62–72
4. Buffat M, Le Penven L, Cadiou A, Montagnier J (2013) DNS of bypass transition in entrance channel flow induced by boundary layer interaction. Eur J Mech B Fluids 43:1–13
5. Cadiou A, Buffat M, Le Penven L (2013) Visualisation in-situ pour l'étude de la transition sous-critique. HPC Mag 7:68–69
6. Cadiou A, Buffat M, Le Penven L, Montagnier J (2014) DNS of turbulent by-pass transition at the entrance of a plane channel. In: Progress in Turbulence V, vol 149. Springer Proceedings in Physics, pp. 59–64

7. Capuano M, Cadiou A, Buffat M, Le Penven L (2014) DNS of the turbulent flow evolving in a plane channel from the entry to the fully developed state. In: iTi conference on turbulence, Bertinoro, Italy, 21–24 Sept 2014
8. Jeong J, Hussain F (1995) On the identification of a vortex. J Fluid Mech 285:69–74
9. Montagnier J, Cadiou A, Buffat M, Le Penven L (2013) Towards petascale simulation for transition analysis in wall bounded flow. Int J Num Meth Fluids 72(7):709–723
10. Moser R, Kim J, Mansour N (1999) Direct numerical simulation of turbulent channel flow up to $Re_\tau = 590$. Phys Fluids 11(4):943–945
11. Orszag SA (1969) Numerical methods for the simulation of turbulence. Phys Fluids 12(12)
12. Orszag SA, Patterson GS (1972) Numerical simulation of three-dimensional homogeneous isotropic turbulence. Phys Rev Lett 28:76–79
13. Requena S (2013) Big data et HPC. In: Conférence Big Data, Paris
14. Spalart PR, Leonard A (1985) Direct numerical simulation of equilibrium turbulent boundary layer. In: 5th Symposium on turbulent shear flows
15. VisIt. web site https://wci.llnl.gov/codes/visit/home.html
16. Wu X, Moin P (2010) Transitional and turbulent boundary layer with heat transfer. Phys Fluids 22(8)
17. Yokokawa M, Itakura K, Uno A, Ishihara T, Kaneda Y (2002) 16.4-Tflops direct numerical simulation of turbulence by a Fourier spectral method on the earth simulator. In: Supercomputing, ACM/IEEE 2002 conference

Fluid Flow and Turbulence Description in the Vicinity of Liquid/Liquid Interfaces

L.D.O. Campos, P. Gardin, S. Vincent and J.P. Caltagirone

Abstract Fluid flow in the vicinity of a liquid/liquid interface was computed with CFD and measured via LDA technique. The flow presents some similarities to wall bounded flow with the presence of a viscous boundary layer of wall unit thickness $y^+ = 10$. It was seen that the turbulence is almost completely damped in this viscous boundary layer. Even with velocity mean values close to zero, the interface has an oscillatory movement and a very low value of the turbulence intensity was found at the points close to the interface. The viscosity ratio was suggested as a parameter to predict the existence of a viscous boundary layer close to the interfaces between immiscible fluids.

1 Introduction

In metallurgical industry, processes like oxidation, chemical reduction and product refining are in close relation to mass transfer across different interfaces, e.g. liquid/gas, liquid/liquid and liquid/solid, with or without chemical reactions. The mass transfer occurs in the thin mass boundary layer, where mass flux is proportional to the concentration gradients and mass transfer coefficients. It is of major importance to accurately calculate these parameters to predict the rate of reactions and improve industrial performance. Many researchers in the last century tried to include the physical properties considered relevant to mass transfer processes and predict the mass transfer coefficients [5, 9, 11, 12]. On the other hand, the details of mass and viscous boundary layers are determined by physicochemical and hydrodynamic properties at

L.D.O. Campos (✉) · P. Gardin
ArcelorMittal Global RD, Maizières-lès-Metz, France
e-mail: leandro.deoliveiracampos@arcelormittal.com

S. Vincent
UPEst, Champs-sur-Marne, France
e-mail: stephane.vincent@u-pem.fr

J.P. Caltagirone
University of Bordeaux, Bordeaux, France

the interface, and the concentration boundary layer is related to the viscous boundary layer by

$$\delta_c^+ \propto \sqrt{\frac{\delta_u^+}{Sc}} \tag{1}$$

according to Calmet and Magnaudet [2], where δ_c^+ is the normalized concentration boundary layer thickness and δ_u^+ is the normalized viscous boundary layer thickness. Sc is the Schmidt number, a dimensionless number defined as the ratio of the momentum diffusivity (viscosity) to the mass diffusivity. In steelmaking processes Sc can reach values of the order of 1×10^5. These high values of Schmidt numbers prohibit any attempt of computing the mass boundary layer due to the mesh size required. Because of this, mass transfer models are used to predict the mass transfer coefficients based on flow characteristics that can be calculated via CFD, such as the friction velocity or the divergence of the velocity field parallel to the interface [2, 3]. Physical models can be used to verify the accuracy of these calculations.

In the present study, a water model 1:3 scale of a continuous casting (CC) machine was used to assess the flow in the vicinity of a liquid/liquid interface. Laser Doppler Anemometry (LDA) was used to measure the velocity field.

2 Experimental Apparatus

A schematic view of the CC is shown in Fig. 1a with the various phases present in the process. The water model used in this study is presented in Fig. 1b. Water is used to simulate liquid steel as they have very similar kinematic viscosity ($\nu_{water} = 1.0 \times 10^{-6} \text{m}^2/\text{s}$ and $\nu_{steel} = 0.8 \times 10^{-6} \text{m}^2/\text{s}$). Silicon oil was used to simulate melted flux powder. The vertical, v, and horizontal, u, components of the velocity field were measured with a LDA equipment as close as possible to the water/oil interface. For each point, ten minutes of measurements with an average data rate of
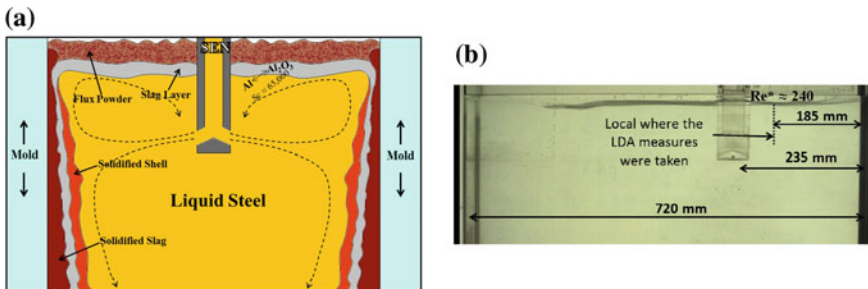
Fig. 1 Different phases in a CC mold in (**a**) and CC water model [3] in (**b**)

80 Hz allowing to obtain the mean velocities and root mean square (rms) over 50000 measures in each point. In a first attempt the SEN was moved towards the lateral side and several experiments were performed [3, 4].

3   Mathematical Model

The most stable configuration described in Campos et al. [3] was modeled. The mold has sectional area of $100 \times 720 \, \text{mm}^2$, SEN depth of 68 mm and water flow rate of $1.6 \, \text{m}^3$/h with an oil layer thickness of 15 mm, density of 970 kg/m^3 and viscosity of 0.34 Pa.s.

The CFD code Thetis was used in this study. The approximation of the conservation equations was carried out with an implicit finite volume technique of second order in time and space on a fixed Cartesian staggered grid. An implicit Augmented Lagrangian procedure is implemented to ensure the incompressibility constraint [6, 13, 14]. Centered schemes are used to discretize the space derivatives in the inertia and the viscous terms of the momentum equations. An iterative Bi-Conjugate Gradient Stabilized II solver [15], preconditioned under a modified and incomplete LU approach [8], is used to solve the linear system. The free surface evolutions are simulated with the Piecewise Linear Interface Construction (PLIC) Volume of Fluid (VOF) interface tracking method of Youngs et al. [17]. The surface tension is modeled and discretized with the Continuum Surface Force (CSF) [1, 16] to include the interfacial force as a volume force in the momentum equations. The turbulence was computed via the Large Eddy Simulation (LES) approach with a mixed sub-grid scale (SGS) model.

The comparison between the velocity field measured by LDA and the computations are shown in Fig. 2a, b:

The CFD calculation shows good agreement with experiments. It is visible that the interface movement can strongly affect the measured velocities. In fact, the wave dynamics induces extra motion to the flow and the velocity field may be thought of as a combination of mean coherent and non-coherent (turbulence) contributions:
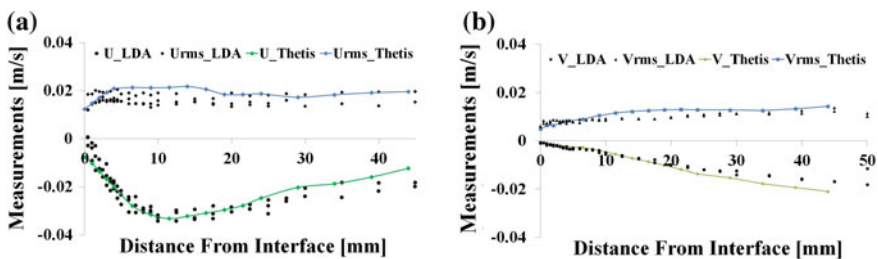
Fig. 2 Comparison between **a** horizontal component and **b** vertical component of the velocity field calculations and LDA measures [3]
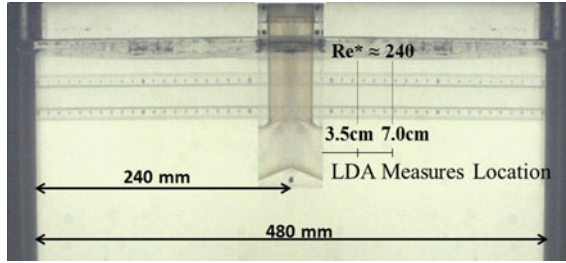
Fig. 3 Physical apparatus with the indication of the LDA measurements positions
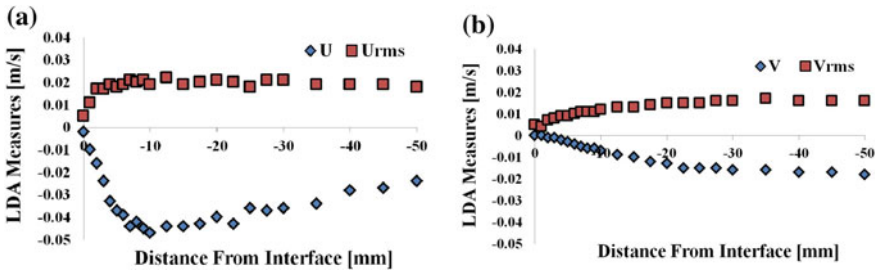
Fig. 4 Velocity profiles measured with LDA. In **a** horizontal component and **b** vertical component of the velocity field

$$\mathbf{u} = \overline{u} + u' + \widetilde{u} \tag{2}$$

where $\overline{u}$ is the mean velocity, $\widetilde{u}$ is the flow composition induced by the orbital motion and u' is the turbulent fluctuation. To analyze the coherent field one may subtract somehow the wave induced velocity from the velocity field or find a configuration in which the interface wave motion can be neglected.

To avoid the need of further data treatment, a new configuration was proposed. This time the mold width is reduced to 480 mm, the nozzle depth to 60 mm and the oil layer thickness is fixed in 10 mm. In this configuration the velocities can be measured in two different locations at 3.5 and 7 cm to the right from the SEN (Fig. 3).

The velocity field is shown in Fig. 4. The flow close to the interface is predominantly horizontal, with a very low vertical component. Based on these observations, the flow is compared to open channel flows to clarify the trends observed.

4 Comparison with Open Channel Flows

Fulgosi et al. [7], during their water/air simulations, pointed out that the flow close to interfaces presents similarities to wall bounded flow depending on the density differences between the fluids. Figure 5a shows the velocity field normalized by the
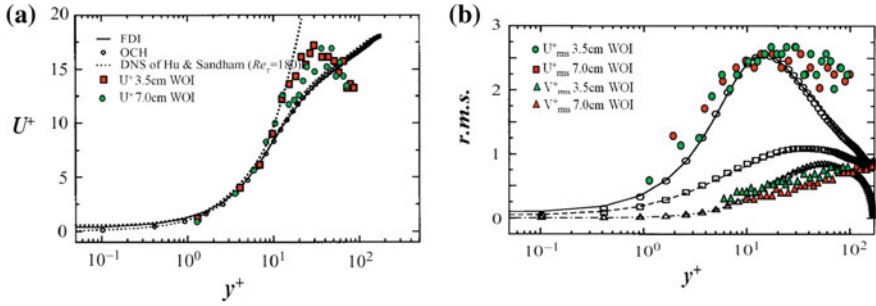
Fig. 5 a Profiles of the mean streamwise velocity and **b** root-mean-square profiles. *Lines* and symbols are used to identify FDI and OCH [7], respectively: − and ◯ as streamwise velocity; − − − and ◇ as spanwise component, and − • − and △ as normal component. The results from the present study are labeled by *colors* in the graph

shear velocity, where $y^+ = 0$ represents the interface/wall position. Here one may see the results from Fulgosi et al. [7] for a free deformable interface, FDI, and an open Chanel configuration, OCH, as well as the DNS of a closed-channel flow from Hu and Sandham [10] and the present LDA measures. The DNS studies were performed for a flow field with $Re^* \approx 180$ based on the total depth and shear velocity. The LDA measures were taken with $Re^* \approx 240$ based on water mold width and shear velocity at interface.

The observed velocities are quite the same for $y^+ < 10$. The rms profiles of the velocity fluctuations are presented in Fig. 5b. As in a wall bounded flow, the turbulence is damped in the viscous boundary layer, $y^+ < 10$. However, because of the oscillatory movements in the WOI and FDI, the rms values do not reach the zero value at the interface. The results show a wall-flow-like velocity profile. The difference between the WOI and wall bounded flows is the viscous boundary layer thickness, defined as the region where $u^+ = y^+$, which is thicker for interfaces ($\delta_u^+ \approx 10$) than the ones of wall bounded flows ($\delta_u^+ \approx 5$).

5 Conclusions

By comparing the experimental results with the ones of numerical simulations in similar configurations, it was found that liquid/liquid interfaces have very similar characteristics as wall bounded flows: There is a viscous boundary layer with wall unit thickness $y^+ \approx 10$ in interface cases; The turbulence is dumped in the viscous boundary layer; As interfaces move with low velocities, the rms of the velocities have finite values instead of having a null value as in the cases of wall bounded flows. It was seen that the viscosity ratio, R_μ, could indicate the presence of a viscous boundary layer. The limiting case, where $R_\mu \to 0$ presents a wall bounded flow aspect. Since industrial and natural multiphase flows have, in their majority, viscosity differences

of, at least, one order of magnitude (e.g. water/air, liquid steel/liquid slag, water/oil), it is expected to find a viscous boundary layer in most of the configurations of these practical cases. It is, then, reasonable to treat the turbulence close to those interfaces in a similar way as it is treated in wall bounded flows.

References

1. Brackbill J, Kothe B, Zemach C (1992) A continuum method for modelling surface tension. J Comput Phys 100(335):335–354
2. Calmet I, Magnaudet J (1997) Large-eddy simulation of high-Schmidt number mass transfer in turbulent channel flow. Phys Fluids (9):438–455
3. Campos LD, Gardin P, Vincent S, Caltagirone J-P (2015) Physical modeling of turbulent multi-phase flow in a continuous casting steel mold. In: 8th international conference on computational and experimental methods in multiphase and complex flow
4. Campos LD, Gardin P, Vincent S, Caltagirone J-P (2015) Fluid flow description in the vicinity of a liquid steel-slag interface. In: The 6th international congress on the science and technology of steelmaking
5. Dankwerts PV (1951) Significance of liquid-film coefficients in gas absorption. Ind Eng Chem 43(6):1460–1467
6. Fortin M, Glowinski R (1982) Mthodes de lagrangien augment. Dunod, Application la rsolution numrique de problmes aux limites
7. Fulgosi M, Lakehal D, Banerjee S, De Angelis V (2003) Direct numerical simulation of turbulence in a sheared airwater flow with a deformable interface. J Fluid Mech 482:319–345
8. Gustafsson I (1978) On first and second order symmetric factorization methods for the solution of elliptic difference equations
9. Higbie R (1935) The rate of absorption of a pure gas in a still liquid during short periods of exposure. Am Inst Chem Eng 31:365–390
10. Hu Z, Sandham N (2001) Large-domain simulation of Couette and Poiseuille flow. In: Lindborg AJE (ed) Proceedings of 2nd international symposium on turbulent and shear flow phenomena
11. Lamont JC, Scott DS (1970) An eddy cell model of mass transfer into the surface of a turbulent liquid. AIChE J 16(4):513–519
12. Lewis DK, Whitman WG (1924) Principles of gas absorption. Ind Eng Chem 16:1215–1220
13. Vincent S, Caltagirone J, Lubin P, Randrianarivelo T (2004) An adaptative augmented lagrangian method for three-dimensional multi-material flows. Comput Fluids 33:1273–1289
14. Vincent S, Randrianarivelo T, Pianet G, Caltagirone J (2007) Local penalty methods for flows interacting with moving solids at high reynolds numbers. Comput Fluids 36:902–913
15. Van Der Vorst H (1992) A fast and smoothly converging variant of BI-CG for the solution of non-symmetric linear systems. J Sci Stat Comput 44:631644
16. Vincent S, Caltagirone J (2000) A one cell local multigrid method for solving unsteady incompressible multiphase flows. J Comput Phys 163:172–21
17. Youngs D, Morton K, Baines M (1982) Time-dependant multimaterial flow with large fluid distortion. In: Numerical method for fluid dynamics

On the Vortex Dynamic of Shear-Driven Deep Cavity Flows with Asymmetrical Walls

D. Cornu, L. Keirsbulck, R. Chovet, C. Chovet, M. Lippert, F. Kerhervé, R. Mathis and F. Aloui

Abstract The influence of the wall asymmetry on the flow dynamics, in two-dimensional rectangular deep cavities, is studied experimentally by combining wall-pressure and PIV measurements. Main cavity flow statistics [2] have been analyzed and they have shown that the flow features are strongly affected by the asymmetry. An emphasis is given concerning the behavior of the shear-layer oscillations that are compared to the analytical deep-cavity model prediction proposed by Block (Noise response of cavities of varying dimensions at subsonic speeds. Technical Report D-8351. NASA Technical Note, 1976 [4]). The results show that, by adjusting the convection velocity, the model seems to be still able to predict the cavity self-sustained oscillations in the case of the asymmetric cavities. Stochastic estimation of the cavity flows demonstrates that convective structures are involved downstream of the cavity along the wall and highlights the physical nature of the pressure-producing flow structures.

1 Introduction

Models for understanding the unsteady features of cavity flows present a great interest for the design of large amounts of engineering applications. These models may be used to guide designs and also to enhance the feedback control performance [8]. Cavity flows are known to be potential sources of significant vibrations and other kinds of perturbations. For high subsonic Reynolds numbers, the most common mechanism of self-sustaining oscillations is the one referred to Rossiter's feedback mechanism [6]. Cavity flows are also generally classified according to their length-to-depth (L/H) and length-to-width (L/W) ratios [3] and can be qualified as deep

D. Cornu (✉) · L. Keirsbulck · R. Chovet · C. Chovet · M. Lippert · F. Aloui
LAMIH UMR 8201, 59313 Valenciennes, France
e-mail: denis.cornu@transport.alstom.com

F. Kerhervé
PPrime CNRS, UPR 3346, 86962 Chasseneuil, France

R. Mathis
LML UMR 8107, 59650 Villeneuve D'ascq, France

Fig. 1 Generic scheme of the cavities
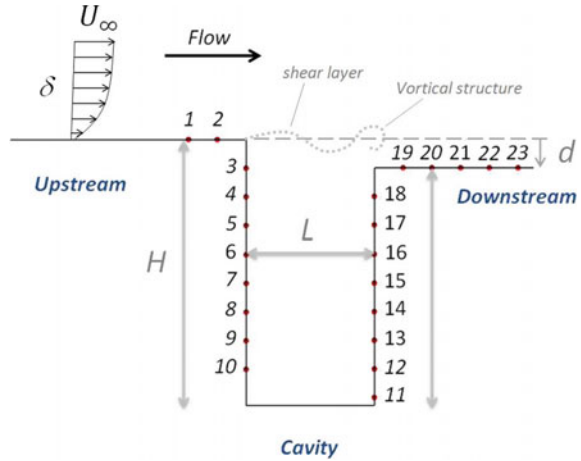
if $L/H < 1$ and two-dimensional if $L/W < 1$. In literature, the cavity configuration examined is usually rectangular and symmetrical i.e. with the upstream wall-height equal to the downstream one. However, the asymmetrical cavity flow represents the geometry of numerous engineering applications such as the railway equipments encountered over the roof of many kinds of trains (Fig. 1). Such configurations are, to our knowledge, poorly described in the literature (only [1] refers to asymmetric cavity configurations). Although the classical Rossiter's mechanism seems to be very insensitive to geometrical variations due to the robustness of the self-sustained feedback mechanism, there is no information provided concerning the limitation of this model. In addition, very deep cavity configurations are also poorly documented, and the behavior of the shear layer oscillations in particular cases of deeper cavity is not clearly established up-to-now. In order to complete the knowledge regarding the canonical configuration (shallow and symmetrical) and also to prevent highly undesirable effects, the present paper studies two different asymmetrical cavity configurations and focuses on the interaction of the shear layer downstream of the cavity. The three main objectives discussed here are (i) to study the self-sustaining cavity flow oscillations, (ii) to analyze the relationship between the vortical structures and the wall-fluctuating pressure, (iii) to characterize their evolution downstream the reattachment and inside the cavity. To this aim, simultaneous PIV and wall-pressure measurements have been carried out inside and downstream the cavity. The first section of this paper presents the experimental setup and the data acquisition, the following sections deal with the wall-pressure and flow statistics, the cavity flow oscillations and the dynamical flow behavior induced by the two asymmetrical cavity flows.

2 Experimental Setup

2.1 Facility and Flow Configuration

All the experiments for this investigation were conducted in the close-loops subsonic wind tunnel facility of the LAMIH at the University of Valenciennes and Hainaut-Cambresis. The wind tunnel has a 6.25:1 contraction upstream of a 2 m wide by 2 m high by 10 m long test section. The case of asymmetrical cavity flows as illustrated in Fig. 2 is here examined. Henceforth, we used the cavity depth H (186 mm) and the upstream quantity U_∞ as the respective length and velocity scales references. The length L of the cavity was 120 mm corresponding to a Reynolds number of $Re_L = 2.4 \times 10^5$. The different studied cases are detailed in Table 1. They include positive (I), neutral (II) and negative (III) asymmetrical configurations, with a length-to-width ratio of $L/W = 0.06$ and a length-to-height ratio of $L/H = 0.6452$. Regarding the cavity flow classification, the present configuration corresponds to a "two-dimensional deep cavity". For this study, the free-stream velocity was set to 30 m/s, resulting in a Reynolds number based on the cavity height of $Re_H = 5.58 \times 10^6$ and corresponding to a Mach number of 0.088. For the flow field illustration, a Cartesian coordinate system was chosen whose streamwise origin was located at the cavity trailing edges. For all the configurations considered, the incoming boundary layer is turbulent with a thickness $\delta = 21$ mm, corresponding to a Reynolds number of $Re_\delta = 6.3 \times 10^5$.
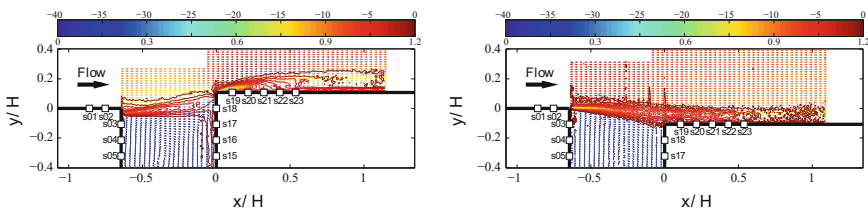
Fig. 2 Vector plots of the mean-velocity magnitude ($\|\mathbf{U}\|/U_\infty$—lower colorbar scale) and the mean-spanwise vorticity ($\Omega_z^+ = \Omega_z.H/U_\infty$—upper colorbar scale). Cases I (*left*) and III (*right*). Vector lengths are normalized in order to enhance the visibility of the flow feature inside the cavity

Table 1 Mean-cavity flow parameters

Cases	d (mm)	$d/H(\%)$	Symbols
(I)	+20	+10.75	●
(II)	0	0.00	▲
(III)	−20	−10.75	■

2.2 Instrumentation and Data Acquisition

The various cavity flow configurations were examined in details thanks to simultaneous low-speed PIV and time-resolved pressure measurements. Two cameras were used to survey the flow inside the cavity and downstream of the trailing edge in order to examine the unsteady vortices induced by the cavity shear-layer. The PIV system included high-resolution POWERVIEW cameras with full resolution of 2048×2048 pixels, micro NIKKOR 50 mm lenses and a light sheet provided by a double-pulsed ND- YAG laser (QUANTEL BSLT220) operating at 532 nm which is able to produce 220 mJ per pulse. For each flow case, 2000 pairs of images are acquired with a frame rate of 7 Hz. The processing consisted of one pass with 32×32 pixels integration windows followed by a 16×16 pixels integration windows and 50% overlap. Survey of the wall-pressure is effected thanks to 23 flush mounted differential Kulite XCQ-080 sensors with pressure range of 350mBar, located before, inside and after the cavity. The distance between two sensors is constant and equal to 20 mm ($\approx 0.1H$). The pressure readings were synchronized with the PIV measurements using a TTL signal triggered by a Q-switch of the first laser cavity. Pressure signals are first low-pass filtered at 5kHz and a 12 bit A/D converter from a DEWESOFT SIRIUS- 8STG M PLUS acquisition system is used to acquire the filtered signals at a sampling frequency of 10kHz. The static pressures were also taken using pressure taps located at the same positions than that of the fluctuating sensors, and 18 additional taps stations were installed in the continuity of the downstream wall with the same spacing in order to obtain complementary information about the full recovery of the flow downstream of the cavity.

3 Effect of the Cavity Asymmetry on the Main Flow Features

3.1 Flow Statistics

Averaged PIV results are first analyzed in order to establish the main flow features and to evaluate the effect of the asymmetrical configuration upon the mean flow. For the case I, the turbulent boundary layer at the leading edge forming a shear-layer, impacts upon the cavity trailing edge and leads to the formation of a separation area onto the downstream wall. Due to local acceleration at the trailing edge, strong negative values of mean-spanwise vorticity ($\Omega_z^+ < 20$) are observed in the separation area. Moreover, high activity of vorticity is also manifest inside the cavity along the trailing side wall. This particular behavior will be discussed later. Concerning the case III, a different physical mechanism is at play. Looking at the mean-velocity magnitude distribution, the shear layer region is found to extend far downstream from the cavity trailing edge with a reattachment about $0.5H$ downstream (near sensor 23) (Fig. 3).
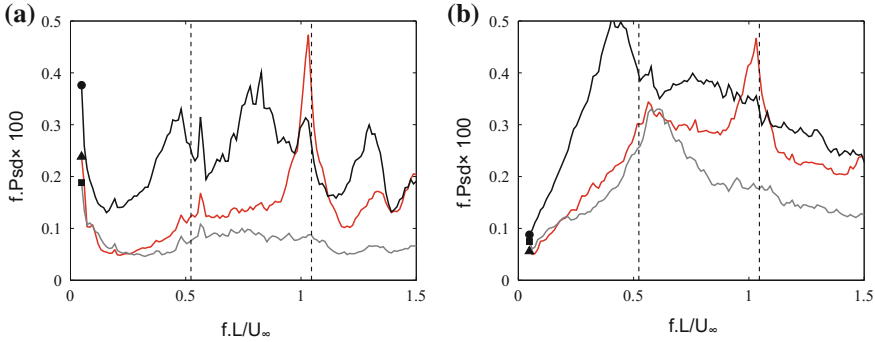
Fig. 3 Premultiplied and normalized PSD of wall-pressure fluctuations (**a**) and (**b**) the *black dashed line* shows the first and the second modes from the Block's prediction with regard to the aspect ratio ($\kappa = 0.57$)

In this case, the shear layer do not impact on the trailing edge. The concentration of substantial negative vorticity within the flow field is confined to the shear layer and especially near the leading edge of the cavity. At this location, the shear layer is very thin and the vorticity is the highest. The previously discussed vortical activity on the trailing side wall of the cavity can be detailed by the time history of the synchronous fluctuating pressure measurements for the two cases. For the case I, the footprint of the convected vortical structure involved close to the trailing side wall of the cavity (sensors 12–18) can be observed. But in the case III, we can not observe any interaction between the shear-layer and the flow inside the cavity. Results show no variation of the spatial pressure footprint on the leading side wall of the cavity. However strong fluctuations on the other side of the cavity are observed in the case I [5], compared to the other case, where any activity occurred. Downstream of the leading edge, in both cases, unsteady activity due to the separation phenomenon is also observed.

Mean and rms-values of the pressure coefficient defined along the cavity walls and obtained thanks to the static tap sensors are reported in Fig. 4 as:

$$C_p = (p - p_{ref})/(1/2\rho U_\infty^2) \text{ (with reference taken at the end of the test section)}$$

The mean-pressure distribution shows different behaviors; a classical cavity pressure profile with no significant variation is observed for the reference case II (without asymmetrical walls), a strong pressure lost occurs at the trailing edge for the case I due to the upstream flow impact previously discussed, and for the case III, a pressure increasing is clearly observed in the downstream wall region of the cavity. The rms-pressure coefficient, $C_{p\,rms} = p'_{rms}/(1/2\rho U_\infty^2)$, which essentially gives information on the unsteadiness of the flow examined, shows, only in the region of the trailing edge, significant activities for case I. Impact of shear-layer with the trailing side wall generates a separation area, thus produces an increasingly strong wall-pressure foot-
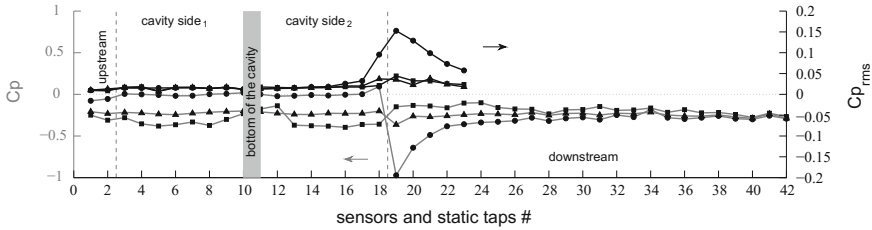
Fig. 4 Mean- and rms-pressure spatial distribution for all the studied cases. Cavity side$_1$ denotes the leading side wall of the cavity and the cavity side$_2$ refers to the other side. *Grey lines* represent C_p (refers to the *left* axis) and *black lines* represent $C_{p\ rms}$ (refers to the *right* axis)

print. The rms-pressure coefficient reaches a maximum level in the vicinity where the flow reattaches (L_R) as encountered in separated flows [10]. For case III, the wall pressure fluctuations are predominantly associated with footprints of growing shear-layer convective vortical structures moving closer to the wall.

4 Concluding Remarks

This paper is focused on adjusting linear models of cavity oscillations that are useful for feedback control purposes in the case of asymmetric cavity walls. Two typical behaviors based on different flow physics have been observed for case I and for case III. Like to the standard shear-driven deep cavity flow, a feedback mechanism between the shear layer instabilities and acoustic [9] forcing is observed in the studied asymmetrical configurations. For both cases, the classical Block's model is able to predict the cavity self-sustain oscillations by adjusting the convection velocity, although the flow dynamics are quite different. The case III shows classical shear-layer configuration with associated instability mechanism of shedding, function of the wall variation d, observed downstream the cavity trailing edge. The case I associated to a raise of the downstream cavity wall exhibits a more complex flow feature, a separate area is observed and interacts with shear-layer vortices that involves downstream of the cavity along the wall. This interaction could be a source of strong non-linear pressure-producing flow structures phenomena highlighted thanks to the stochastic analysis of the flow fields.

References

1. Yamamoto H, Seki N, Fukusako S (1983) Forced convection heat transfer on a heated bottom surface of cavity with different wall-height. Warme und Stoffubertragung 17:73–83
2. Adrian RJ, Moin P (1988) Stochastic estimation of organized turbulent structure-homogeneous shear-flow. J Fluid Mech 190:531–559

3. Larchevêque L, Sagaut P, Mary I, Labbé O, Comte P (2003) Large-eddy simulation of a compressible flow past a deep cavity. Phys Fluids 15:193–210
4. Block PJW (1976) Noise response of cavities of varying dimensions at subsonic speeds. Technical Report D-8351. NASA Technical Note
5. Block PJW (1977) Measurements of the tonal component with theory. NASA Technical Paper 1013
6. Rossiter JE (1964) Wind-tunnel experiments on the flow over rectangular cavities at subsonic and transonic speeds. Rep Aero Res Counc R M Tech
7. Rowley CW, Colonius T, Basu AJ (2002) On self-sustained oscillations in two-dimensional compressible flow over rectangular cavities. J Fluid Mech 455:315–346
8. Clarence W, Williams DR, Colonius T, Murray RM, Macmynowski DG (2006) Linear models for control of cavity flow oscillations. J Fluid Mech 547:317–330
9. El Hassan M, Labraga L, Keirsbulck L (2007) Aero-acoustic oscillations inside large deep cavities. In: 16th Australasian fluid mechanics conference, pp 421–428
10. Farabee M, Casarella MJ (1986) Measurements of fluctuating wall pressure for separated/reattached boundary layer flows. ASME J Vib Acoust Stress Reliab Des 108:301

Numerical Study of the Air Flow and Aerosol Particle Transport in a Model of the Human Respiratory Tract

Dusica Dragojlovic, Nathan Ricks, Sylvia Verbanck, Chris Lacor and Ghader Ghorbaniasl

Abstract In this study, the deposition of aerosol particles has been numerically examined in a model of the human airways. The geometry represents a simplified upper airway model merged with a CT-scan based intrathoracic airways up to the 5th generation of the tracheobronchial tree. Calculations are performed for flow rates of 30 and 60 L/min using large eddy simulation with the rotation rate based Smagorinsky model as subgrid-scale model. Monodisperse particles (2–10 µm in diameter) are tracked in LES frozen fields using a one-way coupling Lagrangian approach. It is observed that right lung receives more flow ventilation and particle distribution than the left lung. The particle deposition in the upper airways increases with the flow rate and with particle size, which is consistent with the data from the literature. The deposition in the tracheobronchial tree remains relatively low, which is confirmed by experiments performed on the same geometric model.

1 Introduction

Particulate matter, smaller than about 10 µm, can reach the deepest part of the lungs, and if toxic, may be a potential health risk for even healthy individuals. On the other hand, lungs are an attractive target for drug delivery. Lungs provide direct access to respiratory diseases and a large surface area for medication absorption. In order to deliver the appropriate amount of drug to the desired region of the airways, particles

D. Dragojlovic (✉) · N. Ricks · S. Verbanck · C. Lacor · G. Ghorbaniasl
Vrije Universiteit Brussel, Brussel, Belgium
e-mail: gu.dusica@gmail.com

N. Ricks
e-mail: nathan.james.ricks@vub.be

S. Verbanck
e-mail: sylvia.verbanck@uzbrussel.be

C. Lacor
e-mail: chris.lacor@vub.ac.be

G. Ghorbaniasl
e-mail: ghader.ghorbaniasl@vub.ac.be

must be properly designed and injected to travel through the complex geometry of the respiratory tract. Therefore, understanding the transport of the inhaled aerosols plays a crucial role in achieving therapeutic effectiveness in treating pulmonary diseases. Numerous researchers have previously studied drug delivery to the lungs using numerical (e.g. [1–3]) and experimental (e.g. [4, 5]) approaches. In particular, computational fluid dynamics (CFD) is an accurate and efficient numerical approach to obtain detailed aerosol transport information. However, experimental investigations of aerosol transport are required for validation of the CFD data.

In the present study, LES results are compared with experimental and RANS data obtained on the same geometry, providing direct comparison between simulations and experiments. Furthermore, simulation results are compared with data from the literature.

2 Methods

The present airway geometry, shown in Fig. 1, consists of a simplified upper airway model, based on the work of Brouns et al. [3], and a CT-scan based intrathoracic region. The upper airways include oral cavity, pharynx, larynx and trachea. The intrathoracic region is comprised of the first 5 generations of the tracheobronchial tree. There are five lung lobes—left upper lobe (LUL), left lower lobe (LLL), right upper lobe (RUL), right middle lobe (RML), and right lower lobe (RLL). The entire geometry is discretized with 4.2 million tetrahedral cells. High resolution in the boundary layer is ensured by using near wall clustering and hexahedral cells with a stretching ratio of 1.1 [1]. In order to capture the particle deposition in the upper airways and in each generation, cross sections are created at the entrance of airway branches.
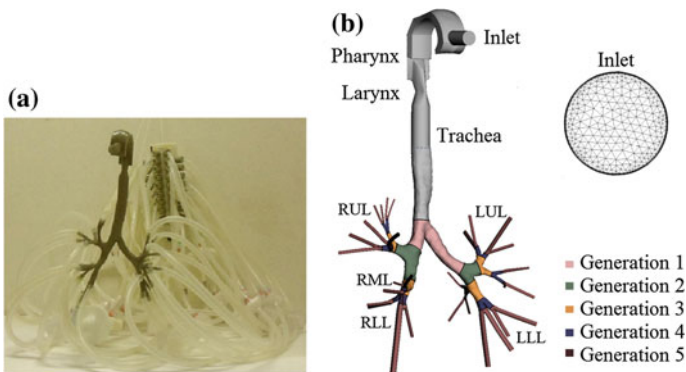
Fig. 1 Geometry of the human airway geometry applied in **a** the experiments and **b** simulations

The airflow calculations are performed for an inhalation flow rate of 30 L/min (Reynolds number Re≈ 2500) and 60 L/min (Re≈ 5000). The fluid density and the dynamic viscosity are set to $\rho = 1.2 \, \text{kgm}^{-3}$ and $\mu = 1.884\text{e}^{-5} \, \text{Nsm}^{-2}$, respectively. The simulation conditions are chosen in accordance with the experimental setup. A steady parabolic velocity profile is imposed at the model inlet and zero gauge pressure applied at the outlets. A no slip condition is utilized on the wall surface. The flow field is solved using LES with the rotation rate based Smagorinsky model [7] as the SGS model. A second order implicit formulation for temporal discretization and central differencing for spatial discretization of the momentum equations are chosen.

Particle tracking is carried out as a post processing operation in 66 LES frozen fields. The number of frozen fields is determined based on POD analysis [1]. 8000 monodisperse particles with density $\rho_p = 912 \, \text{kgm}^{-3}$ and diameters (2–10 μm) are tracked using the one-way coupling Lagrangian approach. In this method, an equation of motion is solved for each individual particle. Due to the large particle-to-air density ratio ($\rho_p/\rho \approx 800$), the considered flow rate, and the particle size, only drag force and gravity are included in the particle equation of motion. Particle deposition due to sedimentation and inertial impaction has been evaluated by conducting Lagrangian simulations with and without the gravity term. The particles are injected at the model inlet with a random distribution and an initial velocity set equal to the fluid velocity. The particles are assumed deposited as soon as they reach the wall. The particle deposition is presented as a function of Stokes number as proposed by Finlay [6].

In the experiments, the particle deposition and distribution in a 3D-printed cast of the geometry is measured for flow rates of 30 and 60 L/min, and with both 3 and 6 μm particles. RANS calculations with $k - \omega$ SST turbulence model are performed on the same grid and for the same flow conditions and particle size as in LES. For RANS particle tracking, the Lagrangian solver uses a modification of the eddy interaction model proposed by Matida et al. [9].

3 Results and Discussion

3.1 Flow Field

Figure 2 depicts contours of the mean velocity and the corresponding turbulent kinetic energy in two planes—one through the upper airways and one through the upper airways with main bronchi. The sudden cross section changes at the larynx leads to flow recirculation and jet movement towards the tracheal wall. In this area, the highest levels of turbulent kinetic energy are observed. Further down the trachea, the turbulent character of the flow decreases and the flow reaches the bronchi as almost laminar. The overall flow distribution in the lungs for both flow rates is approximately 53% to the right lung (17% RUL, 8% RML, 28% RLL) and 47% to the left lung (16% LUL, 31% LLL). Similar values are measured in the experiments.
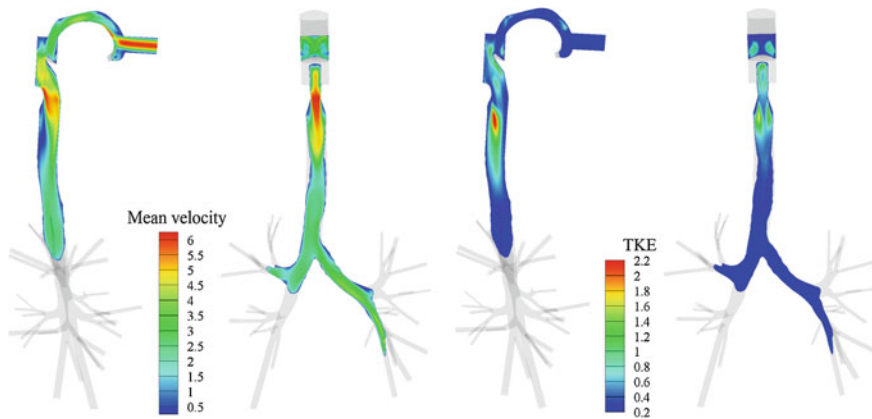
Fig. 2 Contours of mean velocity (ms^{-1})—*left* and turbulent kinetic energy (m^{2}s^{-2})—*right* at 30 L/min

3.2 Particle Deposition

Figure 3 shows the total particle deposition as a function of Stokes number at the model inlet. The LES results are compared to the RANS results, the experimental data for 3 and 6 μm, and with the LES results obtained by Lambert et al. [8]. In their study [8], the airway model consists of a realistic geometry of the upper airways and six generations of bronchi. For both flow rates, the LES particle deposition results are much closer to Lambert et al. [8] results than those obtained with RANS. However, the deposition values for particles with Stokes number Stk< 10^{-2}, at 30 L/min, are noticeably lower in the current study compared to Lambert et al. [8]. The lower deposition may be caused by the difference in the geometry (the present model contains simplified upper airways and one generation less).

In comparison with the experimental data, at 30 L/min, LES overpredicts the deposition for small 3 μm particles while RANS are closer to experimental results. For 6 μm particles, the LES values better match the experimental results than the RANS results. For 60 L/min, the LES deposition for both 3 and 6 μm particles well fit the experimental measurements.

Increasing the flow rate and the particle size leads to significant increase of the local deposition in the upper airways (up to 99.1% for 10 μm and 60 L/min). However, the particle deposition in the bronchial region is quite low and very similar in both flow rates. This is in accordance with the experimental results (less than 8% in simulations and 3.5% in experiments).

Figure 4 presents the distribution of 3 and 6 μm particles and the gas ventilation in the lung lobes (amount of flow and particles entering each specific lobe compared to the total amount of flow and particles entering all 5 lobes) obtained during experiments and with LES. The full line in Fig. 4 corresponds to an equal distribution of
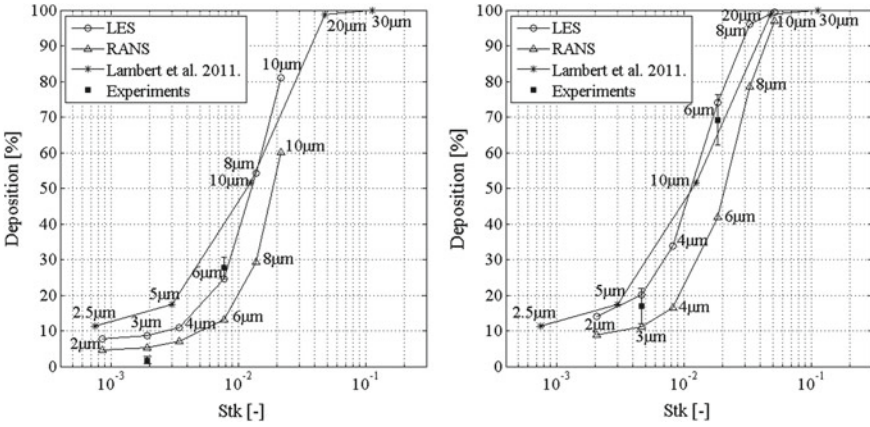
Fig. 3 Total particle deposition (in the entire geometry) at 30 L/min (*left*) and 60 L/min (*right*)
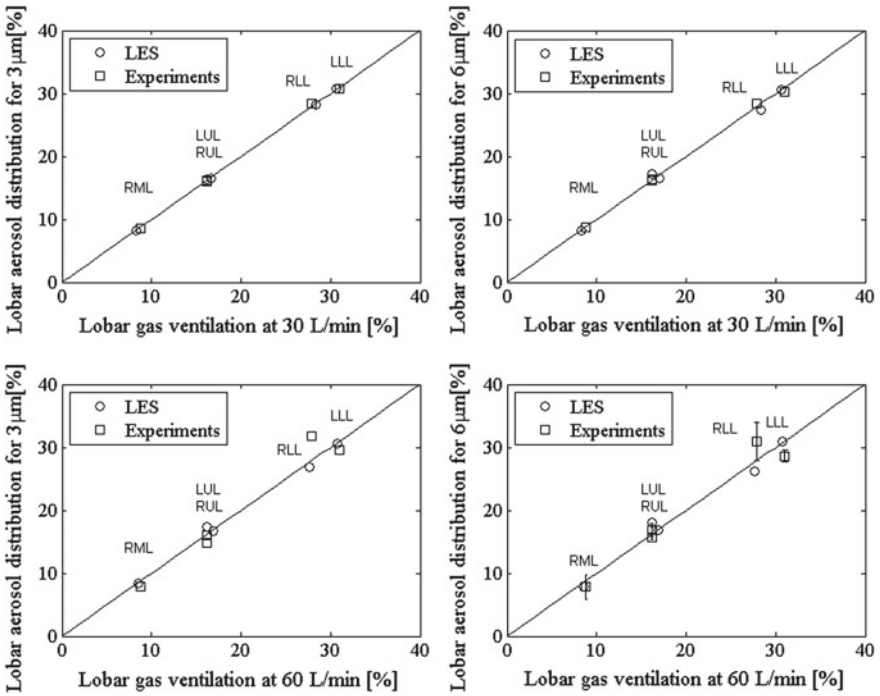
Fig. 4 Air ventilation and particle distribution for 3 μm (*left*) and 6 μm (*right*) at 30 L/min (*top*) and 60 L/min (*bottom*)

particles and carrier flow in the lobes and is shown for a better understanding of the obtained results.

The LES results show that at the lobar level aerosol particles follow the air flow: variation between gas ventilation and particle distribution in each lobe is less than 2% at 30 L/min and 5% at 60 L/min. Similar values of air ventilation and aerosol distribution in each lobe are observed experimentally. These results suggest that the distribution of particles in each lobe is primarily dependent on the gas ventilation to each lobe.

Neglecting gravity in the calculations leads to less than 3% change in the deposition efficiency in the bronchial tree for both flow rates. This indicates that impaction is the dominant particle deposition mechanism in the lung lobes.

4 Conclusions

In the present study, the use of LES in predicting aerosol transport in a model of the human tracheobronchial tree was evaluated. The LES results are compared with the RANS results and experimental measurements obtained on the same geometry, and also with data from the literature. A good agreement between LES and the experimental values was found, with considerable improvement over RANS calculations. However, LES overpredicts the deposition of the smallest particles, indicating that deposition of the small size particles requires further investigation.

It has been shown that the local deposition in the the upper airways significantly increases with the particle size and the flow rate, while deposition in the bronchial tree remains relatively low and uniform. Neglecting gravity showed that impaction is the dominant deposition mechanism in the tracheobronchial tree.

The experimental and numerical investigation of the flow ventilation and particle distribution both confirm that the right lobes receive more airflow than the left lobes. Further to this, the results show that at the lobar level, the particles follow the airflow independent of their size and the flow rate. This suggests that the distribution of particles in each lobe is largely proportional to the flow ventilation.

References

1. Agnihotry V (2014) Modeling air and particle transport in the human upper and tracheobronchial airways using RANS and LES. VUB press, Brussels, Belgium
2. Agnihotri V, Ghorbaniasl G, Verbanck S, Lacor C (2014) On the multiple LES frozen field approach for the prediction of particle deposition in the human upper respiratory tract. J Aerosol Sci 68:58–72
3. Brouns M, Jayaraju ST, Lacor C, Mey JD, Noppen M, Vincken W, Verbanck S (2007) Tracheal stenosis: a flow dynamics study. J Appl Physiol 102(3):1178–1184
4. Chan T, Lippmann M (1980) Experimental measurements and empirical modeling of the regional deposition of inhaled particles in humans. Am Ind Hyg Assoc J 41:399–409

5. Cheng YS, Zhou Y, Chen BT (1999) Particle deposition in a cast of human oral airways. Aerosol Sci Technol 31:286–300
6. Finlay WH (2001) The mechanics of inhaled pharmaceutical aerosols. Academic press, London, UK
7. Ghorbaniasl G, Agnihotri V, Lacor C (2013) A self-adjusting flow dependent formulation for the classical Smagorinsky model coefficient. Phys Fluids. doi:10.1063/1:4804393
8. Lambert A, O'Shaughnessy P, Tawhai M, Hoffman E, Lin C (2011) Regional deposition of particles in an image-based airway model: large-eddy simulation and left-right lung ventilation asymmetry. J Aerosol Technol 45:11–25
9. Matida EA, Finlay WH, Lange CF, Grgic B (2004) Improved numerical simulation of aerosol deposition in an idealized mouth-throat. Aerosol Sci 35:1–19

Real-Time Reconstruction of Separated Flow Flapping Motion

F. Fadla, A. Graziani, F. Kerhervé, R. Mathis, M. Lippert, D. Uystepruyst and L. Keirsbulck

Abstract The ability of electrochemical sensors to properly measure wall-shear stress is here considered to use them as potential candidates for time-resolved estimation of a large-scale activity occurring at the flow separation region downstream a bump. The inflow Reynolds number considered, based on the channel full height and the incoming bulk velocity, is $Re_b = 1735$. The methodology implemented consists in combining the electrochemical sensors with PIV measurements and to build an estimation model of a low-order representation of the flow field. This estimation model is based on a multi-time reformulation of the complementary technique originally introduced by Bonnet et al. (Exp Fluids 17(5):307–314, 1994 [1]). The present paper shows the potential of electrochemical sensors for properly resolving the low-frequency flapping mode whose control was recently shown by Gautier et al. (J Fluid Mech 770:442–457, 2015 [2]), and its potential as a candidate to significantly reduce separation.

1 Introduction

Flow separation has been considered for more than a century as a very complex academic challenge. It has numerous industrial impacts due to the large energy losses associated with its occurrence and has been extensively studied since the famous Prandtl's paper in 1904. The process of separation is connected with complex unsteady instability mechanisms. One of them, associated to low-frequency oscillations and known as "flapping" phenomenon identified by Cherry et al. [3], is

F. Fadla · M. Lippert · D. Uystepruyst · L. Keirsbulck (✉)
LAMIH CNRS, UMR 8201, Valenciennes, France
e-mail: laurent.keirsbulck@univ-valenciennes.fr

R. Mathis
LML CNRS, UMR 8201, Villeneuve D'ascq, France

A. Graziani
Institut de Recherche Technologique Railenium, Famars, France

F. Kerhervé
PPRIME CNRS, UPR 3346, Chasseneuil, France

not yet fully understood and considerable discussions are still ongoing to explain the onset of such mechanism [4]. The ability of stochastic methods such as linear or quadratic stochastic estimations (LSE/QSE respectively) to capture conditional estimates of a given field associated with given events (or observers) is now well-accepted. These methods have proven to be efficient in a wide range of purposes and flow configurations. Where flow separation is concerned, the use of wall-shear stress measurements as observers can be considered as a potential candidate due to its asymptotical nature with the velocity field near the wall. The electrochemical (or the electrodiffusion) method—see [5] for a thorough review—based on the determination of the limiting diffusion current at the surface of electrodes placed along the wall provides accurate time-resolved information on the wall-shear stress fluctuations. This method of investigation of local hydrodynamical characteristics has recently found an extensive application for turbulent flows analysis [6] and also for separated boundary layer flows [7]. The main objective of the present paper is to demonstrate the ability of electrochemical sensors for real-time estimation of the low-frequency flapping mode occurring downstream of a bump when the flow separates. The methodology implemented combines a low-order description of the flow field known as Proper Orthogonal Decomposition (hereafter POD) and a multi-time formulation of the LSE for time-resolved estimation of the first temporal POD mode which is found to well capture the flapping mode.

2 Experimental Procedure and Description of the Separate Flow

The experimental investigations were conducted in the closed-loop hydrodynamic channel at the LAMIH. Boundary layer separation is induced by the presence of a smooth bump at the bottom wall of the test section (for more details about the channel configuration and the bump geometry see [8]). The considered inflow Reynolds number based on the bulk velocity is $Re_b = 1735$. Throughout this paper, the coordinates x and y refer to the streamwise and wall-normal directions, respectively. Superscript $\star$ refers to dimensionless scalings using the half-height channel, H and the bulk velocity, U_b. Superscript $+$ refers to dimensionless scalings using the recirculating length, L_R and the inflow centerline velocity, U_c.

Synchronized particle image velocimetry (hereafter refers as STAND- PIV) and wall-shear stress measurements are made in a streamwise-wall-normal plane. The wall-shear stress is experimentally determined using seven rectangular micro-sensors flush mounted on the separated flow region of the bump at $x^\star = 0.5$, 0.72, 1.00, 1.26, 1.50, 1.75 and 2.00 as shown in Fig. 1. The streamwise mean velocity field obtained in the $x - y$ plane from the STAND- PIV measurements clearly shows a large recirculation region (Fig. 1). Examination of the mean recirculation patterns shows that the free stream flow is divided into two direction and reveals the separation point thanks to their deviation towards the wall. The tangential mean velocity gradient,
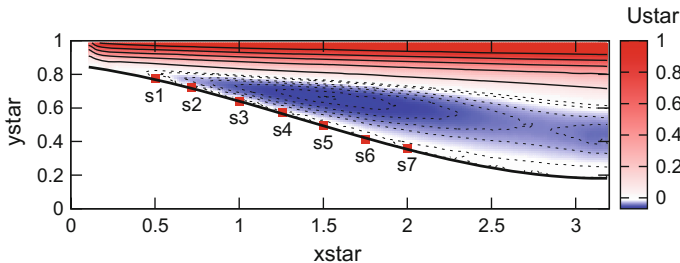
Fig. 1 Iso-contours of mean streamwise velocity. The *red* squares represent the wall sensors

reaches zero at the normalized position $x_s^\star \approx 0.6$. The reattachment point can be estimated to be located approximately at $x_r^\star \approx 6.1$ downstream, corresponding to a dimensionless recirculation length of $L_R^\star \approx 5.5$.

3 Time-Resolved Reconstruction of the Flapping Motion

The Proper Orthogonal Decomposition (hereafter POD) is here applied to the STAND-PIV snapshots with two objectives: (i) to better appreciate the low-order dynamics of the examined flow field and (ii) to properly capture the flapping mode instability. In order to better understand the nature of the connections between the flow and the shear-stress measurements, the conventional "snapshot method" of Sirovitch [9] and a multi-time delay linear stochastic estimation (MLSE) is implemented. Presently, the conditional variables (the quantities to evaluate) comprise the fluctuating velocity components measured by STAND- PIV, hereafter $\{\mathbf{u}(\mathbf{x}, t_i)\}_{i=1,...,N_t}$, while the set of observables is formed by the measured wall shear-stress, hereafter $\tau'(x_j, t)_{j=1,...,N_s}$. The MLSE formulation adds new conditions associated with time-delayed observations and has the benefit to make the estimated variables richer in terms of spectral content [10]. The linear approximation $\tilde{\mathbf{u}}'(\mathbf{x}, t)$ of the fluctuating velocity field reads as,

$$\tilde{\mathbf{u}}'(\mathbf{x}, t) = \sum_{k=1}^{N_\tau} \sum_{j=1}^{N_s} \alpha_{j|k}(\mathbf{x})\tau'(\mathbf{y}_j, t - \tau_k) \tag{1}$$

with N_τ the number of time delays considered. Minimizing the least-square error defined as $J = ||\tilde{\mathbf{u}}'(\mathbf{x}, t) - \mathbf{u}'(\mathbf{x}, t)||_2^2$ (in the conventional L_2-norm sense), the coefficients $\alpha_{j|k}(\mathbf{x})$ can be obtained by solving for each point $\mathbf{x}$ a system of linear equations of the form $A\Lambda = B$, where A is a real-symmetric square matrix containing cross-correlations of the observers, B is a real matrix with correlations between velocity points and observers, and Λ a real matrix containing the unknown coefficients.

Instead of directly estimate the velocity field, the same methodology can be applied to the n-th temporal POD coefficients. This is known as the complementary technique, originally introduced by Bonnet et al. [1]. Equation (1) may therefore be rewritten as:

$$\tilde{a}^{(n)}(t) = \sum_{k=1}^{N_\tau} \sum_{j=1}^{N_s} \alpha_{j|k}^{(n)} \tau'(\mathbf{y}_j, t - \tau_k) \tag{2}$$

For the present purpose, the number of time delays considered has been arbitrarily chosen such that the correlation peak between the sensors and the temporal POD coefficients can be properly discretized. A parametric study (not shown here) has been conducted and showed that a number of 11 delays regularly distributed offers a good compromise between the computational cost and the estimation error. The low-order time-resolved estimates of the flow field (multi-time complementary technique named hereafter mCT) can thus be obtained thanks to,

$$\tilde{\mathbf{u}}(\mathbf{x}_i, t) = \overline{\mathbf{u}}(\mathbf{x}) + \sum_{n=1}^{N_g} \tilde{a}^{(n)}(t)\phi^{(n)}(\mathbf{x}), \quad n = 1, \dots, N_g \tag{3}$$

with N_g the number of POD modes retained and $\phi(\mathbf{x})$ is the spatial eigenvectors for the n-th mode.

A sample of the time history of the first POD temporal coefficient obtained from the STAND- PIV snapshots and that estimated from the electrochemical sensors is given in Fig. 2. The time evolution of the POD coefficient is globally well recovered despite the higher frequency content of the wall-shear stress signals.

We now performed a low-order reconstruction of the velocity field using only the first mode (Eq. 2 with $N_g = 1$) in order to visualize dominated wall-normal motions of the shear layer. Snapshots at two different instants have been selected to illustrate specific events and are reported on the right hand side in Fig. 3. For comparison, the original STAND- PIV snapshots are reported on the left hand side. To ease the visu-
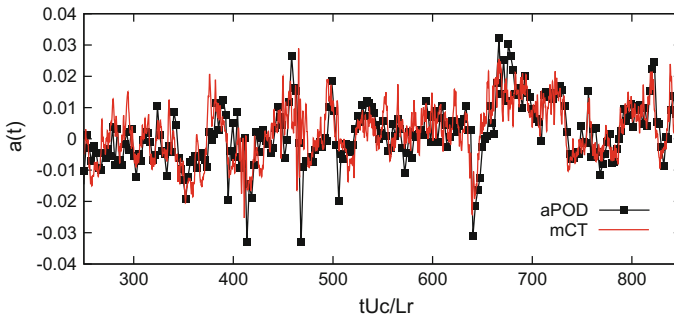
Fig. 2 Time history of the first temporal POD coefficients (*black line* with symbols) obtained direclty from the STAND-PIV set of data and (*red line*) estimated using mCT
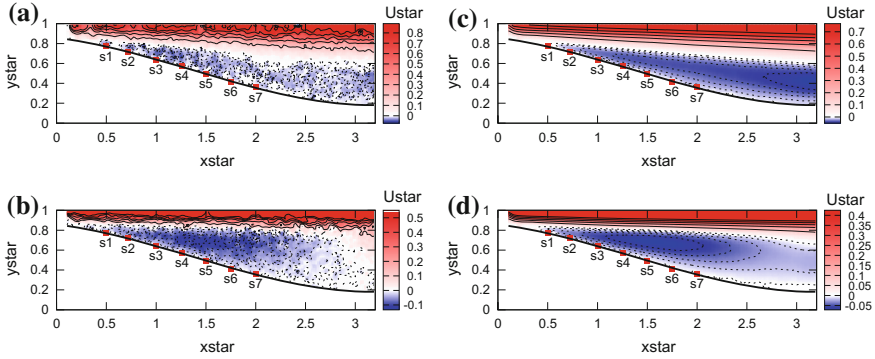
Fig. 3 Snapshots of **a** and **b** STAND- PIV data, **c** and **d** low-order reconstructed streamwise velocity component with $N_g = 1$ at two different instants (*top* and *bottom*)

alization, only regions corresponding to instantaneous negative streamwise velocity are shown. The elongated region observed for the reconstructed field (Fig. 3c, d) may be interpreted as a low-order approximation of the overall recirculation region well identified in the original PIV snapshots (Fig. 3a, b). During most of the examined sequence, this large region is found to remain attached to the wall, with its main axis pointing downwards the wall, similar to the snapshots of Fig. 3a, c). However, a detachment from the wall of the downstream part is occasionally observed, similarly to that observed in Fig. 3b, d).

These specific events correspond to a significant decrease of the recirculation region, with an injection of fluid inside the bubble near the reattachment point. Most of the time, the reattachment point is outside of the PIV field of view, characteristic of an extended negative streamwise velocity region as highlighted before in Fig. 1.

Intermittent fluctuations in the reattachment point causes significant motions in the wall-normal direction of the recirculation region, and hence of the overall shear layer. Attempt into identifying a specific frequency of this wall-normal motion based
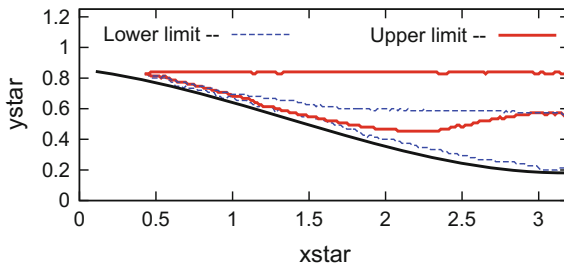
Fig. 4 Extrema positions of the edges of the recirculation region during a long examined time sequence. Upper (*red*) and lower (*blue*) positions. Results are obtained using the time-resolved low-order estimate of the streamwise velocity component ($N_g = 1$)

on the time evolution of the borders of the reconstructed recirculation region has proved to be difficult. Nevertheless, the extrema locations of the border observed during a long time sequence (more than 1000 turnover time) are illustrated in Fig. 4. Note that the upper border (red line) is here limited by the PIV region investigated. The recirculation region is shown to intermittently deviates upwards (red lines) from the most encountered regime (blue lines). It should be emphasized that at such a low Reynolds number, the separated flow is strongly influenced by the incoming laminar boundary layer. Intermittent perturbations directly drive large changes in the reattachment point location and in the overall dynamics of the recirculation area.

4 Conclusions

Measurements of wall-shear stress using electrochemical sensors along a bump in a channel flow, simultaneously with low-speed PIV are reported to build a low-order estimate of the low-frequency large-scale flapping mode. While the methodology implemented is now well-accepted, the use of electrochemical sensors for such a purpose has not yet been reported. A low-order description of the flow field, based on a multi-time delay formulation of the linear stochastic estimation technique, seems to be very efficient in order to obtained a real-time estimation of the flapping motion. The presented work is of particular interest for future control applications based either on drag or separation area reduction. Sequences of PIV snapshots can be used to compute offline the spatial eigenfunction of the first mode while the later can be used online to estimate the global dynamic of the recirculation region using only real-time information from wall-shear stress sensors.

References

1. Bonnet JP, Cole DR, Delville J, Glauser MN, Ukeiley LS (1994) Stochastic estimation and proper orthogonal decomposition: complementary techniques for identifying structure. Exp Fluids 17(5):307–314
2. Gautier N, Aider JL, Duriez T, Noack BR, Segond M, Abel M (2015) Closed-loop separation control using machine learning. J Fluid Mech 770:442–457
3. Cherry NJ, Hiller R, Latour MP (1984) Unsteady measurements in a separating and reattaching flow. J Fluid Mech 46:144–157
4. Robinet J-Ch (2013) Instabilities in laminar separation bubbles. Focus Fluids J Fluid Mech 732:1–4
5. Hanratty T, Campbell J (1983) Measurement of wall shear stress. In: Goldstein RJ (ed) Fluid mechanics measurements. Hemisphere Publishing, Co., pp 559–615
6. Keirsbulck L, Labraga L, Gad-el-Hak M (2012) Statistical properties of wall-shear-stress fluctuations in turbulent channel flows. Int J Heat Fluid Flow 37:1–8
7. Tihon J, Legrand J, Legentilhomme P (2001) Near-wall investigation of backward-facing step flows. Exp Fluids 31(5):484–493
8. Fadla F, Keirsbulck L, Aloui F, Laval J-P (2014) Proceedings of the ASME 2014 fluids engineering summer meeting, August 3–7. Chicago, Illinois, USA

9. Sirovich L (1987) Turbulence and the dynamics of coherent structures. Quat Appl Maths 45:561–590
10. Tinney CE, Coiffet F, Delville J, Hall AM, Jordan P, Glauser MN (2006) On spectral linear stochastic estimation. Exp Fluids 41(5):763–775

LES Modeling with a Multifield Approach

Solene Fleau, Stephane Vincent and Stephane Mimouni

Abstract In nuclear power plants, flow studies with a Computational Fluid Dynamics (CFD) approach require the ability of dealing with inclusions of different sizes and shapes and turbulence effects. For this purpose, multifield methods have been developed to simulate separately the small spherical bubbles and the large deformable ones. In this article, we consider an approach in which the first range of bubbles are followed by an Eulerian dispersed method and the second structures are tracked by interface tracking methods within a two-fluid model. To deal with these large inclusions, we present and validate, in this paper, a model, called the Large Bubble Model, introduced for the simulation of large deformable interfaces between two continuous fields. The Large Bubble Model includes a surface tension model, a new drag force expression to couple the velocity of the two fields at the interface and the resolution of an interface sharpening equation to limit the numerical smearing induced by the two-fluid model. To take into account the turbulence effects, an *a priori* two-phase LES filtering is proposed with the two-fluid equations and the interfacial forces of the Large Bubble Model. This filtering highlights new subgrid terms compared to previous works done on the single-fluid model. Finally, DNS simulations are performed with a phase inversion test case to evaluate the order of magnitude of these terms and to compare five different turbulence models.

S. Fleau (✉) · S. Mimouni
Electricite de France, R&D Division, Chatou, France
e-mail: solene.fleau@edf.fr

S. Mimouni
e-mail: stephane.mimouni@edf.fr

S. Vincent
Laboratoire de Modelisation et Simulation Multi-Echelle,
Universite Paris-Est Marne la Vallee, Champs-sur-Marne, France
e-mail: stephane.vincent@u-pem.fr

1   Introduction

The simulation of flows occurring in nuclear power plants remains a scientific challenge due to the complexity induced by the presence of bubbles with a large range of sizes and shapes and the necessity of dealing with the turbulence effects induced by the bubbles and the tubes topology. Therefore, in the code NEPTUNE_CFD, a multifield approach based on the two-fluid model of Ishii [8] has been developed. In this method, the large deformable bubbles are resolved whereas the small spherical bubbles are considered as a dispersed field. The required models for the interfacial transfers related to this dispersed field have been well studied and validated [11]. However, for the large deformable bubbles, a special treatment is necessary to locate the interfaces precisely and to take into account the velocity jump at the interface. Thus, in this article, we present a model, called the Large Bubble Model, developed specifically for the simulation of these interfaces between two continuous fields. This method includes the definition of a surface tension model, a drag force expression to couple the velocity of the two fields at the interface and the resolution of an interface sharpening equation to limit the numerical interface smearing induced by the two-fluid model. In the previous publications related to the Large Bubble Model [6, 7], the studies considered only laminar flows. Therefore, in this paper, we propose an *a priori* two-phase LES filtering with the simulation of the inversed phase benchmark [9, 10, 17]. The two-fluid model equations are filtered to exhibit the specific subgrid terms of the model. Their order of magnitude is then compared with three grids and different turbulence models are applied to find the more appropriate for each subgrid term.

2   Large Bubble Model

In this section, we propose a description of the Large Bubble Model devoted to the simulation of large interfaces between two continuous fields within the two-fluid approach. This model has been implemented in the code NEPTUNE_CFD, which is based on an Eulerian approach with a finite volume discretization. The flow motion is followed using the two-fluid model of Ishii [8] extended to n-phase. In this model, the density, the viscosity and the local velocity are defined for each field in each cell. This study is restricted to incompressible and isothermal cases with $\rho_k = cst$. No mass transfers are considered at the large interfaces. The following governing equations are solved for each field k:

1. The mass balance equation:

$$\frac{\partial}{\partial t}(\alpha_k \rho_k) + \nabla . (\alpha_k \rho_k \mathbf{u}_k) = 0 \tag{1}$$

   with α_k the volume fraction of phase k, ρ_k its density and $\mathbf{u}_k$ its velocity.

2. The momentum equation:

$$\frac{\partial}{\partial t}(\alpha_k \rho_k \mathbf{u}_k) + \nabla.(\alpha_k \rho_k \mathbf{u}_k \otimes \mathbf{u}_k) = -\alpha_k \nabla P + \nabla.(\alpha_k \mu_k S_k) \\ + \alpha_k \rho_k \mathbf{g} + \mathbf{F}_k \tag{2}$$

with μ_k the dynamic viscosity of phase k, S_k the viscous stress tensor, P the pressure field, $\mathbf{g}$ the gravitational constant and $\mathbf{F}_k$ extra source terms due to the pressure of large scale interfaces (surface tension) or coupling terms between the continuous fields (drag forces).

The Continuum Surface Force (CSF) model proposed by Brackbill et al. [4] and adapted to the volumetric formulation [6, 7] is used for the simulation of the large interfaces:

$$F_{CSF} = \alpha_k \sigma \kappa \nabla \alpha_k \tag{3}$$

With σ the surface tension coefficient and $\kappa = -\nabla \cdot \left(\frac{\nabla \alpha_k}{\|\nabla \alpha_k\|}\right)$ the local curvature.

Moreover, a drag force law has been developed to couple the velocity of the two continuous fields at the interface. Details can be found in [7]:

$$\alpha_2 < 0.3: \qquad \mathbf{F}_{bubble} = \alpha_1 \alpha_2 \frac{18\mu_1}{\alpha_1 d_p^2}(\mathbf{u}_1 - \mathbf{u}_2)$$

$$\alpha_2 > 0.7: \qquad \mathbf{F}_{droplet} = \alpha_1 \alpha_2 \frac{18\mu_2}{\alpha_2 d_p^2}(\mathbf{u}_1 - \mathbf{u}_2) \tag{4}$$

$$0.3 \le \alpha_2 \le 0.7: \mathbf{F}_{mix} = \frac{0.7 - \alpha_2}{0.7 - 0.3}\mathbf{F}_{bubble} + \frac{\alpha_2 - 0.3}{0.7 - 0.3}\mathbf{F}_{droplet}$$

The characteristic length scale d_p is equal to $\sqrt{\frac{\mu_2}{\mu_1}}\frac{\alpha_p}{\|\nabla \alpha_p\|}$ close to the large interfaces, for $0.1 < \alpha_1 \alpha_2 < 0.25$, and to the diameter of the dispersed bubbles/droplets far from them, for $\alpha_1 \alpha_2 < 0.02$. Between these two regions, a linear extrapolation of these two values is defined.

Finally, to limit the interface smearing induced by the resolution of the two-fluid equations, the interface sharpening equation proposed by Olsson and Kreiss [13] and adapted to the two-fluid formulation is solved for each continuous field [7]:

$$\frac{\partial \alpha_k}{\partial \tau} + \nabla \cdot \alpha_k (1 - \alpha_k)\mathbf{n} = \varepsilon \nabla \cdot (\nabla \alpha_k) \tag{5}$$

With $\mathbf{n} = \frac{\nabla \alpha_k}{\|\nabla \alpha_k\|}$ the interface normal vector. The values of the parameters $\Delta \tau = \frac{\Delta x}{32}$ and $\varepsilon = \frac{\Delta x}{2}$ (Δx denotes the cell size) are chosen to obtain a final interface thickness always equal to 5 cells whatever the initial interface diffusion [6].

A large range of isothermal and laminar validation test cases has been simulated to validate the Large Bubble Model with free surface test cases, convergence studies, evaluation of spurious velocities and comparison with other models [7].

3 *A Priori* LES Study on a Two-Phase Flow

For this study, the inversed phase benchmark [9, 10, 17] has been simulated with the Large Bubble Model. In this test case, an oil drop with a cubic shape (size of L/2) is initially placed in a cubic box (size $L=0.1$ m) containing liquid water (see Fig. 1). At the end of the simulation, the oil phase is supposed to be located in the top part of the box with the liquid water beneath. The fluid properties are: $\rho_{oil} = 900$ kg.m^{-3}, $\mu_{oil} = 0.1$ Pa.s, $\rho_{water} = 1000$ kg.m^{-3} and $\mu_{water} = 1.10^{-3}$ Pa.s, $\sigma = 0.045$ N.m. The test case is simulated with three different mesh refinements: 128^3 cells, 256^3 cells and 512^3 cells. The time steps are kept constant and are respectively equal to 0.8, 0.2 and 0.05 ms. The simulations have been performed with 144 cores for the first mesh and 1152 for the two others during respectively 7 h, 47 h and 2 months to reach 13 physical seconds.

First, we study different macroscopic quantities to validate the Large Bubble Model in this configuration. Thus, Fig. 2 shows the evolution of the normalized kinetics energy, potential energy and enstrophy [18]. The results reproduce the same trends observed with other CFD codes [17]. Oscillations are observed for the potential and kinetics energies due to the sloshing motion of oil when it reaches the top of the box. Concerning the enstrophy, the location of the peak is also found to occur at around 3 in dimensionless time.
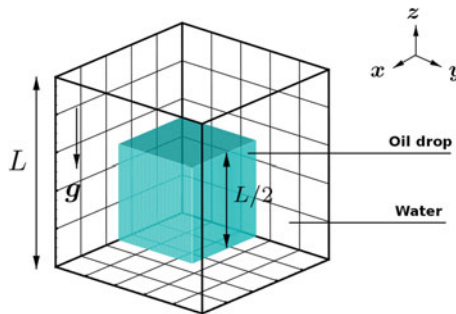
Fig. 1 Initial conditions of the inversed phase benchmark
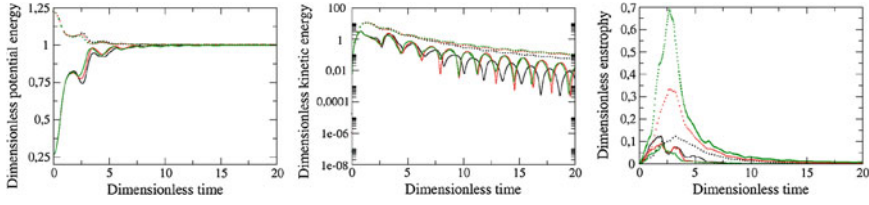
Fig. 2 Evolution of the dimensionless potential energy, kinetic energy and enstrophy, the *solid lines* correspond to the oil phase, the *dashed lines* to water, the *black curves* refer to the coarser mesh: 128^3 cells, the *red* ones to the intermediate mesh: 256^3 cells and the *green* ones to the refined mesh: 512^3 cells

3.1 Subgrid Terms Contribution in the Filtered Two-Fluid Equations

The subgrid terms appearing in the filtered two-fluid equations are displayed in Table 1. The drag force subgrid term is obtained with the same method applied to the surface tension term using Eq. (4).

These subgrid terms are compared in terms of order of magnitude to find the predominant and negligible ones. This analysis allows identifying the subgrid terms, which will require modeling efforts. For this purpose, a top hat filter (filter size of 2) is applied to the simulation results extracted at the peak of enstrophy for the three grids. Each subgrid term in the momentum equation is normalized by the convection resolved term and the interfacial subgrid term τ_{interf} by its corresponding resolved part. The subgrid term τ_{time} is not considered in this study since the analysis is proposed only for one time. The results are presented in Fig. 3. As documented in [9, 10, 17], the subgrid term τ_{superf} is predominant for the oil phase. Moreover, a small contribution of the diffusion subgrid term τ_{diff} is observed for the two phases. Nevertheless, it cannot be neglected for the oil phase. The Favre's averaging does not affect the classification of the subgrid terms. Finally, as expected, we also observed a decrease of the magnitude of each term when the mesh is refined except for τ_{superf} in the oil phase. The contribution of the drag subgrid term τ_{Drag} is not mentioned in Fig. 3 in the interests of clarity but its order of magnitude is largely higher than the contribution of the other subgrid terms.

3.2 Turbulence Models

Finally, we apply five different turbulence models to these subgrid terms: the Smagorinsky's model [15], the Wall-Adapting Local Eddy-Viscosity (WALE) model [12], the Bardina's model [2], the mixed Smagorinsky-Bardina's model [3] and the Adaptative Deconvolution Model (ADM) [1] with an order of 6. In Fig. 4, we present the relative error of each model with the DNS prediction of each subgrid term. This

Table 1 Subgrid term appearing in the filtered two-fluid equations, $\tilde{\mathbf{u}}_k = \frac{\overline{\alpha_k \mathbf{u}_k}}{\overline{\alpha_k}}$ being the Favre's average of $\tilde{\mathbf{u}}_k$ and $\hat{\kappa} = -\nabla \cdot \left(\frac{\nabla \overline{\alpha_k}}{\|\nabla \overline{\alpha_k}\|} \right)$ the filtered local curvature

Subgrid terms	τ_{time}	τ_{conv}	τ_{diff}	$\tau_{pressure}$	τ_{superf}	τ_{Drag}	τ_{interf}
Simple filtering	$\rho_k \left(\frac{\partial \overline{\alpha_k \mathbf{u}_k}}{\partial t} - \frac{\partial \overline{\alpha_k}\, \overline{\mathbf{u}_k}}{\partial t} \right)$	$\rho_k \left(\nabla \cdot \overline{(\alpha_k \mathbf{u}_k \otimes \mathbf{u}_k)} - \nabla \cdot (\overline{\alpha_k}\, \overline{\mathbf{u}_k} \otimes \overline{\mathbf{u}_k}) \right)$	$\mu_k \left(\nabla \cdot \overline{(\alpha_k S_k)} - \nabla \cdot (\overline{\alpha_k}\, \overline{S_k}) \right)$	$\overline{\alpha_k \nabla P} - \overline{\alpha_k} \nabla \overline{P}$	$\sigma \left(\overline{\alpha_k \kappa \nabla \alpha_k} - \overline{\alpha_k} \hat{\kappa} \nabla \overline{\alpha_k} \right)$	$\overline{\mathbf{F}}_{Drag} - \hat{\mathbf{F}}_{Drag}$	$\rho_k \left(\nabla \cdot \overline{(\alpha_k \mathbf{u}_k)} - \nabla \cdot (\overline{\alpha_k}\, \overline{\mathbf{u}_k}) \right)$
Favre's averaging	–	$\rho_k \left(\nabla \cdot \overline{(\alpha_k \mathbf{u}_k \otimes \mathbf{u}_k)} - \nabla \cdot (\overline{\alpha_k} \tilde{\mathbf{u}}_k \otimes \tilde{\mathbf{u}}_k) \right)$	–	$\overline{\alpha_k \nabla P} - \overline{\alpha_k} \nabla \overline{P}$	$\sigma \left(\overline{\alpha_k \kappa \nabla \alpha_k} - \overline{\alpha_k} \hat{\kappa} \nabla \overline{\alpha_k} \right)$	$\overline{\mathbf{F}}_{Drag} - \tilde{\hat{\mathbf{F}}}_{Drag}$	–

Fig. 3 Order of magnitude of the normalized subgrid terms for the oil phase, only the z component is displayed
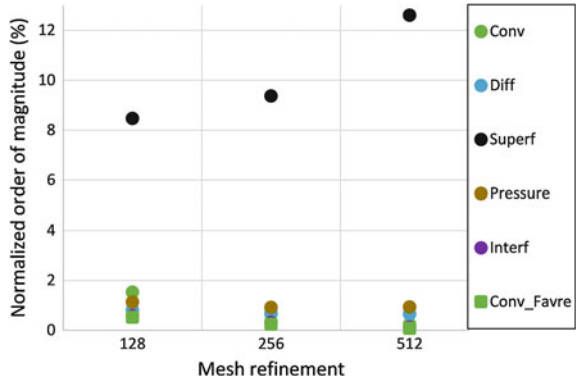
Fig. 4 Relative error obtained by comparison between the modeled subgrid term and the terms obtained by DNS for the oil phase, similar results are obtained with the water phase, mesh with 512^3 cells
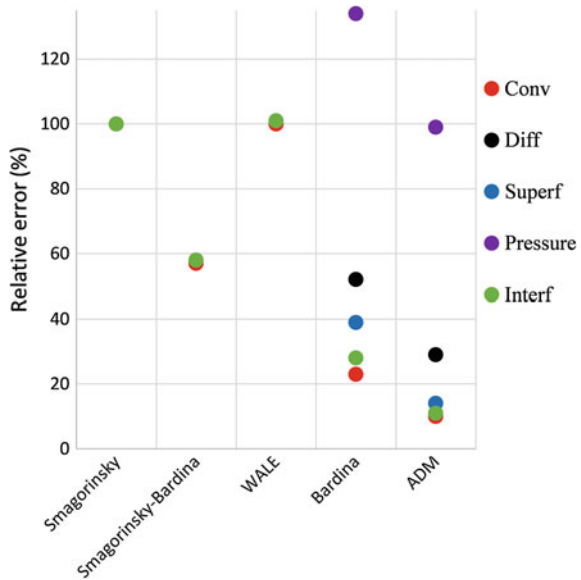
figure highlights that ADM is the most appropriate model for all the subgrid terms. Figure 5 displays the dispersion and the slope obtained between each model and the DNS results for the convective subgrid term. ADM is the only model to present a slope close to 1 with a limited dispersion. Moreover, for all the turbulence models, the error is stable when the mesh is refined. For the drag subgrid term, the error is always higher than 100%. As shown in Fig. 5, this is probably due to the region splitting of the drag force expression, which induces a deviation of the modeled subgrid term at the boundaries [5, 14]. A solution could be to adapt the phase-conditioned filtering proposed by Trontin et al. [16] to the regions defined in the drag force expression.
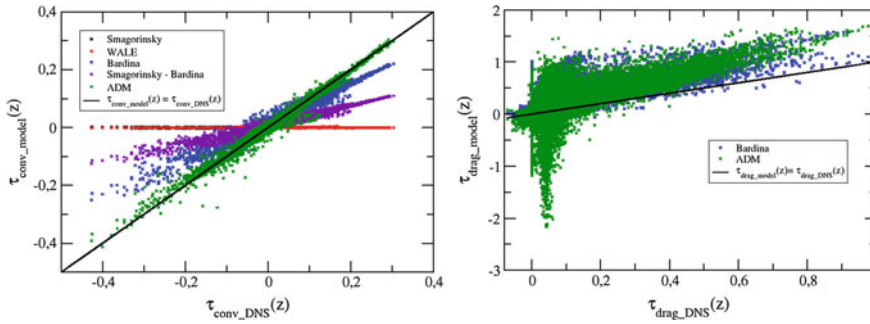
Fig. 5 Correlation between the turbulence models and the DNS results, *left* convective subgrid term for the oil phase, *right* drag subrid term in the intermediate region $0.3 \leq \alpha_2 \leq 0.7$, only the component in the z direction is considered, mesh with 128^3 cells

4 Conclusion

A specific model, called the Large Bubble Model, has been developed to simulate accurately a large range of two-phase flows with large deformable interfaces within the multifield approach. Work is still in progress to extend the validations to cases with a dispersed field and transitions between the small spherical bubbles and the larger ones. This article has been devoted to the LES study of the two-fluid equations. The filtered equations highlighted new subgrid terms with non negligible orders of magnitude. The turbulence models comparison showed that the best correlation with DNS results has been obtained with ADM for all the subgrid terms. The same study should be performed in the future on other test cases involving large rising bubbles and the phase inversion benchmark in a more turbulent configuration, in which smaller spherical bubbles are created.

References

1. Adams N, Stolz S (2002) A subgrid-scale deconvolution approach for schock capturing. J Comput Phys 178(2):391–426
2. Bardina J et al (1980) Improved subgrid scale models based on large eddy simulation. AIAA Paper 80:1357
3. Bardina J et al (1983) Improved turbulence models based on large eddy simulation of homogeneous, incompressible, turbulent flows. Technical Report Thermosciences Division, Department of Mechanical Engineering, Standford University

4. Brackbill JU et al (1992) A continuum method for modeling surface tension. J Comput Phys 100:335–354
5. Carrara MD, DesJardin PE (2008) A filtered mass density function approach for modeling separated two-phase flows for LES II: simulation of a droplet laden temporally developing mixing layer. Int J Multiph Flow 34:748–766
6. Denfle R et al (2015) Multifield hybrid approach for two-phase flow modeling Part 1: adiabatic flows. Comput Fluids 113:106–111
7. Fleau S et al (2015) Validation of a multifield approach for the simulations of two-phase flows. Comput Therm Sci 7(5–6):441–457
8. Ishii M (1975) Thermo-fluid dynamic. Theory of two-phase flow. Eyrolles
9. Labourasse E et al (2007) Towards large eddy simulation of isothermal two-phase flows: governing equations and a priori tests. Int J Multiph Flow 33:1–39
10. Larocque J et al (2010) Parametric study of LES subgrid terms in a turbulent phase sparation flow. Int J Heat Fluid Flow 31:536–544
11. Mimouni S et al (2011) Combined evaluation of second order turbulence model and poly-dispersion model for two-phase boiling flow and application to fuel assembly analysis. NED 241(11):4523–4536
12. Nicoud F, Ducros F (1999) Subgrid-scale stress modelling based on the square of the velocity gradient tensor. Flow Turbul Combust
13. Olsson E, Kreiss G (2005) A conservative level set method for two phase flow. J Comput Phys 210:225–246
14. Sagaut P, Germano M (2005) On the filtering paradigm for LES of flows with discontinuities. J Turb 6(23)
15. Smagorinsky J (1963) General circulation experiments with the primitive equations. Month Weath Rev 91:99–165
16. Trontin P et al (2012) A phase-conditioned filtering of incompressible interfacial multiphase flow equations: a priori study for the modeling of LES subgrid scale terms. In: Proceedings of turbulence and interactions 2012, La Saline-les-Bains. La Runion, France
17. Vincent S et al (2008) Numerical simulation of phase separation and a priori two-phase LES filtering. Comput Fluids 37(7):898–906
18. Vincent S et al (2015) A phase inversion benchmark for multiscale multiphase. J Comput Phys. (submitted to)

Experimental and Numerical Investigations of the Aeroacoustics in a Corrugated Pipe Flow

Gaëtan Galeron, Daniel Mazzoni, Muriel Amielh, Pierre Olivier Mattei and Fabien Anselmet

Abstract Our study is focused on the singing risers phenomenon which is encountered in corrugated channels under flow. Internal corrugations are responsible for flow instabilities that synchronize with longitudinal acoustic modes of the channel giving powerful pure tones. Experiments are performed in a specifically designed facility. Numerical simulations of the flow based on a lattice Boltzmann method (LBM) are faced to the experimental results. They aimed at investigating the ability of a LBM based simulation to predict the aeroacoustics of corrugated channels. Acoustic modes and turbulence in the corrugated channel are quite well predicted except the sound pressure levels that need better description of the acoustic boundary conditions.

1 Introduction

The intense noise generation when passing a flow in a corrugated pipe has intrigued researchers for more than a century [3]. Works carried out in recent years agree to show that the sound generation is related to an interaction between the flow and acoustic resonance in the pipe [4, 10, 12]. The turbulence of the flow, the interaction between the cavities forming the corrugation and finally the feedback whistling of the flow are related to the geometry of the pipe. Due to their flexibility and local stiffness, corrugated pipes are used in many engineering applications. In particular, they are widely used in the oil industry as for the transport of natural gas. Under

D. Mazzoni · M. Amielh · F. Anselmet
Aix Marseille Université CNRS Centrale Marseille IRPHE UMR,
7342 F-13384 Marseille, France
e-mail: daniel.mazzoni@centrale-marseille.fr

G. Galeron (✉) · P.O. Mattei
CNRS - UPR 7051, 13453 Marseille, France
e-mail: gaetan.galeron@centrale-marseille.fr

certain conditions of geometries and flow, the pipes may whistle, generating harmful vibrations to the adjoining industrial facilities. A well-known example is the "singing riser" phenomenon observed on some natural gas installations in the North Sea.

In our studies, the lengths of the pipes are large with respect to the dimensions of the cavities. The flow at the center of the pipe remains subsonic with velocities corresponding to a Mach number of less than 0.1. The flow over cavities inducing a sound field is a classic study area [6]. In the case of shallow cavity subjected to an incompressible flow, the hydrodynamic instability of the shear layer that develops on the opening of the cavity is held responsible for the feedback phenomenon [9]. In addition, when, as in our previous study [1], the input of the pipe section has a sufficiently sharp angle, a flow separation occurs near the wall and a veina contracta accelerates the flow on the axis of the pipe. Within this veina contracta, the vortex interaction with a cavity located at a short distance downstream was shown to be the source of strong excitation of pipe longitudinal modes [5].

The aim of the present research is to study both the acoustic and aerodynamic fields within a corrugated pipe under singing conditions. A short description of the especially laboratory designed facility is here given. Simulations with LBM method are faced to experimental results obtained for different flow configurations. Comparisons between experiments and calculations concern velocity and pressure.

2   Experimental Set-up

For the experimental purpose, a rectangular cross section pipe, 2 m long, 20 mm wide, 100 mm high, has been manufactured (Fig. 1). It is made by transparent Plexiglas,
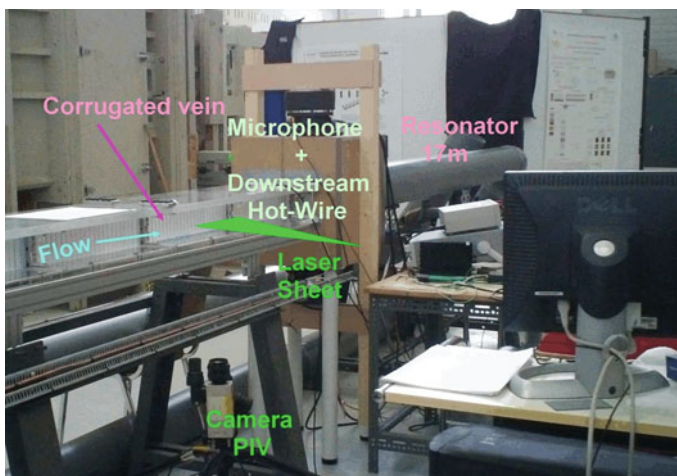
Fig. 1 View of the experiment
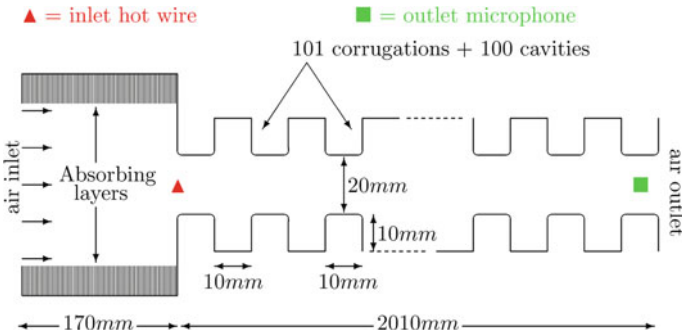
Fig. 2 Computed geometry

thereby allowing the use of optical diagnostics like PIV (Particle Image Velocimetry). The 100 wall-cavities are square-shaped of dimensions $10 \times 10 \, \text{mm}^2$. The upstream edge of each cavity is rounded with the radius $r_{up} = 2.5 \, \text{mm}$ while the downstream edge is sharp ($r_{down} = 0 \, \text{mm}$). These cavities are $10 \, \text{mm}$ deep and $10 \, \text{mm}$ spaced [1]. Point-wise measurements of velocity and acoustic pressure are made respectively by hot-wire anemometry and by microphone. The velocities measured $10 \, \text{mm}$ upstream of the vein entry and downstream, inside the vein, $19 \, \text{mm}$ just upstream of the channel exit section, are used for comparisons with the numerical simulation results (Fig. 2).

3 Discrete Boltzmann Equation

The Lattice Boltzmann Method LBM is a recently developed approach used to compute fluid flows. It is based on the kinetic theory for a fluid flow and from the Boltzmann Transport Equation from the classical kinetic theory of gases. The discrete Boltzmann equation with the Bhatnagar-Gross-Krook (BGK) approximation [13] governs the evolution of the probability density function $f_i(\mathbf{x}, t) = f(\mathbf{x}, \boldsymbol{\xi}_i, t)$ of finding a particle at the point x, at the date t, with velocity ξ_i, in absence of external forces. For the two dimensional nine velocities lattice (D2Q9) used in the present study, ξ_i are the nine possible velocities ($i = 0, ..., 8$) for the particles in this discrete velocity space.

$$\frac{\partial f_i}{\partial t} + \boldsymbol{\xi}_i \cdot \nabla_{\mathbf{x}} f_i = -\frac{1}{\tau} \left[f_i - f_i^{eq} \right] \tag{1}$$

where f_i^{eq} is the discrete probability density function in absence of any collision, f_i^{eq} is usually taken as the second order expansion of the Maxwell velocity distribution leading to:

$$f_i^{eq}(\rho, \mathbf{u}) = w_i \rho \left(1 + \frac{\boldsymbol{\xi}_i \cdot \mathbf{u}}{c_{LB}^2} + \frac{(\boldsymbol{\xi}_i \cdot \mathbf{u})^2}{2c_{LB}^4} - \frac{\mathbf{u}^2}{2c_{LB}^2} \right) \tag{2}$$

where **u** is the local resultant velocity vector. $w_0 = 4/9$, $w_{1,...4} = 1/9$, $w_{5,...9} = 1/36$ are Gauss integration points. $c_{LB} = 1/\sqrt{3}$ is the lattice constant. τ is the relaxation time related to fluid viscosity, see Eq. 6. The macroscopic fluid density and velocity are the moments of the discrete density function f_i:

$$\text{Mass density: } \rho = \sum_i f_i = \sum_i f_i^{eq} \tag{3}$$

$$\text{Momentum flux: } \rho\mathbf{u} = \sum_i \boldsymbol{\xi}_i f_i = \sum_i \boldsymbol{\xi}_i f_i^{eq} \tag{4}$$

Integrating the Boltzmann equation (1) along the characteristics $\boldsymbol{\xi}_i$, for a space-step equal to one ($\Delta x = 1$), denoting $\mathbf{e}_i$ the unit vector pointing in the direction of the velocity vector $\boldsymbol{\xi}_i$, and supposing that the particles move of one cell per time step Δt (i.e. $\Delta x \, \mathbf{e}_i = \Delta t \, \boldsymbol{\xi}_i$), one obtains the lattice Boltzmann equation (LBE):

$$f_i(\mathbf{x} + \mathbf{e}_i, t + \Delta t) - f_i(\mathbf{x}, t) = -\frac{\Delta t}{\tau}\left[f_i(\mathbf{x}, t) - f_i^{eq}(\mathbf{x}, t)\right] \tag{5}$$

Chapman-Enskog analysis [7] shows that in the limit of long-wavelengths, low-frequency, the LBE reproduces exactly the Navier-Stokes equation for weakly compressible flows with an ideal equation of state that is: $P = \rho c_s^2$ where P is the pressure and where $c_s = 343\,\mathrm{ms}^{-1}$ is the speed of sound in air. The kinematic viscosity of the fluid ν is:

$$\nu = c_s^2\left(\tau - \frac{\Delta t}{2}\right) \tag{6}$$

Given the limitation of low Mach number of the LBM, the main interest of the remaining compressibility is to bring the acoustic phenomena. The LBM ability to simulate the propagation of acoustic waves is presented in [2]. Recent developments of the LBM acoustic behaviour are proposed in [15].

4   Results: Comparisons with Experiments

Parallel computations are performed by using the Palabos [11] lattice Boltzmann code with around 50 cores of the mesocentre [8] of Aix Marseille University. The velocity of the particles on the lattice u_{LB} are calculated assuming that the Mach number is conserved so that $u_{LB} = c_{LB} \, u_0/c_s$ where (u_0, u_{LB}) and (c_s, c_{LB}) are the flow velocities and the speeds of sound respectively in the physical space and on the lattice. The geometry is a two-dimensional channel 2.01 m long, 20 mm wide, with corrugated walls (Fig. 2). The wall-cavities are similar to the experiment except the upstream and downstream edges with the radii $r_{up} = 5$ mm and $r_{down} = 1$ mm. The inlet section of this corrugated channel is connected to a tranquillizer chamber of dimensions $170 \times 100\,\mathrm{mm}^2$ with absorbing walls. The role of this tranquillizer chamber is to introduce a sudden change of section of the flow path leading firstly to the flow destabilization and secondly to an approximated Dirichlet acoustic bound-

Fig. 3 Acoustic modes in the corrugated pipe
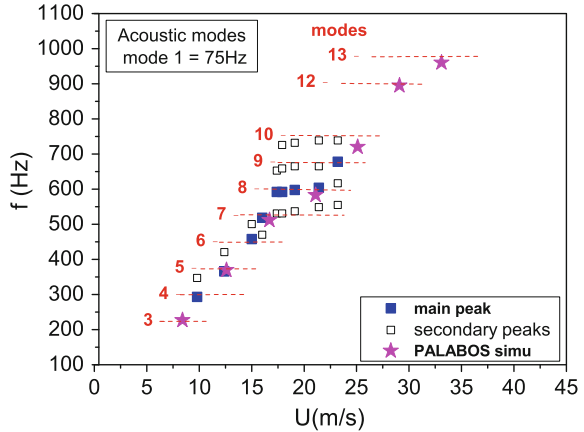
ary condition. The whole domain is meshed with a $10\,\mu$m constant step grid. The boundary conditions on the walls are obtained by the "bounce-back" procedure. At the inlet of the domain, a turbulent pipe flow with a $1/7$ power law velocity profile is used. At the outlet, a constant density condition is imposed that writes $\rho = 1$ in the dimensionless form and insures acoustic Dirichlet boundary conditions.

Seven flow velocity cases are simulated during $1s$ for $u_j = 8.4, 13, 17, 21, 25, 29, 33$ ms^{-1} ($j = 1, .., 7$). These reference velocities are those calculated on the axis, 5 mm downstream of the corrugated channel entry. Acoustic waves effectively travel in the corrugated channel as shown by spectral analysis of the density calculated by the LBM. When the flow velocity increases, successive acoustic modes of the pipe appear (Fig. 3). The frequencies of the acoustic modes observed on the flow simulations agree with the theoretical eigen frequencies of an open pipe: $f_{th_n} = nc_{eff}/2L$ with an acceptable relative error lower than 5%. The efficient speed of sound used for this modal identification, $c_{eff} = 299$ ms^{-1}, has been calculated numerically by measuring the velocity of an acoustic plane wave propagating in the corrugated channel and agrees with the experimental value [1]. The turbulence of the velocity field in the numerical simulation is compared at $u_4 = 21$ ms^{-1} to the experiment on Fig. 4. At this velocity, a strong whistling was experimentally observed. This comparison is given at the position of the downstream hot-wire (19 mm upstream of the exit). At this location, the turbulence has developed so that the downstream hot-wire velocity spectrum fits the usual $f^{-5/3}$ decay rate. For the numerical simulation, the decay of the turbulence spectrum fits a f^{-3} slope, that is an expected result regarding the two-dimensional geometry [14]. The upstream hot-wire is mainly sensitive to the acoustic velocity. The observed strong peaks correspond to the acoustic eigenfrequencies of the corrugated channel. Corresponding acoustic modes are presented in

Fig. 4 Spectral analysis
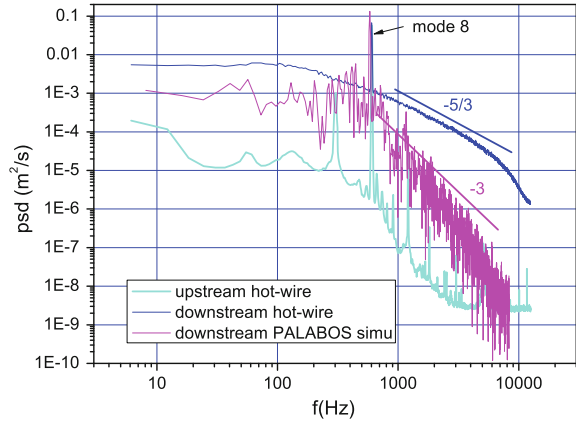
Fig. 5 Simulated acoustic pressure level (dB)
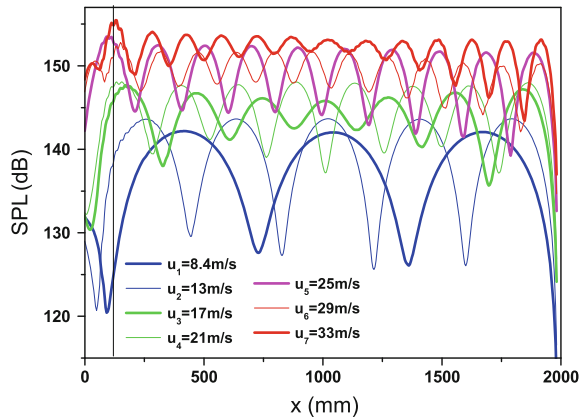
Fig. 3. A good agreement between experiment and simulation is obtained with the reference velocities. Figures 5 and 6 concern acoustic (SPL) and turbulence levels (U_{rms}). In Fig. 5, one observes the main acoustic mode for each reference velocity. In the experiment, the whistling occurs from the reference velocity $17\,\mathrm{ms}^{-1}$ with a strong amplification of the SPL and of the U_{rms} on the upstream hot-wire. This threshold on SPL is not observed on the simulation results, moreover the simulated SPL level is higher than experimental ones. The lack of radiating boundary pressure conditions at the extremities of the pipe induces an overestimation of the internal SPL. Nethertheless, the turbulence velocity levels U_{rms} are correctly predicted in the downstream part of the corrugated channel.

Fig. 6 Comparison of U_{rms} and SPL with experiment
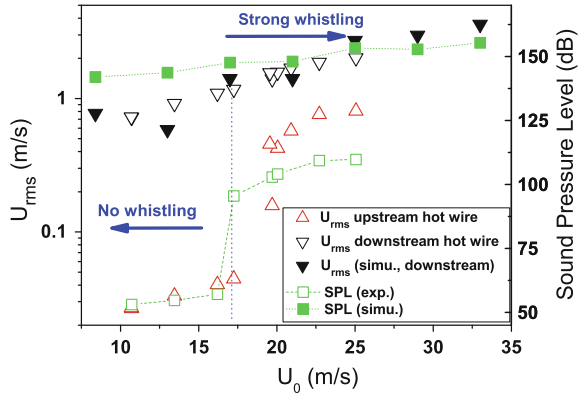
5 Conclusion–Perspectives

First 2D-computations are performed by using a LBM open source code (Palabos) to predict whistling in a corrugated channel under flow. Results from experiments performed in similar configurations are used for comparisons. Acoustic mode shapes are correctly predicted for the reference velocities. However the acoustic levels are overestimated due to acoustic boundary conditions that have to be improved. Perspectives are now to develop 3D-simulations for better prediction of turbulence and also parametric studies on the influence of corrugation geometry on the whistling.

References

1. Amielh M, Anselmet F, Jiang Y, Kristiansen U, Mattei PO, Mazzoni D, Pinhède C (2014) Aeroacoustic source analysis in a corrugated flow pipe using low-frequency mitigation. J Turb, 15(10), 650676
2. Buick JM, Greated CA, Campbell DM (1998) Lattice BGK simulation of sound waves. Enrophys Lett 43(3):235–240
3. Burstyn W (1922) Eine neue Pfeife (a new pipe). Z Tech Phys Leipzig, 3, 179180
4. Kristiansen UR, Wiik GA (2007) Experiments on sound generation in corrugated pipes with flow. J Acoust Soc Am 121, 1337–1444
5. Kristiansen U, Mazzoni D, Krogvig AB (2007) Aeroacoustic investigation of a flow pipe with a small cavity using the lattice Boltzmann method. In: Proceedings of the 35th scandinavian symposium on physical acoustics, Geilo, Norway (2012)
6. Howe MS (1998) Acoustics of fluid-structure interactions. Cambridge monographs on mechanics. University Press, Cambridge

7. Martinez DO, Matthaeus WH, Chen S, Montgomery DC (1994) Comparison of spectral method and lattice Boltzmann simulations of two-dimensional hydrodynamics. Phys Fluids 6:1285
8. https://equipex-mesocentre.univ-amu.fr/
9. Morris SC (2011). Shear-layer instabilities: particle image velocimetry measurements and implications for acoustics. Ann Rev Fluid Mech 43, 529–550 (2011)
10. Nakiboglu G, Manders HBM, Hirschberg A (2012) Aeroacoustic power generated by a compact axisymmetric cavity: Prediction of self-sustained oscillation and influence of the depth. J Fluid Mech, 703, 163–191
11. http://www.palabos.org
12. Petrie AM, Huntley ID (1980) The acoustic output produced by a steady airflow through a corrugated duct. J Sound Vib 70, 19
13. Qian Y, D'Humieres D, Lallemand P (1992) Lattice BGK models for navier-stokes equation. Europhys Lett 17(6):479–484
14. Tabeling P (2002) Two-dimensional turbulence: a physicist approach. Phys Rep 362:1–62
15. Xu H, Sagaut P (2011) Optimal low-dispersion low-dissipation LBM schemes for computational aeroacoustics. J Comput Phys 230:5353–5382

On the Connection Between Two Low-Frequency Instabilities Induced by the Flow Surrounding a Forward Facing Step at High Reynolds Number

A. Graziani, M. Lippert, D. Uystepruyst, L. Keirsbulck and F. Kerhervé

Abstract These last years, convoying covered trucks by railroad highways had improved our manner to transport freight supplies. However, this kind of transportation generate truck's tarpaulin breakout, forcing the train to stop until the problem is fixed. Instabilities induced by the separation of the flow facing the truck are mainly responsible for this phenomena. In such a context, the present paper focuses on the flow surrounding a forward facing step whose separated region is governed by complex dynamics which reproduce the aerodynamics involve on the truck's flapping tarpaulin. The dynamics of the low-frequency large-scale flapping motion and its connection with the dynamics of the flow just upstream of the step are investigated. The connection between the two recirculation regions and particularly more the influence of the upstream bubble on the downstream bubble shear layer is shown. The study suggests the importance of these mechanisms which can be key features for further flow control purposes.

A. Graziani (✉)
Institut de Recherche Technologique Railenium, 59300 Famars, France
e-mail: anthony.graziani@railenium.eu

M. Lippert · D. Uystepruyst · L. Keirsbulck
LAMIH CNRS, UMR 8201, Mont Houy, 59313 Valenciennes Cedex, France
e-mail: marc.lippert@univ-valenciennes.fr

D. Uystepruyst
e-mail: david.uystepruyst@univ-valenciennes.fr

L. Keirsbulck
e-mail: laurent.keirsbulck@univ-valenciennes.fr

F. Kerhervé
PPRIME CNRS, UPR 3346, Blv. Marie et Pierre Curie, 86962 Chasseneuil Cedex, France
e-mail: franck.kerherve@univ-poitiers.fr

1 Introduction

Rolling highway introduced as a greener transportation solution for merchandise being transported over long distances is currently under fast development. Transportation trucking is currently being pushed forward. On the aerodynamic side, one difficulty with this kind of convoying method is the truck's tarpaulin tearing, forcing the freight train to stop on the railway for safety reasons. In order to suggest technical solutions to alleviate the drawback induced by such tearing, it is first necessary to understand the aerodynamics phenomena which occur on the flow surrounding the train. The nature of the geometries involved in freight transport leads to divide the flow around a wagon in three main categories:

- Backward facing step flow.
- Forward facing step flow (hereafter FFS).
- Cavity flow.

The unsteady behavior of the flow over a FFS is the best candidate to understand the main mechanisms of the turbulence generated by the edges of the trucks, because it is identified as the worst configuration for tarpaulin tearing [3]. The flow topology is quite different from other studies because of the high sensitivity of the flow to a significant number of parameters [2]. As illustrated in Fig. 1a, two recirculation regions are formed respectively upstream and downstream the leading edge of the step. The first one is adverse pressure gradient induced (hereafter APG) by the vertical face which force the boundary layer to separate at $L_{R,Up} \simeq 1$–$1.2\,\mathrm{H}$ (where H is the step height) in front of the obstacle, and reattachs on the step at $h_R \simeq 0.6\,\mathrm{H}$ [6]. The leading edge of the model generates a massive separation zone with a mixing length $L_{R,Down}$ highly dependent on the flow parameters $\frac{\delta}{H}$ and $\frac{L}{H}$ (where δ is the boundary layer thickness, and L the length of the step) [7], and isolated from the free stream by a high turbulent shear layer.
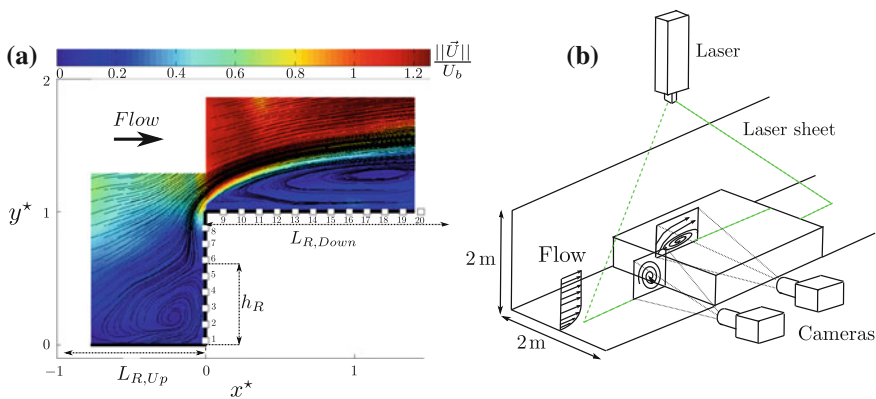
Fig. 1 **a** Streamlines and velocity magnitude, **b** PIV setup

The objective of this study is to identify the most energetic phenomena governing the flow behavior of the FFS for given flow parameters and which are also involve in the truck tarpaulin tearing. This work is also a first step for further flow control studies.

2 Experimental Setup

Measurements were conducted in the wind-tunnel facility of the LAMIH. The test section is a $2 \times 2\,m^2$ square duct of $10\,m$ length, with sides and top walls made in perspex for optical measurements. A 2D wood-made FFS is used and has been wall-mounted on a the side wall. The step height is $H = 0.166\,m$ and his length is $L = 0.5\,m$. To ensure a two-dimensional behavior of the flow, the model spans the entire wind-tunnel section (i.e.: $W = 2\,m$). The boundary layer thickness was measured at a distance of $l_{BL} = 9H$ upstream from the step to be sure that the APG had not influence on velocity profile. In this configuration, the boundary layer thickness to step height ratio, $\frac{\delta}{H} = 0.49 < 1$ and the step length aspect ratio, $\frac{L}{H} \simeq 3$ ensure a downstream reattachment length between 4 and $5H$ [7]. The Reynolds number of the flow, based on the step height is $R_e = \frac{U_b.H}{\nu} \simeq 10^5$ where $U_b = 10\,m/s$ is the freestream velocity and $\nu = 1.47 10^{-5}$ is the air's kinematic viscosity.

Particle Image Velocimetry (PIV) and wall-pressure measurements were performed simultaneously. Unsteady flush-mounted pressure sensors (type Kulite) were used for pressure surveys along the step. As illustrated in Fig. 3a, 8 sensors are located on the front side of the step while 12 sensors are regularly distributed over the step. The probes operate at a sampling frequency $f_{WP} = 10\,kHz$ which is here found sufficient to cover the entire frequency range of interest. A 8th order Bessel's anti-aliasing filter with a cut-off frequency $f_c = 3\,kHz$ is implemented to remove the unwanted noise.

The PIV setup (Fig. 1b) is composed with two high definition CCD cameras ($2048 \times 2048\,pixels^2$) and a double pulsed ND:YAG laser operating at a wave length $\lambda_{Piv} = 532\,nm$. The PIV snapshots are sampled at $f_{PIV} = 7\,Hz$. The size of the final interrogation windows is 16×16 pixels with 50% overlap,leading to a final spatial resolution of the vector fields of $124.06\,\mu m/pixels$ on **x** and **y** direction!. The time between two frames is $dt = 10\,\mu s$. A Nyquist grid coupled to a direct cross-correlation algorithm is used to compute the 2000 vector fields [5].

An external trigger is used to synchronise both the PIV snapshots and wall-pressure signals.

3 Results and Discussion

This section focuses on the results related with the link phenomenon between both upstream and downstream recirculation regions.

3.1 Dynamic Behavior

The premultiplied energy spectra of the wall-pressure probes located on the front side of the step are reported in Fig. 2a, b for the probes located above the step. The Strouhal number, $St = f \frac{L_{R,Down}}{U_c}$, is based on the downstream separation length $L_{R,Down} = 5\,H$ and the velocity of the free stream on top of the step $U_c = 10.90\,\text{m/s}$. On the front side, only one low-frequency peak appear, around $St \simeq 0.1$, from sensors 5 to 8, potentially linked to the flapping of the upstream recirculation region. Above the step, while the low frequency peak is still manifest, at $St \simeq 0.12$ corresponding to the flapping motion of the downstream bubble, a second frequency peak emerges as we move downstream from the edge. The second peak ($St_{KH} \simeq 3.5$) corresponds to Kelvin-Helmholtz instability which further downstream degenerates into a wide-band vortex shedding ($St_{VS} \simeq 0.6 - 0.8$) [4].

3.2 Complementary Technique Analysis

The wall-pressure sensors only give a limited amount of information on the flow dynamics over the step. In the meantime, the sampling frequency of the PIV snap-
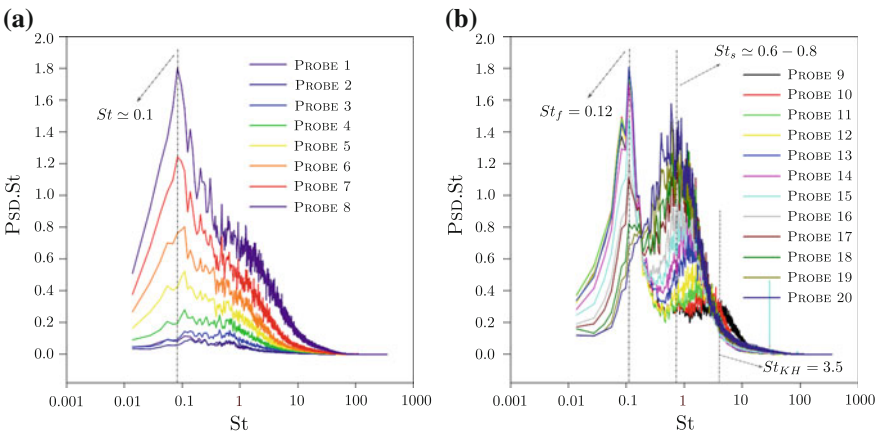
Fig. 2 PSD: **a** Upstream region, **b** Downstream region
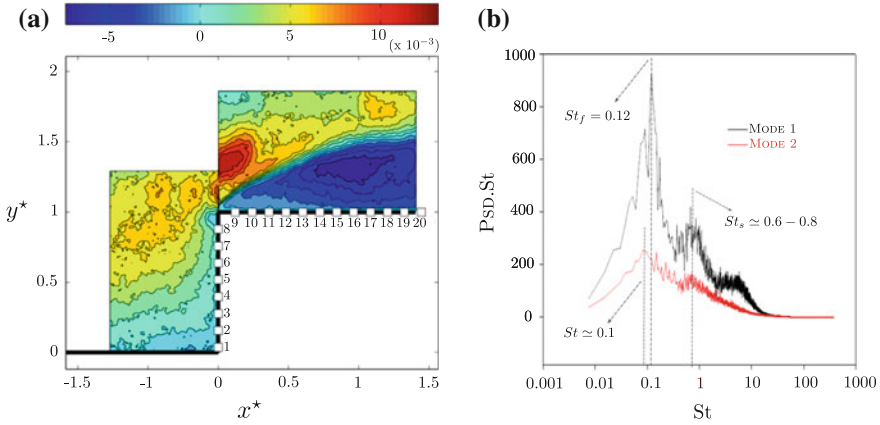
Fig. 3 Pod: **a** Spatial mode 2, **b** PSD of modes 1 and 2

shots is far below the frequencies of interest identified previously. We thus propose to use here the complementary technique originally introduced by Bonnet et al. [1]. This technique combines Proper Orthogonal Decomposition (POD) and Linear Stochastic Estimation (LSE) and allows to obtain low-order and time-resolved estimate of the PIV data from time-resolved point informations only, here the wall-pressure measurements. POD is first applied to the PIV snapshots to extract spatial eigenfunctions and temporal coefficients associated to the most energetic "structures" of the flow field. A time-resolved estimates of the temporal coefficient is then obtained thanks to the LSE.

In the present case, the first spatial POD eigenfunction (not shown here) is found to be linked with strong activity in the region downstream of the edge only. In contrast, the second POD eigenfunction, reported in Fig. 3a, exhibit two large-scale structures, one associated with the recirculation bubble above the step, and one which connect the dynamics in the upstream region with that in the downstream region above the shear layer axis. Figure 3b shows the premultiplied energy spectra of the two first estimated temporal POD coefficients associated with the spatial eigenfunction described previously. For the first mode (black line), the two frequency peaks discussed in the previous section are retrieve, indicating that this mode is effectively associated with the dynamics of the flow above the step only. For the second mode (red line) only a single frequency peak is identified at $St \simeq 0.1$ which, according to wall-pressure spectra on the front side of the step, is associated with the low-frequency dynamics of the upstream recirculation bubble. A communication between the upstream and downstream regions is here manifest and the complementary technique allows to better appreciate which frequencies and scales are involved. Further investigation are necessary in order to understand how this connection is modified with regards to various parameters such as the Reynolds number or the aspect ratio $\frac{\delta}{H}$.

4 Concluding Remarks

The present work investigates the connection between the two recirculation regions formed by the flow surrounding a FFS at a given high Reynolds number. The complementary technique, which combines POD and mLSE is implemented. At this stage, large-scale highly energetic mechanism at low-frequency was identified as being responsible for the large scale motion of the recirculating bubbles. The effect of the Reynolds number and the geometry of the step on this mechanism are currently under investigations.

References

1. Bonnet JP, Cole DR, Delville J, Glauser MN, Ukeiley LS (1994) Stochastic estimation and proper orthogonal decomposition: complementary techniques for identifying structure. Exp Fluids 17(5):307–314
2. Bradshaw P, Wong F (1972) The reattachment and relaxation of turbulent shear layer. J Fluid Mech 52(1):113–135
3. Eaton J, Johnston J (1981) A review of research on subsonic turbulent flow reattachment. Am Inst Aeronaut Astronaut J 19:1093–1100
4. Fadla F (2015) Caractrisation exprimentale de la dynamique du décollement de couche limite induit par un gradient de pression adverse et un effet de courbure. PhD thesis
5. Keane RD, Adrian RJ (1983) Theory of cross-correlation analysis of PIV images. Appl Sci Res 49:191–215
6. Leclercq D, Jacob M, Louisot A, Talotte C (2001) 2001 Forward-backward facing step pair: aerodynamic flow wall pressure and acoustic characterization. Proceedings of the seventh AIAA/CEAS aeroacoustic conference vol 1249, pp 075113-1–075113-13
7. Sherry M, Jacono DL, Sheridan J (2010) An experimental investigation of the recirculation zone formed downstream of a forward facing step. J Wind Eng Ind Aerodyn 98(12):888–894

LES on a Pitching Airfoil: Analysis of the Lift Coefficient Unsteadiness

N. Guillaud, G. Balarac and E. Goncalvès

Abstract Large Eddy Simulations (LES) have been performed on a pitching NACA 0012 airfoil at the Reynolds number $Re_c = 2.10^4$. The influence of the reduced frequency is investigated, regarding the lift drop incidence delay in comparison with a static case. The initiation and the growth of a Leading-Edge Vortex (LEV) after the static stall incidence is highlighted for the highest reduced frequency cases. The lift drop incidence delay is mainly due to this LEV, which maintains a high lift coefficient level after the static stall incidence. The LEV seems to initiate at the static stall incidence and its life-time seems to be independent of the reduced frequency. As the reduced frequency increases, the LEV goes through higher incidences during its life-time and leads to a higher lift drop incidence delay. The reduced frequency influence on the instantaneous lift coefficient during the motion upstroke has also been studied. At upstroke beginning, a sinusoidal type behaviour due to alternating stalls from the trailing edge is put in evidence. Alternating stalls are then replaced by a fully turbulent flow for the lowest reduced frequency case whereas very few structures are observed at the rear part of the airfoil for higher reduced frequency cases. This leads to the loss of the lift coefficient sinusoidal type behaviour. It is replaced by a noisy signal for the lowest reduced frequency and by a smoothed signal for the higher reduced frequencies.

N. Guillaud (✉) · G. Balarac
Univ. Grenoble Alpes/CNRS, LEGI UMR 5519, 1209-1211 rue de la piscine,
38400 Saint Martin d'Hères, France
e-mail: Nathanael.Guillaud@legi.grenoble-inp.fr

G. Balarac
e-mail: Guillaume.Balarac@legi.grenoble-inp.fr

E. Goncalvès
ISAE-ENSMA/CNRS, Pprime UPR 3346, Téléport 2, 1 Avenue Clément Ader,
BP 40109, 86961 Futuroscope Chasseneuil Cedex, France
e-mail: Eric.Goncalves@ensma.fr

163

1 Context and Motivations

Dynamic stall phenomenon appears when flow incidence on an airfoil is time dependant. It differs from static stall phenomenon and is responsible for efficiency losses in various industrial cases (e.g. helicopter rotor dynamic, vertical axis hydrokinetic turbine). Due to its large application field and its complexity, it has been studied for decades (e.g. [3, 5]). A common case used to study the dynamic stall phenomenon is the pitching airfoil configuration where the airfoil incidence varies as $\alpha(t) = \alpha_m + \alpha_a \sin(2\pi f_0 t)$ where α_m is the mean angle, α_a the amplitude, f_0 the airfoil oscillation frequency and t the time. Previous studies showed that a key parameter is the reduced frequency $k_0 = \pi f_0 c / V_0$, where V_0 is the freestream velocity and c the airfoil chord length. The present study aims to better understand the influence of this parameter on the lift coefficient evolution.

2 Study Cases and Numerical Set up

A NACA0012 airfoil with a pitch axis located at 1/4-chord from the leading edge is used. The airfoil motion is that described in the Sect. 1 with $\alpha_m = \alpha_a = 10°$. Three reduced frequencies have been investigated: 0.025, 0.1 and 0.2. The chord length based Reynolds number is equal to 2.10^4. The mesh for the LES contains approximately 5 million cells, which allows to insure first cells smaller than 5 wall unit along the airfoil. Computations were performed using the YALES2 flow solver [6]. This code solves the low-Mach number Navier-Stokes equations for turbulent flows on unstructured meshes using a projection method for pressure-velocity coupling [1]. It relies on 4th-order central finite-volume schemes and on highly efficient linear solvers [4]. The Smagorinsky dynamic subgrid-scale model is used. To avoid rotor/stator interface, equations are expressed in a rotating frame and a rotating velocity condition is imposed at the inlet. The domain extension is equal to 30c around the airfoil and 0.5c in spanwise direction where periodic boundary conditions are imposed.

3 Results and Discussion

Figure 1 shows the phase averaged lift coefficient function of incidence for the three studied cases. The present study will focus on the upstroke, which is plotted in plain lines. Static airfoil case data are taken from [2]. With $k_0 = 0.025$, the obtained lift curve is comparable to that obtained with a static airfoil. This case could thus be considered as quasi-static. A lift drop incidence delay is observed for higher reduced frequency cases, this delay being higher when k_0 increases. Figure 2 shows the instantaneous lift coefficient function of a dimensionless time for the lowest and

Fig. 1 Phase averaged lift coefficient function of incidence
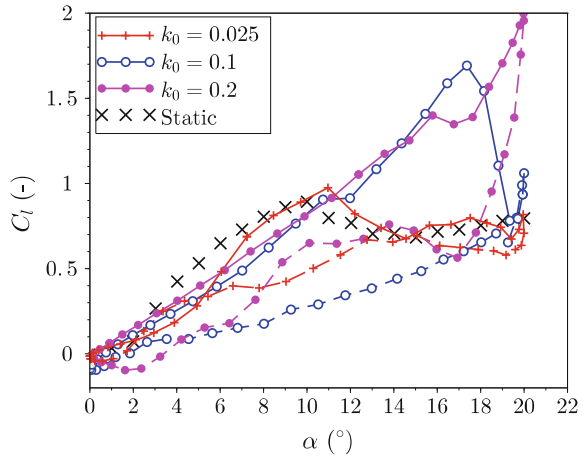
Fig. 2 Instantaneous lift coefficient function of a dimensionless time
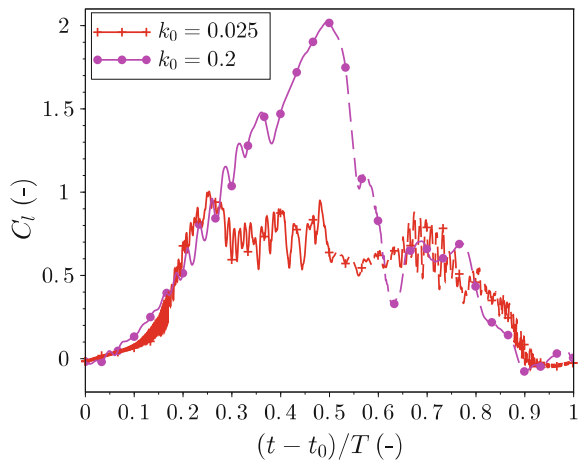
the highest reduced frequency cases (T is the pitching period). The case $k_0 = 0.1$ provides similar results to $k_0 = 0.2$ and has not been reported here. At the upstroke beginning, a sinusoidal type behaviour is observed for all cases. Then, depending on the reduced frequency value, the sinusoidal type behaviour is abruptly replaced by a noisy signal ($k_0 = 0.025$) or by a smoothed signal ($k_0 = 0.2$).

Two reduced frequency impacts on the lift coefficient have been highlighted: a drop incidence delay which increases with k_0 and a modification of the lift instantaneous behaviour. The following analysis aims to better understand these impacts.

3.1   Lift Drop Incidence Delay Analysis

To analyse the lift drop incidence delay, a local lift coefficient is employed. It is obtained by the integration of the dimensionless lift force on spanwise strips from the leading edge to the trailing edge. Each airfoil region contribution to the lift coefficient is thus quantified. Local lift coefficient amplitude function of airfoil incidence and position along airfoil suction side is depicted in Fig. 3. The leading edge and the trailing edge correspond to values of $x/c = 0$ and 1, respectively. Airfoil screen shots under colour maps show spanwise vorticity field around the airfoil for selected incidences. Lift repartition can thus be linked to flow topology. High lift level after the static stall incidence (10°) for medium and high reduced frequency cases is maintained by a vortex which initiate from the leading edge and grows along the airfoil. It is commonly named Leading Edge Vortex (LEV). The lift fall happens once the LEV is stalled into the wake. LEV stall occurs at higher incidence as the reduced frequency increases. Figure 4 shows the local lift coefficient function of time instead of incidence for medium and high reduced frequency cases. The time origin corresponds to 10° of incidence, i.e. at the initiation of the LEV. It shows that the lifetime of the LEV is independent of the reduced frequency. The medium and high reduced frequency case flow topologies at equal time intervals after 10° of incidence are similar, from the LEV commencement to its stall into the wake. It then takes the same time to the LEV to be stalled into the wake, but due to the difference of oscillation frequency, it represents a greater interval of incidence. Thus,

(a) $k_0 = 0.025$ (b) $k_0 = 0.1$ (c) $k_0 = 0.2$
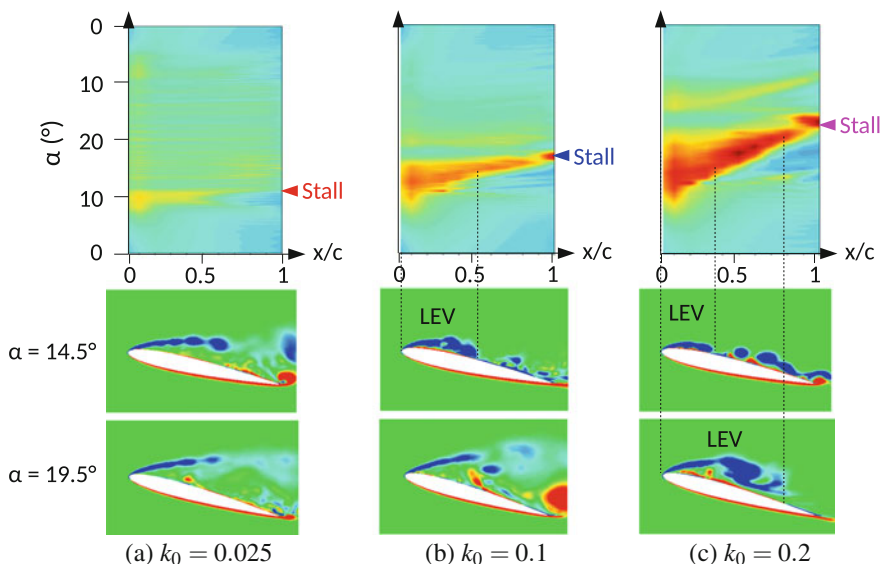
Fig. 3 On *top* local lift coefficient function of dimensionless position along airfoil suction side and incidence. *Below* airfoil mid-plane coloured by spanwise vorticity for different airfoil incidences
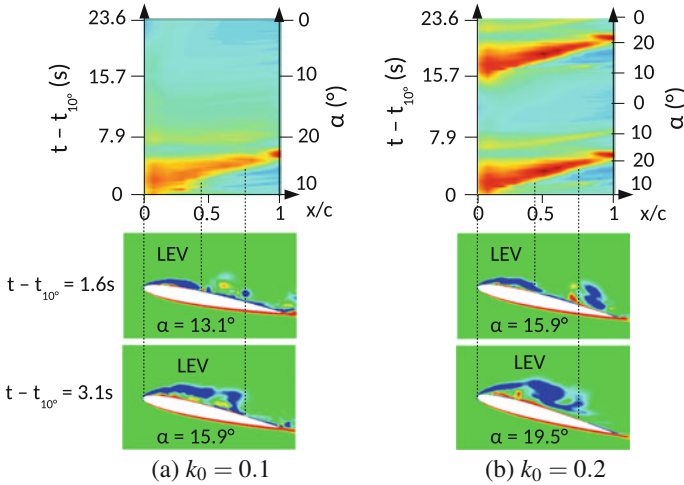
Fig. 4 On *top* local lift coefficient function of dimensionless position along the airfoil suction side and time starting at the initiation of the LEV. *Below* airfoil mid-plane coloured by spanwise vorticity for different times after static stall incidence

as the reduced frequency increase, the LEV goes through higher incidences during its life-time and leads to a higher lift drop incidence delay as the reduced frequency increase.

3.2 Lift Coefficient Instantaneous Evolution Analysis

Short-Time Fourier Transform (STFT) have been applied to the lift coefficient signal and to the spanwise vorticity signal at the airfoil trailing edge. Figure 5 depicts the frequency amplitudes function of dimensionless frequency and time for both signals. The obtained results are very similar. The lift coefficient sinusoidal type behaviour is due to alternating stalls from the trailing edge (cf. Fig. 6a). When airfoil incidence goes beyond a reduced frequency depending critical value, alternating stalls from the trailing edge disappear. There are replaced by a fully turbulent flow for the lowest reduced frequency case whereas very few structures are observed at airfoil rear part for higher reduced frequency cases (cf. Fig. 6b, c). This leads to the loss of the instantaneous lift coefficient sinusoidal type behaviour. It is replaced by a noisy signal for the lowest reduced frequency case and a smoothed signal for the higher reduced frequency cases. Further studies must be performed to know if the LEV is responsible for a gathering of the airfoil rear part structures and thus the smoothing of the lift coefficient signal.

(a) $k_0 = 0.025$, lift coefficient

(b) $k_0 = 0.025$, spanwise vorticity

(c) $k_0 = 0.2$, lift coefficient

(d) $k_0 = 0.2$, spanwise vorticity
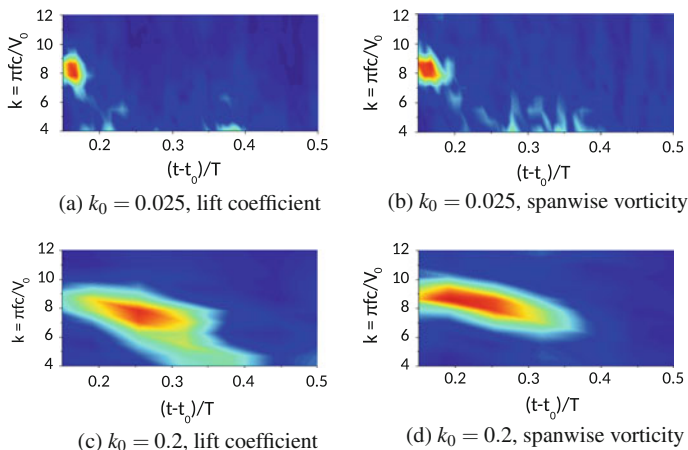
Fig. 5 Instantaneous lift coefficient and trailing edge spanwise vorticity signal frequency amplitudes obtain by STFT function of dimensionless frequency and time

(a) Low incidence for all cases

(b) High incidence before lift drop, $k_0 = 0.025$

(c) High incidenc before lift drop, $k_0 = 0.2$
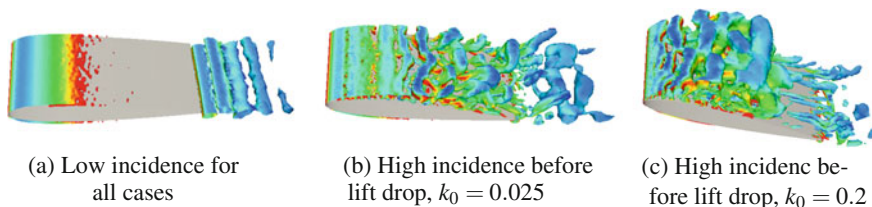
Fig. 6 Flow over the airfoil illustrated by isosurface of Q criterion coloured by vorticity magnitude

4   Conclusions

The present study goal was to better understand the reduced frequency influence on the lift coefficient evolution in a pitching airfoil configuration. A lift drop incidence delay is observed on highest reduced frequency cases. It is mainly due to a Leading Edge Vortex (LEV) which maintains a high lift coefficient level after the static stall incidence. The LEV seems to initiate at the static stall incidence and its life-time is independent of the reduced frequency. As the reduced frequency increase, the LEV goes through higher incidences during its life-time and leads to a higher lift drop incidence delay. Regarding the instantaneous lift coefficient evolution, a sinusoidal type behaviour due to alternating stalls from the trailing edge is observed at upstroke beginning. Alternating stalls are then replaced by a fully turbulent flow for the lowest reduced frequency case whereas very few structures are observed at the airfoil rear part for higher reduced frequency cases. This leads to the loss of the lift coefficient sinusoidal type behaviour. It is replaced by a noisy signal and a smoothed signal for the lowest reduced frequency case and the higher reduced frequency cases respectively.

References

1. Chorin AJ (1968) Numerical solution of the navier-stokes equations. Math Comput 22(104):745–762
2. Cleaver DJ, Wang Z, Gursul I (2010) Vortex Mode Bifurcation and Lift Force of a Plunging Airfoil at Low Reynolds Numbers. In: 48th AIAA aerospace sciences meeting. Orlando, Florida
3. Lee T, Gerontakos P (2004) Investigation of flow over an oscillating airfoil. J Fluid Mech 512:313–341
4. Malandain M, Maheu N, Moureau V (2013) Optimization of the deflated conjugate gradient algorithm for the solving of elliptic equations on massively parallel machines. J Comput Phys 238:32–47
5. McCroskey WJ (1981) The phenomenon of dynamic stall. NASA, California, USA, p 81264
6. Moureau V, Domingo P, Vervisch L (2011) Design of a massively parrallel cfd code for complex geometries. C R Mec 339:141–148

Assessment of Hybrid LES Formulations for Flow Simulation Around the Ahmed Body

E. Guilmineau, G.B. Deng, P. Queutey and M. Visonneau

Abstract This paper presents numerical simulations for the prediction of the flow around the Ahmed body, with the 25° and 35° slant angles, obtained with the flow solver ISIS-CFD. A RANS (Reynolds Averaged Navier-Stokes) turbulence model, as EARSM (Explicit Algebraic Stress Model) and two hybrid RANS-LES models, as DES (Detached Eddy Simulation) and IDDES (Improved Delay Detached Eddy Simulation) models, are used. All these turbulence models are based on the k-ω model. The use of a hybrid RANS-LES model, and more particularly the IDDES model, offers an advantage over RANS models in term of the force coefficients, and general flow field.

1 Introduction

The external aerodynamics of a car determines many relevant aspects of an automobile such as stability, comfort and fuel consumption at high cruising speed [6]. The flow around vehicles is characterized by highly turbulent and three-dimensional separations. There is a growing need for more insight into the physical features of these dynamical flows, on the one hand, and powerful numerical tools to analyze them on the other hand. Computations based on RANS equations are common in industry today. Although they are very successful in predicting many parts of the flow around a vehicle, they are unable to predict unsteadiness in the wake regions. The failure in predicting the base pressure is the major reason for large discrepancy in drag prediction between experiments and numerical simulations.

In an attempt to improve the predictive capabilities of turbulence models in highly separated regions, Spalart et al. [10] proposed a hybrid approach which combines

E. Guilmineau (✉) · G.B. Deng · P. Queutey · M. Visonneau
LHEEA, CNRS UMR 6598, Ecole Centrale de Nantes, 1 rue de la Noë, BP 92101,
44321 Nantes Cedex 3, France
e-mail: Emmanuel.Guilmineau@ec-nantes.fr

features of classical RANS formulations with elements of Large Eddy Simulations (LES) method. This concept has been termed Detached Eddy Simulation (DES) and is based on the idea of covering the boundary layer by a RANS model and of switching the model to a LES mode in detached regions. Compared to classical LES methods, DES save orders of magnitude of computing power for high Reynolds number flows, due to the moderated costs of a RANS model in the boundary layer region, but still offers some of the advantage of a LES method in separated regions. A variant of the DES model, like Improved Delayed DES, IDDES, seems to be attractive. The numerical simulations, with these turbulence models, are carried out with the ISIS-CFD flow solver.

The purpose of this paper is to conduct a validation of the flow around the Ahmed body [1] to compare RANS model and hybrid RANS-LES methodologies. Both the 25° and 35° slant back angles are investigated in this study to assess the capability of each turbulence model to capture the important changes in flow physics. The flow is at a Reynolds number of 2.8×10^6, based on the length of the model, L, and the upstream velocity $U_\infty = 40$ m/s.

2 ISIS-CFD at Glance

ISIS-CFD, developed by the Ecole Centrale de Nantes and CNRS and available as a part of the FINE/Marine computing suite, is an incompressible unsteady Reynolds-averaged Navier-Stokes (URANS) method. The solver is based on the finite volume method to build the spatial discretization of the transport equations. The unstructured discretization is face-based, which means that cells with an arbitrary number of arbitrarily shaped faces are accepted. A second order backward difference scheme is used to discretize time. The solver can simulate both steady and unsteady flows. The velocity field is obtained from the momentum conservation equations and the pressure field is extracted from the mass equation constraint, or continuity equation, transformed into a pressure equation. In the case of turbulent flows, transport equations for the variables in the turbulence model are added to the discretization. A detailed description of the solver is given by Queutey and Visonneau [9].

The solver features sophisticated turbulence models: apart from the classical two-equation k-ε and k-ω models, the anisotropic two-equation Explicit Algebraic Reynolds Stress Model (EARSM), as well as Reynolds Stress Transport Models, are available, see Duvigneau et al. [3] and Deng and Visonneau [2]. All these are RANS models. A Detached Eddy Simulation (DES) approach has been introduced, see Guilmineau et al. [5]. Recently, some modifications of this formulation proposed by Griskevich et al. [4] includes recalibrated empirical constants in the shielding function and a simplification of the original Spalart-Allmaras-based formulation. This new model is called Improved Delayed Detached Eddy Simulation (IDDES).

3   Numerical Simulation Set-up

The computational domain starts $2\,L$ in front of the model and extends to $5\,L$ behind the model. The width of the domain is $1.87\,m$ and its height is $1.4\,m$. These dimensions are recommended for the ERCOFTAC workshop on Refined Turbulence Modelling [8]. The mesh is generated using Hexpress, an automatic unstructured mesh generator. This software generates meshes containing only hexahedrals. For the surface of the car model and the floor, a no-slip boundary condition is used and the wall normal resolution is set $0.0007\,mm$, i.e. $y^+ \leq 0.7$. For the $25°$ slant angle, the mesh consists of 23.1×10^6 cells and the model is described by $384{,}090$ faces. For the $35°$ slant angle, the mesh consists of 22.2×10^6 cells and the model is described by $379{,}358$ faces.

For the RANS simulations, the time step is $\Delta t = 0.001\,s$ while with the hybrid RANS-LES models, the time step is $\Delta t = 2.5 \times 10^{-4}\,s$. With the RANS simulations, the numerical simulation converge to a steady flow while with the hybrid RANS-LES models the flow is unsteady and the averaging time, $t \times U_\infty/L$ is 40.

4   Results

4.1   35° Slant Angle

Figure 1 shows a comparison of the streamwise velocity in the symmetry plane for the Ahmed body with the $35°$ slant angle. The experimental profiles are those obtained by Lienhart et al. [7]. All turbulence models predict the correct flow, a fully separated flow, in the symmetry pane. The IDDES model gives a better agreement at the shear layer region.

(a) Over the slant   (b) In the wake

Fig. 1 35° slant angle—streamwise velocity on the rear slant and in the wake
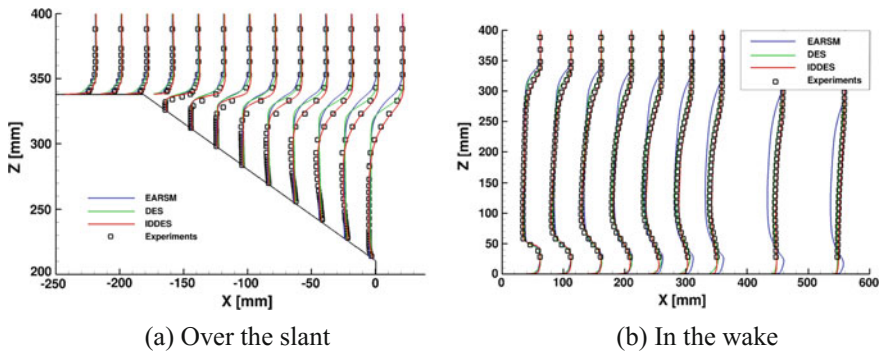
(a) Over the slant   (b) In the wake
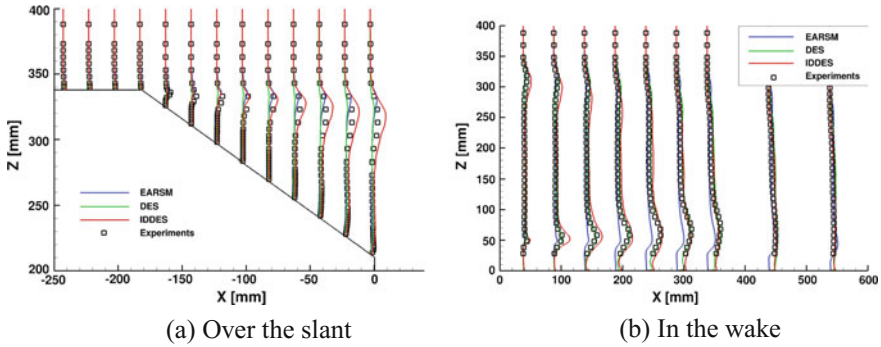
Fig. 2 35° slant angle—turbulent kinetic energy on the rear slant and in the wake

Table 1 35° slant angle—drag and lift coefficients

Model	C_D	C_L
EARSM	0.260	−0.039
DES	0.316	−0.015
IDDES	0.355	−0.014
Experiments [1]	0.256	n/a

Figure 2 presents the turbulent kinetic energy (TKE) in the symmetry plane. Each model gives a good agreement with the experimental data. At the shear layer, the IDDES model overpredicts TKE while the other models underpredict TKE. In the wake, a bette agreement with the experimental data is obtained with the hybrid RANs-LES models.

A comparison of the drag and lift coefficients is given in Table 1. The numerical results represent the total force, i.e. the force obtained on the model and the feet, while in experiments [1], it is only the model. For the lift coefficient, the value obtained with the EARSM turbulence model is lower than the values obtained with the hybrid RANS-LES models which give similar values.

4.2   25° Slant Angle

Figure 3 offers a comparison of the streamwise velocity in the symmetry plane for the Ahmed body with the 25° slant angle. The EARSM turbulence model fails to describe correctly the velocity field and overestimates the size of the recirculation region. The hybrid RANS-LES models provide an improved prediction. With the DES model, the separation covers the whole slant while, with the IDDES model, the reattachment point is located at X = 168 mm, from the upstream edge of the slant,

(a) Over the slant   (b) In the wake

Fig. 3 25° slant angle—streamwise velocity on the rear slant and in the wake
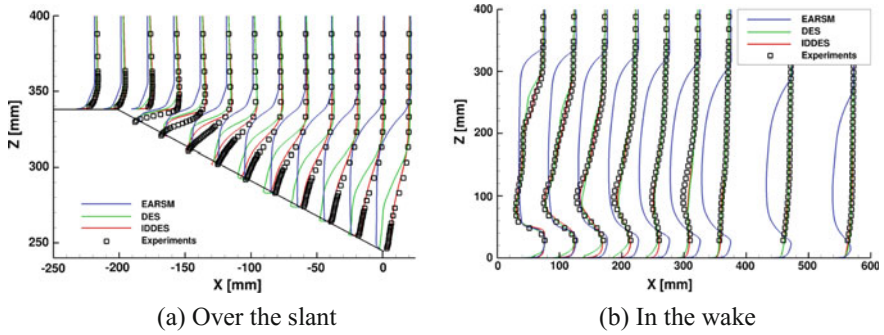
(a) Over the slant   (b) In the wake
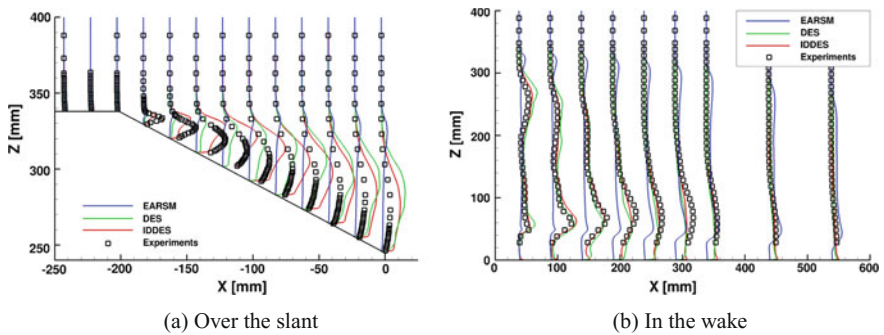
Fig. 4 25° slant angle—turbulent kinetic energy on the rear slant and in the wake

Table 2 25° slant angle—drag and lift coefficients

Model	C_D	C_L
EARSM	0.280	0.008
DES	0.437	0.376
IDDES	0.382	0.327
Experiments [1]	0.285	n/a
Experiments [12]	0.384	0.422

which is in good agreement with the experimental measurement of Thacker [11] for which the value is X = 160 mm.

A comparison of TKE is presented in Fig. 4. The TKE obtained with the EARSM turbulence model is underestimated on the slant which means less turbulent mixing and thus a greater recirculation region. With the hybrid RANS-LES models, TKE is larger than the values obtained with the RANS model. In the initial separated region, TKE predicted with the IDDES model is in good agreement with the experimental value.

Table 2 presents a comparison of the drag and lift coefficients. Compared to the previous slant angle, the drag and lift coefficients have increased. The drag coefficient is dependent to the turbulence model while the lift coefficient is similar for the hybrid RANS-LES model and higher than the value obtained with the EARSM turbulence model. If we compare the drag coefficient measured by Thacker et al. [12], the IDDES model gives the better agreement. However, the lift coefficient is underestimated.

5   Conclusions

In this paper, an investigation of RANS and hybrid RANS-LES models for the Ahmed car body at 25° and 35° slant angle cases has been conducted. It has been shown that the use of a hybrid RANS-LES model, in particular the IDDES model, offers an advantage over RANS model in terms of the force coefficients and general flow field, even for the 25° test case where the reattachment of the flow is correctly predicted.

References

1. Ahmed SR, Ramm G, Faltin G (1984) Some salient features of the time-averaged ground vehicle wake. SAE World Congress, Paper No 840300
2. Deng GB, Visonneau M (1999) Comparison of explicit algebraic stress models and second-order turbulence closures for steady flow around ships. In: 7th symposium on numerical ship hydrodynamics, Nantes, France, pp 4.1–4.15
3. Duvigneau R, Visonneau M, Deng GB (2003) On the role played by turbulence closures in hull ship optimization at model and full scale. J Mar Sci Technol 8:11–25
4. Gritskevich MS, Garbaruk AV, Schütze J, Menter FR (2012) Development of DDES and IDDES formulations for the k-ω shear stress transport model. Flow Turbul Combust 88:431–449
5. Guilmineau E, Deng GB, Wackers J (2011) Numerical simulation with a DES approach for automotive flows. J Fluids Struct 27:807–816
6. Hucho WH (1998) Aerodynamics of road vehicles. SAE International
7. Lienhart H, Stoots C, Becker S (2000) Flow and turbulence structures in the wake of a simplified car model (Ahmed model). In: DGLR fach symposium der AG STAB, Stuggart University
8. Manceau R, Bonnet J (eds) (2002) 10th joint ERCOFTAC/IAHR/QNET-CFD workshop on refined turbulence modelling
9. Queutey P, Visonneau M (2007) An interface capturing method for free-surface hydrodynamic flows. Comput Fluids 36:1481–1510
10. Spalart PR, Jou W, Strelets M, Allmaras S (1997) Comments on the feasibility of LES for wings and on a hybrid RANS/LES approach. In: Liu CZ (ed) 1st AFOSR international conference on DNS/LES, Advances in DNS/LES. Greyden Press
11. Thacker A (2010) Contribution expérimentale à l'analyse stationnaire et instationnaire de l'écoulement à l'arrière d'un corps de faible allongement. PhD thesis, Université d'Orléans
12. Thacker A, Aubrun S, Leroy A, Devinant P (2012) Effects of suppressing the 3D separation on the rear slant on the flow structures around the Ahmed body. J Wind Eng Ind Aerodyn 107–108:237–243

Numerical Properties and GPU Implementation of a High Order Finite Volume Scheme

J.-M. Le Gouez and J.M. Etancelin

1 Introduction

We present the main features of a spatially high order Finite Volume scheme for compressible fluid flows. This scheme is based on a polynomial reconstruction by Weighted Least Squares of conservative variable only known from their cell averages. The subsequent projection of these polynomials on the interfaces to compute the integral of exchanged normal flux densities is extremely CPU efficient and does not make use of limiters. However it requires a very high memory throughput to reach the objective 4th order on irregular unstructured grid systems. The spatial resolution of the scheme in terms of grid wave numbers is verified from the spectrum of the integral operators representing linear convection and diffusion on unit squares meshed with a variety of triangles. The solver is then tested on the case of the viscous Taylor-Green vortex in the conditions of the High order CFD Workshop [1]. The GPU version of the code is used and systematic tests of strong and weak scalabilty are performed on a full hybrid cluster using up to 128 NVIDIA Tesla K20Xm. The full solution covering 20 time units for 1024^3 dofs per equation is obtained in only 8 h.

J.-M. Le Gouez (✉)
ONERA DMFN, Châtillon, France
e-mail: jean-marie.le_gouez@onera.fr

J.M. Etancelin
ROMEO HPC Center, University of Reims Champagne-Ardennes, Reims, France
e-mail: jean-matthieu.etancelin@univ-reims.fr

Fig. 1 Sketch of a stencil for
polynomial reconstruction
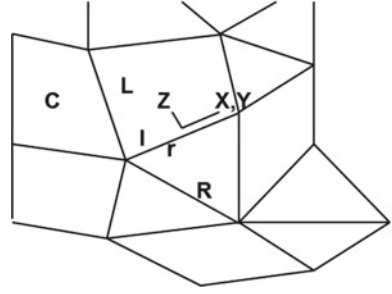
2 Higher Order Space Interpolation from Volume-Averaged Quantities

The scheme is based on a polynomial reconstruction of the conservative variables by
WLSQ, followed by a projection of these polynomials on the interface to compute
the fluxes.

In the local reference frame (X, Y, Z), centred on the c.o.g. of the cell L, we fit a
polynomial function of arbitrary order to the averages values of a field in the cells of
the stencil : $\varphi_a(X, Y, Z) = a_{\{ijk\}} X^i Y^j Z^k$, where $\{ijk\}$ is a unique index numbering
the momonials, combining i, j, k, and varying from 1 to n_{mo}. For accuracy reasons,
the working coordinates X, Y, Z are expressed in this local reference frame are also
non-dimensionalized by a reference cell size.

We want to minimize, over the stencil volume, the square of the distance between
the volume averages of the reconstructed polynomial field and the mean values in
the cells, each of volume $\Omega_{c(s)}$. The quantity $\bar{\varphi}_{c(s)}$ is an arbitrary distribution of
cell-averaged discrete values for the field φ. This distance is represented by the
functional :

$$\psi = \sum_{s=1}^{ns} \varpi_s \left(\Omega_{c(s)} \bar{\varphi}_{c(s)} - \int_{\Omega_{c(s)}} \varphi_a(X, Y, Z) dV \right)^2 \tag{1}$$

A number of supplementary free parameters are represented by arbitrary coefficients
(weights between 0 and 1) ϖ. These are decreasing values in each cell as a function
of the distance to the center of the stencil, like Gaussian functions $\varpi(d) = e^{-\alpha \frac{d^2}{h^2}}$ with
h some parameter related to the cell sizes, and α of the order of 0.3.

The functional is of quadratic form with positive coefficients of the coefficients
of the polynomial, and it is linear in the quantities $a_{\{ijk\}} \bar{\varphi}_{c(s)}$ that arise from the cross
products. A global minimum is found by expressing, for each monomial coefficient:

$$\frac{\partial \psi}{\partial a_{\{ijk\}}} = \sum_{s=1}^{ns} \varpi_s \left(-2\, \Omega_{c(s)} \bar{\varphi}_{c(s)} \mathfrak{R}_{c(s)}^{\{ijk\}} + 2\, \mathfrak{R}_{c(s)}^{\{ijk\}} \sum a_{\{i'j'k'\}} \mathfrak{R}_{c(s)}^{\{i'j'k'\}} \right) = 0$$

with $\mathfrak{R}_c^{\{ijk\}} = \int\limits_{\Omega_c} X^i Y^j Z^k dV$ the volume moment of order $\{ijk\}$ of each cell. This provides a linear system that links the vector of coefficients $A = \left[a_{\{ijk\}}\right]^T$ to the vector of cell-average values of the field $\bar{\varphi}_S = \left[\bar{\varphi}_{c(s)}\right]^T$. We solve then this linear system on the stencil :

$$\text{P } A = \text{M } \bar{\varphi}_S ==> A = \text{P}^{-1} \text{ M } \bar{\varphi}_S = \kappa \ \bar{\varphi}_S \tag{2}$$

This represents the reconstruction phase, where the array κ is computed that expresses that the coefficients of the polynomial are each a linear combination of the discrete values of the field.

The projection phase can be done on a target such as a cell interface, gauss points, nodes, or a target cell of a fixed overset grid [2]. The pre-processor is further extended in the following way, for example for an evaluation of an average of the polynomial on the interface lr :

$$\widehat{\varphi}_{lr} = \frac{1}{S_{lr}} \int\limits_{\partial\Omega_{lr}} \varphi_a(X, Y, Z) dS = \frac{\int\limits_{\partial\Omega_{lr}} X^i Y^j Z^k dS}{S_{lr}} a_{\{ijk\}} = \widehat{v}_{\{ijk\}} a_{\{ijk\}} \tag{3}$$

The average components of the gradient on the interface can be expressed in the same way:

$$\vec{\nabla}\widehat{\varphi}_{lr} = \frac{1}{S_{lr}} \int\limits_{\partial\Omega_{lr}} \vec{\nabla}\varphi_a(X, Y, Z) dS = \frac{\int\limits_{\partial\Omega_{lr}} \vec{\nabla}(X^i Y^j Z^k) dS}{S_{lr}} a_{\{ijk\}}$$

$$\vec{\nabla}\widehat{\varphi}_{lr} = \frac{\int\limits_{\partial\Omega_{lr}} (iX^{i-1}Y^j Z^k \vec{e}_x + jX^i Y^{j-1} Z^k \vec{e}_y + kX^i Y^j Z^{k-1} \vec{e}_z) dS}{S_{lr}} a_{\{ijk\}} = \widehat{\vec{\eta}}_{\{ijk\}} a_{\{ijk\}}$$

$$\widehat{\vec{\eta}}_{\{ijk\}} = i\widehat{v}_{\{i-1jk\}} \vec{e}_X + j\widehat{v}_{\{ij-1k\}} \vec{e}_Y + k\widehat{v}_{\{ijk-1\}} \vec{e}_Z$$

From Eq. (2), $A = \left[a_{ijk}\right]^T$ being a linear combination of $\bar{\varphi}_S = \left[\bar{\varphi}_{c(s)}\right]^T$, we obtain the compact representation of the interpolation coefficients :

$$\widehat{\varphi}_{lr} = \widehat{v}_{\{ijk\}} a_{\{ijk\}} = \widehat{v}_{\{ijk\}} \kappa_{\{ijk\},c} \ \bar{\varphi}_c = \lambda_{lr} \bar{\varphi}_c$$

$$\vec{\nabla}\widehat{\varphi}_{lr} = \widehat{\vec{\eta}}_{\{ijk\}} a_{\{ijk\}} = \widehat{\vec{\eta}}_{\{ijk\}} \kappa_{\{ijk\},c} \ \bar{\varphi}_{c(s)} = \vec{\mu}_{lr} \bar{\varphi}_c$$

The linear interpolation coefficients λ et $\vec{\mu}$ are functions of the volume and surface moments of the cells and the interface, and of the choice of the polynomial basis. For the array P to be inverted, the stencil needs to be balanced according to the set of monomials. The condition number of this array measures the ability to represent a given order polynomial base over the retained stencil. The integral of the inviscid and viscous fluxes over the interface can be computed from the extrapolated and face averaged conservative values and their gradient.
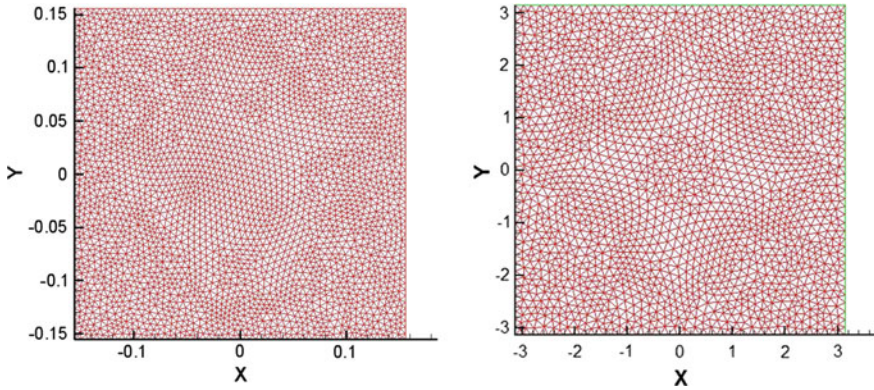
Fig. 2 Arbitrary triangle mesh of a unit square (by gmsh)

3 Resolution Properties of the Scheme

The spectra of the linear convection and linear diffusion operators obtained respectively with a constant convection velocity (inclined at Pi/6 with respect to the x-axis) and for a constant diffusion coefficient (Laplacian operator) are computed on a unit square meshed by triangles with different options in the gmsh grid generator, shown on Fig. 2. Periodic boundary conditions are retained. For the convective operator, the resolution in wave numbers is multiplied by a factor 3 by going from a linear reconstruction of the MUSCLE type to a 4th degree polynomial fitting, as shown on Fig. 3. Some eigenvectors of the two integral operators are represented on Fig. 4, mapped on the grid. It shows that these eigenvectors can be captured with a resolution of the order of 6 to 8 points per wavelength even on arbitrary triangles. To confirm this high resolution property of the scheme, we have computed the case of the TAYLOR-GREEN vortex at Reynolds 1600 with this compressible solver at Mach 0.1, in the conditions of the High Order CFD Workshop [1]. Rather than computing on a cartesian grid, we use here a grid made of anisotropic wedges, from a mesh of triangles of the plane x-y extruded in the z direction. A very good convergence with the grid size is shown on Fig. 5 and the entropy field at $t = 6$ is plotted for the computation with 512^3 dof per equation, with a fine resolution of flow details.

4 GPU Computing

The increasing popularity of GPU accelerated numerical simulations is mainly due to an architecture gathering thousands of cores. It provides high computational power and an intensive parallelism capabilities. One of main features of a GPU is an execution model based on a hierarchical structure which is directly linked to the hardware.
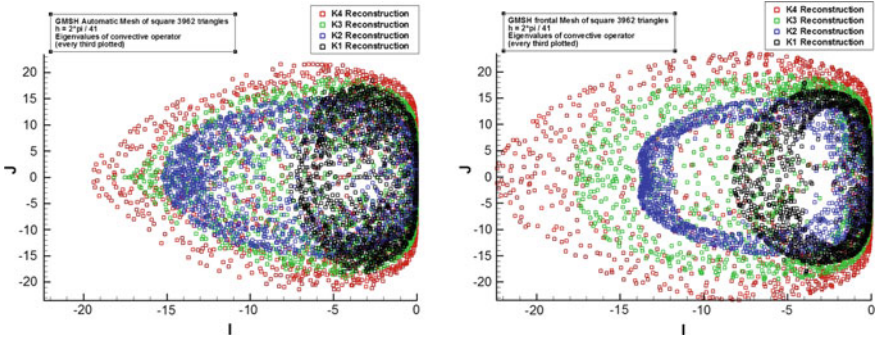
Fig. 3 Distribution of the eigenvalues of the convective operator on 2 types of meshes for different reconstruction degrees
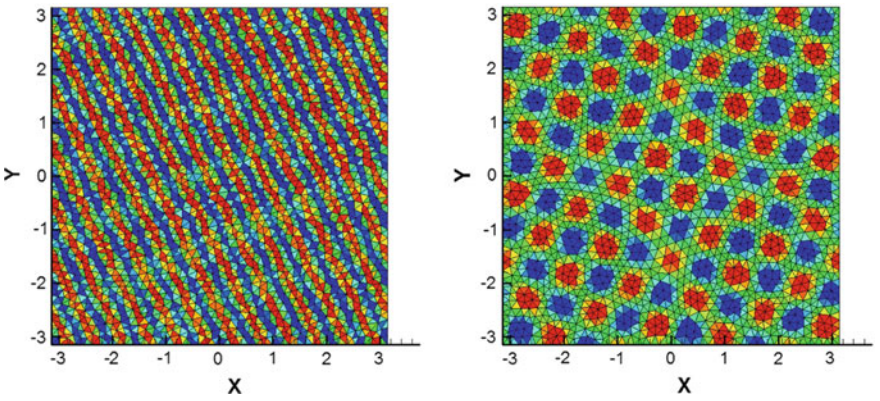
Fig. 4 Maping on the unstructured grid of typical high wave number eigenvectors for the convective and diffusive operators
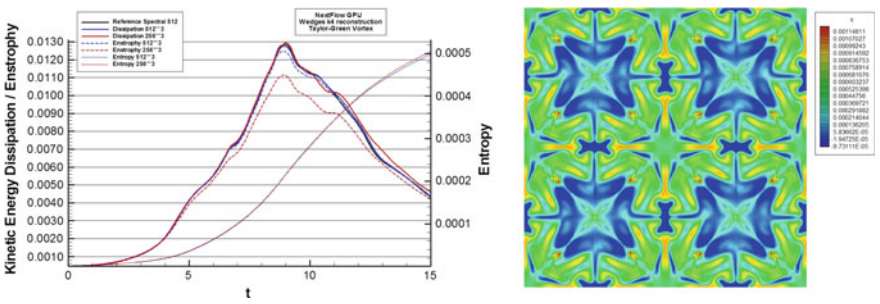
Fig. 5 TAYLOR-GREEN vortex 256^3 and 512^3 dofs per equation—Variation of the total Entropy, Enstrophy and Dissipation rate as a function of time—Plot of the entropy field on a slice at $t = 6$

At some levels, threads are sharing physical resources (registers, cache, memory, multiprocessor, …) that require a precise usage for high performance. An other key feature is the separation of the device and the host memory spaces. This is generally a strong bottleneck for applications performances since the data must be explicitly transferred between host and device through a bandwidth limited PCI-Express bus. Like many numerical methods, finite volumes schemes are quite well adapted to GPUs since the same computations are repeated on every mesh elements.

This current implementation rely on a 2D mesh extruded along the third space direction that enables wide vectorization on both CPU and GPU architectures. The CUDA execution model is mapped to the mesh so that the grid of blocks is covering the 2D part and the threads of each blocks are handling the elements of the transverse direction. Data are organized as structures of arrays that enable coalescent access along the threads in order to maximize memory bandwidth. Careful investigations on limiting registers usage and shared memory allocations enable us to get the best tradeoff between occupancy and performances. We exploit the Thrust library to manage lists of element indices to resolve most of conditionals branches at compile time using templated kernels.

Coarse level of parallelism is achieved by a domain decomposition of the 2D mesh. Because of the stencil scheme, the computations of elements located on sub-domains edge require non-local data that must be copied from from neighbours sub-domains. We use a *GPU-aware* MPI implementation (MVAPICH2 [3]) that simplifies and optimizes the communications of data located in devices memories. This implementation also take advantage of the NVIDIA GPUDirect technology for multi-GPU systems with InfiniBand networks. The most significant performance improvement was obtained thanks to asynchronous CUDA streams that enables an overlapping of the MPI non-blocking communications by computations. The sub-domains handled by each GPU are further divided into an internal and a near-edge parts. Therefore, these two parts are independant since internal elements computations do not depend on exchanged data. In practice, internal elements can be computed while near-edges data are exchanged through MPI. This overlapping gives us a significant improvement in computational times and enables high scalability results up to 128 NVIDIA K20Xm GPUs of the ROMEO HPC Center.

5   Performance Study

In this section we provide a performance analysis based on scalability and parallel efficiency measurements using from 1 to 128 GPUs. Each one is characterised by 6.1 GBytes of main memory and 896 double precision cores.

First, we perform an extensibility analysis when increasing the number of GPU for each fixed mesh size. These strong scalability results are shown on Fig. 6 where several meshes sizes from 128^3 to a billion of elements are solved.
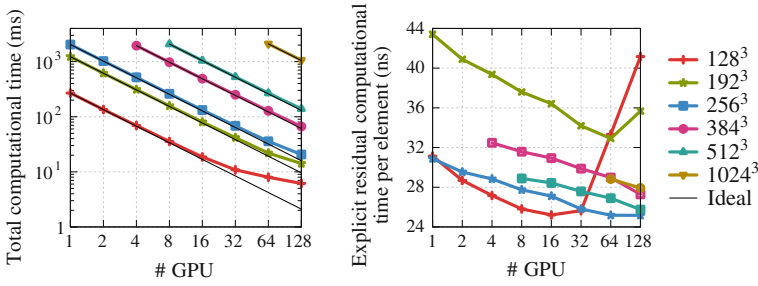
Fig. 6 Strong scalability of 10^3 iteration of a Taylor-Green Vortex simulation for different meshes
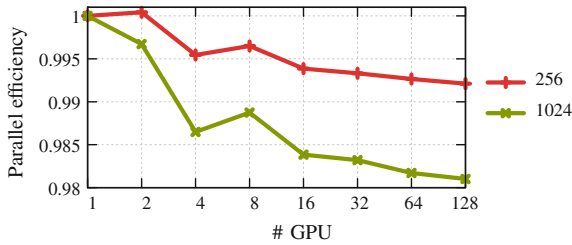
Fig. 7 Parallel efficiency on Taylor-Green Vortex simulation configured for 22 million of elements per GPU with different discretization in the transverse direction using more than 5.8 GB per GPU

As expected, we observe a perfect linear decrease of the computational time with respect to the increase of resources. The scaling start to slow down for small configurations (less than 256^3 elements) that are not adapted to large amount of resources. This under-utilization of the GPUs lead to the sharp rise of computational time per mesh element on the right Fig. 6. The time to compute a flux balance (RHS) at order 4 on one cell is below 30ns in most cases, i.e. one explicit time step with 4 R-K stages on 22 million cells (the maximum that can be stored on one K20Xm) takes 2.6 s of wall clock time. With a weak scalability study, we get rid of under-utilization by keeping a constant work load per GPU. The aim is to measure the impact of communications on the overall computational time. As show on Fig. 7, we obtain more than 98% of efficiency up to 128 GPUs. In these cases, even if the communications time is growing, it remains hidden by internals computations.

6   Conclusion

A CFD solver for compressible flows that provides a high spatial resolution and is well adapted to the computation of transitionnal flows was ported to GPU and CPU clusters and optimized for HPC. As compared with the CPU implementation that uses OpenMP on each node and is automatically vectorized on long well-aligned vectors

in the 3rd dimension of space, we obtain a ratio in efficiency on the GPUs of 20 to 1 per socket (one Tesla K20Xm is 20 times faster than an Intel IvyBridge with 8 cores). It shows that for this type of solver that is memory-bounded, the access patterns and the bandwidth to the main memory are crucial. In a future work, we plan to increase the hardware exploitation by addressing some asynchroneous co-processing to the CPU during the GPU computations.

References

1. Wang ZJ et al (2012) High-order CFD methods: current status and perspective. Int J Numer Meth Fluids 00:1–42
2. Le Gouez JM (2016) High-order overset interpolation via weighted least-square polynomial reconstruction for finite volume CFD, 54th AIAA ASM, San Diego
3. Wang H, Potluri S, Bureddy D, Panda DK (2014) GPU-aware MPI on RDMA-enabled cluster: design, implementation and evaluation. IEEE Trans Parallel Distrib Syst 25(10):2595–2605

Assessment of Static and Dynamic Wall-Adapting Subgrid-Scale Models for Turbulent Channel and Square Duct Flows

Shahriar Mohammadi and Romuald Skoda

Abstract We present a detailed assessment of the accuracy and performance of four SGS models on two wall-resolved test cases, channel flow at $\mathrm{Re}_\tau =180$, and square duct flow at $\mathrm{Re}_\tau =300$, and 450. The choice of models is based on avoiding the shortcomings of static Smagorinsky model, such as global prescription of a single value as the model constant, lack of inherent near-wall damping behaviour, and inability to capture two-component/two-dimensional, transitional, or rotation-dominated flows. A localised dynamic Smagorinsky model Zang et al. [1] and two static wall-adapting models [2] and Sigma Nicoud et al. [3] are assessed. Moreover, a modified global dynamic procedure Hubert et al. [4] is applied to the Sigma model operator to eliminate the uncertainty in the choice of proper value for the model constant. The results of all test cases are compared with existing DNS databases.

1 Introduction

The eddy viscosity based turbulence models have been the most widely-adopted class of SGS models in simulation of academic and industrial flows for years. This is mainly due to numerical stability, low computational cost, and ease of implementation of these models. Although the static Smagorinsky model [5] has been proven to reproduce the main features of simple flow problems, it has certain drawbacks that will lead to inaccurate results for certain complex flows. Ad hoc prescription of a single model constant for the entire flow domain, dependence of the model constant on mesh resolution and flow regime, and the need for eddy viscosity damping at wall vicinity are some of the major drawbacks. Although Germano's dynamic procedure [6], often used together with the least-square minimisation routine proposed by Lilly [7], can remove some of the mentioned drawbacks, it has downsides of its own. In addition to increased cost of computation, it requires some form of averaging to avoid the dynamic constant becoming ill-conditioned; either averaging on the

S. Mohammadi (✉) · R. Skoda
Chair of Hydraulic Fluid Machinery, Ruhr University Bochum
Universitätsstraße 150, 44801 Bochum, Germany
e-mail: Shahriar.Mohammadi@rub.de

direction(s) of statistical homogeneity [6], along the flow trajectories calculated by solving additional transport/integral equations [8], or local averaging and excessive clipping of large negative values of computed constant [1], with the latter being the most widely-used procedure for simulations of complex industrial flows.

Wall-Adapting Local Eddy Viscosity (WALE) model, proposed by Nicoud and Ducros [2], has the advantage of inherent correct near-wall asymptotic behaviour, sensitivity to rotation rate, as well as the capability to capture transition, and laminarisation. However, although not to the extent of classic Smagorinsky model, WALE is also sensitive to the choice of its constant, and requires ad hoc constant-tuning [9]; besides, its operator fails to vanish in case of solid body rotation. Nicoud et al. presented an improved static model [3] (abbreviated as SSig) based on the singular values of the filtered velocity gradient tensor to improve the performance of WALE at conditions such as solid body rotation, two-dimensional/two-component flow regions and axisymmetric expansion or contraction. Baya Toda et al. [10], Ben-Cheikh et al. [9], and Rieth et al. [11] reported that conventional dynamic procedures are not suitable for models with reformed eddy viscosity operators and lead to inferior accuracy, especially at the near-wall region, due to obstruction of the corrected behaviour of the model operators. Baya Toda et al. proposed modified dynamic procedures for WALE [10] and Sigma models [4], and showed in the respective publication that such procedures lead to improved accuracy compared to dynamic Smagorinsky model on channel flow test case. However, further assessments of such procedures have not been made on more complex flow problems.

The aim of the present study is firstly to investigate any possible improvement by SSig compared to WALE, and secondly if the proposed modified dynamic procedure for Sigma model (abbreviated as DSig) yields more accurate results than the widely-used Localised Dynamic Smagorinsky model (hereafter abbreviated as LDS). In addition to channel flow, square duct flow was chosen as a more complex test case for these assessments. Turbulent flow through non-circular conduits is considerably anisotropic, and existence of mean streamwise vorticity makes the problem interesting for turbulence modelling and model evaluation. Moreover, availability of DNS results for square duct flow makes it an ideal validation test case.

2   Subgrid-Scale Models

All the SGS models assessed in this study are algebraic and based on eddy viscosity assumption,

$$\nu_m = \left(C_m \overline{\Delta}\right)^2 \overline{\text{OP}}_m \tag{1}$$

where ν_m is the SGS viscosity, C_m is the model constant, $\overline{\Delta}$ is the width of a top-hat filter and is equal to cubic root of the cell volume, and $\overline{\text{OP}}_m$ is the operator of the model.

In the Localised Dynamic Smagorinsky model (LDS) [1] the operator is a function of the magnitude of strain rate,

$$\overline{OP}_S = \left| \overline{S} \right| = \sqrt{2 \overline{S}_{ij} \overline{S}_{ij}} \tag{2}$$

where $\overline{S}_{ij}$ is strain rate and is equal to the symmetric part of the filtered velocity gradient tensor, $\overline{S}_{ij} = \frac{1}{2} \left(\overline{g}_{ij} + \overline{g}_{ji} \right)$. The constant of this model is calculated using a dynamic procedure according to Lilly [7]:

$$C_S^2 = \frac{1}{2} \frac{\langle L_{ij} M_{ij} \rangle}{\langle M_{ij} M_{ij} \rangle} \tag{3}$$

where for LDS model $\langle \cdot \rangle$ stands for local averaging over the neighbour cells, and L_{ij} and M_{ij} are calculated as follows:

$$L_{ij} = \widehat{\overline{u_i u_j}} - \hat{\overline{u}}_i \hat{\overline{u}}_j \tag{4}$$

$$M_{ij} = \hat{\Delta}^2 \widehat{\overline{OP}_m} \hat{\overline{S}}_{ij} - \overline{\Delta}^2 \widehat{\overline{OP}_m \overline{S}_{ij}} \tag{5}$$

where overline stands for filter width equal to grid size, and caret for test filter. For LDS model $\overline{OP}_m$ is substituted by Eq. 2. In the dynamic localisation procedure large negative values of SGS viscosity are clipped such that

$$\nu + \nu_m \geq 0 \tag{6}$$

to ensure numerical stability, while allowing for small backscattering, when $-\nu \leq \nu_m \leq 0$.

WALE's operator [2] is constructed as:

$$\overline{OP}_W = \frac{\left(\overline{\mathscr{G}}_{ij}^{\text{dev}} \overline{\mathscr{G}}_{ij}^{\text{dev}} \right)^{3/2}}{\left(\overline{S}_{ij} \overline{S}_{ij} \right)^{5/2} + \left(\overline{\mathscr{G}}_{ij}^{\text{dev}} \overline{\mathscr{G}}_{ij}^{\text{dev}} \right)^{5/4}} \tag{7}$$

where $\overline{\mathscr{G}}_{ij}^{\text{dev}}$ is the deviatoric of the symmetric part of the square of filtered velocity gradient tensor,

$$\overline{\mathscr{G}}_{ij}^{\text{dev}} = \frac{1}{2} \left(\overline{g}_{ij}^2 + \overline{g}_{ji}^2 \right) - \frac{1}{3} \overline{g}_{kk}^2 \delta_{ij} \tag{8}$$

A model constant of $C_W = 0.325$ is assumed in this study.

The operator of Sigma model [3] is built using the singular values of the filtered velocity gradient tensor.

$$\overline{\mathrm{OP}}_\sigma = \frac{\sigma_3 \left(\sigma_1 - \sigma_2\right) \left(\sigma_2 - \sigma_3\right)}{\sigma_1^2} \tag{9}$$

with σ_i being the singular values of the filtered velocity gradient tensor, and $\sigma_1 \geq \sigma_2 \geq \sigma_3$. A model constant of $C_\sigma = 1.22$ is assumed in this study for the static variant of Sigma model (SSig). The dynamic procedure considered for Sigma model (DSig) is proposed by Baya Toda et al. [4]. This procedure makes use of global averaging, as in Eq. 3, over the entire computation domain, while the Sigma model operator is substituted in Eq. 5. The Shear and Vortex Sensor (SVS) inspired by the WALE model operator written in a dimensionless form,

$$\frac{\left(\overline{\mathscr{G}}_{ij}^{\mathrm{dev}} \overline{\mathscr{G}}_{ij}^{\mathrm{dev}}\right)^{3/2}}{\left(\overline{S}_{ij} \overline{S}_{ij}\right)^3 + \left(\overline{\mathscr{G}}_{ij}^{\mathrm{dev}} \overline{\mathscr{G}}_{ij}^{\mathrm{dev}}\right)^{3/2}} \tag{10}$$

is employed according to Baya Toda et al. [4]. The SVS, whose value varies between 0 and 1, gradually excludes the influence of the near-wall regions on the dynamically calculated constant with a correct near-wall asymptotic behaviour. The global constant is then calculated as

$$\left(C_\sigma^{\mathrm{dyn}} \Delta\right) = -\frac{\left\langle L_{ij} M_{ij} \right\rangle_{\mathrm{glob.\ SVS}}}{2 \left\langle M_{ij} M_{ij} \right\rangle_{\mathrm{glob.\ SVS}}} \tag{11}$$

where $\langle \cdot \rangle_{\mathrm{glob.\ SVS}}$ denotes a global averaging procedure, in which the sensor in Eq. 10 is employed as a weighting factor for contribution of each cell in the procedure, and M_{ij} is calculated using Eq. 5 with the operator being that of the SSig model.

3   Numerical Method and Computational Set-Ups

The computational domains of all test cases are designed at two mesh resolution levels (coarse and fine), mainly to obtain the convergence pattern of results with mesh refinement, and to investigate the effect of models' contribution through variation of filter width. A summary of the computational details of the test cases is presented in Table 1. Here x is considered as the streamwise, y as the normal, and z as the spanwise directions (See Fig. 1), and N stands for the number of grid points in each direction. Reynolds numbers Re_b and Re_τ are calculated using bulk velocity (u_b) and wall shear velocity (u_τ) as respective velocity scales, and length scales channel half-width (δ) for channel flow and duct hydraulic diameter (D) for square duct flow. The set-ups for the square duct flow at $\mathrm{Re}_\tau = 300$ consist of a cell number about 5%

Table 1 Summary of the computational details of the test cases

Case	Resolution	Re_τ	Re_b	$L_x \times L_y \times L_z$	$N_x \times N_y \times N_z$	$\Delta x^+ \times \left[\Delta y^+_{min}, \Delta y^+_{max}\right] \times \Delta z^+$	$t_{neglected}$	$t_{averaging}$
Channel	Coarse	180	2767	$2\pi\delta^{(a)} \times 2\delta \times \pi\delta$	$38 \times 24 \times 60$	$29.7 \times [1.8, 29] \times 9.42$	≈ 22 FTT^b	≈ 110 FTT
	Fine				$80 \times 66 \times 96$	$14.1 \times [0.6, 10.1] \times 5.9$		
Duct	Coarse	300	4410	$16\delta \times 2\delta \times 2\delta$	100×36^2	$24 \times [1.9, 5.9]^2$	≈ 20 LETOT^c	≈ 50 LETOT
	Fine				128×64^2	$18.7 \times [0.75, 3.5]^2$		
	Coarse	450	7000		140×54^2	$26 \times [3, 6.4]^2$		
	Fine				164×110^2	$20 \times [1, 4.2]^2$		

^{a}channel/duct half-width
^{b}flow-through time
^{c}large eddy turn-over time

Fig. 1 Coordinate system
and schema of duct geometry
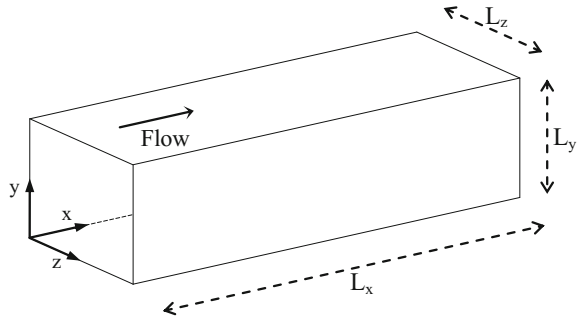
on the coarse mesh, and 20% on the fine mesh compared to the cell number simulated
by Zhang et al. [12] using direct numerical simulation. Our domains are however
significantly longer to ensure that the turbulence fluctuations are uncorrelated in the
streamwise direction.

For initialisation of simulations velocity fields are artificially generated using the
Filtered Noise method of Klein et al. [13]. Periodic boundary condition is applied in
the streamwise direction of both test cases. Spanwise ends of the channel domain are
of a boundary condition of the same type. Flow forcing is achieved using constant
flow rate prescription.

The finite-volume CFD library OpenFOAM 2.3.x is used to solve the implicit-
filtered incompressible Navier-Stokes equations. A second order central scheme is
employed to discretise the convective term. The temporal term is discretised using a
second order implicit scheme. Time steps are dynamically controlled using a maxi-
mum CFL criterion of 0.15 for channel flow and 0.2 for duct flow.

4 Results and Discussion

In this section the DNS results of Vreman and Kuerten [14] (hereafter DNS-VK)
are chosen for assessment of channel flow at $Re_\tau = 180$. For square duct flow at
$Re_\tau = 300$ and 450 the results of Pinelli et al. [15], computed using a pseudo-spectral
solver, are selected as reference (abbreviated as DNS1). Additionally, the recently
published square duct flow results of Zhang et al. [12] (abbreviated as DNS2), com-
puted using a finite-volume solver, are considered as a second reference for duct flow
at $Re_\tau = 300$.

4.1 Channel Flow

4.1.1 Velocity Profiles

Profiles of time-averaged streamwise velocity are obtained by averaging in stream-wise and spanwise directions, and presented in Fig. 2. Velocity scaling is done by wall shear velocity u_τ of each simulation. Wall-normal distance y^+ is normalised by ν/u_τ. For the sake of clarity the fine mesh results are shifted by 10 wall units in the ordinate direction. The coarse mesh results of all models are in fair agreement with DNS data, while a significant improvement is achieved with mesh refinement. The difference between the results of different models is minor and hardly distinguishable from the velocity profiles. In order to magnify these small differences the absolute deviations of models from DNS-VK data are calculated using piecewise cubic interpolation of the simulation results on a uniform grid and presented in Fig. 2. The DSig model shows the smallest deviation from DNS-VK data at both mesh resolution levels. This superior accuracy can be attributed to utilisation of a proper dynamic procedure, in which smoothing of the calculated constant is not achieved by systematic clipping of the constant values, while maintaining a proper near-wall behaviour. WALE also shows a good agreement with DNS results. This is mainly due to the inherent near-wall damping behaviour and the proper choice of model constant, which has been found to yield satisfactory results for a variety of flow problems, e.g. [16, 17]. SSig showed the largest deviation from the DNS data, which might be due to the chosen model constant in this study.
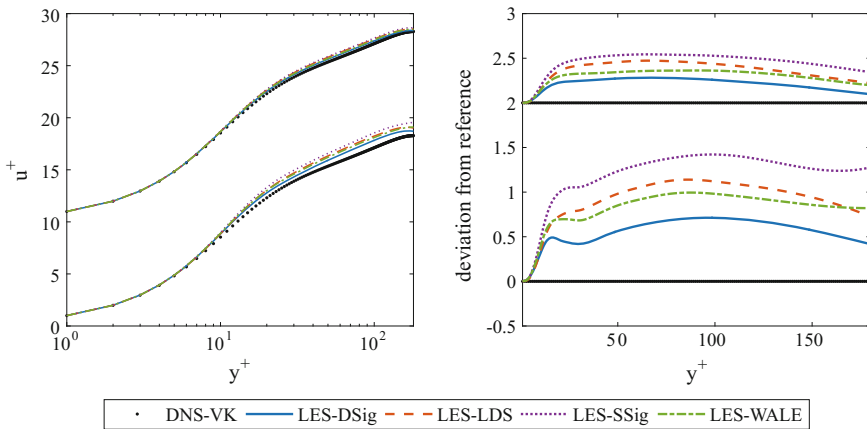
Fig. 2 *Left* Time-averaged streamwise velocity profile; *Right* Deviation from the DNS-VK data

4.1.2 Dissipation Rate Profiles

Since the dissipation budget of turbulence kinetic energy provides information about the amount of dissipation the SGS model brings about, it can be helpful in evaluation of models. Besides, accurate prediction of energy dissipation by SGS model leads to accurate prediction of Reynolds stresses. Therefore, a comparison of the calculated dissipation rates of the investigated models is shown in Fig. 3. These plots are presented in dimensionless form using u_τ^4/ν as the scaling factor and computed as sum of the resolved and modelled turbulence kinetic energy dissipation, $\varepsilon = -(\nu + \nu_m)\left|\overline{S}'\right|^2$, where $\left|\overline{S}'\right|$ is the magnitude of the time-averaged fluctuating strain rate tensor. Again, fine mesh results are shifted in the ordinate direction. As can be seen all LES models yield evident discrepancies on both mesh resolutions compared to DNS results, specially in the near-wall region. This is presumably the result of large numerical error of the employed low-order spatial discretisation scheme, and was found to be present even at DNS-level fine grids [18], although to a lesser extent. DSig results are slightly less deviated from DNS data up to $y^+ \approx 12$, after which point with increasing the distance from the wall the difference between LES models seems to become insignificant compared to the discrepancy between LES and DNS.

4.2 Square Duct Flow

Due to availability of reliable DNS results at $\mathrm{Re}_\tau = 300$, and 450 [12, 15], we have selected square duct flow at these Reynolds numbers for evaluation of the turbulence models. Validations of each of these results with the premier DNS simulation
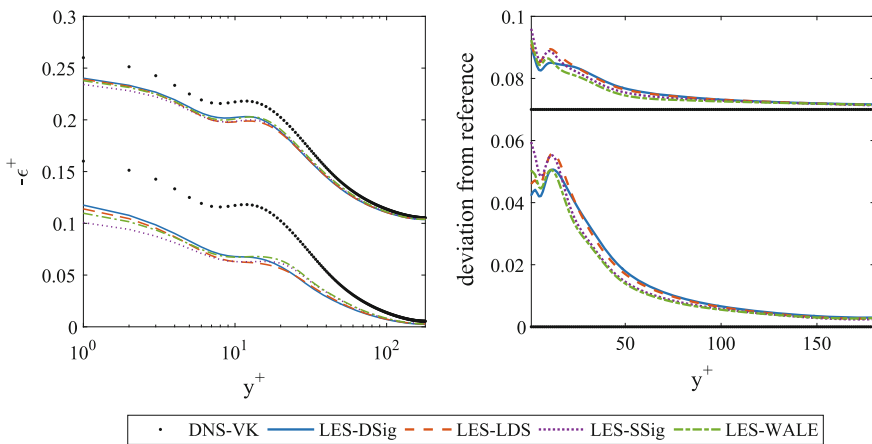
Fig. 3 *Left* Time-averaged dissipation budget of turbulence kinetic energy; *Right* Deviation from the DNS-VK data

by Gavrilakis [19] were performed by the corresponding authors in the respective publication. Both sets of data were acquired from the online databases [20, 21]. The calculated time-averaged LES results are averaged in the streamwise direction. Moreover, all four LES models' results, as well as the reference DNS data are averaged over the eight octants of the cross-section to eliminate any asymmetry of the velocity field.

4.2.1 Primary Flow Profiles

Profiles of time averaged primary velocity scaled by centre-line velocity (u_c), along the wall-bisector of the duct are plotted and presented in Figs. 4 and 5 for $\mathrm{Re}_\tau = 300$ and $\mathrm{Re}_\tau = 450$, respectively.

For both Reynolds numbers a satisfactory overall agreement is obtained by all models with respect to DNS results. Looking closely at the deviations of LES results from DNS data on the coarse grid at $\mathrm{Re}_\tau = 300$, near-wall velocity is underestimated by all models, with DSig showing the least deviation. With mesh refinement all models except for SSig produce near-wall results within the discrepancy of two DNS databases. In the wall-distant region however all LES models overestimate both DNS profiles, which do not seem to improve with mesh refinement. This overestimation is present for $\mathrm{Re}_\tau = 450$ on the whole length of wall-bisector and decreases slightly with mesh refinement. Since in the overestimated regions the difference between LES results is minor compared to deviation from DNS data, the source of persisting discrepancy can be assumed to be numerical error contamination.
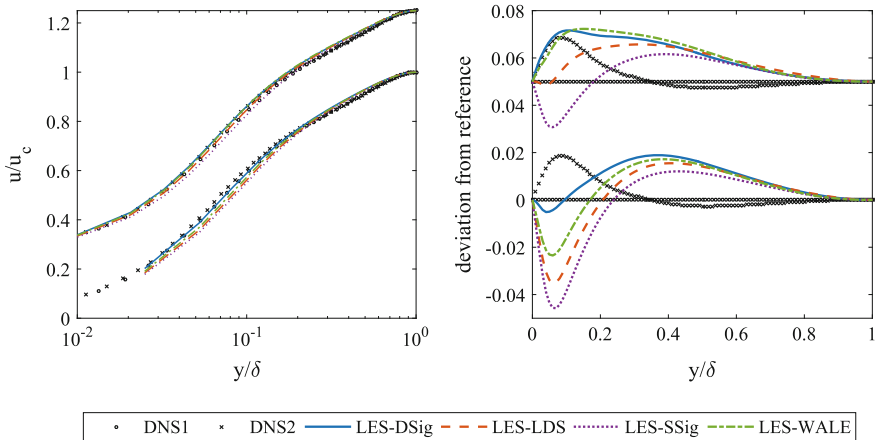
Fig. 4 *Left* Time-averaged primary velocity along the wall-bisector for $\mathrm{Re}_\tau = 300$; *Right* Deviation of the data from DNS1 reference. Fine mesh results are shifted in the ordinate direction for the sake of clarity
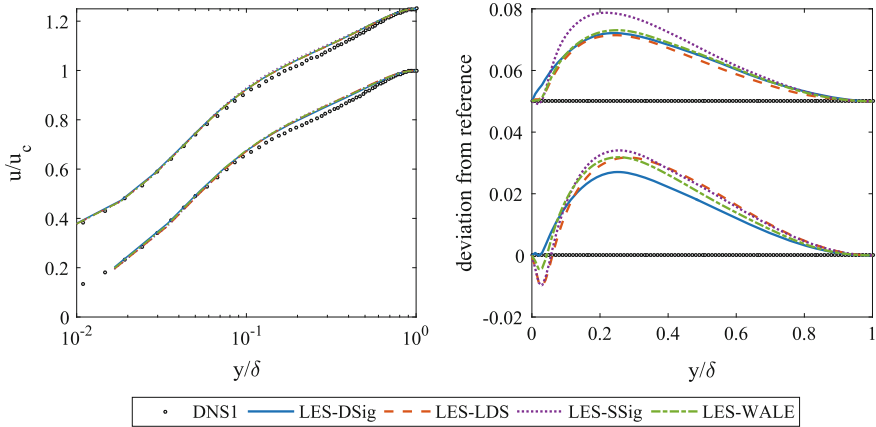
Fig. 5 *Left* Time-averaged primary velocity along the wall-bisector for $Re_\tau = 450$; *Right* Deviation of the data from DNS1 reference. Fine mesh results are shifted in the ordinate direction for the sake of clarity

4.2.2 Secondary Flow Profiles

In addition to the primary velocity, evaluation of secondary flow is of interest. The magnitude of secondary flow is calculated using the two cross-stream components, scaled by the bulk velocity (u_b), and is evaluated for LES results of different models and the reference DNS data, and presented in Figs. 6 and 7 for $Re_\tau = 300$ and 450,
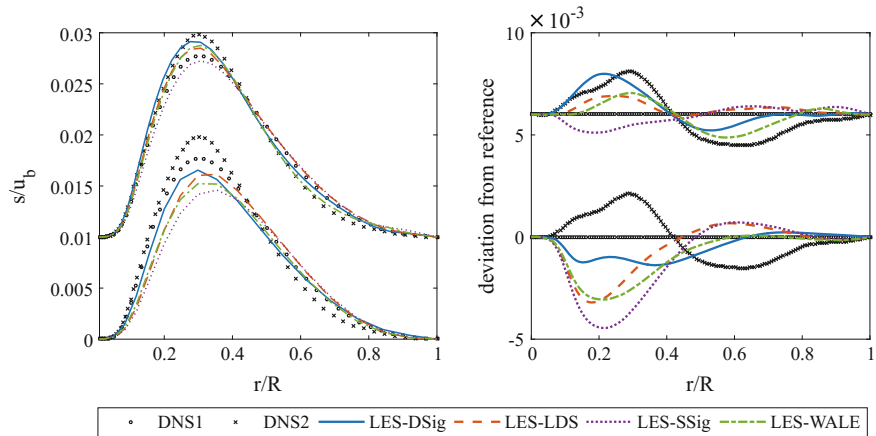
Fig. 6 *Left* Time-averaged secondary velocity magnitude on the corner-bisector for $Re_\tau = 300$; *Right* Deviation of the data from DNS1 reference. Fine mesh results are shifted in the ordinate direction for the sake of clarity
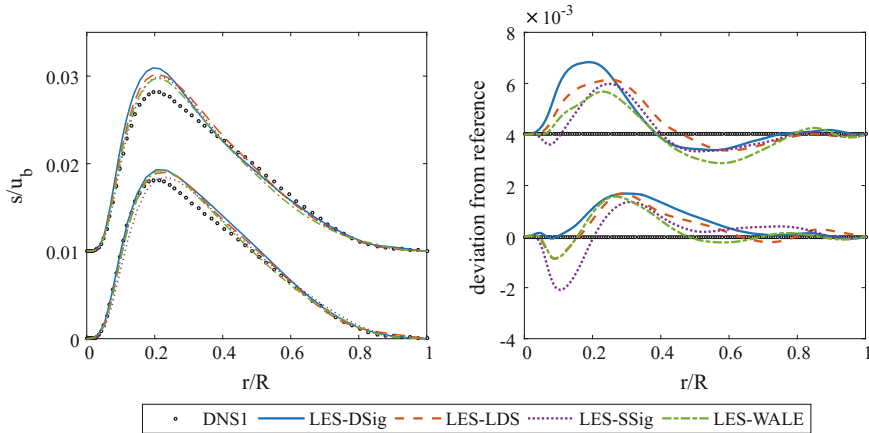
Fig. 7 *Left* Time-averaged secondary velocity magnitude on the corner-bisector for $Re_\tau = 450$; *Right* Deviation of the data from DNS1 reference. Fine mesh results are shifted in the ordinate direction for the sake of clarity

respectively. Corner-biscector of the duct is chosen as the abscissa, because the secondary flow magnitude exhibits a significant variation along the diagonal.

Noticeable for $Re_\tau = 300$ is the significant discrepancy between the two DNS data. For $Re_\tau = 300$ similar to primary velocity, secondary flow is underestimated by all models on the coarse mesh, and refining the mesh drives LES results into the discrepancy range of two DNS data. The deviation graphs demonstrate underestimation of the near-corner secondary flow on the coarse mesh by all models, with DSig displaying smallest deviation. On the fine mesh the LES results are in the discrepancy gap between two DNS data. For $Re_\tau = 450$ LES overestimates DNS1 maximum secondary flow magnitude, and deviations seem to worsen with mesh refinement.

5 Conclusions

Performance of static and dynamic wall-adapting SGS models are assessed using LES of turbulent channel and square duct flows. For the channel flow the adopted dynamic procedure for Sigma model [3, 4] showed the best agreement with DNS data. For duct flow it was generally observed that with mesh refinement the discrepancies between LES results become smaller compared to the deviation from DNS data. It is concluded that the deviations are dominated by numerical errors, rather than modelling errors. Several studies have reported that without any explicit filtering, numerical error of Large Eddy Simulation using low-order centred schemes tend to mask the contribution of SGS models, see for instance [22–24].

Considering the existing uncertainty between DNS results of duct flow, evaluation of models based on convergence to either one of the references is misleading, and

rather the scatter in DNS results must be taken into account. Performing a DNS using the same solver as the present study is planned by the authors to further clarify the contribution of numerical errors and make a sensible evaluation of SGS models. Nevertheless, it is important to realise that the comparison of primary and secondary velocity profiles presented for duct flow is entirely based on the profiles on a few individual sampling lines. A detailed comparison of the velocity field and higher order statistics are needed for evaluation of the accuracy of SGS models.

Despite the existing discrepancies, dynamic Sigma proves to rectify the uncertainty about the value of the model parameter of its static variant. In order to be able to reach a conclusive verdict about the accuracy of SGS models, further investigations of duct flow as well as extension of the assessments to more complex test cases are necessary.

References

1. Zang, Y, Street, RL, Koseff, JR (1993) Application of a dynamic subgrid-scale model to turbulent recirculating flows
2. Nicoud F, Ducros F (1999) Subgrid-scale stress modelling based on the square of the velocity gradient tensor. Flow Turbul Combust 62(3):183–200
3. Nicoud F, Toda HB, Cabrit O, Bose S, Lee J (2011) Using singular values to build a subgrid-scale model for large eddy simulations. Phys Fluids 23(8):085106
4. Hubert BT, Cabrit O, Truffin K, Gilles B, Nicoud F (2011) A Dynamic procedure for advanced subgrid-scales models and wall-bounded flows. In: 7th International Symposium on Turbulence and Shear Flow Phenomena
5. Smagorinsky J (1963) General circulation experiments with the primitive equations: I. The basic experiment*. Mon Weather Rev 91(3):99–164
6. Germano M, Piomelli U, Moin P, Cabot WH (1991) Cabot a dynamic subgrid-scale eddy viscosity model. Phys Fluids A Fluid Dyn (1989-1993), 3(7): 1760–1765
7. Lilly DK (1992) A proposed modification of the Germano subgrid-scale closure method. Phys Fluids A 4(3):633
8. Meneveau C, Lund TS, Cabot WH (1996) A Lagrangian dynamic subgrid-scale model of turbulence. J Fluid Mech 319:353–385
9. Ben-Cheikh N, Hammami F, Campo A, Ben-Beya B (2012) A dynamic sub-grid scale model for large eddy simulation of turbulent flows in a lid-driven cubical cavity. C R Mécanique 340:721–730 Oct
10. Baya Toda H, Truffin K, Nicoud F (2010) Is the dynamic procedure appropriate for all SGS model. In: V european conference on computational fluid dynamics, ECCOMAS, Lisbon, Portugal, pp 14–17
11. Rieth M, Proch F, Stein O, Pettit M, Kempf A (2014) Comparison of the sigma and smagorinsky LES models for grid generated turbulence and a channel flow. Comput Fluids 99:172–181 July
12. Zhang H, Trias FX, Gorobets A, Tan Y, Oliva A (2015) Direct numerical simulation of a fully developed turbulent square duct flow up to Reτ=1200. Int J Heat Fluid Flow 54:258–267
13. Klein M, Sadiki A, Janicka J (2003) A digital filter based generation of inflow data for spatially developing direct numerical or large eddy simulations. J Comput Phys 186:652–665 Apr
14. Vreman AW, Kuerten JGM (2014) Comparison of direct numerical simulation databases of turbulent channel flow at Reτ= 180. Phys Fluids 26(1):015102
15. Pinelli A, Uhlmann M, Sekimoto A, Kawahara G (2010) Reynolds number dependence of mean flow structure in square duct turbulence. J Fluid Mech 644:107 Feb

16. Montorfano A, Piscaglia F, Onorati A (2014) Wall-adapting subgrid-scale models to apply to large eddy simulation of internal combustion engines. Int J Comput Math 91:62–70 Jan
17. Fluent A (2012) 14.5, Theory Guide Inc., Canonsburg, PA
18. Komen E, Shams A, Camilo L, Koren B (2014) Quasi-DNS capabilities of OpenFOAM for different mesh types. Comput Fluids 96:87–104 June
19. Gavrilakis S (1992) Numerical simulation of low-Reynolds-number turbulent flow through a straight square duct. J Fluid Mech 244:101–129
20. http://www-cfd.ifh.uni-karlsruhe.de/uhlmann/home/report_2.html
21. http://www.cttc.upc.edu/downloads/DuctFlow/
22. Vreman B, Geurts B, Kuerten H (1994) Discretization error dominance over subgrid terms in large eddy simulation of compressible shear layers in 2d. Commun Numer Methods Eng 10(10):785–790
23. Ghosal S (1996) An analysis of numerical errors in large-eddy simulations of turbulence. J Comput Phys 125(1):187–206
24. Kravchenko A, Moin P (1997) On the effect of numerical errors in large eddy simulations of turbulent flows. J Comput Phys 131:310–322

Eulerian-Eulerian Large-Eddy Simulations in Bubble-Columns

Dimitrios Papoulias, Mohit Tandon, Andrew Splawski and Simon Lo

Abstract In this paper the Eulerian-Eulerian two-fluid model implemented in STAR-CCM+ is used to predict the turbulent mixing of a bubble-column flow. Calculations are performed using the Reynolds-averaged Navier-Stokes equations (RANS) and typical two-point turbulence closure models, as well as by means of large-eddy filtering techniques (LES), based on the Smalgorinsky subgrid-scale method (SGS). The bubble and fluid phases are coupled by integrating momentum exchange terms due to drag, lift and virtual-mass forces, while turbulent dispersion effects are also accounted. Validation of the multiphase Eulerian model is performed against available Laser Doppler Anemometry measurements (LDA), reported in the experimental work of Deen et al. (Chem Eng Sci 56: 6341–6349, 2001 [1]).

1 Introduction

Understanding the unsteady and stochastic behaviour of multiscale turbulence in bubbly-flows is a challenging task. Due to the obscure nature of the underlying physics, much of the knowledge in this field is gained by experimental research in basic flow arrangements. To this end, Rensen et al. [13] characterized the development of homogeneous shear turbulence in bubbly channel flows, by using hot-film probes. The findings of this study indicated that bubbles tend to reenergize the dissipative eddies through direct forcing, and smooth the velocity fluctuations of the bulk liquid inherited by the larger scales. Mazzitelli et al. [11] linked this effect—the reduction of

D. Papoulias (✉)
CD-adapco, 200 Shepherds Bush Road, London W6 7NL, UK
e-mail: dimitrios.papoulias@cd-adapco.com

M. Tandon
CD-adapco, Parakh House, 1 Boat Club House, Pune 4110010, India

A. Splawski · S. Lo
CD-adapco, Trident House, Basil Hill Road, Didcot OX11 7HJ, UK

the overall energy dissipation-rates—to the role of the lift force, by performing direct numerical simulations (DNS) and Lagrangian tracking of bubbles in homogeneous turbulence. According to these calculations, buoyant bubbles under the influence of lift appeared to transport increments of their momentum to nearby small-eddies, at the expense of residing in downflow zones. Clustering in high-vorticity zones was also sustained by microbubbles with sizes equivalent to the Kolmogorov length scales (η), which preferred to pair with small-eddies instead of migrating to low-pressure cores. Lance et al. [8] argued that large bubbles in channel flows act as inertial linkages between different eddy scales and therefore, instead of suppressing turbulence dissipation they essentially accelerate the energy cascade, depending also on their population size. This process appeared to be responsible for gradually scaling the slope of the classical power-law from $-5/3$ to $-8/3$, leading to a steeper energy decay of the high-frequency spectrum.

To a certain degree, experiments in turbulent bubbly flows have contributed to the development of moment-closures for multiphase Eulerian-Eulerian solvers. However, so far most of the existing turbulence models for fluid-particle flows are derived directly by analogy to single-phase turbulence models, following a phenomenological approach. To this extent, Hinze [7] and Tchen [17] developed a theory for modelling the in-phase and cross-phase turbulent diffusivities of isolated Stokesian particles, based on Lagrangian autocorrelation functions. Similar source-terms for the particle-induced production and dissipation of turbulence are also proposed by Gosman [6] and Troshko and Hassan [22]. Closure models for the turbulent dispersion of particles—the correlation between the instantaneous volume-fraction and fluid velocity fluctuations—are formulated in the work of Deutsch and Simonin [2], in terms of the Boussinesq hypothesis. Thai Van et al. [19] verified the aforementioned empirical closures in a variety of dilute bubble regimes. Despite the physically realistic prediction of macroscopic RANS models, several concerns have been raised regarding the realizability of this approach given the multiscale character of turbulent bubbly flows [4]. In order to provide a modelling framework which preserves the underlying flow processes of multiphase turbulence, Fox [3] and Tenneti et al. [18] derived moment-closures starting from a microscopic description of the problem, by means of high fidelity DNS calculations in gas-particle flows.

The predictive capabilities of the aforementioned closure techniques are evaluated in the forthcoming analysis, with the aid of an Eulerian-Eulerian multiphase model. For this purpose, unsteady RANS and LES calculations are performed in order to simulate the genesis and development of turbulence in a bubble-column flow. The calculated results are validated against experimental LDA measurements reported in [1]. The formulation of the utilized solution models is briefly described in the following sections.

2 Turbulence Modelling in Multiphase Flows

In the context of the Eulerian-Eulerian multiphase approach different flow phases are treated as interpenetrating continua, therefore the interacting fluids are allowed to coexist in time and space. This method requires the solution of a separate set of Navier-Stokes equations for each phase, in addition to several closure models for integrating physical sub-grid processes of the dispersed phase. The momentum coupling terms are essential in recovering information from the microscopic level of the flow, which is lost due to the time and volume averaging of the instantaneous conservation equations. The macroscopic realization of the basic equations governing the mass and momentum conservation of the flow phases is given below:

$$\frac{d\langle \alpha_i \rangle}{dt} + \nabla \cdot \langle \alpha_i \rangle \langle \mathbf{u}_i \rangle_i = 0 \tag{1}$$

$$\frac{d\langle \alpha_i \rangle \langle \mathbf{u}_i \rangle_i}{dt} + \nabla \langle \alpha_i \rangle \big(\langle \mathbf{u}_i \rangle_i \otimes \langle \mathbf{u}_i \rangle_i + \langle \mathbf{u}_i'' \mathbf{u}_i'' \rangle \big) = \langle \alpha_i \rangle \big(-\langle \nabla p \rangle_i + \nabla \langle \tau_i \rangle_i + \langle \sum \mathbf{F} \rangle_i \big) \tag{2}$$

In Eqs. 1 and 2 $\langle \phi \rangle$ and $\langle \phi \rangle_i$ represent the Reynolds and phase average of ϕ, where the latter is defined with respect to phase i. The different variables hosted in these expressions stand for the volume-fraction α, the velocity vector $\mathbf{u}$, the Reynolds stress tensor $\mathbf{u}'' \mathbf{u}''$, the pressure p, the viscous stress tensor τ and the body forces acting between the flow phases $\sum \mathbf{F}$. For the case considered in this study, the following force-balance is modelled:

$$\sum \mathbf{F} = F_D + F_B + F_L + F_{VM} + F_{TD} \tag{3}$$

The resultant force in Eq. 3 includes components due to drag F_D, buoyancy F_B, lift F_L, virtual-mass F_{VM} and turbulent dispersion F_{TD} effects. Typical correlations for calculating drag and lift forces in bubbly flows are formulated in the experiments of Tomiyama et al. [20, 21]. The latter contribution in Eq. 3, also known as drift velocity, is responsible for the redistribution of non-uniformities in the dispersed phase concentration due to turbulence. In RANS models it appears as the covariance between the fluctuations of the particle volume-fraction and the fluid phase velocity $\langle \alpha_p' \mathbf{u}_f'' \rangle$, terms which originate from the averaging of the drag force. Typically, this term is treated as a turbulent flux by means of the Boussinesq gradient [2].

Additional particle induced turbulent-fluxes are generated due to the work done by the drag force against the fluctuating fluid velocity [22]; $\tau_D \langle \alpha_p (\mathbf{u}_f - \mathbf{u}_p) \mathbf{u}_f'' \rangle$, where τ_D is the response time. Accordingly, a production source-term is inserted in the turbulent kinetic energy of the fluid S_k, while part of the extracted mean-energy is inherited to the dissipative scales S_ε in the form of an eddy-viscosity model [14].

Closure models are also required for the non-linear turbulent stresses $\mathbf{R}_{ij} = \langle \mathbf{u}_i'' \mathbf{u}_i'' \rangle_i$ in Eq. 2. The simplest approach for modelling this tensor is by means of an isotropic eddy-viscosity model:

$$- \langle \mathbf{u}_i'' \mathbf{u}_j'' \rangle = v_t \langle \mathbf{S}_{ij} \rangle - \frac{2}{3} k \delta_{ij}, \tag{4}$$

where $\mathbf{S}$ is the mean strain-rate tensor and δ the Kronecker delta. The underlying assumptions in Eq. 4 reduce the problem to two scalar-transport equations, one for the production-rate of turbulent kinetic energy (k) and one for its dissipation-rate (ε). To account for the directional sense of eddies, therefore preserve their anisotropy, the entire stress-tensor $\mathbf{R}$ is solved by employing a Reynolds-stress models (RSM):

$$\frac{D\mathbf{R}_{ij}}{Dt} = D_{ij} + P_{ij} + \Pi_{ij} + \Omega_{ij} - \varepsilon_{ij} \tag{5}$$

In Eq. 5 the total rate of change of turbulent stresses is balanced against diffusion (D), production (P), pressure-strain redistribution (Π) and rotation effects (Ω), while a part is also diffused (ε). The calculation of most of these contributions can be performed either directly (P, ε) or by using the standard gradient hypothesis (D), apart from the pressure-strain which requires modelling. For treating this model term, two alternative methods are employed; the model of Gibson and Launder [5] and the elliptic-blending approach proposed by Manceau and Hanjalic [10].

Despite the performance benefits of RANS models, the developing multiscale processes of dispersed flows often require resolution of the instantaneous flow-field by applying large-eddy simulation filters (LES). Based on the mixing-length hypothesis, Smagorinsky [15] suggested the following sub-grid eddy-viscosity model:

$$v_t = l_S^2 \mid \mathbf{S}_{ij} \mid = (C_S \Delta)^2 \mid \mathbf{S}_{ij} \mid, \Delta \approx \sqrt[3]{V_{cell}} \tag{6}$$

In Eq. 6 l_S is the Smagorinsky length-scale, C_S is a scaling constant and Δ is the size of the filter, which is usually assumed proportional to the mean cell-size $\sqrt[3]{V_{cell}}$.

Following the brief formulation description of turbulence closures for Eulerian multiphase models, the analysis proceeds with the evaluation of these techniques against documented experiments for a bubble-column flow. The simulation details and results of the undertaken parametric study are discussed in the next section.

3 Unsteady RANS and LES Calculations in Bubble-Columns

The parametric flow calculations presented in this study are collected in Table 1. In all cases, the adopted differencing schemes for integrating in space and time retained terms up to second-order [9]. For the discretization of the solution domain, a

Table 1 Parametric simulation cases; solution models and physical flow conditions

Case	Turbulence model	Spatial scheme	Temporal scheme	Grid size	Time step	Flow conditions
1	LES ($C_s = 0.1$)	2nd order bounded-CD	2nd order implicit Euler	720k structured hex-cells	0.001 s	$U_{bubble} = 0.12\,\frac{m}{s}$ $D_{bubble} = 4\,mm$ $\rho_{fluid} = 995\,\frac{kg}{m^3}$ $\nu_{fluid} = 10^{-6}\,\frac{m^2}{s}$
2	$k - \varepsilon$	2nd order upwind				
3	Linear RSM					
4	Elliptic RSM					
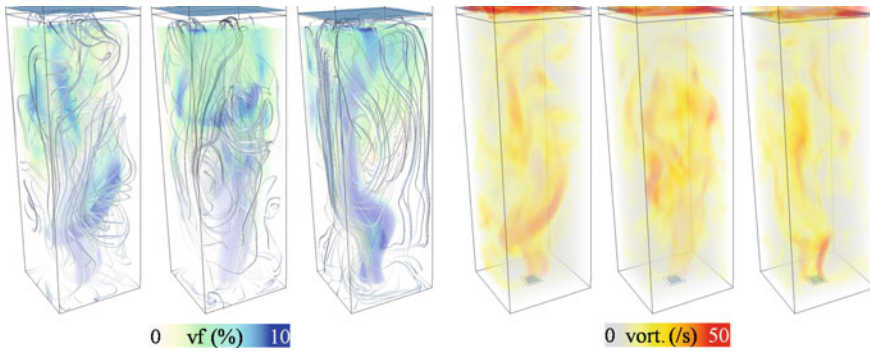
Fig. 1 LES results of the instantaneous bubble volume-fraction and liquid vorticity

structured grid was generated consisting of 720 k hexahedral elements ($\Delta x \approx 6$ mm), with extra layers of cells near the walls.

LES predictions of the instantaneous flow-field are illustrated in Fig. 1, in terms of the bubble volume-fraction and the liquid vorticity gained during the mixing process. Starting from the base of the tank, the bubble-column begins to rise against the stagnant water liquid, which is perturbed due to the induced relative motion. Eddies appear at the trails of the emerging bubbles, forming shedding wakes of vorticity as a by-product of their buoyant motion.

Model predictions of the mean and fluctuating liquid-velocities for the mixing bubble flow are plotted against available LDA measurements at the mid-section of the column in Fig. 2. From these results it appears that the RANS models underestimated the liquid-phase fluctuations and also predicted relatively higher velocities for the core of the bubbly-plume. In addition, the recirculation currents developing at the side walls surrounding the bubble-column are also overestimated. Transfer of momentum at the separated flow regions near the walls is motivated when resolving the instantaneous interactions between the bubbles and the developing large-eddies.
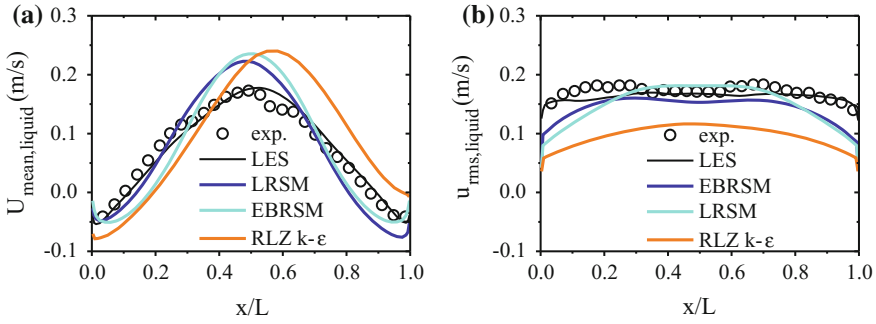
Fig. 2 **a** Mean and **b** rms axial liquid velocity (y/H = 0.56)
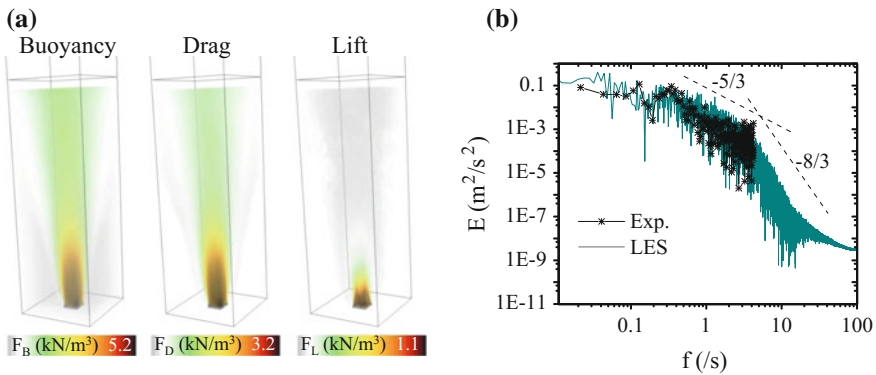
Fig. 3 **a** Averaged bubble-forces and **b** turbulence energy spectrum

In this case the mean velocity profile is flattened, as part of the bulk flow diffuses towards the walls, and the fluctuations are increased to reach comparable levels.

The volume-averaged forces acting on the bubbles are illustrated in Fig. 3. As expected buoyancy and drag forces are the main momentum exchange mechanisms in this type of flows, driving the bubbles to their terminal velocity ($D_b = 4$ mm ~ 0.2 m/s). The lift force is responsible for the gradual migration of bubbles towards the surrounding walls; the lateral displacement of the bubble phase may also explain the twin-peaks noticed on the rms levels.

The energy spectrum of the turbulent bubbly-flow is plotted in Fig. 3. Both the numerical LES calculations and the experimental measurements appear to match the cascading slope of the inertial sub-range ($-5/3$), as suggested by Pope [12]. For the smaller dissipative scales, a steeper energy decay is predicted ($-8/3$); according to Lance [8] this effect is triggered by the forming bubbles wakes, which continuously generate eddies and thereby transport energy from the mean flow to the viscous structures.

4 Synopsis

In this study the turbulent behaviour of buoyant bubbles has been simulated with second-moment RANS closure models as well as the Smagorinsky LES technique. Despite the relative simplicity of the tested mutliphase flow, typical two-point closure models are found to be inadequate for predicting the pseudo turbulence levels generated by rising bubbles at low terminal velocities. Realistic imitation of the diffusive character of the dispersed bubbly flow required resolution of the turbulent motion triggered by large-scale eddies. Through the process of interaction with eddies, bubbles acted as inertial linkages and continuously supplied energy to the dissipative viscous structures accelerating in this way the energy cascade.

References

1. Deen NG, Solberg T, Bjrn HH (2001) Large eddy simulation of the gas-liquid flow in a square cross-sectioned bubble column. Chem Eng Sci 56:6341–6349
2. Deutsch E, Simonin O (1991) Large eddy simulation applied to the motion of particles in stationary homogeneous fluid turbulence. ASME FED 110:35–42
3. Fox RO (2012) Large-eddy-simulation tools for multiphase flows. Annu Rev Fluid Mech 44:47–76
4. Fox RO (2014) On multiphase turbulence models for collisional fluid-particle flows. J Fluid Mech 742:368–424
5. Gibson MM, Launder BE (1978) Ground effects on pressure fluctuations in the atmospheric boundary layer. J Fluid Mech 86(3):491–511
6. Gosman AD, Issa RI, Lekakou C, Looney MK, Politis S (1992) Multidimensional modelling of turbulent two-phase flows in stirred vessels. AIChE J 38(12):1946–1956
7. Hinze JO (1959) Turbulence. McGraw-Hill, NY
8. Lance M, Bataille J (1991) Turbulence in the liquid phase of a uniform bubbly airwater flow. J Fluid Mech 222:95–118
9. Leonard BP (1991) The ULTIMATE conservative difference scheme applied to unsteady one-dimensional advection. Comp. Methods in. Appl Mech Eng 88:17–74
10. Manceau R, Hanjalic K (2000) A new form of the elliptic relaxation equation to account for wall effects in RANS modeling. Phys Fluids 12(9):2345–2351
11. Mazzitelli IM, Lohse D, Toschi F (2003) On the relevance of the lift force in bubbly turbulence. J Fluid Mech 488:283–313
12. Pope SB (2000) Turbulent Flows. Cambridge University Press, UK
13. Rensen J, Luther S, Lohse D (2005) The effect of bubbles on developed turbulence. J Fluid Mech 538:153–187
14. Sato Y, Sekoguchi K (1975) Liquid velocity distribution in two-phase bubble flow. Int J Multiphase Flow 2:75–95
15. Smagorinsky J (1963) General circulation experiments with the primitive equations. Mon Weather Rev 91(3):99–164
16. Speziale CG, Sarkar S, Gatski TB (1991) Modelling the pressure-strain correlation of turbulence: an invariant dynamical systems approach. J Fluid Mech 227:245–272
17. Tchen CM (1947) Mean value and correlation problems connected with the motion of small particles suspended in a turbulent fluid. PhD thesis, Delft
18. Tenneti S, Subramaniam S (2014) Particle-resolved direct numerical simulation for gas-solid flow model development. Ann Rev Fluid Mech 46:199–230

19. Thai-Van D, Minier JP, Simonin O, Freydier P, Olive J (1994) Multidimensional two-fluid model computation of turbulent dispersed two-phase flows. ASME FED 185:277–291
20. Tomiyama A, Kataoka I, Zun I, Sakaguchi T (1998) Drag coefficients of single bubbles under normal and microgravity conditions. JSME (B) 41(2):472–479
21. Tomiyama A, Tamai H, Zun I, Hosokawa S (2002) Transverse migration of single bubble in simple shear flow. Chem Eng Sci 57:1849–1858
22. Troshko AA, Hassan YA (2001) Two-equation turbulence model of turbulent bubbly flows. Int J Multiphase Flow 27:1965–2000

A Wavelet Based Adaptive Discontinuous Galerkin Method for Incompressible Flows

Brijesh Pinto, Marta de la Llave Plata and Eric Lamballais

Abstract This paper outlines the development of a wavelet based adaptive discontinuous Galerkin spectral element method (DG-SEM) for unsteady incompressible flows. The proposed approach possesses arbitrary high formal accuracy and permits adaptivity in a way that is computationally cheap and efficient. An element wise discretisation of the domain is performed. Two sets of basis functions are employed per element—the Lagrange polynomials at the Gauss-Legendre-Lobatto (GLL) points which acts as the nodal basis for the DG-SEM method and the second generation wavelets (SGW) which can be looked upon as either a nodal or modal basis, subject to convenience, and is responsible for facilitating the adaptivity. The projection of the signal onto the wavelet space provides information about the local frequency content of the signal. An accumulation of high frequency components acts as an indicator for dynamic mesh refinement via thresholding. The main advantage of using the SGW basis is the low cost of the transform, *O(N)* per direction.

1 Introduction

High-order simulations of unsteady incompressible turbulent flows are very challenging, especially at high Reynolds numbers (Re) and in complex geometries. Grid resolution scales as $\frac{\eta}{L} = \left(\frac{1}{Re}\right)^{\frac{9}{4}}$, thus at high Re, the large grid sizes required, make

B. Pinto (✉) · M. de la Llave Plata
ONERA, 92322 Châtillon, France
e-mail: brijesh_emmanuel.pinto@onera.fr

M. de la Llave Plata
e-mail: marta.de_la_llave_plata@onera.fr

E. Lamballais
Laboratoire d'Etudes Aérodynamiques, UMR 6609 Université de Poitiers, CNRS,
Téléport 2 - Bd. Marie et Pierre Curie, B.P. 30179, 86962 Futuroscope Chasseneuil Cedex, France
e-mail: eric.lamballais@univ-poitiers.fr

DNS infeasible. A way to overcome this problem is via large eddy simulation (LES) and *hp*-adaptivity. Both these techniques require the usage of efficient high-order discretization schemes. In response to this requirement we are working on the development of high-order, *hp*-adaptive incompressible flow solvers for DNS and LES. In general, modern solver methods should possess several beneficial properties such as high formal order of accuracy, relatively low operation count and good parallel performance.

Spectral methods (SM) and spectral element methods (SEM) using continuous Galerkin (CG) [1] have seen widespread use for fluid flow problems, albeit on simple geometries. Although they possess remarkable accuracy, their principal failing is their instability in convection dominated flows. The discontinuous Galerkin spectral element method (DG-SEM) is a variant of SEM employing a non-conforming approximation space [2], leading to superior performance in the convection dominated regime. In addition, DG-SEM also possesses a a compact stencil, important for parallel computations wherein interprocess passes are sought to be kept to a minimum [3]. However as a general rule spectral methods are computationally expensive. *hp*-adaptivity seeks to overcome this problem via concentrating computational resources where they are most needed. However typically adaptivity necessitates an error estimator or refinement indicator to highlight those regions in the flow where refinement is needed. For unsteady incompressible flows there is a severe deficiency of suitable error estimators. The usage of wavelets for adaptivity and LES in incompressible flows has a rich history [4]. Thus we intend to use second generation wavelets (SGW) as a refinement indicator. The multi-resolution analysis (MRA) (constructed using SGW) of the flow field gives us information regarding the signal regularity. A local loss in regularity indicates the need for *hp*-refinement. Here we utilize SGW in conjunction with DG-SEM for incompressible flows. Recent work along similar lines, albeit in the compressible flow regime [5] lends credence to this approach. In this paper we first describe the variant of DG-SEM method which we use. Next we describe the wavelet basis and its applications to adaptivity. We conclude with some results.

2 Discontinuous Galerkin Method for Incompressible Flows

The incompressible Navier–Stokes equations are given as:

$$\begin{aligned}
\partial_t \mathbf{u} - \nu \triangle \mathbf{u} + \nabla . \mathscr{F}(\mathbf{u}) + \nabla p &= f \;\; in \;\; \Omega, \;\; t \;\; \varepsilon \;\; [0, T] \\
\nabla . \mathbf{u} &= 0 \;\; in \;\; \Omega, \;\; t \;\; \varepsilon \;\; [0, T] \\
\mathbf{u} &= \mathbf{g} \;\; on \;\; \partial\Omega_g, \;\; t \;\; \varepsilon \;\; [0, T] \\
(\nu \nabla \mathbf{u}) . \hat{n} &= \mathbf{h} \;\; on \;\; \partial\Omega_h, \;\; t \;\; \varepsilon \;\; [0, T]
\end{aligned} \tag{1}$$

where $\mathscr{F}(\mathbf{u}) = (\mathbf{u} \otimes \mathbf{u})$. Over the last decade there has been a proliferation of discretization techniques based on non-conforming approximation spaces. We have chosen a local discontinuous Galerkin (LDG) discretization strategy which uses $Q_k - Q_k$ velocity-pressure approximation space (equal order) and pressure-jump stabilization for satisfaction of the *inf-sup* condition [2, 6, 7]. Such a method ensures the satisfaction of *inf-sup* condition independent of the grid. It also offers the additional benefit of allowing all velocity components and pressure to be hosted at the same element node in a nodal DG setting, greatly simplifying the construction of the code and removing the need for costly interpolations. This property also dovetails rather nicely with the SGW transform which acts upon the element degrees of freedom as will be seen in Sect. 3.

We briefly present the details of the LDG discretisation. The domain (Ω) is first partitioned into elements $\Omega = \bigcup_j \mathbf{T}_j$. The collection of these element forms the mesh $\mathbb{T} = \{\mathbf{T}\}$. The boundaries of the domain are denoted as $\partial\Omega$ while element boundaries are denoted by $\partial\mathbf{T}$. Let $\mathbf{T}_1$ and $\mathbf{T}_2$ be two adjacent elements. We define an *interface* as $F^i = \partial\mathbf{T}_1 \cap \partial\mathbf{T}_2$. Similarly a *boundary face* is defined by $F^b = \partial\mathbf{T} \cap \partial\Omega$. The set of all faces is defined by $\mathbb{F} = \{F^i \cup F^b\}$. Each face has an associated length scale denoted as $h_\mathbf{F}$.

At the faces, the following definitions are needed. Let u be a piecewise-smooth scalar variable. The trace of u along the *interface* of two elements $\mathbf{T}_1$ and $\mathbf{T}_2$ is denoted as $u|_{\partial\mathbf{T}_1}$ and $u|_{\partial\mathbf{T}_2}$ respectively. Then $[\![u]\!] = (u|_{\partial\mathbf{T}_1} - u|_{\partial\mathbf{T}_2})$ represent the *jump* across the interface. Furthermore $\{\!\{u\}\!\} = \frac{1}{2}(u|_{\partial\mathbf{T}_1} + u|_{\partial\mathbf{T}_2})$ represents the *average* along the *interface*. For a piecewise-smooth vector variable $\mathbf{u}$ we can define a jump across the *interface* as $[\![\mathbf{u}]\!] = (\mathbf{u}|_{\partial\mathbf{T}_1}.\hat{n} - \mathbf{u}|_{\partial\mathbf{T}_2}.\hat{n})$, where $\hat{n}$ is the unit normal to the interface, while the average is defined as $\{\!\{\mathbf{u}\}\!\} = \frac{1}{2}(\mathbf{u}|_{\partial\mathbf{T}_1}.\hat{n} + \mathbf{u}|_{\partial\mathbf{T}_2}.\hat{n})$.

We equip each element with an appropriate local polynomial space, of maximum degree k in each variable, denoted as $Q_k(\mathbf{T})$. Then we define the following broken polynomial spaces for velocity and pressure:

$$V_h(\mathbb{T}) = \{\mathbf{v} \; \varepsilon \; [L^2(\Omega)]^d \mid \mathbf{v}|_\mathbf{T} \; \varepsilon \; [Q_k]^d(\mathbf{T}), \; \forall \, \mathbf{T} \, \varepsilon \, \mathbb{T}\}$$
$$Q_h(\mathbb{T}) = \{q \; \varepsilon \; L^2(\Omega) \mid q|_\mathbf{T} \; \varepsilon \; Q_k(\mathbf{T}), \; \forall \, \mathbf{T} \, \varepsilon \, \mathbb{T}\}$$

where d is the dimension. Thus the weak form of the LDG discretisation of Eq. 1 is given as: $\{\mathbf{u}_h, p_h\} \, \varepsilon \, \{V_h, Q_h\}$ such that

$$\partial_t(\mathbf{v}_h, \mathbf{u}_h) + \nu a_h^{sip}(\mathbf{v}_h, \mathbf{u}_h) + \mathscr{A}_h^{nl}(\mathbf{v}_h, \mathbf{u}_h) + b_h(p_h, \mathbf{v}_h) - b_h(q_h, \mathbf{u}_h) + s_h(q_h, p_h)$$
$$= (\mathbf{v}_h, f) + G_h(\mathbf{v}_h) \tag{2}$$

is satisfied $\forall \{\mathbf{v}_h, q_h\} \, \varepsilon \, \{V_h, Q_h\}$. In Eq. 2, a_h^{sip} represents the symmetric interior penalty (SIP) bilinear form of the viscous term, given by:

$$a_h^{sip}(\mathbf{v}_h, \mathbf{u}_h) = \sum_{\mathbf{T}\varepsilon\mathbb{T}} \int_{\mathbf{T}} \nabla_h\mathbf{v}_h : \nabla_h\mathbf{u}_h dx - \sum_{\mathbf{F}\varepsilon\mathbb{F}} \int_{\mathbf{F}} \{\{(\nabla_h\mathbf{u}_h).\hat{n}\}\}.[\![\mathbf{v}_h]\!]ds$$

$$- \sum_{\mathbf{F}\varepsilon\mathbb{F}} \int_{\mathbf{F}} \{\{(\nabla_h\mathbf{v}_h).\hat{n}\}\}.[\![\mathbf{u}_h]\!]ds + \sum_{\mathbf{F}\varepsilon\mathbb{F}} \frac{\eta}{h_{\mathbf{F}}} \int_{\mathbf{F}} [\![\mathbf{v}_h]\!].[\![\mathbf{u}_h]\!]ds$$

where η represents the penalty parameter. $\mathscr{A}_h^{nl}(\mathbf{v}_h, \mathbf{u}_h)$ represents the weak form of the non-linear term, given by:

$$\mathscr{A}^{nl}(\mathbf{v}_h, \mathbf{u}_h) = -\sum_{\mathbf{T}\varepsilon\mathbb{T}} \int_{\mathbf{T}} \nabla_h\mathbf{v}_h : \mathscr{F}(\mathbf{u}_h)d\mathbf{x} + \sum_{\mathbf{F}\varepsilon\mathbb{F}} \int_{\partial T} \mathscr{F}^N(\mathbf{u}_h^+, \mathbf{u}_h^-).[\![\mathbf{v}_h]\!]ds$$

with $\mathscr{F}^N(\mathbf{u}_h^+, \mathbf{u}_h^-)$ as a central numerical flux given by:

$$\mathscr{F}^N(\mathbf{u}_h) = \frac{\mathscr{F}(\mathbf{u}_h^-).\hat{n} + \mathscr{F}(\mathbf{u}_h^+).\hat{n}}{2}$$

and:

$$\mathbf{u}_h^- = \begin{cases} \mathbf{u}_h|_{\partial\mathbf{T}_1} & in\ \mathbf{F}\ \varepsilon\ F^i \\ \mathbf{u}_h|_{\partial\mathbf{T}} & in\ \mathbf{F}\ \varepsilon\ F_g^b \end{cases} \qquad \mathbf{u}_h^+ = \begin{cases} \mathbf{u}_h|_{\partial\mathbf{T}_2} & in\ \mathbf{F}\ \varepsilon\ F^i \\ \mathbf{g} & in\ \mathbf{F}\ \varepsilon\ F_g^b \end{cases}$$

In Eq. 2, b_h is the bilinear form for the pressure and divergence operators given by:

$$b_h^{div}(\mathbf{v}_h, q_h) = \sum_{\mathbf{T}\in\mathbb{T}} \int_{\mathbf{T}} \mathbf{v}_h.\nabla_h q_h dx - \sum_{\mathbf{F}\in F^i} \int_{\mathbf{F}} \{\{\mathbf{v}_h.\hat{n}\}\}[\![q_h]\!]ds$$

$S_h(q_h, p_h)$ is the pressure-jump stabilization bilinear form given by:

$$S_h(q_h, p_h) = \sum_{\mathbf{F}\varepsilon\mathbb{F}^i} \frac{h_{\mathbf{F}}}{\nu} \int_{\mathbf{F}} [\![q_h]\!][\![p_h]\!]ds$$

and finally $G_h(\mathbf{v}_h)$, containing the boundary terms, is given by:

$$G_h(\mathbf{v}_h) = \sum_{\mathbf{F}\varepsilon F_h^b} \int_{\mathbf{F}} \mathbf{v}_h.\mathbf{h}ds - \sum_{\mathbf{F}\varepsilon F_g^b} \int_{\mathbf{F}} \left(\nu\ \mathbf{g}.(\nabla_h\mathbf{v}_h).\hat{n} + \nu\ \frac{\eta}{h_{\mathbf{F}}}\mathbf{v}_h.\mathbf{g} + q_h\mathbf{g}.\hat{n}\right)ds$$

The temporal discretisation is performed via classical second order pressure correction techniques detailed in [2, 8].

3 Second Generation Wavelets (SGW), Multi-resolution Analysis (MRA) and Adaptivity

In principle the decay of coefficients of an approximating polynomial series is linked directly to the regularity of the target function. As an example, the projection of a target function onto a Fourier basis provides data about which frequencies contribute the most energy. However modal bases (like Fourier) are typically well localized in frequency space and poorly localized in physical space, making it impossible to determine where in space to refine to better capture the signal.

A solution to this problem is to use a wavelet basis, one which is well localized in both space and frequency. Wavelet bases may be used to construct a hierarchy of space-frequency windows each with its own space-frequency range. This construction is called a *multi-resolution analysis* (MRA). By projecting a target function upon an MRA and by then examining the coefficients within each space-frequency tile we can refine in exactly the correct spatial location as the signal demands. In this work we will use a *second generation wavelet* (SGW) basis [9], one which can be built directly in physical space and upon bounded domains.

The MRA denoted by **M**, is the partitioning of the function space $L^2(R)$, by a sequence of nested closed subspaces V_j, called *scaling function space*, such that $\mathbf{M} = \{V_j \subset L^2(R) \mid j \; \varepsilon \; \mathbb{J} \subset Z\}$. This set of subspaces must satisfy the following properties:

1. Nestedness of spaces:

$$V_{-\infty} \subset ...V_{-2} \subset V_{-1} \subset V_0 \subset V_1 \subset V_2... \subset V_j \subset V_{j+1} \subset ...V_{+\infty} \quad j \; \varepsilon \; Z$$

   with resolution increasing towards continuum as $j \to \infty$.
2. Closure of $L^2(R)$:
$$\overline{\bigcup_j V_j} = L^2(R) \quad j \; \varepsilon \; Z$$

3. For each $j \; \varepsilon \; \mathbb{J}$, V_j has a Riesz basis given by *scaling functions* $\{\phi_k^j \mid k \; \varepsilon \; \mathbb{K}(j)\}$. $\mathbb{K}(j)$ is an index set such that $\mathbb{K}(j) \subset \mathbb{K}(j+1)$. We may consider two cases for the index set $\mathbb{J}$:

   a. $\mathbb{J} = N$. In such a case the coarsest level exists and is V_0.
   b. $\mathbb{J} = Z$. This is a bi-infinite setting.

We now define the *wavelet space*, denoted by W_j. A set of functions $\{\psi_m^j \mid j \; \varepsilon \; \mathbb{J}, \; m \; \varepsilon \; \mathbb{M}(j) \mid \mathbb{M}(j) = \mathbb{K}(j+1)/\mathbb{K}(j)\}$, are the basis functions of the space W_j and are called *wavelets*. The *wavelets* and the spaces which they span must satisfy the following properties:

1. The space W_j is the complement space of V_j in V_{j+1} i.e. $V_{j+1} = V_j \oplus W_j$
2. The wavelet space is complete:

$$\overline{\bigcup_j W_j} = L^2(R) \quad j \; \varepsilon \; Z$$

3. a. if $\mathbb{J} = N$. Then the set $\{\psi_m^j/||\psi_m^j||, \; j \; \varepsilon \; \mathbb{J}, \; m \; \varepsilon \; \mathbb{M}(j)\} \bigcup \{\phi_k^0/||\phi_k^0||, \\ k \; \varepsilon \; \mathbb{K}(0)\}$ is a Riesz basis for $L^2(R)$
   b. if $\mathbb{J} = Z$. Then the set $\{\psi_m^j/||\psi_m^j||, \; j \; \varepsilon \; \mathbb{J}, \; m \; \varepsilon \; \mathbb{M}(j)\}$ is a Riesz basis for $L^2(R)$

We now define the *dual* MRA $\tilde{\mathbf{M}} = \{\tilde{V}_j \subset L^2(R) \mid j \; \varepsilon \; \mathbb{J} \subset Z\}$. The space $\tilde{V}_j$ is termed as *dual scaling function space* and it is spanned by the *dual scaling functions* denoted as $\tilde{\phi}_k^j$. Similarly we define a *dual wavelet space* denoted by $\tilde{W}_j$ with basis functions as *dual wavelets* denoted as $\tilde{\psi}_m^j$. The space $\tilde{W}_j$ is the complement to the space $\tilde{V}_j$.

Consider a function $f(x) \; \varepsilon \; L^2(R)$. We denote P_j as the projection operator onto the space V_j. We define the *scaling function coefficient* as $s_k^j = (f, \tilde{\phi}_k^j)$. Similarly let Q_j be the projection operator onto W_j. We define the *wavelet coefficient* as $d_m^j = (f, \tilde{\psi}_m^j)$. Thus we have the following series representation:

$$P_j f(x) = \sum_{k \varepsilon \mathbb{K}(j)} s_k^j \phi_k^j \qquad Q_j f(x) = \sum_{m \varepsilon \mathbb{M}(j)} d_m^j \psi_m^j$$

For computational purposes spatial localization is extremely important, as it directly influences the computational stencil, which in turn dominates parallel performance. Thus we utilize the SGW basis functions element wise in a DG-SEM discretisation. Thus a signal over the elements may be represented as:

$$f(x) \simeq P_J f(x) = \sum_{\mathbb{T}} \left(\sum_k s_k^0 \phi_k^0 + \sum_{j=0}^{J-1} \sum_m d_m^j \psi_m^j \right)$$

Using this description of a function, we can now describe the adaptive algorithm based upon the wavelets. We begin by constructing a coarse approximation space with a given number of elements. During the course of the computation the flow variables are subjected to an MRA. The *scaling functions* serve as low-pass filters while the *wavelets* serve as high-pass filters. Thus we examine the magnitude of the *wavelet coefficients* and compare them to a predefined *threshold* (ε). In the smooth regions of the flow the wavelet coefficients are predominantly zero. A proliferation of wavelet coefficients exceeding the threshold, in any region of the flow, indicates the presence of structures that contributes to the high frequencies in a spectral analysis and thus to the numerical errors. To resolve these regions better, mesh refinement is performed locally. It should be noted that this refinement indicator is completely

Fig. 1 Streamline pattern
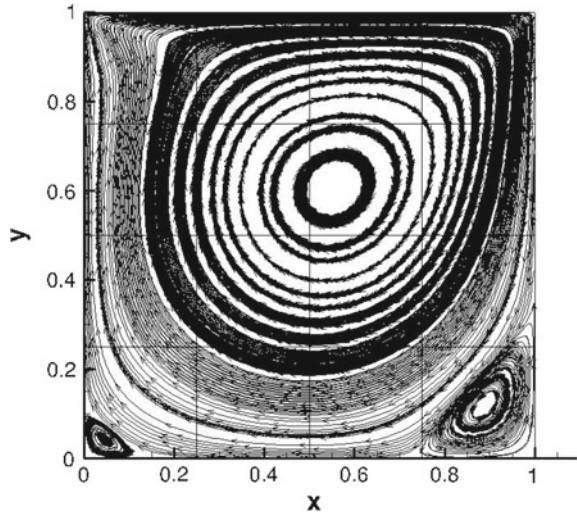
blind to sudden jumps across the *interfaces* which is fortuitous as DG-SEM by its very nature produces a discontinuous solution across elements.

4   Numerical Test

The method proposed above has been implemented into an unstructured code for 2D and 3D. It has been written in C++ and uses MPI for parallel multi-domain calculations. We demonstrate the method via a classic test case—the lid driven cavity problem at $Re = 400$. DNS data for this test case is available in [10]. We perform a DG-SEM calculation on a domain discretized with 4×4 elements, with Q_8–Q_8 discontinuous velocity-pressure approximation space per element, providing a total of $1,296$ degrees of freedom (G1) (Fig. 2). We then perform a single cycle of h-adaptivity based upon the MRA of the u component of the velocity to produce a geometrically non-conforming grid (G2) (Fig. 2) with $3,969$ degrees of freedom.

For comparison we extract the u and v velocities along the vertical and horizontal center-lines and compute the vorticity (ω_z) along the moving wall for grids G1 and G2. These quantities are compared with the reference data. The curves in Fig. 3 clearly illustrated the benefit of the wavelet adapted grid. We see that although the u and v velocity predictions exhibit a negligible improvement the ω_z prediction has improved dramatically particularly in the region $0 \leq x \leq 0.3$. Although this test case is extremely mild it serves to demonstrate the method in its entirety and demonstrates how adaptivity may be performed in incompressible flows cheaply and effectively.
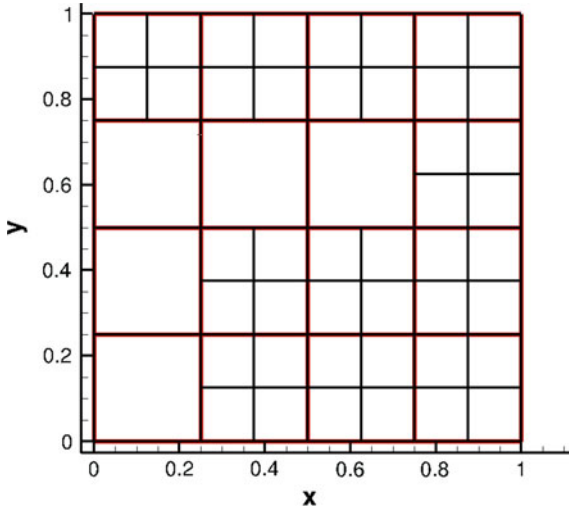
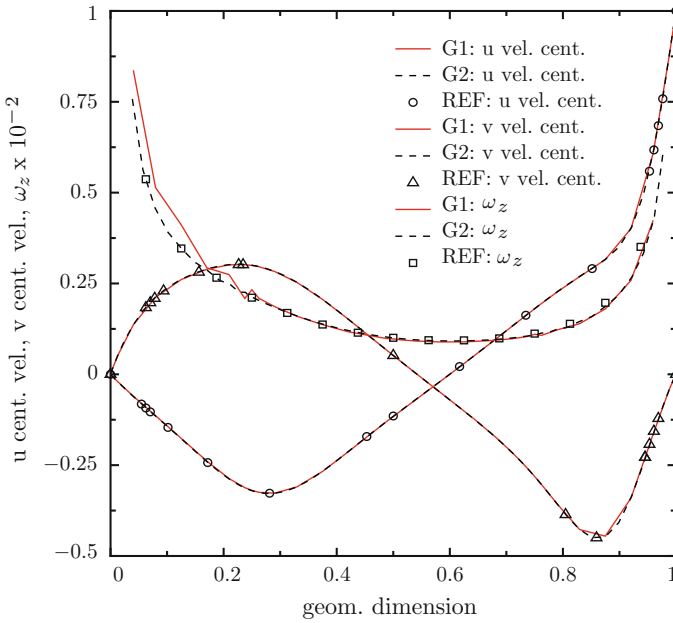**Fig. 2** G1 in *red*, G2 in *black*

Fig. 3 Comparison of *centreline* velocity (*u*, *v*) and moving wall vorticity ω_z

5   Conclusions

We have outlined the development of a wavelet based adaptive DG-SEM scheme for incompressible flows. The usage of DG-SEM in conjunction with the SGW appears to have a number of advantages which we have demonstrated via the lid driven cavity test case. The overall strategy is fairly unique and should prove useful for unsteady detached flows for which error estimators and refinement indicators are severely lacking. However work must be done in determining the flow variables upon which the MRA should be performed as well as the appropriate choice of the threshold. In the near future we hope to extend our approach to more challenging turbulent flow problems such as the prediction of the skin-friction coefficient in the recirculation region of the backward-facing step.

References

1. George EM (2004) Karniadakis and spencer sherwin, spectral/hp element method for computational fluid dynamics. Oxford Science Publications
2. Ern A, Di Pietro D (2010) Mathematical aspects of discontinuous Galerkin methods. Springer, Heidelberg
3. Chapelier J-B, De La Llave Plata M, Renac F, Lamballais E (2014) Evaluation of a high-order discontinuous Galerkin method for the DNS of turbulent flows. Comput Fluids 95(22): 210226
4. Schneider K, Vasilyev OV (2010) Wavelet methods in computational fluid dynamics. Annu Rev Fluid Mech 42:473–503
5. Gerhard N, Iacono F, May G, Muller S, Schafer R (2015) A high-order discontinuous Galerkin discretisation with multiwavelet-based grid adaptation for compressible flows. J Scient Comput
6. Cockburn B, Kanschat G, Schötzau D (2009) An equal-order DG method for the incompressible Navier–Stokes equations. J Scient Comput 40:188–210
7. Shahbazi K, Fischer PF, Ethier CR (2007) A high-order discontinuous Galerkin method for the unsteady incompressible Navier–Stokes equations. J Comput Phys 222:391–407
8. Guermond JL, Minev P, Shen J (2006) An overview of projection methods for incompressible flow. Compu Methods Appl Mech Eng 195:6011–6045
9. Sweldens W, Schröder P (1995) Building your own wavelets at home, Industrial Mathematics Initiative, Department of Mathematics, University of South Carolina, Technical Report 1995:5
10. Ghia U, Ghia KN, Shin CT (1982) High-Re solutions for incompressible flow using the Navier–Stokes equations and a multigrid method. J Comput Phys 48:387–411

Validation of the Rotation Rate Based Smagorinsky Model for Unconfined Shear Flow

Nathan Ricks, Chris Lacor and Ghader Ghorbaniasl

Abstract The rotation rate based Smagorinsky model is a recently proposed subgrid-scale model by Ghorbaniasl et al. (Phys Fluid Mech, 2013) [1]. The model proposes a new efficient formula for calculating the classical Smagorinsky model coefficient. In this paper, validation of the model for unconfined shear flow is realised through a test case of a spatially developing free round jet at a Reynolds number of 2400. The results show good agreement between the rotation rate based Smagorinsky model and the dynamic Smagorinsky model, as well as between both models and reference data. It is observed that there is significant improvement in the computational efficiency of the rotation rate based Smagorinsky model, as compared to the dynamic Smagorinsky model.

1 Introduction

Subgrid-scale (SGS) models are utilised in large eddy simulations (LES) to account for turbulence that is smaller than the filter (or grid) width. SGS models contribute a significant proportion to the computational requirements of LES, and also to the overall accuracy. Thus, SGS models have become a focus of extensive investigation (e.g. see [2–5]).

The rotation rate based Smagorinsky model (RoSM) is a recently proposed SGS model by Ghorbaniasl et al. [1]. In the paper of Ghorbaniasl et al. [1], four validation cases are presented. Further to this, the model was utilised by Matouk et al. [6]. In brief, the RoSM has previously been validated for inhomogeneous flow in one and two directions, transition to turbulence, complex geometry and high Reynolds number flow. A common property of these cases is the presence of walls.

N. Ricks (✉) · C. Lacor · G. Ghorbaniasl
Vrije Universiteit Brussel, Brussel, Belgium
e-mail: nathan.james.ricks@vub.be

C. Lacor
e-mail: chris.lacor@vub.ac.be

G. Ghorbaniasl
e-mail: ghader.ghorbaniasl@vub.ac.be

In this paper, we investigate the behaviour of the RoSM in unconfined shear flow, a case where wall calculations are not involved. This is realised through a test case of a spatially developing free round jet at a Reynolds number of 2400.

The paper begins with a brief outline of Smagorinsky [2] based SGS models, one of which is used as a benchmark model. An outline of the RoSM is provided, followed by details on the present validation test case and the numerical results. The observations are finally summarised in the conclusion.

2 Smagorinsky Model

Smagorinsky [2] developed one of the original SGS models. The basis of the classical Smagorinsky model is the eddy viscosity equation:

$$\nu_t = L^2 |\overline{S}| = (C_s \Delta)^2 |\overline{S}|. \tag{1}$$

Here, L is the Smagorinsky length scale of the unresolved motion, $\overline{S}$ is the second invariant of the resolved strain rate tensor, C_s is the Smagorinsky coefficient, and Δ is the filter width. In the classical Smagorinsky model, the Smagorinsky coefficient is a constant value with some damping towards the wall to achieve vanishing turbulent viscosity on the wall.

Germano et al. [3] proposed the dynamic Smagorinsky model (DSM), where the Smagorinsky coefficient is calculated locally using a series of test filters. This increases the accuracy compared to the classical Smagorinsky model and inherently satisfies the zero turbulent viscosity condition on the wall. However, this method also has disadvantages. The test filters can be difficult to define in complex geometries and unstructured grids.

Moreover, in the DSM, the Smagorinsky coefficient can vary significantly in space and time, and is prone to negative and excessively high values. This can lead to numerical instabilities that require control algorithms. The aforementioned method adds to the complexity of the model, and results in a high computational cost. The DSM is used as a benchmark to assess the performance of the RoSM, as the DSM is currently one of the most prevalent SGS models.

3 Rotation Rate Based Smagorinsky Model

The rotation rate based Smagorinsky model is a recently proposed SGS model by Ghorbaniasl et al. [1]. The model provides a new method of calculating the Smagorinsky model coefficient. The aim of Ghorbaniasl et al. [1] was to develop an SGS model where

1. C_s is a function of the resolved flow solution,
2. C_s is space and time dependent,
3. Zero contribution is enforced for subgrid scales in laminar flow regions and in the viscous sublayer in turbulent bounded wall flows (i.e. $C_s \to 0$), and
4. There is no need for stability control algorithms, wall functions, or test filters.

The desired outcome of satisfying these conditions is an easy to implement SGS model that is significantly more efficient from a computational perspective, as compared to the DSM. Provided here is the final formulation of the model. For further details of the development of the model, please refer to the paper of Ghorbaniasl et al. [1].

The final formulation for the RoSM is a new method for calculating the Smagorinsky coefficient, which is applied to the eddy viscosity equation as seen in Eq. 1. The new formulation has the form:

$$C_s = \min(G_x, G_y, G_z), \tag{2}$$

where

$$G_x = \frac{|\overline{\Omega}_x \overline{u}_x|}{2D}, \quad G_y = \frac{|\overline{\Omega}_y \overline{u}_y|}{2D}, \quad G_z = \frac{|\overline{\Omega}_z \overline{u}_z|}{2D} \tag{3}$$

and

$$D = \sqrt{(\overline{\Omega}_x \overline{u}_x)^2 + (\overline{\Omega}_y \overline{u}_y)^2 + (\overline{\Omega}_z \overline{u}_z)^2}, \tag{4}$$

with the resolved rotation rates defined as

$$\overline{\Omega}_x = \frac{1}{2}\left(\frac{\partial \overline{u}_z}{\partial y} - \frac{\partial \overline{u}_y}{\partial z}\right), \quad \overline{\Omega}_y = \frac{1}{2}\left(\frac{\partial \overline{u}_x}{\partial z} - \frac{\partial \overline{u}_z}{\partial x}\right), \quad \overline{\Omega}_z = \frac{1}{2}\left(\frac{\partial \overline{u}_y}{\partial x} - \frac{\partial \overline{u}_x}{\partial y}\right). \tag{5}$$

Here, $\overline{u}_i$ refers to the resolved velocity in each direction. The model is defined to be in a frame fixed to the grid, in order to satisfy the Galilean invariance.

One of the significant features of the RoSM, as compared to the DSM, is the obviation of the need for test filtering and numerical stability control. It is shown by Ghorbaniasl et al. [1] that the RoSM gives a Smagorinsky coefficient in the range $0 \le C_s \le 0.2886$.

4 Present Test Case

The present validation test case for the RoSM is a spatially developing free round jet at a Reynolds number of 2400, based on jet diameter and inlet velocity. For this test case, the simulation is conducted using the RoSM and DSM, with all other setup conditions remaining unchanged. The results are assessed and compared to DNS

Fig. 1 Cross section of computational domain, with 'buffer zone' shown with a patterned fill
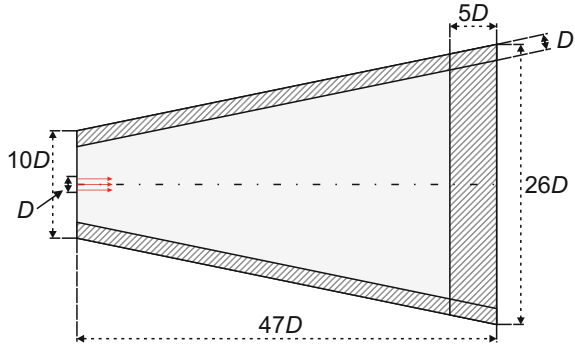
results of Boersma et al. [7] and experimental measurements of Hussein et al. [8], both in their investigation of self-similarity in round jets.

4.1 Model Setup

The computational domain is a tapered cylinder, with a cross section and dimensions as shown in Fig. 1. The mesh consists of approximately 1×10^6 nodes; it is finest at the inlet orifice and spreads with the computational domain. The mesh coarsens at the lateral and outlet boundaries, within the patterned zone in Fig. 1, in order to minimize the influence of the boundary conditions on the bulk of the flow. The data in this area is also disregarded for the post-processing.

A top-hat velocity profile is applied at the jet orifice, and a zero coflow velocity is applied at the inlet outside of the orifice. A pressure outlet boundary condition is applied on the lateral and outlet boundaries. Simulations are conducted in ANSYS Fluent where the RoSM is applied as a simple user-defined function. A fixed time step of 5×10^{-6} s is utilised, as well as the SIMPLE scheme, bounded central differencing scheme for momentum and a second order implicit transient formulation.

4.2 Results

For assessment of the RoSM, mean and turbulent statistics will be compared to the DSM, and assessed against the reference data. Most statistics are presented as a function of the self-similarity coordinate (SSC), $\eta = r/(z - z_0)$; this is for consistency with Boersma et al. [7] and Hussein et al. [8]. Here, r is the radius, z is the distance to the orifice, and z_0 is the distance to the virtual origin.

The mean statistics that are assessed are the mean centreline velocity decay and the mean axial velocity as a function of the SSC. In both instances, shown in Fig. 2a,
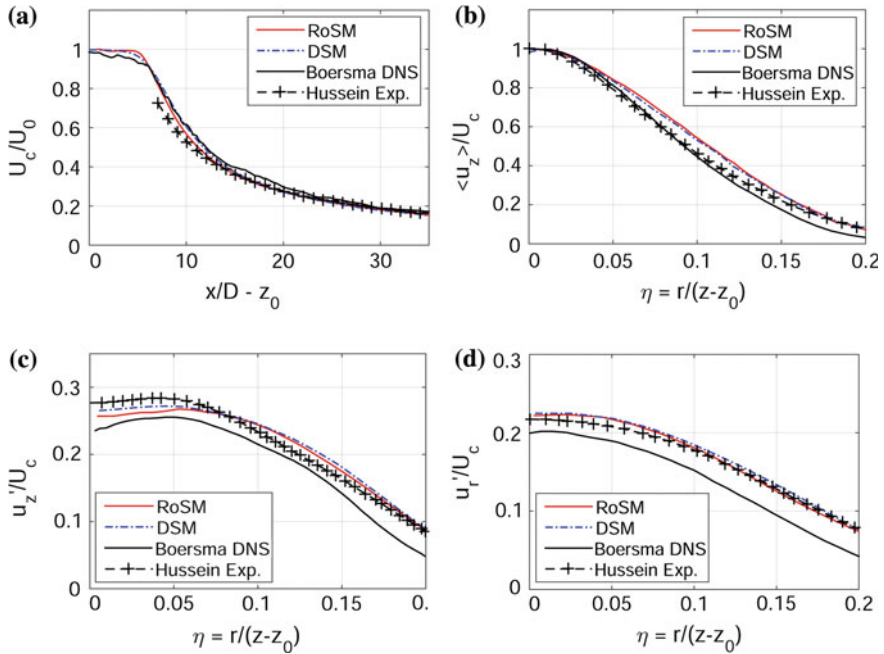
Fig. 2 **a** The mean centreline velocity decay. **b** The mean axial velocity as a function of the SSC. **c** The turbulence intensity in the axial direction as a function of the SSC. **d** The turbulence intensity in the radial direction as a function of the SSC

b, the results of the RoSM well duplicate those of the DSM while being in good agreement with the reference data. The trends seen in all data is consistent.

The same conclusions can be drawn from the results for the turbulent statistics, shown in Fig. 2c, d. The turbulence intensity in the axial and radial direction as a function of the SSC are presented. The RoSM and DSM show a good match, and there is a good agreement to reference data. In this case, there is a marginal improvement in some statistics when using the RoSM over the DSM.

These general conclusions are consistent with the conclusions of Ghorbaniasl et al. [1] and Matouk et al.[6] in their respective validation cases.

4.3 Computational Time

It has been shown that the RoSM provides results consistent with the DSM, an industry standard SGS model. The defining feature of the RoSM is the reduction in computational requirements. This outcome has been tested via a computational time test, where the same case was tested on the same system, with the singular difference being the SGS model.

Table 1 Computational time comparison for RoSM and DSM

SGS Model	Time steps	Time (min)	Computational time reduction
DSM	100	15.07	–
RoSM	100	12.20	20%

The results of the computational time test are shown in Table 1. It is observed that a computational time reduction of approximately 20% is achieved by utilising the RoSM. This is a significant development as the computational requirements of LES is a major factor hindering its usage.

5 Conclusion

The present paper investigated the behaviour of the rotation rate based Smagorinsky model, a recently proposed subgrid-scale model by Ghorbaniasl et al. [1], in unconfined shear flow. The representative test case was the spatially developing free round jet at a Reynolds number of 2400. This was a unique test case, since all previous validation by Ghorbaniasl et al. [1] and Matouk et al. [6] had involved wall calculations.

The calculated results well matched the conclusions seen in the previous test cases. The results showed a consistency between the RoSM and the DSM, and a good agreement to reference data. Furthermore, in some instances there were signs of improvement when the RoSM was utilised.

A significant observation from the realised study is the reduction of computational requirements. It was shown that the RoSM reduced computational time by approximately 20% as compared to the DSM. This occurs whilst still maintaining results matched to the quality of the DSM, an industry standard subgrid-scale model.

Since computational time is still one of the most significant factors in the computational fluid dynamics field, a time reduction of 20% with the RoSM is a noteworthy development.

References

1. Ghorbaniasl G, Agnihotri V, Lacor C (2013) A self-adjusting flow dependent formulation for the classical Smagorinsky model coefficient. Phys Fluids. doi:10.1063/1:4804393
2. Smagorinsky J (1963) General circulation experiments with the primitive equation. Mon Weath Rev 91(3):99–165
3. Germano M (1992) Turbulence: the filtering approach. J Fluid Mech 238:325–336
4. Bardina J, Ferziger JH, Reynolds WC (1980) Improved subgrid scale models for LES. AIAA Paper No. 80-1357

5. Zang Y, Street L, Koseff JR (1993) A dynamic mixed subgrid-scale model. Phys Fluids A 5:3186–3196
6. Matouk R, Degrez G, Christophe J (2014) Aerodynamics and aeroacoustics study of the flow around an automotive fan airfoil. In: WCCM XI, Conference
7. Boersma BJ, Brethouwer G, Nieuwstadt FTM (1998) A numerical investigation on the effect of the inflow conditions on the self-similar region of a round jet. Phys Fluids 10(4)
8. Hussein HJ, Capp SP, George WK (1994) Velocity measurements in a high Reynolds number, momentum-conserving axisymmetric turbulent jet. J Fluid Mech 258:31–75

Experimental Study of Turbulent Rayleigh-Bénard Convection Using Large-Scale Tomo-PIV and High-Density PTV

Daniel Schiepel, Sebastian Herzog and Claus Wagner

Abstract Flow field measurements of turbulent Rayleigh-Bénard Convection (RBC) in a cubic cell filled with water are performed using Tomographic Particle Image Velocimetry (Tomo-PIV) and a newly developed high-density particle tracking velocimetry (HD-PTV) technique. With these two techniques, the flow field in RBC at a Prandtl number Pr = 6.9 and a Rayleigh number of $Ra = 1.0 \cdot 10^{10}$ is measured and compared. It is shown that a three-dimensional (3D) large-scale circulation is reflected in a diagonal plane of the sample in both, the vector fields obtained with Tomo-PIV and the particle trajectories resulting from HD-PTV. Additionally, the latter requires 56 times less CPU time and 125,000 times less disk space.

1 Introduction

Turbulent thermal convection occurs frequently in nature as well as in numerous technical applications such as atmospheric flows and room or cabin ventilation. Most thermal convection studies focus on the heat transport which depends on the three-dimensional velocity and temperature fields. However, in experiments, the velocity fields are often measured in selected planes. Thus, the complete three-dimensional velocity distribution is usually not available in experimental studies.

In order to fill this gap and to access all three velocity components, large-scale Tomographic Particle Image Velocimetry (Tomo-PIV) [1] is applied to study

D. Schiepel (✉) · S. Herzog · C. Wagner
German Aerospace Center, Bunsenstr. 10, 37073 Göttingen, Germany
e-mail: daniel.schiepel@dlr.de

S. Herzog
e-mail: sebastian.herzog@dlr.de

C. Wagner
Technische Universität Ilmenau, 100565, 98684 Ilmenau, Germany
e-mail: claus.wagner@tu-ilmenau.de; claus.wagner@dlr.de

the large-scale flow structures developing in turbulent Rayleigh-Bénard convection (RBC), see e.g. [2, 3]. The major drawback of the correlation-based Tomo-PIV approach is the limited spatial resolution of the obtained velocity fields. Hence, the small-scale flow structures, typically found in turbulent flows, cannot be resolved in large measurement volumes. Though, the smaller flow structures are important since small-scale turbulence is interacting with the large-scale circulation (LSC) developing in our convection sample along the diagonal. Thus, the objective of the present study is to develop and apply Particle Tracking Velocimetry (PTV) in such a way that structures of different scales are resolved. This is a prerequisite for the analysis of the interaction of structures of different scales. In addition, previous Tomo-PIV studies [3] have shown that RBC in a cubical container is characterised by secondary structures, which develop perpendicularly to the LSC. However, these two smaller structures in the corners are not fully resolved in Tomo-PIV. In order to be able to measure the extension, the nature of turbulent flow structures of different scales in general and more specifically the secondary structures in our RBC cell, a new PTV approach suitable for high seeding densities was developed. This high-density PTV (HD-PTV) allows to resolve small-scale structures before they are dissipated.

2 Experimental Setup

The measurements of turbulent RBC are conducted in a cubical sample with a side length of 500 mm enclosed by 10 mm thick glass walls. At a mean sample temperature of $\overline{T} = 21°C$, water is used as a working fluid yielding the corresponding Prandtl number of $Pr = 6.9$. At a Rayleigh number of $Ra = 1.0 \cdot 10^{10}$, TiO_2-coated latex particles, which are neutral with respect to buoyancy, are added to the flow as tracer particles. The entire volume is illuminated using a high-power LED array as light source. Two subsequent light-pulses are separated by $\Delta t = 0.35$ s and the scattered light from the tracer particles is recorded using 4 b/w PCO-Pixelfly CCD-cameras are equipped with $f_\sharp = 21$ mm Zeiss lenses. More details can be found in [3].

3 High-Density PTV

In Fig. 1, the process of the new HD-PTV approach is illustrated. The experimental setup is the same as the one used for Tomo-PIV with four cameras observing the measurement volume under different angles. Each camera records two images at the two time steps t and $t + \Delta t$. The particle distribution in 3D space is determined using a modified version of the iterative particle reconstruction (IPR) [4], see Sect. 3.1. At high seeding densities, it is challenging to keep track of the particle in the next time step. Thus, a prediction is needed to improve the assignment. Once, the motion of a particle i is known up to $t + \Delta t$, a first guess of its position at $t + 2\Delta t$ is made by applying the velocity components $\mathbf{X}_i(t + 2\Delta t, i) = \mathbf{X}_i(t + \Delta t, i) + \Delta t \cdot \mathbf{V}_i(t, i)$.
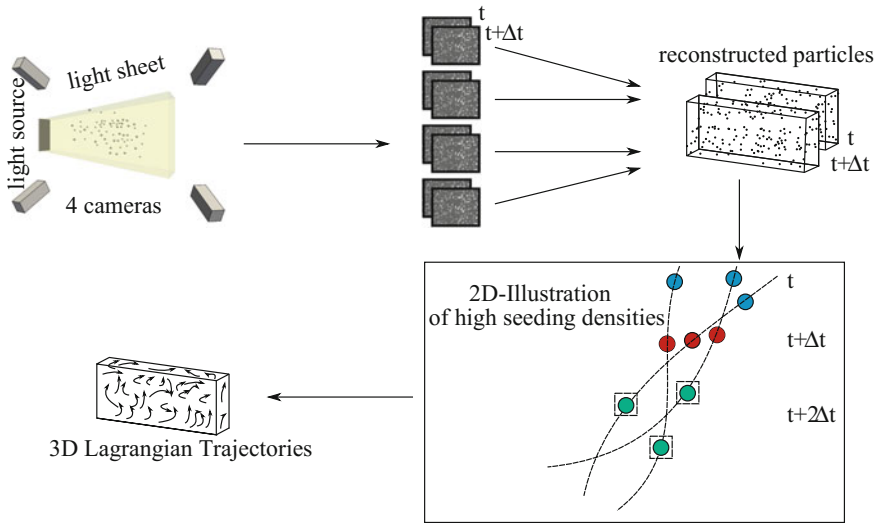
Fig. 1 Illustrates the HD-PTV software chain. First, the volume is illuminated and the scattered light is recorded using 4 CCD cameras. Secondly, the 3D particle distribution is reconstructed for image pairs at the times t and $t + \Delta t$. A prediction model is used to compute the particle trajectories

Since the residuum of the predicted and the actual particle position can be very large, a more sophisticated particle position predictor step is needed.

3.1 Three Dimensional Particle Reconstruction

Using PTV, the main challenge for analysing 3D measurements with a highly dense particle distribution is to obtain the accurate particle position for each time step. This challenge is approached by using particles with certain imaging properties and the application of a modified version of an iterative particle reconstruction [4], see Fig. 2. In the first step, a uniform particle distribution is initialised by placing $125 \times 125 \times 125$ particles within the volume. The projections are computed and compared to the recorded images. The candidates with the lowest residuals are kept and their position in 3D space is corrected by varying it in every direction until the residual does not decrease any further. The developed HD-PTV approach is based on an initialisation procedure including the identification of several particle positions and the tracking of the associated particles for the first n_{init} time steps—typically 5–10.

Particle tracking is applied by introducing a simplified Gaussian Mixture Model to find a compact representation for each trajectory in order to not rely on an individual treatment of every single snapshot of the particle distribution. Thus, the time dependencies between the single snapshats are used to increase the tracking accuracy [5].
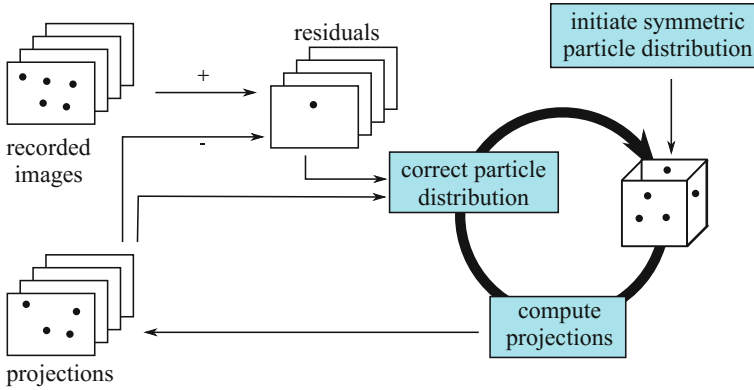
Fig. 2 Shows an illustration of the modified iterative particle reconstruction

For n_{init} time steps, particles are tracked just by residual minimisation. In the following processing steps however, the particle positions are used to calculate a trajectory as mentioned above. This allows an accurate prediction of the particle position for the next time step, just by applying the velocity components to the position of the particle and thereby saving huge amounts of computational time. All other particles are placed by regularisation in order to minimise the variance of their position and intensity and to fit them to the existing trajectories. Particles with no allegiance to a trajectory are used in further time steps to generate new trajectories as described or to extend already existing ones.

4 Results

With Tomo-PIV 500 time-resolved instantaneous velocity fields are obtained for the entire convection sample. The time-averaged velocity field reveals a LSC, which is oriented along the X-Z-diagonal of the sample with a maximum velocity of $\overline{\mathbf{V}}_{\text{max}} = 12\,\text{mm/s}$. The vertical velocity is of the same magnitude and symmetrically placed at the opposite corners of the sample, shown in Fig. 3a. Furthermore, the development of two smaller counter-rotating flow structures perpendicular to the LSC can be observed. Using the maximum velocity of the LSC, a Reynolds number of $Re = 6275$ is determined. From the measured mean velocity profiles the viscous boundary layer thickness of $\delta_u = 5.2\,\text{mm}$ is determined by means of the slope method [3]. The corresponding root mean square (rms) of the velocity fluctuations is shown in Fig. 3b. The large fluctuations along the LSC indicate that the small-scale turbulence interacts with the LSC. More details are not resolvable based on Tomo-PIV since the interrogation windows are too large.
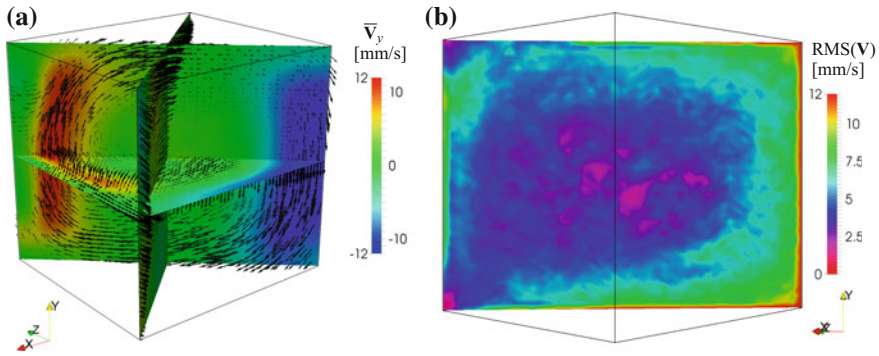
Fig. 3 **a** shows the measurement of the mean vertical velocity field $\overline{\mathbf{V}}_y$ at Ra $= 1.0 \cdot 10^{10}$ and Pr $= 6.9$ with colour coding according to the vertical velocity. In addition, three component vectors are added. **b** depicts the RMS of the velocity fields in the layer of the LSC

In order to better resolve the small structures, HD-PTV is employed. The first aim is to resolve the large-scale motion in comparison with the Tomo-PIV results. Therefore, trajectories and their positions, obtained with HD-PTV in the first 60 time steps, which reflect the LSC, are shown in Fig. 4a. In the considered time period, 2351 particles could be tracked and their velocities were deduced. Only trajectories with an extension of more than 25 time steps are considered. In Fig. 4a, particles at the end of a trajectory are marked with white dots and particle trajectories for the preceding 20 time steps are shown. To be able to distinguish between trajectories in different regions and to follow them more easily, they are coloured with the particle ID. Especially the wall-parallel particle trajectories reflect that a LSC is resolved and qualitatively agrees with the Tomo-PIV field as shown in Fig. 4b. Further, by applying a spatial kernel of 10 mm, to mimic the spatial resolution of the Tomo-PIV, a maximum mean velocity of 12.64 mm/s could be obtained from the HD-PTV fields, which is in good agreement with the value of 12.22 mm/s obtained from Tomo-PIV.

In addition, the CPU time requirements of HD-PTV and Tomo-PIV are compared in Table 1. Evaluating the Tomo-PIV for 500 time steps consumed 35.000 CPU hours—mainly needed by the SMART intensity reconstruction and the 3D cross-correlation both performed in each time step. The first five initialisation steps in the HD-PTV evaluation are expensive in terms of CPU hours by consuming 24 CPU hours. The subsequent time steps required significantly less CPU time since only 68 CPU hours were required for the remaining 55 evaluated data points. Consequently, with the new HD-PTV method, the flow field analysis is faster by a factor of 45.64–56.60. Therefore, it will be possible to achieve even larger improvements for longer time series. Similar findings were made with respect to the storage requirements. A single evaluation of Tomo-PIV requires 8100 MB of disk space. HD-PTV, on the other hand, requires just as little as 0.064 MB which is factor 125,000 times less.

(a)

(b)
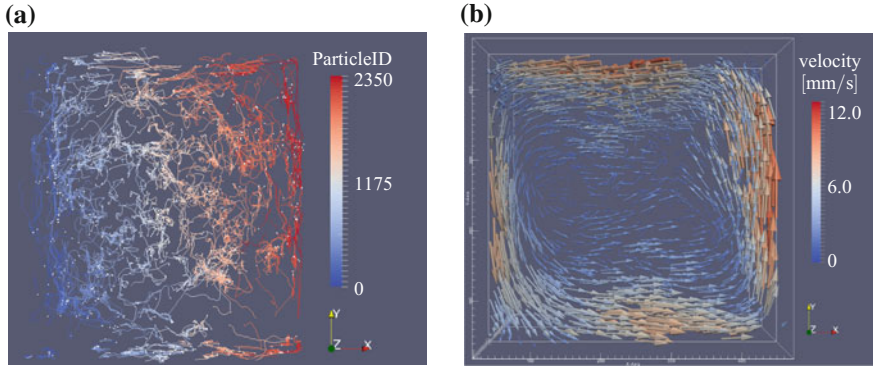
Fig. 4 **a** shows the particle trajectories with an extension of more than 25 time steps in the entire measurement volume. The particles are indicated using *white dots* and the particle paths are colour-coded according to their unique ID. **b** represents a subvolume of the sample ranging from 30 to 70% depth. Deduced from Tomo-PIV, the 3D-3C velocity is indicated using vectors with colour-coding applied according to the velocity magnitude

Table 1 Comparison of the computational time and efficiency of the applied two methods

Method	Time-steps	Time (CPU-hours)	Efficiency (time steps/CPU hours)
Tomo-PIV	500	35.000	0.01429
HD-PTV	First 5	24	0.20833
HD-PTV	Subsequent 55	68	0.80882
HD-PTV	60	92	0.65217

5   Conclusion and Outlook

Measurements of the large-scale flow structures in turbulent RBC were performed with the well-established Tomo-PIV and a new HD-PTV method. Both methods revealed a LSC in the diagonal of the convection cell. Mapping the particle-based velocities of HD-PTV to a uniform grid, the velocity magnitudes were compared and similar values of 12.22 and, respectively 12.64 mm/s found. In comparison to Tomo-PIV, 56.60 times less CPU-time was needed for HD-PTV and the storage requirements decreased by a factor of 125,000. In the future, this method will be applied to investigate small-scale turbulence and to analyse the interaction of these structures with the LSC.

References

1. Kühn M, Ehrenfried K, Bosbach J, Wagner C (2011) Large-scale tomo PIV using helium-filled soap bubbles. Exp Fluids 50:929–948
2. Ahlers G, Grossmann S, Lohse D (2009) Heat transfer and large scale dynamics in turbulent Rayleigh-Bénard convection. Rev Mod Phys 81:503–537
3. Schiepel D, Bosbach J, Wagner C (2013) Tomographic particle image velocimetry of turbulent Rayleigh-Bénard convection in a cubic sample. JFVIP 20(1–2):3–23
4. Wieneke B (2013) Iterative reconstruction of volumetric particle distribution. Meas Sci Technol 24(2):024008
5. Schanz D, Schröder A, Gesemann S, Michaelis D, Wieneke B (2013) Shake the box: a highly efficient and accurate tomographic particle tracking velocimetry (TOMO-PTV) method using prediction of particle positions. In PIV13. Delft, The Netherlands

Effects of Error on the Onset and Evolution of Rayleigh–Taylor Instability

Aditi Sengupta, Tapan K Sengupta,
Soumyo Sengupta and Vidyadhar Mudkavi

Abstract Here we investigate effects of error in simulating Rayleigh Taylor insta-
bility (RTI). The error metrics are evaluated based on the correct spectral analysis
of a model equation by Sengupta et al. (J Comput Phys 226:1211–1218, 2007) [13].
The geometry for RTI consists of a rectangular box with a partition at mid-height
separating two volumes of air kept at a temperature difference of 70 K. This helps
avoiding Boussinesq approximation and the present time-accurate computations for
compressible Navier–Stokes equation (NSE) in 2D are reported. Computations for
CFL numbers of 0.09 and 0.009 shows completely different onset of RTI, while the
terminal mixed stage appears similar. The difference is traced to very insignificant
difference in the value of numerical amplification factor for the two CFL numbers.

1 Introduction

RTI arises at the interface of fluids of different densities, with the heavier one resting
above the lighter fluid [8, 11, 15]. We study RTI, where initially air with two different
constant temperatures (and hence density) is placed across a non-heat conducting

A. Sengupta (✉)
Department of Engineering, University of Cambridge, Cambridge, UK
e-mail: dolaaditi@gmail.com

T.K. Sengupta
HPCL, IIT Kanpur, Kanpur 208016, India
e-mail: tksen@iitk.ac.in

S. Sengupta
Department of Mechanical and Aerospace Engineering, OSU, Columbus, OH, USA
e-mail: sengupta.41@osu.edu

V. Mudkavi
Head, CTFD Div. CSIR-NAL, Bangalore 560017, India
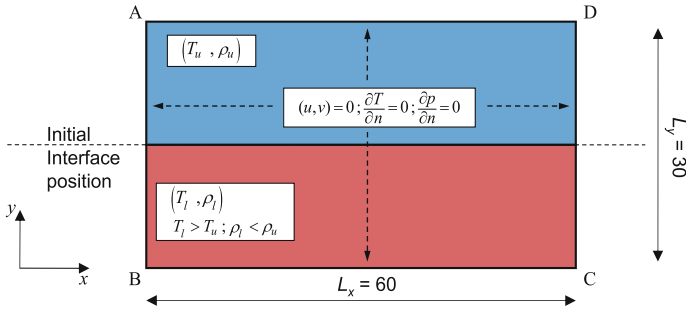e-mail: vm@ctfd.cmmacs.ernet.in

Fig. 1 Physical and computational domain of RTI problem solved

interface, inside a rectangular 2D insulated box. Using same fluid alleviates the problem of tracking the interface. Large discontinuous jump in temperature ($\Delta T = 70K$) will not allow one to apply Boussinesq approximation [6]. Most of RTI simulations [2, 3, 5] are reported using incompressible formulation. Present use of compressible NSE [1, 4] helps remove this major discrepancy. It is noted [6] that *the issue of compressibility is highly challenging and direct numerical simulations are the best way to assess the validity of Boussinesq approximation.* Thus the time evolution of the RTI is traced here by high resolution dispersion relation preserving (DRP) compact scheme for DNS.

Upon removal of the partition, RTI ensues by linear and nonlinear mechanisms with vortices created by the baroclinic source term ($\nabla p \times \nabla \rho / \rho^2$) triggered by background disturbances. The schematic with boundary conditions are shown in Fig. 1. Onset of instability occurs at very high wavenumbers at the junctions of the interface with sidewalls, which propagates along the interface [9]. Thus, the disturbance migrates from very small to larger scales. It has been reasoned [14] that if one uses a diffusive/dissipative numerical method, then these small scales are attenuated and the process of RTI is not captured. This has prompted many researchers [2, 3, 7, 10, 16] to perform 3D simulations with large scale excitation at the interface, hoping that the smaller scales would be created via vortex stretching subsequently via direct cascade. Such external forcing was also necessary for 3D simulations as the variables were treated as periodic in each horizontal planes.

2 Validation of RTI with Experiment

Present non-periodic simulations reproduce all the experimental features [9], as compared in Fig. 2. Details of numerical methods and auxiliary conditions are described in [14]. In the figure, density contours are shown for early times to trace the RTI onset process. Even at later times ($t = 12, 21$ and 34) the match between
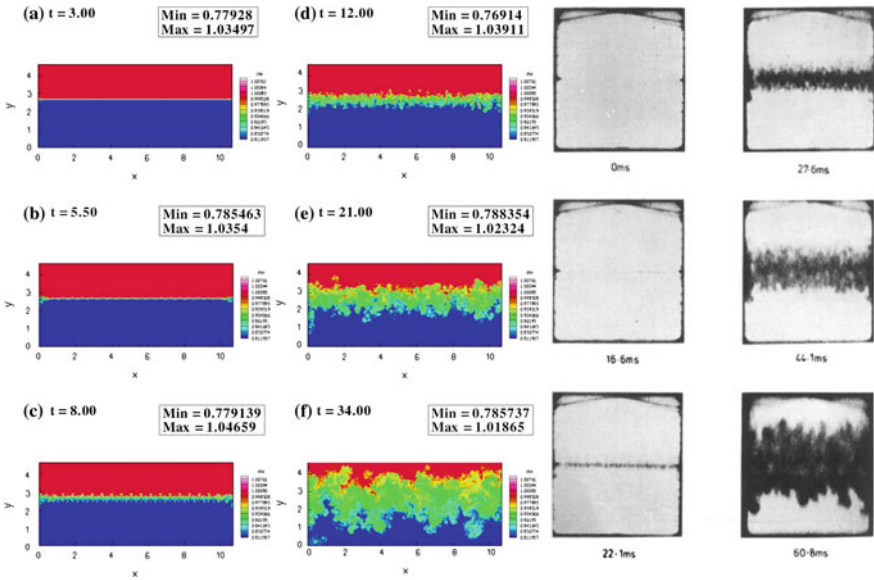
Fig. 2 Comparison of computed (*left*) solution with experimental results of [9] for RTI problem

experiment and computation is excellent. One notes the origin of disturbances at the side-walls and Subsequently, very small scale disturbances all along the interface. Such excellent match with experiment suggests superiority of non-periodic over periodic formulation.

One of the motivations of the present work originated from the observation [2] that *the availability of even more powerful computers has led to a somewhat ironic state of affairs, in that agreement between simulations and experiments is worse today than it was several decades ago.* To understand this problem, we performed two simulations, with CFL number reduced from 0.09 to 0.009. These exercises will help us understand why results deteriorate with refined calculation.

While contamination from side walls continue after the onset, in the interior also the disturbances grow with structures known as spikes and bubbles. These are shown in Fig. 3 for both the CFL number cases, with the lower CFL number case (in frame (a)) showing slower growth of forming spikes and bubbles. It is important to note that both these elements are heavier than surrounding fluids, yet the one in top is termed as bubble. With passage of time nonlinear growth helps formation of vortices which promote mixing.

(a) **Refined Time Step** GRID SIZE : 3000x1800

(b) GRID SIZE : 3000x1800
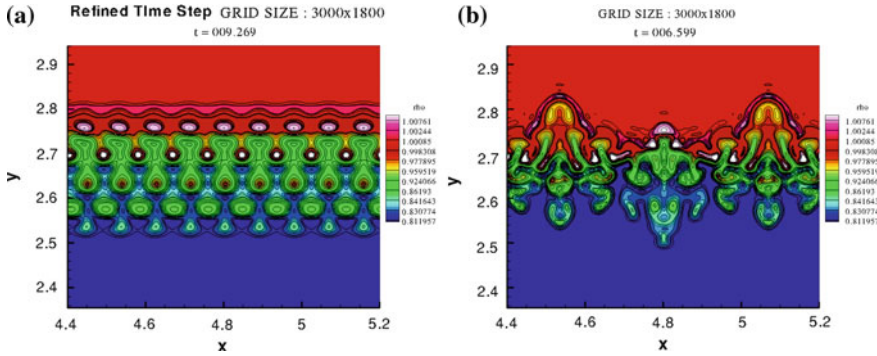
Fig. 3 Spikes and bubbles formation during RTI by numerical solution using CFL number of 0.009 (*left*) and 0.09 (*right*)

3 Error Dynamics and Spectral Analysis

To understand the numerical method for computing RTI, we adopt the 1D wave equation

$$\frac{\partial u}{\partial t} + c\frac{\partial u}{\partial x} = 0 \tag{1}$$

One can express the unknown in a hybrid representation as $u(x, t) = \int U(k, t) e^{ikx} dk$, with a numerical amplification factor defined as, $G = U(k, t + \Delta t)/U(k, t)$. If the initial condition is given by, $u(x, t = 0) = \int A_0(k) e^{ikx} dk$, then the numerical solution can be expressed as $u_N(x, t) = \int A_0(k)|G|^{t/\Delta t} e^{ik(x-c_N t)} dk$, where the numerical phase speed (c_N) is k dependent and not the constant physical phase speed, c. Thus, the numerical dispersion relation is given by $\omega_N = c_N k$, instead of the physical dispersion relation, $\omega = ck$, where ω and ω_N are physical and numerical circular frequency, respectively. Details of this analysis is available in [12, 13]. If we define error by $e(x, t) = u(x, t) - u_N(x, t)$, then the error propagation equation is given by

$$\frac{\partial e}{\partial t} + c\frac{\partial e}{\partial x} = \left(1 - \frac{c_N}{c}\right)\frac{\partial u_N}{\partial x} - \int\int\frac{dc_N}{dk}\left[ik' A_0|G|^{t/\Delta t} e^{ik'(x-c_N t)} dk'\right] dk$$

$$-\int\frac{Ln|G|}{\Delta t} A_0|G|^{t/\Delta t} A_0|G|^{t/\Delta t} e^{ik(x-c_N t)} dk \tag{2}$$

The second term on the right hand side can be further simplified as $\frac{dc_N}{dk} = (V_{gN} - c_N)/k$, with the numerical group velocity given by, $V_{gN} = d\omega_N/dk$. Thus, the error dynamics for convection dominated problems are given by the error metrics: $|G|$, c_N/c and V_{gN}/c, as functions of nondimensional number kh (with h as the uniform spacing) and the CFL number ($N_c = c\Delta t/h$). For least error, one must have a
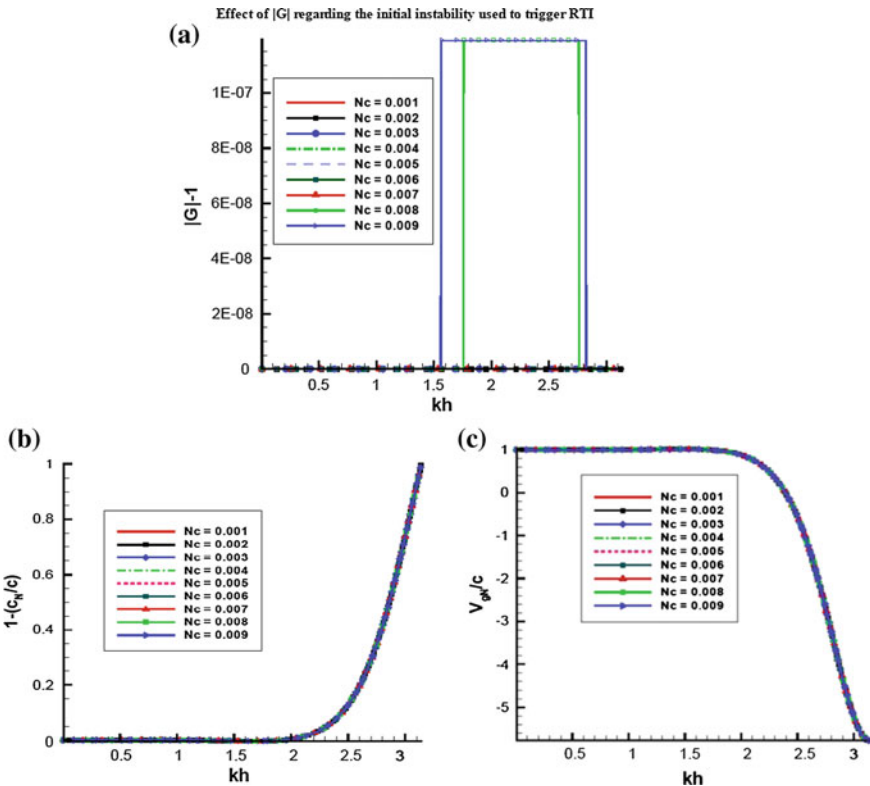
Fig. 4 Numerical properties of used method for solving 1D convection equation: Numerical amplification factor (*top*), normalized numerical phase speed and numerical group velocity (*bottom*)

neutrally stable method ($|G| \simeq 1$) which is dispersion error free (i.e., $v_{gN}/c \simeq 1$ and $c_N/c \simeq 1$) for combinations of N_c and kh values, near the origin in (kh, N_c)-plane.

These properties are shown in Fig. 4, for N_c from 0.001 to 0.009 with higher digit precision. In frame (a), the quantity $(|G| - 1)$ is shown. One notices that this retains a numerical zero value for $N_c = 0.007$. There is mild instability in an intermediate range of k for $N_c = 0.008$ and 0.009. This explains, why we do not need extrinsic excitation to trigger RTI. For $N_c = 0.09$ case, the ensuing instability will be even stronger across wider range of k's, as evident in Fig. 3. In frames (b) and (c) of Fig. 4, one does not notice any discernible difference of dispersion properties for the range of N_c shown. This also establishes that $|G|$ make all the differences between the two N_c values differing by a factor of ten. We note that in [2], the value of N_c is larger than 0.09, yet the authors required external large scale forcing, as the used filters and sub-grid scale models employed attenuated disturbances with $|G| \leq 1$.
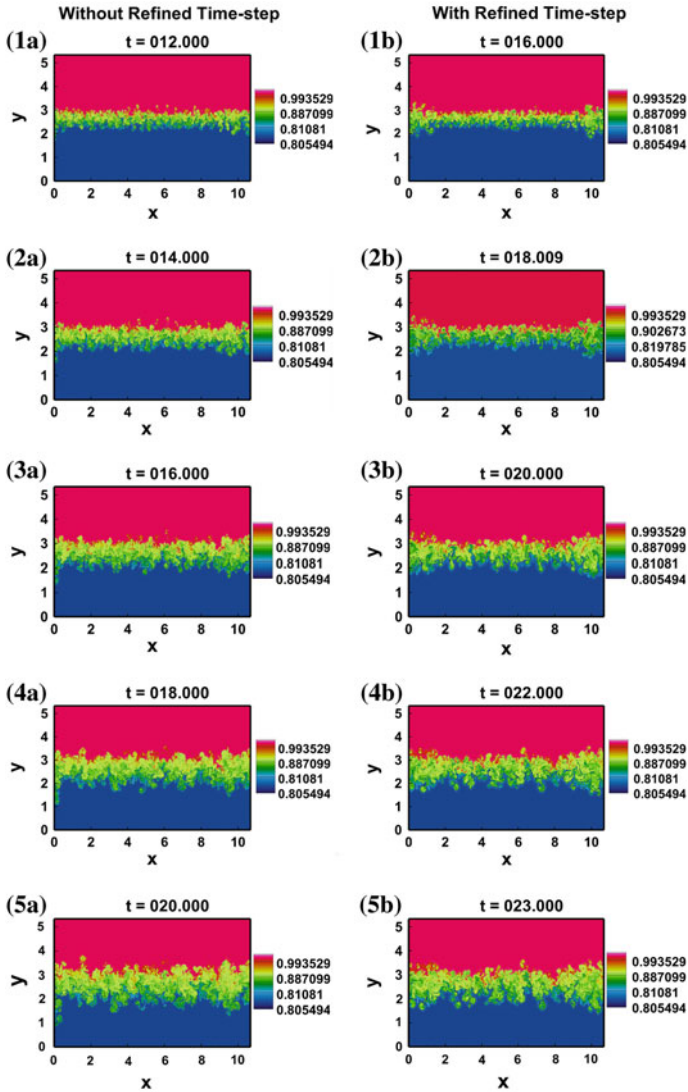
Fig. 5 Computed RTI solutions using CFL no. of 0.09 (*left*) and 0.009 (*right*)

4 Summary and Conclusion

One of the interesting aspects of nonlinear stage of RTI and resultant mixing near the interface is the final state of the system. For both the N_c cases, the density contours are shown in Fig. 5 at later times. It is evident that the vortices at the interface promote mixing and in the long run, flows look similar. The width of the mixing region though

evolves at different rates. This inference does not imply that 2D non-periodic flow and 3D periodic flow (in the horizontal plane) would be eventually same. It is due to different dynamics of periodic and non-periodic flows, which causes the energy to appear from the opposite end of the spectrum and the migration of energy across different scales proceed exactly in opposite direction, so much so that the comments in [2] is now understood in its true spirit. The recorded failure in [2] is also compounded by overtly dissipative numerical method, which forced the authors to apply external forcing at the interface at the large scale and expect vortex stretching to take the flow in the right direction via direct cascade mechanism.

References

1. Bhole A, Sengupta S, Sengupta A, Shruti KS, Sharma N, Sawant N (2015) Rayleigh–Taylor instability of a miscible fluid at the interface: direct numerical simulation. In: Proceedings of the IUTAM Symposium. World Sci. Publ. Co., Singapore
2. Cabot WH, Cook AW (2006) Reynolds number effects on Rayleigh–Taylor instability with implications for type 1a supernoveau. Nature 2:562–568
3. Cook AW, Cabot W, Miller PL (2004) The mixing transition in Rayleigh–Taylor instability. J Fluid Mech 511:333–362
4. Hoffmann KA, Chiang ST (1998) Computational fluid dynamics, II, engineering education systems. Kansas, USA
5. Lawrie AGW, Dalziel SB (2011) Rayleigh–Taylor mixing in an otherwise stable stratifications. J Fluid Mech 688:507–527
6. Mikaelian KO (2014) Boussinesq approximation for Rayleigh–Taylor and Richtmyer-Meshkov instabilities. Phys Fluids 26:054103
7. Ramaprabhu P, Dimonte G, Woodward P, Fryer C, Rockefeller G, Muthuram K, Lin PH, Jayaraj J (2012) The late-time dynamics of the single-mode Rayleigh–Taylor instability. Phys Fluids 24:074107
8. Rayleigh L (1887) On the stability or instability of certain fluid motions. Scient Papers 3:17–23
9. Read KI (1984) Experimental investigation of turbulent mixing by Rayleigh–Taylor instability. Phys D 12:45–58
10. Reckinger SJ, Livescu D, Vasilyev OV (2010) Adaptive wavelet collocation method simulations of Rayleigh–Taylor instability. Phys Scr T 142:014064
11. Sengupta TK (2012) Instabilities of flows and transition to turbulence. CRC Press, Taylor & Francis Group, Florida, USA
12. Sengupta TK (2013) High accuracy computing methods: fluid flows and wave phenomenon. Cambridge University Press, USA
13. Sengupta TK, Dipankar A, Sagaut P (2007) Error dynamics: beyond von neumann analysis. J Comput Phys 226:1211–1218
14. Sengupta TK, Sengupta A, Sengupta S, Bhole A, Shruti KS (2015) Non-equilibrium thermodynamics of Rayleigh–Taylor instability. Int J Thermophys (Under Review)
15. Taylor GI (1950) The instability of liquid surfaces when accelerated in a direction perpendicular to their planes. Proc Roy Soc Lond 201:192–196
16. Wei T, Livescu D (2012) Late-time quadratic growth in single-mode Rayleigh–Taylor instability. Phys Rev E 86:046405

Constructing Physically Consistent Subgrid-Scale Models for Large-Eddy Simulation of Incompressible Turbulent Flows

Maurits H. Silvis and Roel Verstappen

Abstract We studied the construction of subgrid-scale models for large-eddy simulation of incompressible turbulent flows, focusing on consistency with important mathematical and physical properties. In particular, we considered the symmetries of the Navier-Stokes equations, and the near-wall scaling and dissipation behavior of the turbulent stresses. After showing that existing models do not all satisfy the desired properties, we discussed a general class of subgrid-scale models based on the local filtered velocity gradient. We provided examples of models from this class that preserve several of the symmetries of the Navier-Stokes equations and exhibit the same near-wall scaling behavior as the turbulent stresses. Furthermore, these models are capable of describing nondissipative effects.

1 Introduction

It is well known that the governing equations of fluid dynamics, the Navier-Stokes equations, are form invariant under transformations like instantaneous rotations of the coordinate system and the Galilean transformation [13]. Such transformations, also referred to as symmetries, play an important physical role, because they make sure that the description of fluids is the same in all inertial frames of reference. Furthermore, they relate to conservation and scaling laws [14]. To ensure physical consistency it is desirable that the basic equations of large-eddy simulation, which are used to study the large-scale behavior of turbulent flows, satisfy the same principles. Speziale [17] was the first to emphasize the importance of Galilean invariance of subgrid-scale models for large-eddy simulation. Later, Oberlack [10] formulated

M.H. Silvis (✉) · R. Verstappen
University of Groningen, PO Box 407, 9700 AK Groningen, The Netherlands
e-mail: m.h.silvis@rug.nl

R. Verstappen
e-mail: r.w.c.p.verstappen@rug.nl

requirements to make subgrid-scale models compatible with all the symmetries of the Navier-Stokes equations. Aside from preserving symmetries, it is desirable that subgrid-scale models share some basic properties with the turbulent stresses, such as the observed near-wall scaling [2] and the dissipation behavior [20]. In the current work we aim to construct subgrid-scale models that preserve these and other properties of the Navier-Stokes equations and the turbulent stresses.

In Sect. 2 we will outline several model requirements, after which, in Sect. 3, we analyze the properties of existing subgrid-scale models. Section 4 is devoted to the construction of new subgrid-scale models. Conclusions are presented in Sect. 5.

2 Model Constraints

In large-eddy simulation, the large-scale behavior of incompressible turbulent flows is described by the filtered Navier-Stokes equations, [15]

$$\frac{\partial \bar{u}_i}{\partial x_i} = 0 , \qquad \frac{\partial \bar{u}_i}{\partial t} + \bar{u}_j \frac{\partial \bar{u}_i}{\partial x_j} = -\frac{1}{\rho} \frac{\partial \bar{p}}{\partial x_i} + \nu \frac{\partial^2 \bar{u}_i}{\partial x_j \partial x_j} - \frac{\partial}{\partial x_j} \tau_{ij} . \qquad (1)$$

The turbulent stresses, $\tau_{ij} = \overline{u_i u_j} - \bar{u}_i \bar{u}_j$, are not solely expressed in terms of the filtered velocity field and therefore have to be modeled. In what follows we will discuss requirements that make sure that specific properties of the Navier-Stokes equations and the turbulent stresses are preserved in this modeling process.

2.1 Symmetry Requirements

We would like to ensure that the basic equations of large-eddy simulation, (1) with a subgrid-scale model in place of the turbulent stresses, admit the same symmetries as the unfiltered Navier-Stokes equations. Assuming that the filtering operation does not destroy symmetry properties, we need the following transformation behavior for the modeled subgrid-scale stresses, τ^{mod} [10].

$$\hat{\tau}_{ij}^{\mathrm{mod}} = \tau_{ij}^{\mathrm{mod}} , \qquad\qquad (2)$$

$$\hat{\tau}_{ij}^{\mathrm{mod}} = Q_{im} Q_{jn} \tau_{mn}^{\mathrm{mod}} , \qquad\qquad (3)$$

$$\hat{\tau}_{ij}^{\mathrm{mod}} = \mathrm{e}^{-2a+2b} \tau_{ij}^{\mathrm{mod}} , \qquad\qquad (4)$$

$$\hat{\tau}_{ij}^{\mathrm{mod}} = R_{im}(t) R_{jn}(t) \tau_{mn}^{\mathrm{mod}} . \qquad\qquad (5)$$

In (2) the hat indicates the time (S1) or pressure translation (S2), or the generalized Galilean transformation (S3). Conditions (3) and (4) ensure invariance under, respectively, instantaneous rotations and reflections (S4), and scaling transformation (S5),

for an orthogonal matrix Q, and real a and b. Material frame-indifference in the limit of a two-component flow (S6) holds when (5) is satisfied for a constant-in-rate rotation about an axis perpendicular to the flow directions, described by $R(t)$. In principle, (2) also has to hold under time reversal (S7) [10, 11, 14].

2.2 Near-Wall Scaling Requirements

Using numerical simulations, Chapman and Kuhn [2] have revealed the near-wall scaling behavior of the time-averaged turbulent stresses. We will require that the modeled stresses show the same asymptotic behavior, but then instantaneously (P1). Denoting the wall-normal distance by x_2, we can express this property as

$$
\begin{aligned}
\tau_{11}^{\text{mod}}, \tau_{13}^{\text{mod}}, \tau_{33}^{\text{mod}} &= \mathcal{O}(x_2^2) \,, \\
\tau_{12}^{\text{mod}}, \tau_{23}^{\text{mod}} &= \mathcal{O}(x_2^3) \,, \\
\tau_{22}^{\text{mod}} &= \mathcal{O}(x_2^4) \,.
\end{aligned}
\tag{6}
$$

This ensures that, for instance, dissipative effects fall off quickly enough near walls.

2.3 Requirements Relating to the Production of Subgrid-Scale Kinetic Energy

We now focus on the production of subgrid-scale kinetic energy, also referred to as subgrid dissipation. Given the rate-of-strain tensor, see (12), it can be expressed as

$$
D_\tau = -\text{tr}(\tau \bar{S}) \,.
\tag{7}
$$

Vreman's Model Requirements Vreman [20] requires that the modeled production of subgrid-scale kinetic energy vanishes for flows for which the actual production is known to be zero. Preferably, also the converse is true. In summary, P2a,b:

$$
D_{\tau\,\text{mod}} = 0 \text{ when } D_\tau = 0 \,,
\tag{8}
$$

$$
D_{\tau\,\text{mod}} \neq 0 \text{ when } D_\tau \neq 0 \,.
\tag{9}
$$

These conditions are aimed at making sure that subgrid-scale models are neither overly (P2a), nor underly dissipative (P2b).

Nicoud et al. Model Requirements On the basis of physical grounds, Nicoud et al. [8] argue that certain flows cannot be maintained if energy is transported to subgrid scales. They therefore require that the modeled subgrid dissipation vanishes for all two-component flows (P3a) and for the pure axisymmetric strain (P3b). Note

that these requirements are not compatible with the mathematical properties of the turbulent stresses as found by Vreman [20] and thus not with requirements P2a,b.

Consistency with the Second Law of Thermodynamics In turbulent flows, energy can be transported from large to small scales (forward scatter) and vice versa (backscatter). The second law of thermodynamics requires that the net transport of energy is of the former type, P4 [14]:

$$D_{\tau^{\text{mod}}} \geq -2\nu \, \text{tr}(\bar{S}^2) \, . \tag{10}$$

3 Analysis of Existing Subgrid-Scale Models

Before aiming to create subgrid-scale models that satisfy the constraints discussed in the previous section, we present a summary of the properties of several existing models in Table 1. A detailed discussion of results is omitted, but observe that the models do not necessarily satisfy all the desired properties. Because we assume the use of an isotropic filter, results relating to properties P2a,b differ slightly from those of Vreman [20].

4 Examples of Physically Consistent Subgrid-Scale Models

The subgrid-scale models of Sect. 3 are all based on the local filtered velocity gradient. Looking for models of a similar form to satisfy the constraints of Sect. 2, we take [4, 6, 12]

$$\tau^{\text{mod}} = \alpha_0 I + \alpha_1 \bar{S} + \alpha_2 \bar{S}^2 + \alpha_3 \bar{\Omega}^2 + \alpha_4 (\bar{S}\bar{\Omega} - \bar{\Omega}\bar{S}) + \dots \, , \tag{11}$$

where the filtered rate-of-strain and rate-of-rotation tensors are given by

$$\bar{S}_{ij} = \frac{1}{2} \left(\frac{\partial \bar{u}_i}{\partial x_j} + \frac{\partial \bar{u}_j}{\partial x_i} \right) \, , \qquad \bar{\Omega}_{ij} = \frac{1}{2} \left(\frac{\partial \bar{u}_i}{\partial x_j} - \frac{\partial \bar{u}_j}{\partial x_i} \right) \, , \tag{12}$$

and, by isotropy (S4), the coefficients can depend only on the tensor invariants

$$I_1 = \text{tr}(\bar{S}^2) \, , \ I_2 = \text{tr}(\bar{\Omega}^2) \, , \ I_3 = \text{tr}(\bar{S}^3) \, , \ I_4 = \text{tr}(\bar{S}\bar{\Omega}^2) \, , \ I_5 = \text{tr}(\bar{S}^2\bar{\Omega}^2). \tag{13}$$

We now aim to set this dependence in such a way that more constraints of Sect. 2 are fulfilled. Here it is important to keep in mind that the requirements of Nicoud et al. (P3a,b) are incompatible with those of Vreman (P2a,b). Furthermore, no two-dimensional material frame-indifferent quantities (S6) were found that satisfy both of Vreman's requirements. This may point to a limitation of the model ansatz (11).

Combining compatible constraints, we obtain a class of what we will call physically consistent subgrid-scale models. The simplest models in this class with the

Table 1 Summary of the properties of several subgrid-scale models. The properties considered are S1–4: time, pressure, generalized Galilean, and rotation and reflection invariance; S5: scaling invariance; S6: two-dimensional material frame-indifference; S7: time reversal invariance; P1: the proper near-wall scaling behavior; P2a: zero subgrid dissipation for laminar flow types; P2b: nonzero subgrid dissipation for nonlaminar flow types; P3a: zero subgrid dissipation for two-component flows; P3b: zero subgrid dissipation for the pure axisymmetric strain; P4: consistency with the second law of thermodynamics

	Smag. [16]	WALE [9]	Vreman [20]	σ [8]	QR [19]	S3PQR [18]	Clark [3]	EASSM [7]	Ex. 1 (14)	Ex. 2 (15)
S1–4	Yes	Yes	Yes	Yes	Yes	Yes	Yes	Yes	Yes	Yes
S5[a]	No	No	No	No	No	No	No	No	No	No
S6	Yes	No	No	Yes	Yes	Yes[b]	No	No	Yes	Yes
S7[a]	No	No	No	No	No	Yes[b]	Yes	No	Yes	No
P1	No	Yes	No	Yes	No	Yes	No	No	Yes	Yes
P2a	No	No	No	Yes	Yes	Yes[b]	Yes	No	Yes	Yes
P2b	Yes	Yes	Yes	No	No	No	No	Yes	No	No
P3a	No	No	No	Yes	Yes	Yes[b]	Yes	No	Yes	Yes
P3b	No	No	No	Yes	No	No	No	No	No	Yes
P4	Yes	Yes	Yes	Yes	Yes	Yes[b]	No	Yes	No	Yes

[a] The dynamic procedure [5] may restore these symmetries [1, 10, 14]
[b] Depending on the value of the model parameter

proper near-wall scaling behavior (P1) have coefficients that depend only on the invariants of the rate-of-strain tensor, I_1 and I_3. For example (Ex. 1),

$$\tau^{\mathrm{mod}} = c_0 \bar\delta^2 \frac{I_3^4}{I_1^5} I + c_1 \bar\delta^2 \frac{I_3^3}{I_1^4} \bar{S} + c_4 \bar\delta^2 \frac{I_3^4}{I_1^6} (\bar{S}\bar\Omega - \bar\Omega\bar{S}) \ . \tag{14}$$

Here, $\bar\delta$ denotes the filter length. Without additional procedures, the above model satisfies all the symmetries of the Navier-Stokes equations, apart from scale invariance (S5). Being orthogonal to each other, the three terms all have a different role. The first term on the right-hand side models the generalized subgrid-scale kinetic energy, the second describes dissipative processes, whereas the last term represents energy transport among large scales.

In view of the requirements of Nicoud et al. (P3a,b), a possibly attractive model of eddy viscosity type is based on the nonnegative quantity $I_5 - \frac{1}{2}I_1 I_2$, Ex. 2:

$$\tau_{\mathrm{e}}^{\mathrm{mod}} - \frac{1}{3}\mathrm{tr}(\tau_{\mathrm{e}}^{\mathrm{mod}})I = -2(C\bar\delta)^2 \sqrt{I_1} \left(\frac{1}{2} - \frac{I_5}{I_1 I_2}\right)^{3/2} \bar{S} \ . \tag{15}$$

It has the desired near-wall scaling behavior (P1) and it vanishes only in two-component flows, and in states of pure shear and pure rotation.

For comparison, the properties of these example models are summarized in Table 1.

5　Summary

We studied the construction of subgrid-scale models for large-eddy simulation of incompressible turbulent flows, aiming to preserve important mathematical and physical properties of the Navier-Stokes equations and the turbulent stresses. To this end, we first outlined model requirements coming from the symmetries of the Navier-Stokes equations, and from the near-wall scaling and dissipation behavior of the turbulent stresses. An analysis of existing subgrid-scale models showed that they do not all satisfy these requirements. We then considered a general class of subgrid-scale models based on the local filtered velocity gradient and provided examples of 'physically consistent models' that satisfy different combinations of model requirements. Although no models were obtained that exhibit all the desired properties, we believe the current reasoning has led to an interesting class of models, particularly because it allows for the description of nondissipative processes in turbulent flows.

References

1. Carati D, Winckelmans G, Jeanmart H (2001) J Fluid Mech 441:119. doi:10.1017/S0022112001004773
2. Chapman D, Kuhn G (1986) J Fluid Mech 170:265. doi:10.1017/S0022112086000885
3. Clark R, Ferziger J, Reynolds WC (1979) J Fluid Mech 91:1. doi:10.1017/S002211207900001X
4. Gatski T, Jongen T (2000) Progr Aerosp Sci 36:655. doi:10.1016/S0376-0421(00)00012-9
5. Germano M, Piomelli U, Moin P, Cabot W (1991) Phys Fluids A-Fluid 3:1760. doi:10.1063/1.857955
6. Lund T, Novikov E (1992) CTR Ann Res Briefs:27–43
7. Marstorp L, Brethouwer G, Grundestam O, Johansson A (2009) J Fluid Mech 639:403. doi:10.1017/S0022112009991054
8. Nicoud F, Baya H, Toda, Cabrit O, Bose S, Lee J (2011) Phys Fluids 23:085106. doi:10.1063/1.3623274
9. Nicoud F, Ducros F (1999) Flow Turbul Combust 62:183. doi:10.1023/A:1009995426001
10. Oberlack M (1997) Annual research briefs. Stanford University/NASA Ames, Center for Turbulence Research, pp 3–22
11. Oberlack M (2002) Theories of turbulence. In: Oberlack M, Busse F (eds)International centre for mechanical sciences, vol 442. Springer Vienna, 2002, pp 301–366. doi:10.1007/978-3-7091-2564-9
12. Pope S (1975) J Fluid Mech 72:331. doi:10.1017/S0022112075003382
13. Pope S (2011) Turbulent Flows. Cambridge University Press, Cambridge
14. Razafindralandy D, Hamdouni A, Oberlack M (2007) Eur J Mech B-Fluid 26:531. doi:10.1016/j.euromechflu.2006.10.003
15. Sagaut P (2006) Large Eddy simulation for incompressible flows, 3rd edn. Scientific computation. Springer, Berlin. doi:10.1007/b137536
16. Smagorinsky J (1963) Mon Weather Rev 91:99. doi:10.1175/1520-0493091<0099:GCEWTP>2.3.CO;2
17. Speziale C (1985) J Fluid Mech 156:55. doi:10.1017/S0022112085001987
18. Trias FX, Folch D, Gorobets A, Oliva A (2015) Phys Fluids 27:065103. doi:10.1063/1.4921817
19. Verstappen R, Rozema W, Bae H (2014) Proceedings of the summer program. Center for Turbulence Research, Stanford University/NASA Ames, pp 417–426
20. Vreman A (2004) Phys Fluids 16:3670. doi:10.1063/1.1785131

A Priori Study for the Modeling of LES Subgrid Scale Terms in Resolved Scale Multiphase Flows

Mathilde Tavares, Stephane Vincent, Meryem Ould-Rouiss and Jean-Luc Estivalezes

Abstract Modeling accurately the energy transfer across the interface in multiphase flows is difficult. To deal with this phenomenon, the derivation of the governing equations for two-phase flows have been formulated. A priori tests are used in order to evaluate the relative magnitude of unclosed LES specific terms to multiphase flows. There consist in the explicit filtering of 3D Direct Numerical Simulation in order to find LES models appropriated to the different subgrid contributions. In our study, explicit volume filtering and phase weighted filtering have been used in a case of phase separation flow in a cubic closed box between water, the heavier fluid and oil, the lighter fluid, in order to understand the effect of the filtering process on the subgrid contributions.

1 Introduction

Two-phase flows are involved in many industrial and environmental applications such as spray formation, wave breaking or oil transportation. The modeling and simulation of complex interactions between turbulence and interface in multiphase flows remain challenging. As in single phase flow, large Eddy Simulation (LES) solve the problem of large scale while smaller subgrid scales are computed through physical or mathematical models in two-phase flows, involving this way several unclosed subgrid terms characteristic of turbulent and interfacial motion subgrid correlations. Several works [3, 5], have established a hierarchy of unclosed subgrid terms through a priori studies to improve LES simulation of two-phase flows. The main objective of the present work is to characterize the hierarchy of subgrid terms

M. Tavares (✉) · S. Vincent · M. Ould-Rouiss
Laboratoire Modélisation et Simulation Multi-Echelle (MSME),
UMR CNRS 8208, Université Paris-Est Marne-La-Vallée, 77454
Marne-La-Vallée, France
e-mail: mathilde.tavares@u-pem.fr

J.-L. Estivalezes
Onera The French Aerospace Lab, 31055 Toulouse, France

249

for two-phase flows in the case of a phase inversion flow. In the following sections the 1-fluid model is presented and filtered to highlight the unclosed LES terms for two-phase flows. Then, we present the reference simulation, a phase separation flow from a numerical benchmark [6]. Finally the results of a priori tests are discussed to evaluate the relative importance of LES subgrid terms in the reference case.

2 Numerical Modeling

2.1 Navier Stokes Equations/1-Fluid Model for Two-Phase Flows

The two-phase flow numerical modeling is restricted to immiscible, incompressible and isothermal fluids. For two non miscible fluid where an index k refers to one phase if $k = 1$ and the other phase if $k = 2$, the dynamic of each phase k is governed by the Navier-Stokes equations. Thanks to jump relations, mass and momentum conservation is ensured at the interface. By adding these boundary conditions to Navier Stokes equations, it is possible to build in the framework of the 1-fluid formalism of [2] a unique set of equation valid in both phase by introducing the volume fraction function C which is equal to 1 in one phase an 0 elsewhere and describes the interface evolution through a material advection equation Fig. 1a.

$$\nabla \cdot \mathbf{u} = 0 \tag{1a}$$

$$\frac{\partial \rho \mathbf{u}}{\partial t} + \nabla \cdot (\rho \mathbf{u} \otimes \mathbf{u}) = -\nabla P + \rho \mathbf{g} + \nabla \cdot (2\mu \mathbf{S}) + \sigma \kappa \mathbf{n}_i \delta_i \tag{1b}$$

$$\frac{\partial C}{\partial t} + \mathbf{u} \cdot \nabla C = 0 \tag{1c}$$

$\mathbf{u}$ is the velocity, P the pressure, t the time, $\mathbf{g}$ the gravity vector, ρ the density, μ the dynamic viscosity. $\mathbf{S}_k = \frac{1}{2}(\nabla \mathbf{u}_k + \nabla^T \mathbf{u}_k)$ is the viscous stress tensor. $\sigma \kappa \mathbf{n}_i$ is the surface tension force where σ denotes the surface tension coefficient, κ the local curvature and $\mathbf{n}_i$ the normal to the interface.

Local quantities such as density ρ or viscosity μ can be defined by using the volume fraction function C.

$$\rho = \rho_2 + (1 - C)\rho_1 \tag{2a}$$

$$\mu = \mu_2 + (1 - C)\mu_1 \tag{2b}$$

The curvature κ depends on the interface topology. It can modeled using the Continuum Surface formulation of [1]:

$$\kappa \mathbf{n}_i \delta_i = \nabla \cdot \left(\frac{\nabla C}{||\nabla C||} \right) \nabla C, \quad \mathbf{n} = \frac{\nabla C}{||\nabla C||}, \quad \mathbf{n}_i \delta_i = \nabla C \tag{3}$$

(a) Initial conditions
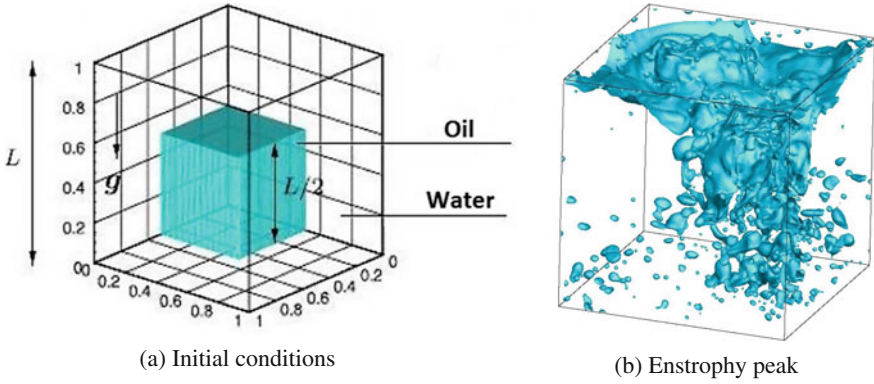
(b) Enstrophy peak

Fig. 1 Initial conditions of phase inversion flow problem (**a**) and DNS solution at enstrophy peak (**b**)

2.2 Filtered Navier-Stokes Equations for Two-Phase Flow

LES formalism required the application of a low-pass frequency filtering to the field to resolve large turbulent scales while the effects of smaller scales are modeled [4]. The filtering operation of a hydrodynamic field is defined on a domain Ω by:

$$\overline{\Phi(x,t)} = G * \Phi \;\; \rightarrow \;\; \overline{\Phi(x,t)} = \int_{\Omega} \int_{-\infty}^{t} G(\bar{\Delta}(x,t), x - x', t - t')\Phi(x',t')dx'dt'$$

(4)

$\bar{\Delta}$ is the cutoff lengthscale of the filter, G a formal operator. It can be assumed that the filtering operator commutes with time and spatial derivatives. Then, the volume filtering of incompressible Navier-Stokes equations depend on $\{\bar{\mathbf{u}}, \bar{P}, \bar{C}, \bar{\rho}, \bar{\mu}, \hat{\kappa}\}$ and can be written as:

$$\nabla \cdot \bar{\mathbf{u}} = 0 \tag{5a}$$

$$\frac{\partial \bar{\rho}\bar{\mathbf{u}}}{\partial t} + \nabla \cdot (\bar{\rho}\bar{\mathbf{u}} \otimes \bar{\mathbf{u}}) - \bar{\rho}\mathbf{g} + \nabla \bar{P} - \nabla \cdot (2\bar{\mu}\bar{\mathbf{S}}) - \sigma\hat{\kappa}\nabla\bar{C} = -\nabla \cdot (\tau_{conv} - \tau_{diff}) +$$

$$\tau_{superf} - \frac{\partial \tau_{temps}}{\partial t} \tag{5b}$$

$$\frac{\partial \bar{C}}{\partial t} + \bar{\mathbf{u}} \cdot \nabla\bar{C} = \tau_{interf} \tag{5c}$$

This approach is divergence free but required modeling of 5 subgrid terms. It can be more convenient to use the Favre average or mass weighted filtering for the velocity field such as

$$\tilde{\mathbf{u}} = \frac{\overline{\rho\mathbf{u}}}{\bar{\rho}} \tag{6}$$

This approach is based on $\{\tilde{\mathbf{u}}, \bar{P}, \bar{C}, \bar{\rho}, \bar{\mu}, \hat{\kappa}\}$.

Table 1 Subgrid terms for two-phase flow

Subgrid terms	Volume filter	Mass weighted filter (Favre)
$\partial \tau_{temps}/\partial t$	$\frac{\partial \overline{\rho \mathbf{u}}}{\partial t} - \frac{\partial \bar{\rho}\bar{\mathbf{u}}}{\partial t}$	$(\rho_2 - \rho_1)\tilde{\mathbf{u}}\tau_{interf}$
$\nabla \cdot \tau_{conv}$	$\nabla \cdot (\overline{\rho\mathbf{u} \otimes \mathbf{u}} - \bar{\rho}\bar{\mathbf{u}} \otimes \bar{\mathbf{u}})$	$\nabla \cdot (\bar{\rho}(\widetilde{\mathbf{u} \otimes \mathbf{u}} - \tilde{\mathbf{u}} \otimes \tilde{\mathbf{u}}))$
$\nabla \cdot \tau_{diff}$	$\nabla \cdot (\overline{2\mu\mathbf{S}} - 2\bar{\mu}\bar{\mathbf{S}})$	$\nabla \cdot (\overline{2\mu\mathbf{S}} - 2\bar{\mu}\tilde{\mathbf{S}})$
τ_{superf}	$\sigma(\overline{\kappa\nabla C} - \hat{\kappa}\nabla\bar{C})$	$\sigma(\overline{\kappa\nabla C} - \hat{\kappa}\nabla\bar{C})$
τ_{interf}	$\overline{\mathbf{u} \cdot \nabla C} - \bar{\mathbf{u}} \cdot \nabla\bar{C}$	$\overline{\mathbf{u} \cdot \nabla C} - \tilde{\mathbf{u}}\nabla\bar{C}$

Table 2 Fluids characteristic for the phase inversion problem

	ρ (kg/m^3)	μ $(Pa\,s)$	σ $(N\,m)$	Re	We	L (m)	η (m)	D_g (m)
Oil	900	0, 1	0, 45	221472	109	1	$4, 515 \times 10^{-4}$	$9, 174 \times 10^{-3}$
Water	1000	0, 001	–	–	–	–	–	–

With this formulation, the velocity field is no more divergence free with the additional source term $\frac{\tau_{interf}(\rho_2-\rho_1)}{\bar{\rho}}$ but only 4 subgrid terms require modeling. A summary of the subgrid term for the classic volume filtering and the phase weighted filtering are given in the Table 1.

3 A Priori Filtering of Phase Separation Flow

3.1 Description of the Problem

Our study is based on the numerical benchmark of [6] where a parametric study on macroscopic quantities such as kinetic or potential energy have been performed with different codes and meshes to characterize vorticity generation on a phase separation flow between water and oil Fig. 1.

We have chosen to deal only with the turbulent case where the properties are given in Table 2.

We have post-processed results of DyJeat (Dynamic of Jet ATomization), a computational in-house code developed at ONERA/DMAE. DyJeat is implemented with the finite volume method for the discretization of Navier-Stokes equations on a staggered mesh. The Ghost-Fluid method is used to deal with surface tension forces, density and viscosity jumps at the interface. The Level-Set approach is also used for tracking interfaces and a Level-Set/VOF coupling is ensured to improve mass conservation. Details of implementation and validation can be found in [6]. All the fields have been taken for a single time at the enstrophy peak Fig. 1b corresponding to the time where the turbulence is maximum. Three meshes (128^3, 256^3, 512^3) have been used in order to study the effect of the mesh on the subgrid contributions. Moreover,
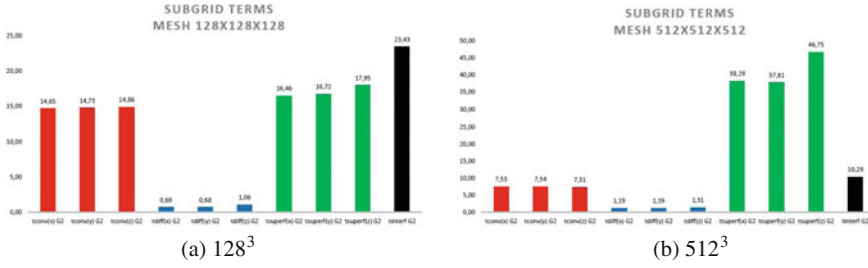
Fig. 2 Subgrid term hierarchy for meshes 128^3 (**a**) and 512^3 (**b**) with volume filtering along x, y, z directions

we have used two different filter size, G2 and G4, and two filter's type, the volume filtering and the mass weighted filtering to evaluate the influence of the type and the size of the filter. The size of the filter G2 is for instance:

$$G^{(2)}(\Phi_{ijk}) = \int_{x_{i-1}}^{x_{i+1}} \int_{y_{j-1}}^{y_{j+1}} \int_{z_{k-1}}^{z_{k+1}} \Phi(x, y, z) dx dy dz \qquad (7)$$

For each subgrid term, a spatial sum have been computed in each direction and compared to the spatial sum of the resolved convective term $\nabla \cdot (\bar{\rho} \bar{\mathbf{u}} \otimes \bar{\mathbf{u}})$ for the momentum equation or the resolved interface advection term $\bar{\mathbf{u}} \cdot \nabla \bar{C}$ for the advection equation to show the order of magnitude of subgrid contributions. Figure 2a, b shows the order of magnitude of subgrid contributions for the meshes 128^3 and 512^3 in each direction. Generally, the highest value of the subgrid contributions is along the z direction which is due to anisotropy of the phase inversion flow. In agreement with [3, 5], our a priori analysis shows that the subgrid viscous term τ_{diff} is always negligible. Besides, τ_{superf}, the subgrid contribution linked to the surface tension, is the dominant term. Indeed, capillarity drives the phase inversion mechanism at the enstrophy peak with important rupture and coalescence phenomena, increasing the contribution of τ_{superf}. The convective τ_{conv} and interfacial τ_{interf} subgrid terms have the same order of magnitude but remain significant. We observe a strong influence of the mesh on unclosed LES terms. Indeed, all the subgrid contributions decrease when the mesh size becomes smaller except for τ_{superf}.

On the other hand, the Fig. 3a shows that subgrid contributions are bigger when we use volume filtering than phase weighted average as shown in literature. According to [3], using volume filtering process overestimates the convective transfer across the interface whereas phase weighted underestimates it. Figure 3b shows that the filter size (G2 and G4) has almost the same effect than the mesh size on the subgrid contributions and for the smaller filter size, unclosed LES terms are weaker even for τ_{superf} in our case.

(a) Comparison filter G2 and G4   (b) Comparison volume and phase weighted filter
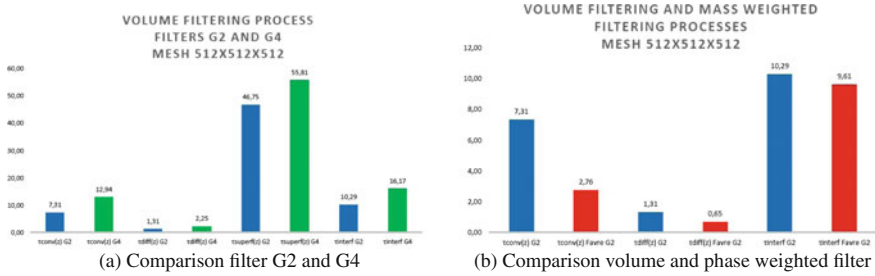
Fig. 3 Subgrid term hierarchy for meshes 512^3 depending on the size of filter (**a**) and the type of the filter (**b**) along z direction

4 Conclusion

In this study, we have shown that the contribution linked to the surface tension has to be taken into consideration. In the case of the phase inversion flow, at the enstrophy peak, τ_{superf} and τ_{interf} has been the predominant term, whatever the mesh considered. It's worth noting that the mesh size here is four times smaller than those studied in literature whereas the Weber is six times smaller. The capillarity effects are then more important and better resolved with our finer grid, increasing the part of the capillary subgrid term. To conclude, this term cannot be neglected and it is then necessary to model it properly to improve LES multiphase flow simulation, in addition to inertial terms. It has to be noted that the τ_{interf} is also not negligible and can lead to non divergence free filtered LES fields.

References

1. Brackbill JU, Kothe DB, Zemach C (1992) A continuum method for modeling surface tension. J Comput Phys 100(2):335–354
2. Kataoka I (1986) Local instant formulation of two-phase flow. Int J Multiphase Flow 12(5):745–758
3. Labourasse E, Lacanette D, Toutant A, Lubin P, Vincent S, Lebaigue O, Caltagirone J-P, Sagaut P (2007) Towards large eddy simulation of isothermal two-phase flows: governing equations and a priori tests. Int J Multiphase Flow 33:1–9
4. Sagaut P (1998) Large Eddy simulation for incompressible flows. Springer
5. Vincent S, Larocque J, Lacanette D, Toutant A, Lubin P, Sagaut P (2008) Numerical simulation of phase separation and a priori two-phase les filtering. Comput Fluid 37:898–906
6. Vincent S, Osmar L, Estivalezes J-L, Zaleski S, Auguste F, Aniszewski W, Ling Y, Menard T, Pedrono A, Magnaudet J, Caltagirone J-P, Berlemont A (2015) A phase inversion benchmark for multiscale multiphase flows. J Comput Phys

A Minimum-Relaxation Model for Large-Eddy Simulation

Roel Verstappen

Abstract This paper is about a relaxation model for large-eddy simulation of turbulent flow that truncates the small scales of motion for which numerical resolution is not available by making sure that they do not get energy from the larger, resolved, eddies. The resolved scales are defined with the help of a box filter. The relaxation parameter is determined in such a way that the production of too small, box-fitting, scales is counteracted by the modeled dissipation. This dissipation-production balance is worked out with the help of Poincaré's inequality, which results in a relaxation model that depends on the invariants of the velocity gradient. This model is discretized and equipped with a Schumann filter. It is successfully tested for isotropic turbulence as well as for turbulent channel flow.

1   Large-Eddy Simulation of Turbulence

As usual, a spatial filter is applied to the (incompressible) Navier-Stokes (NS) equations to obtain a model for the larger eddies. The filtered NS-equations read

$$\partial_t \overline{u} \,+\, \nabla \cdot (\overline{u} \otimes \overline{u}) \,-\, \nu \,\nabla \cdot \nabla \overline{u} \,+\, \nabla \overline{p} \,=\, \nabla \cdot (\overline{u} \otimes \overline{u} - \overline{u \otimes u}) \tag{1}$$

where $\overline{u}$ denotes the filtered velocity field. When the NS-equations are discretized in space, the low-pass characteristics of the discrete operators effectively act as a filter. This numeric filter will inevitably interact with the explicit filter in Eq. (1). So, at the

R. Verstappen (✉)
Johann Bernoulli Institute for Mathematics and Computer Science,
University of Groningen, Groningen, The Netherlands
e-mail: r.w.c.p.verstappen@rug.nl

discrete level, the effective filter is not so clear, unless we use the Schumann filter [1]. Therefore we adopt the Schumann filter, i.e., we take

$$\overline{u} = \frac{1}{|\Omega_h|} \int_{\Omega_h} u(x,t)\,dx,$$

where Ω_h denotes a computational cell that is used in the finite-volume discretization, see [2], e.g. Replacing the right-hand side by a 'model' yields

$$\partial_t v + \nabla\cdot(v \otimes v) - \nu\,\nabla\cdot\nabla v + \nabla\pi = -\nabla\cdot\tau(v) \tag{2}$$

where the variable name is changed from $\overline{u}$ to v (and $\overline{p}$ to π) to stress that the solution of Eq. (2) differs from that of Eq. (1), because the model is not exact.

1.1 Truncation of Scales

The very essence of large-eddy simulation (LES) is that the (explicit) calculation of all small-scale turbulence—for which numerical resolution is not available—is avoided. This sets a condition to the closure model τ. To determine that condition, we consider an arbitrary part of the flow domain with diameter δ. With the aid of the associated box filter,

$$\widetilde{v} = \frac{1}{|\Omega_\delta|} \int_{\Omega_\delta} v(x,t)\,dx, \tag{3}$$

the undesirable small scales in the LES solution v are defined by $v' = v - \widetilde{v}$; here Ω_δ is to selected by the user. It may be emphasized that the filter box Ω_δ will generally differ from the grid box Ω_h that was used to filter the NS-equations; here it is assumed that $|\Omega_\delta| \geq |\Omega_h|$.

The residual of the box filter, $v' = v - \widetilde{v}$, consist of the scales of size smaller than δ. The closure model must be designed so that these small scales are dynamically insignificant. By applying the residual operator to Eq. (2) we find the equation for v' and from that we obtain the evolution of it's $L^2(\Omega_\delta)$ norm:

$$\frac{d}{dt} \int_{\Omega_\delta} \frac{1}{2}||v'||^2 dx = \int_{\Omega_\delta} \left(\nu\,\nabla\cdot\nabla v' - \nabla\pi' \right)\cdot v'dx - \int_{\Omega_\delta} \left(\nabla\cdot(v \otimes v)' + \nabla\cdot\tau' \right)\cdot v'dx \tag{4}$$

The two contributions to the last integral represent the energy that is transferred from the box-filtered velocity field $\widetilde{v}$ to the residual field v' and the eddy dissipation resulting from the closure model, respectively. Equation (2) does not produce residual scales if the eddy dissipation balances the energy transfer at the scale set by the box filter. Now if the closure model is taken so that the production and eddy dissipation terms in Eq. (5) cancel each other out, then

$$\frac{d}{dt} \int_{\Omega_\delta} \frac{1}{2} ||v'||^2 \, dx \; = \; \int_{\Omega_\delta} \left(v \, \nabla \cdot \nabla v' \, - \, \nabla \pi' \right) \cdot v' \, dx \tag{5}$$

and the evolution of the energy of v' does not depend on $\widetilde{v}$. Stated otherwise, the energy of residual scales dissipates at a natural rate, without any forcing mechanism involving $\widetilde{v}$. In this way, the scales $< \delta$ are separated from scales $\geq \delta$.

2   A Scale-Truncation Condition Based on Poincaré's Inequality

The closure model must keep the residual field $v' = v - \widetilde{v}$ from becoming dynamically significant. Our guiding principle is that the residual part of the motion is removed by the action of viscosity, as described by Eq. (5). Therefore the production of small scales of motion it to be balanced by the modelled dissipation:

$$\int_{\Omega_\delta} v' \cdot \left(\nabla \cdot \tau' \right) \, dx = - \int_{\Omega_\delta} v' \cdot \left(\nabla \cdot (v \otimes v)' \right) \, dx \tag{6}$$

Of course, we can verify whether this condition is met during a LES. But that is not very attractive, because it requires a fair approximation of v', which is quite expensive to compute. The more so since the user has chosen the filter length δ in such a way that the residual field v' is not of interest to him. Alternatively, v' might be expressed in terms of the resolved field by means of an approximate deconvolution procedure. However, such a procedure is not attractive either, since it is inherently ill-conditioned. Therefore, we will make use of Poincaré's inequality to get a scale-truncation condition which does not refer to the residual field v', see also [3, 4].

Poincaré's inequality

$$\int_{\Omega_\delta} ||v - \widetilde{v}||^2 \, dx \; \leq \; C_\delta \int_{\Omega_\delta} ||\nabla v||^2 \, dx \tag{7}$$

shows that the $L^2(\Omega_\delta)$ norm of the residual field v' is bounded by a constant (independent of v) times the $L^2(\Omega_\delta)$ norm of ∇v. Payne and Weinberger [5] have shown that the Poincaré constant is given by $C_\delta = (\delta/\pi)^2$ for convex (bounded, Lipschitz) domains Ω_δ. This is the best possible estimate in terms of the diameter alone. In case the filter box Ω_δ is quite anisotropic, the diameter does not provide a sufficiently detailed description of it's geometry. This problem can be sidestepped by using a modified Poincaré inequality, see [6]. For simplicity, it is assumed that the filter box Ω_δ is rectangular with (very different) dimensions δx_1, δx_2 and δx_3. The energy of the sub-filter scales can then be confined using the modified Poincaré inequality:

$$\int_{\Omega_\delta} ||v - \widetilde{v}||^2 \, dx \; \leq \; C \int_{\Omega_\delta} \left(\delta x_i \; \partial_i v_j \right)^2 \, dx$$

where C is a constant independent of δx_i. Thus, whereas the original Poincaré inequality (7) incorporates the dependence on the size of the filter box in the Poincaré constant C_δ, the modified Poincaré inequality incorporates the dependence on the size of the filter box by scaling the velocity gradient $\partial_i v_j$ with δx_i. Further details can be found in Ref. [6]. In this paper, we will assume that the dimensions δx_i are similar, so that the Poincaré inequality need not be scaled. We aim to convert the balance condition (6) to the upper limit set by the Poincaré inequality (7).

Poincaré's inequality (7) shows that the residual field v' can be suppressed by controlling the velocity gradient. According to Eq. (2), we have

$$\frac{\mathrm{d}}{\mathrm{dt}} \int_{\Omega_\delta} \frac{1}{2} ||\nabla v||^2 \, dx \;=\; \int_{\Omega_\delta} \nabla \left(v \, \nabla \cdot \nabla v \;-\; \nabla \pi \;-\; \nabla \cdot (v \otimes v) \;-\; \nabla \cdot \tau \right) : \nabla v \, dx \tag{8}$$

Once again, the latter two terms in the right-hand side represent the nonlinear production and eddy-dissipation, respectively. Thus expressed in terms of the velocity gradient the production-dissipation balance (6) reads

$$\int_{\Omega_\delta} \nabla \nabla \cdot \tau(v) : \nabla v \, dx \;=\; -\int_{\Omega_\delta} \nabla \nabla \cdot (v \otimes v) : \nabla v \, dx \tag{9}$$

Stated differently, if the model τ satisfies Eqs. (9), (8) shows that the Poincaré upperbound of the residual field v'—that is, the $\mathrm{L}^2(\Omega_\delta)$-norm of ∇v—dissipates at it's natural rate (which is set by the fluid viscosity v). Moreover, if the flow is initialized such that the $\mathrm{L}^2(\Omega_\delta)$ norm of ∇v vanishes then (8), (9) and (7) ensure that the $\mathrm{L}^2(\Omega_\delta)$ norm of the residual field v' equals zero for all times. For incompressible flows, the Cayley-Hamilton theorem states that $\nabla v^3 - Q\nabla v + RI = 0$, where the second and third invariant of the velocity-gradient tensor are $Q(v) = \frac{1}{2}\nabla v : \nabla v$ and $R(v) = -\frac{1}{3}\nabla v : \nabla v \nabla v = -\det \nabla v$, respectively. The right-hand side of Eq. (9) can be written in terms of these invariants. Indeed, since $\partial_k v_k = 0$, we have

$$\int_{\Omega_\delta} \partial_i \partial_k \left(v_k v_j \right) \partial_i v_j \, dx = \int_{\Omega_\delta} \partial_i v_k \partial_k v_j \partial_i v_j \;+\; \frac{1}{2} \partial_k \left(v_k \left(\partial_i v_j \right)^2 \right) \, dx$$

$$= -\int_{\Omega_\delta} 3R(v) \, dx \;+\; \int_{\partial\Omega_\delta} Q(v) \, v \cdot n \, ds$$

where n is the outward-pointing normal vector to the boundary $\partial\Omega_\delta$ of Ω_δ.

In conclusion, the convective contribution to the evolution of the $\mathrm{L}^2(\Omega_\delta)$ norm of ∇v is properly balanced by the closure model if

$$\int_{\Omega_\delta} \nabla \nabla \cdot \tau(v) : \nabla v \, dx \;=\; 3 \int_{\Omega_\delta} R(v) \, dx \;-\; \int_{\partial\Omega_\delta} Q(v) \, v \cdot n \, ds \tag{10}$$

3 Relaxation Model

The basic idea of LES is that the large scales of motion remain virtually unchanged, whereas the tail of the modulated spectrum (the spectrum of v) falls of much faster than the spectrum of the NS-solution u. In the present setting, the model τ is chosen properly if the associated box-filtered solution $\widetilde{v}$ approximates the box-filtered NS-solution $\widetilde{u}$. The residual velocity field $v - \widetilde{v}$ does not have any physical significance; it is only used to shorten the energy spectrum. The right-hand side of Eq. (1) does not dissipate energy, but transfers it (on average) towards smaller scales of motion that can dissipate energy at a higher rate. Here, we do not try to model the transport itself, but only just the net effect thereof. So the model should strengthen the dissipation (without producing smaller scales of motion, of course). To that end, we study the relaxation model introduced by Stolz et al. [7]. They used the relaxation

$$\nabla \cdot \tau(v) = \chi(v - \widetilde{v}) \tag{11}$$

to truncate the small scales of motion by dissipating their energy. The attractive feature of their relaxation method is that no (explict) use is made of a differential operator; hence a relaxation model can be discretized accurately near/at the grid cut-off as well as on "awkward" (unstructured, e.g.) grids.

The relaxation parameter χ is determined from the requirement that the production of any fine flow details of size smaller than δ by the convective nonlinearity is counteracted by the dissipation resulting from the relaxation model. The production-dissipation balance associated with the relaxation model is obtained by substituting (11) in (10). This yields

$$\chi = \frac{3 \int_{\Omega_\delta} R \, dx - \int_{\partial \Omega_\delta} Q \, v \cdot n \, ds}{\int_{\Omega_\delta} \nabla(v - \widetilde{v}) : \nabla v \, dx} \tag{12}$$

where the relaxation parameter is taken constant in Ω_δ i.e., δ is assumed to by the smallest scale at which χ varies. If χ is negative, the small box-fitting scales transfer energy to the larger eddies. Since these small scales of motion have no physical significance, χ is set to zero if Eq. (12) yields a negative value (i.e., χ is clipped).

As in Schumann's approach, the spatial discretization of the convective term defines the grid-filter. In one spatial dimension, the convective derivative is approximated to second-order accuracy by $\partial_x \phi_i \approx (\phi_{i+1/2} - \phi_{i-1/2})/h$, where $\phi_{i+1/2} = (\phi_{i+1} + \phi_i)/2$; hence effectively we have $\partial_x \phi_i \approx (\phi_{i+1} - \phi_{i-1})/(2h)$. The diffusive term is approximated using $\partial_{xx}^2 v_i \approx (v_{i+1} - 2v_i + v_{i-1})/h^2$. The discrete convective term does not see a point-to-point oscillation, whereas the discrete diffusive term does see this mode. So the convection-diffusion balance is not approximated correctly at the scale h set by the grid. Therefore we take $\delta = 2h$, see also [6]. In 1D the box filter (3) is approximated by

$$\widetilde{v}_i = \tfrac{1}{2} v_i + \tfrac{1}{4}(v_{i+1} + v_{i-1}) \tag{13}$$

Fig. 1 Results for turbulent
channel flow (Re$_\tau$ = 590):
mean velocity (*upper figure*)
and root-mean-square
velocities
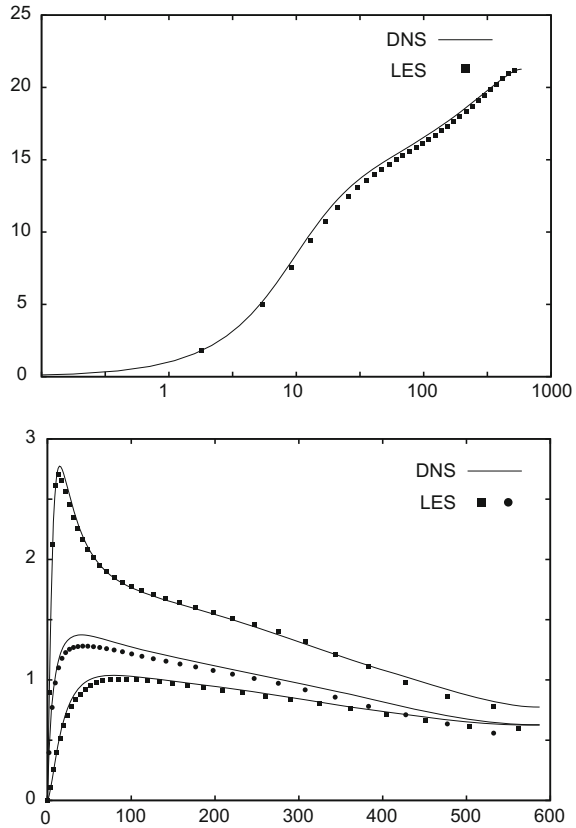
This discretization rule is also applied to the Ω_δ-integrals in Eq. (12). Here it is to
be stressed that we approximate all integrals using the trapezoidal rule with constant
coefficients, even if the grid is non-uniform, since the point-to-point mode must
be an integral part of the residue of the discrete box filter. Moreover, the model is
evaluated directly, i.e., without applying any form of deconvolution to the grid-filter;
so any difficulties associated with the deconvolution procedure are circumvented.
The invariants $Q(v)$ and $R(v)$ are computed from the discrete velocity gradient,
where the gradient is discretized as in the convective term.

The performance of the resulting discrete relaxation model has been investigated
for isotropic tutbulence and turbulent channel flow. As an example results for turbu-
lent channel flow (Re$_\tau$ = 590) are shown in Fig. 1. As is customary in this test-case,
the computational grid for the LES consists of 64^3 points. Details about the numerical
method can be found in Ref. [2].

References

1. Schumann U (1975) J Comp Phys 18:376–404
2. Verstappen RWCP, Veldman AEP (2003) J Comp Phys 187:343–368
3. Verstappen RWCP (2011) J Sci Comput 49:94110
4. R.W.C.P. Verstappen, W. Rozema, H.J. Bae (2014) In: Proceedings of the summer program, CTR, Stanford
5. Payne LE, Weinberger HF (1960) Arch Rat Mech Anal 5:286292
6. Rozema W, Bae HJ, Moin P, Verstappen R (2015) Phys Fluids 27:085107
7. Stolz S, Adams NA, Kleiser L (2001) Phys Fluids 13:997–1015

On the Coupling of a Zonal Body-Fitted/Immersed Boundary Method with ZDES: Application to the Interactions on a Realistic Space Launcher Afterbody Flow

Pierre-Élie Weiss and Sébastien Deck

Abstract One of the next foreseen challenges in CFD consists in the capability to simulate quantitatively the spectral content of the turbulent flow around realistic geometries. In this context, the present work focuses on a new methodology named ZIBC standing for Zonal Immersed Boundary Conditions (Mochel et al. in AIAA J 52(12):2782–2794, 2014, [14]) enabling to account for complex configurations (Hannemann et al. in Launch vehicle base buffeting: recent experimental and numerical investigations. ESTEC, Noordwijk, 2011, [13], Schwane in J Spacecr Rocket 52:54–62, 2014, [21], Pain in AIAA J 52:1967–1979, 2014, [17], Weiss and Deck in ZDES of the flow dynamics on an Ariane 5-type afterbody with and without struts, 2015, [26]) at high Reynolds number. The numerical strategy allowing the coupling between a modelling method (e.g. RANS, URANS, ZDES, LES or DNS) and IBC (Immersed Boundary Conditions) is detailed. In this paper, the modelling method retained is the Zonal Detached Eddy Simulation (ZDES) which has reached a high level of maturity on turbulent separated flows (Deck and Thorigny in Phys Fluids 19(065103), 2007, [8], Weiss et al. in Phys Fluids 21(075103), 2009, [27], Weiss and Deck in Phys Fluids 23(095102), 2011, [24], Weiss and Deck in Flow Turbul Combust 91:687–715, 2013, [25]). Then, the methodology is applied to a full space launcher configuration to assess its capability to return the interactions between the technological details, modelled with IBC, and the simplified afterbody, modelled with a body-fitted (BF) approach consisting in classical no-slip boundary conditions, in the turbulent flow field surrounding the main stage of the space launcher afterbody. The proposed method is thoroughly assessed on a realistic geometry of the European Ariane 5 launcher and the ZIBC simulation is successfully compared with the available experiments.

P.-É. Weiss (✉) · S. Deck
ONERA, The French Aerospace Lab, 92190 Meudon, France
e-mail: peweiss@onera.fr

S. Deck
e-mail: sebastien.deck@onera.fr

1 Introduction: Requirements Regarding Complexity and Accuracy in Applied Aerodynamics

In applied aerodynamics, some numerical strategies have reached a satisfying level of maturity regarding the industrial requirements (see e.g. [2, 3, 18, 23]). One of these methodologies is the Zonal Detached Eddy Simulation (ZDES) proposed by Deck ([4, 5]) that has allowed to return the relevant physical quantities for very different flows such as massively separated turbulent unsteady flows [6, 22] and high Reynolds number turbulent boundary layers [7]. Thus, a modern challenge lies in the taking into account of geometrical complexity without spoiling the quality of the results providing by a proven and effective numerical approach. To solve complex flows around realistic configurations in applied aerodynamics, a coupled approach can be considered. For complex flow aspects including mixing layers interacting with several recirculation bubbles with a wide range of characteristic frequencies, the ZDES is adopted. To extend the capabilities of the methodology to complex geometries which often involve both assembly of simple bodies and many technological details in the field of aerodynamics, the present study aims at demonstrating that the coupling between immersed boundary conditions (IBC) along with ZDES permits to return the main features of a flow dynamics in terms of spectral content and second-order statistics.

2 Proposal of a Coupled Numerical Strategy Named ZIBC

Figure 1 represents different strategies to simulate the unsteady flow around a full space launcher. The first one consists in a body-fitted (BF) approach in which a classical structured grid is built using a mesh topology following the surface curvature of the configuration. Such a methodology, in the framework of a finite volume approach, is able to provide satisfying second-order accurate results, especially for industrial flows. However, the generation of such grids is a very time-consuming task that can rapidly become unfeasible reaching a certain level of geometrical complexity. The second approach requires to model the walls of the considered configuration using IBC only. This global use of immersed boundary conditions (GIBC) implies the design of grids with very high resolution levels or to perform an adaptive mesh refinement (AMR) on a cartesian grid leading to significant changes in a Navier-Stokes solver.

As a consequence, in order to preserve the level of validation of the ZDES method and increase the level of representativeness of the configurations, a low intrusive numerical strategy named Zonal Immersed Boundary Conditions (ZIBC) that has been partly described in Mochel et al. [14] is used. This new numerical strategy couples a numerical approach selected by the user (e.g. RANS, URANS, RANS/LES, LES, DNS, ...) along with the zonal use of IBC, the simple part of a given configuration being modelled with classical no-slip boundary conditions. Thus, in the end,
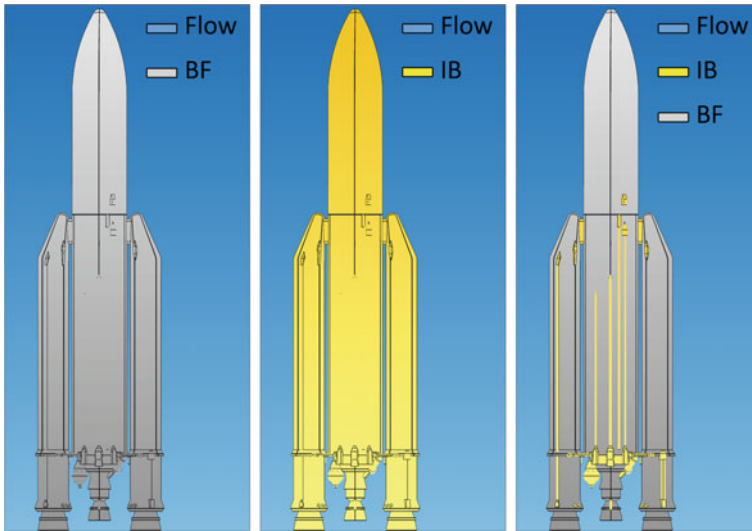
Fig. 1 Sketches depicting possible numerical strategies to impose a boundary condition to the simulated flow field using either an immersed boundary (IB) method or a body-fitted (BF) approach. From *left* to *right* full BF approach, full IB method (GIBC: Global Immersed Boundary Conditions), hybrid BF/IB approach: ZIBC (Zonal Immersed Boundary Conditions)

a hybrid BF/IB modelling of the walls is obtained. In the present paper, the selected numerical approach is the ZDES due to its proven efficiency on various unsteady flows in applied aerodynamics and in particular in the space launcher field (see [8, 24, 25, 27]). A direct IB forcing (see e.g. [9, 15]) is chosen given that the formulation is robust, simple to implement and, as a consequence, very well adapted to curvilinear applications. We have implemented this original IB method (i.e. direct forcing) in both FLU3M code [12], which is ONERA's research code for ZDES, and ONERA's elsA software [2] which allows to perform in both softwares any ZIBC strategy namely the coupling between ZDES and IBC with second-order accurate time and space schemes. The preprocessing needed by the IBC to distinguish mesh cells with a fluid or solid tag to locate the geometry is realized by the external program RAYTRACER3D [14] and the Cassiopée modules [1] for FLU3M and elsA, respectively.

3 Towards Relevant Parameters for Validation in Applied Aerodynamics

A demanding issue is to define when a methodology reaches a satisfying level of maturity. Among the available taxonomies such as the model readiness rate (MRR) [19], Sagaut and Deck [20] proposed a nomenclature to categorize the different

Table 1 Extended nomenclature for levels of validation of simulation techniques added to the original version from Sagaut and Deck [20]

Grade	Level of validation
0	Instantaneous flowfield visualization (coherent structure criteria, numerical schlieren)
1	Integral forces (lift, drag and pitch)
2	Mean aerodynamic field (velocity or pressure profiles)
3	Second-order statistics (r.m.s. quantities)
4	One-point spectral analysis (power spectral densities)
5	Two-point spectral analysis (correlation, coherence and phase spectra)
6	High-order and time-frequency analysis (time-frequency, bicoherence spectra)
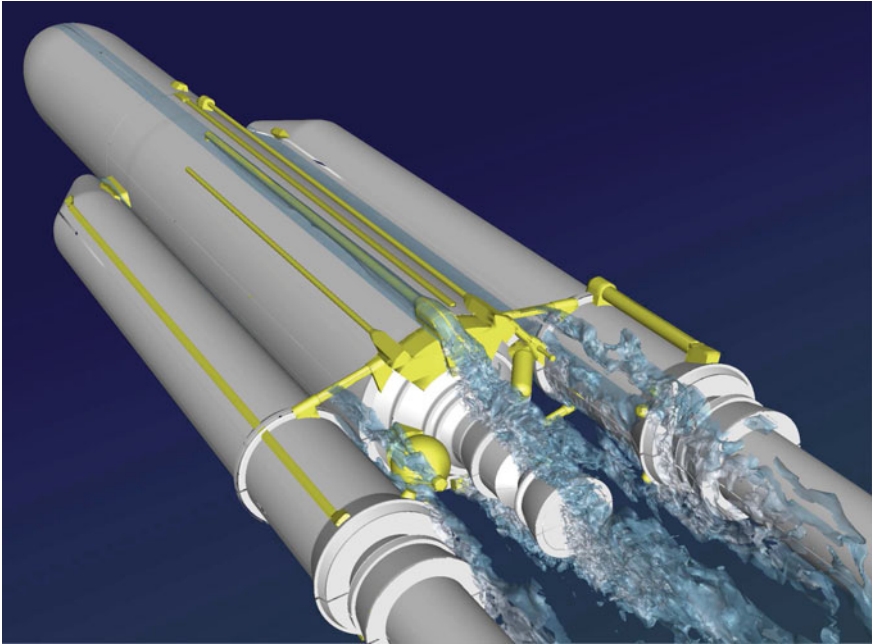
Fig. 2 Snapshot of the instantaneous base flow (ZDES simulation on a 75×10^6-point structured grid). View of the full space launcher modelled with ZIBC: *grey parts* ('clean' configuration) are modelled with a body-fitted (BF) approach, *yellow parts* (technological details) are modelled with an immersed boundary (IB) method. Three slices of iso-surfaces of the dimensionless streamwise velocity ($-0.1U_\infty; 0.1U_\infty; 0.3U_\infty$) are *plotted* showing the IB conditions properly influence the flow field and allow the development of mixing layers and recirculation areas

validation levels in applied aerodynamics. These authors emphasize the need for an increasing level of validation in particular to promote the highest accuracy (and expensive) simulations.

To this classification (see Table 1), an additional level is included and illustrated by Fig. 2. The level 0 is added without any pejorative meaning regarding the grade value zero itself. It only constitutes a mandatory step to qualitatively observe and potentially validate the global overview of the flow field in case experimental visualizations are available. Paradoxically, reaching level 0 can be far from being straightforward in the framework of three-dimensional flows simulated using HPC facilities. In this context, making advanced visualizations on large grids with respect to time becomes a very heavy task to handle.

4 Ariane 5: A Typical Example of Complexity

The considered configuration is a full Ariane 5 model with a 1:60 subscale ratio that has been taken into account along with the Z-shape sting holding the model in NLR's DNW-HST facility in order for the simulation to be representative of the experiment [10, 11, 21]. Such an Ariane 5 model constitutes an excellent test case for the assessment of the coupled ZDES/IBC approach performed with ONERA's FLU3M ZDES research code given it offers a high level of complexity both for the geometry and the flow. Indeed, the geometry at stake is both realistic and complex and the high Reynolds number flow ($Re_D = 1.18 \times 10^6$ with D, the largest cylinder diameter on the main stage and for a freestream Mach number $M_\infty = 0.8$) exhibits massive separation and several shear layers. Moreover, this test case is very well-documented with NLR's steady and unsteady measurements which permit to access different levels of validation (see Table 1). Then, the high validation level will allow a deeper insight into physics.

5 Results and Discussion

The results on the numerical test case are presented in Fig. 3. In the spirit of the aforementioned extended nomenclature for validation in applied aerodynamics, grades 0 to 4 have been reached, given that level 6 is not relevant here due to the statistically stationary nature of the flow (i.e. the spectral content does not evolve in time and a time-frequency analysis would not provide any supplementary information on the flow dynamics). An overview of the flow behaviour in three thick slices of iso-surfaces of the dimensionless streamwise velocity ($-0.1U_\infty$; $0.1U_\infty$; $0.3U_\infty$) has been shown in Fig. 2 allowing to check that the coupling of IBC with different ZDES modes reproduces well the early stages of the instabilities without delay, especially in the area where the technological details are modelled using IBC.
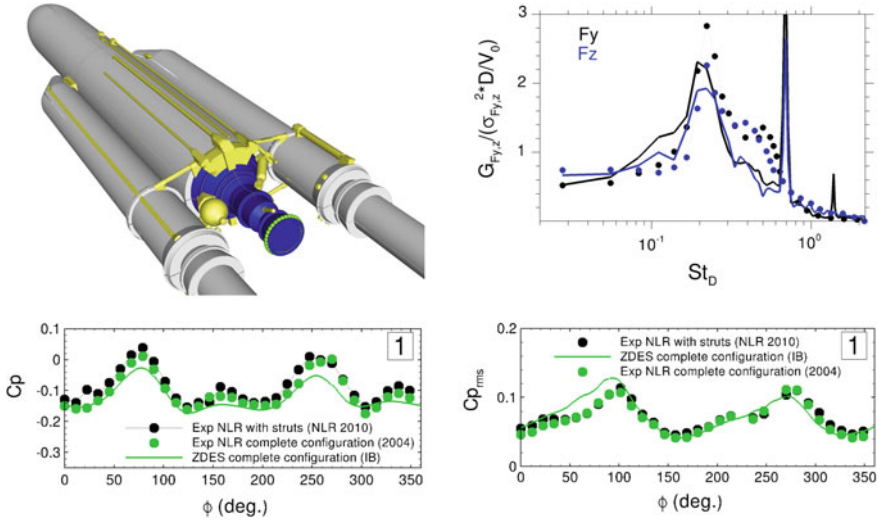
Fig. 3 Comparison of the unsteady quantities of interest between NLR's experiments and ONERA's ZDES/IBC. *Top left* geometry of the full launcher with technological details (*yellow*), surface used for side-load integration (*blue*) and ring on the nozzle used to plot Cp and Cp_{rms} evolutions (*green*). *Top right* PSD of the side loads for the y- and z-components (*solid lines* stand for ONERA's ZDES/IBC and symbols for NLR's experiments). *Bottom left* Azimuthal evolution at the end of the nozzle of the Cp. *Bottom right* Azimuthal evolution at the end of the nozzle of the Cp_{rms}. NLR's experiments on Ariane 5 complete configuration (*green symbols*), NLR's experiments on Ariane 5 with struts linking the main stage to the boosters only (*black symbols*), ONERA's ZDES/IBC on Ariane 5 complete configuration (*green solid lines*)

Figure 3 shows the comparison of the wall pressure coefficient Cp in the azimuthal direction (belonging to level 2) at the end of the nozzle between the NLR's available experiments and the ONERA's ZDES/IBC with all the technological details and with the asymmetrical struts linking the boosters to the main stage only. These results illustrate that the four-pole organization [16, 17] of the mean pressure is well simulated. Then, a level 3 validation, represented in the left bottom part of Fig. 3, shows a very good agreement between the numerical simulation and the experiments for the second-order moment of the pressure coefficient (Cp_{rms}) with a two-pole distribution. Finally, the PSD spectra of the two components (Fy and Fz) of the side loads for ONERA's ZDES/IBC clearly corroborate NLR's experiments.

In conclusion, the coupling of a zonal body-fitted/immersed boundary method with ZDES offers new opportunities to deal with challenging industrial configurations such as space launchers of the Ariane family (e.g. Ariane 5, Ariane 6 or any future launchers) with an increased reactivity resulting in a decrease of the time needed to assess the effect of a targeted technological detail. The readiness of the present approach has been proven up to level 4 of the classification established by Sagaut and Deck [20]. The introduction to this nomenclature of the level 0, especially for HPC simulation purposes, has allowed to emphasize that quantitative results are

obviously challenging to obtain and that it is becoming more and more commonplace for qualitative ones in the frame of big data visualization. Level 5 validations involving two-point spectral analysis constitute the next step to further analyze the flow dynamics of interest. Moreover, given the very well-documented database allowing a high validation level, a deeper insight into physics will be considered in future work.

References

1. Benoit C, Péron S, Landier S (2015) Cassiopee: a CFD pre- and post-processing tool. Aerosp Sci Technol 45:272–243
2. Cambier L, Heib S, Plot S (2013) The Onera elsA CFD software: input from research and feedback from industry. Mech Ind 14(3), 159–174. doi:10.1051/meca/2013056
3. Chalot F, Levasseur V, Mallet M, Petit G, Reau N (2007) LES and DES simulations for aircraft design. In: 45th AIAA aerospace sciences meeting and exhibit, AIAA Paper (2007-0723)
4. Deck S (2005) Zonal-detached-eddy simulation of the flow around a high-lift configuration. AIAA J 43(11):2372–2384
5. Deck S (2012) Recent improvements in the Zonal Detached Eddy Simulation (ZDES) formulation. Theor Comput Fluid Dyn 26(6):523–550. doi:10.1007/s00162-011-0240-z
6. Deck S, Gand F, Brunet V, Khelil SB (2014) High-fidelity simulations of unsteady civil aircraft aerodynamics: stakes and perspectives. Application of Zonal Detached Eddy Simulation (ZDES). Philos Trans R Soc A 372(2022)
7. Deck S, Renard N, Laraufie R, Weiss PE (2014) Large-scale contribution to mean wall shear stress in high-Reynolds-number flat-plate boundary layers up to $Re_\theta = 13650$. J Fluid Mech 202–248. doi:10.1017/jfm.2013.629
8. Deck S, Thorigny P (2007) Unsteadiness of an axisymmetric separating-reattaching flow. Phys Fluids 19(065103)
9. Fadlun EA, Verzicco R, Orlandi P, Mohd-Yusof J (2000) Combined immersed-boundary/finite-difference methods for three-dimensional complex flow simulations. J Comput Phys 161(1):35–60
10. Geurts EGM (2005) Steady and unsteady pressure measurements on the rear section of various configurations of the ariane 5 launch vehicle. In: 6th international symposium on launcher technologies, Munich, Germany (November 2005)
11. Geurts EGM (2010) Unsteady subscale force measurements within a launch vehicle base buffeting environment. Wind tunnel test of buffeting reduction devices (NLR-CR-2010-396-test 7003)
12. Guillen P, Dormieux M (1989) Design of a 3D multi-domain Euler code. In: International seminar of supercomputing. Boston, USA
13. Hannemann K, Pallegoix JF, Lambaré H, Maseland JJ, Frey M, Deck S, Schrijer FFJ, Schwane R (2011) Launch vehicle base buffeting: Recent experimental and numerical investigations. In: Proceedings of the 7th European symposium on aerothermodynamics for space vehicles, ESA Communications, ESTEC, Noordwijk, The Netherlands

14. Mochel L, Weiss PE, Deck S (2014) Zonal immersed boundary conditions: application to a high Reynolds number afterbody flow. AIAA J 52(12):2782–2794

15. Mohd-Yusof J (1997) Combined immersed-boundary/b-spline methods for simulations of flows in complex geometries. In: Annual research briefs, Center for Turbulence Research, pp 317–328

16. Pain R, Weiss PE, Deck S (2013) Three-dimensional spectral analysis of an axisymmetric separating/reattaching flow. In; TSFP 8, international symposium on turbulence and shear flow Phenomena, 28–30 Aug 2013

17. Pain R, Weiss PE, Deck S (2014) Zonal Detached Eddy Simulation of the flow around a simplified launcher afterbody. AIAA J 52:1967–1979

18. Roux A, Reichstadt S, Bertier N, Gicquel L, Vuillot F, Poinsot T (2009) Comparison of numerical methods and combustion models for LES of a ramjet. Combust Aerosp Propuls 337(6–7), 313–572

19. Rumsey CL, Smith BR, Huang GP (2010) Description of a website resource for turbulence modeling verification and validation. In: 40th AIAA fluid dynamics conference and exhibit, AIAA 2010-4742, Chicago, Illinois, 28 June–1 July 2010

20. Sagaut P, Deck S (2009) Large Eddy Simulation for aerodynamics: status and perspectives. Philos Trans R Soc A 367:2849–2860

21. Schwane R (2015) Numerical prediction and experimental validation of unsteady loads on ARIANE 5 and VEGA. J Spacecr Rocket 52:54–62

22. Simon F, Deck S, Guillen P, Sagaut P, Merlen A (2007) Numerical simulation of the compressible mixing layer past an axisymmetric trailing edge. J Fluid Mech 591:215–253

23. Vuillot F, Houssen F, Manoha E, Redonnet S, Jacob J (2011) Applications of the CEDRE unstructured flow solver to landing gear unsteady flow and noise predictions. In: 17th AIAA/CEAS aeroacoustics conference, AIAA Paper (2011–2944)

24. Weiss PE., Deck S (2011) Control of the antisymmetric mode ($m = 1$) for high Reynolds axisymmetric turbulent separating/reattaching flows. Phys Fluids 23(095102)

25. Weiss PE, Deck S (2013) Numerical investigation of the robustness of an axisymmetric separating/reattaching flow to an external perturbation using ZDES. Flow Turbul Combust 91:687–715

26. Weiss PE, Deck S (2015) ZDES of the flow dynamics on an Ariane 5-type afterbody with and without struts. In: 6th european conference for aerospace sciences, flight physics, launcher aerodynamics

27. Weiss PE, Deck S, Robinet JC, Sagaut P (2009) On the dynamics of axisymmetric turbulent separating/reattaching flows. Phys Fluids 21(075103)

Direct Numerical Simulation of Turbulent Mixed Convection in a Vertical Channel for the Assessment of Relaminarization Effects on the Hot Wall

Tim Wetzel and Claus Wagner

Abstract Direct numerical simulations of turbulent mixed convection in an asymmetrically heated vertical channel are performed with a finite volume method. The flow field analysis reveals coherent structures at the colder and warmer walls, which differ in size and intensity. Special attention is given to the effects taking place near the heated channel wall where the chances for relaminarization are high in contrast to the flow close to the colder wall. By analysing two—point correlations, it is shown that the variation of the streaks is more pronounced close to the warmer wall, with lengths between $\lambda_{x,0.15}^+ \approx 284 \ldots 991$, and widths $\lambda_{y,0.15}^+ \approx 23 \ldots 102$ over the channel height.

1 Introduction

Buoyancy driven flows play a major role in industrial applications. Thus, the development of appropriate tools for their simulation is becoming more and more important. Reliable computation of turbulent flows with Direct Numerical Simulation (DNS) requires enormous resources, temporally as well as computationally for problems with industrial relevance. As a consequence, the Large Eddy Simulation (LES) technique was established as means of reducing the amount of computational resources needed while providing information about the large flow structures (eddies). The latter technique is based on spatially filtering the Navier-Stokes equations and on turbulence models approximating the effect of the unresolved scales that are filtered out to compute the motions of the large eddies with a certain accuracy. In order to

T. Wetzel (✉) · C. Wagner
German Aerospace Center (DLR), Bunsenstraße 10, 37073 Göttingen, Germany
e-mail: tim.wetzel@dlr.de

T. Wetzel · C. Wagner
Technische Universität Ilmenau, Ehrenbergstraße 29, 98693 Ilmenau, Germany
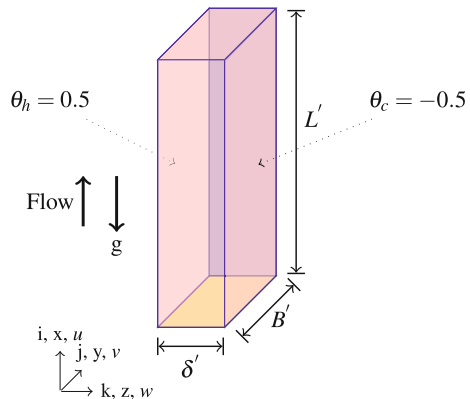e-mail: claus.wagner@dlr.de

evaluate or develop subgrid scale (SGS) models needed for LES, a DNS of turbulent mixed convection through a vertical channel with differentially heated walls was performed with a fourth-order accurate finite volume method for the present study. Since Kasagi and Nishimura [4] have presented low and higher order statistics obtained with a spectral method for the same setup, their results are used for validation purposes. They also analyzed energy budgets and showed resemblance between streaky structures near the walls with injection/suction flow. Additionally, Fabregat et al. [1] analysed coherent structures near the walls which they obtained for a similar setup and reported the averaged size of these structures and their dependency on the Grashof number.

2 Computational Details

2.1 Setup and Governing Equations

Turbulent mixed convection in a vertical channel with asymmetrical heating shown in Fig. 1 is considered. The flow domain is in accordance with the one used in the DNS by Kasagi and Nishimura [4], which serves as the reference for validation. The domain has a length $L = 2.5\pi \times \delta$ and a width $W = \pi \times \delta$ where δ is the channel height. The flow is driven upwards against gravity g along the two impermeable walls. No-slip conditions are prescribed for the velocity components u_i at the walls, thus $u_i|_{wall} = 0$. In the streamwise and spanwise directions, periodic boundary conditions are applied, resulting in $u_i(x) = u_i(x + L)$ and $u_i(y) = u_i(y + B)$. Further, the walls are assumed isothermal with fixed temperatures according to the labels in Fig. 1.

Fig. 1 Geometry of the channel with imposed boundary conditions

$$\frac{\partial u_i}{\partial x_i} = 0 \tag{1}$$

$$\frac{\partial u_i}{\partial t} + u_j \frac{\partial u_i}{\partial x_j} = \frac{1}{Re_b} \frac{\partial^2 u_i}{\partial x_j^2} - \frac{\partial}{\partial x_i}(p + \frac{\delta g x_1}{u_b^2}) + \frac{Gr}{Re_b^2}\, \theta \delta_{1i} \tag{2}$$

$$\frac{\partial \theta}{\partial t} + u_i \frac{\partial \theta}{\partial x_i} = \frac{1}{Pr \cdot Re_b} \frac{\partial^2 \theta}{\partial x_i^2} \tag{3}$$

Equations (1)–(3) reflect the Navier-Stokes equations (NSE) in their dimensionless form solved in the simulation. In Eq. (2), the conservation of momentum is described together with the Boussinesq approximation. The conservation of energy (3) is in this case solely described by the temperature of the fluid. Equations (2) and (3) are coupled, rendering the temperature an active scalar. The dimensionless control parameters considered in the present study are the Reynolds number $Re_b \frac{u_b' \cdot \delta'}{\nu'} = 4328$ (with bulk velocity u_b and kinematic viscosity ν), Grashof number $Gr = \frac{g' \beta' \Delta T' \delta'^3}{\nu'^2} = 9.6 \cdot 10^5$ (with gravitational acceleration g, thermal expansion coefficient β and temperature difference between the walls ΔT) and the Prandtl number $Pr = \frac{\nu'}{\kappa'} = 0.71$ (with thermal diffusion coefficient κ). The friction Reynolds number $Re_\tau^* = \frac{u_\tau'^* \cdot \delta'}{\nu'} \approx 291$ (with averaged friction velocity τ) results from the solutions.

2.2 Numerical Method

Equations (1)–(3) are discretized on staggered grids with $N_x \times N_y \times N_z = 512 \times 256 \times 140$ grid points in streamwise, spanwise and vertical directions, respectively. The grid cell resolutions are thus $\Delta x^+ = 4.4639$, $\Delta y^+ = 3.5711$ and $\Delta z^+ = 0.258 \ldots 4.453$ from the wall to the channel center. The NSE are solved using a finite volume method (FVM). In the wall-normal direction, the grid is refined towards the walls, while equidistant grid spacing is used in the periodic directions. The spatial interpolation scheme employed is a fourth-order accurate central difference method and the temporal integration is performed using an explicit second-order Euler-Leapfrog method with a constant time step of $\Delta t = 3.1441 \cdot 10^{-4}$ for the statistical evaluation. For Eq. (2), the coupling between pressure and velocity field is realized via Chorin's projection method and the resulting Poisson equation is then decoupled in the wall-parallel grid directions using fast fourier transforms (FFT). The yielded tridiagonal matrix equation system is solved directly. The methodology described here was adapted for cartesian grids from the cylindrical formulation of Feldmann and Wagner in [2]. The solution of the energy equation was treated in a similar manner regarding the spatial discretization scheme while the temporal integration is employed in a straightforward manner.

3 Validity of the DNS

In order to demonstrate the validity of our DNS based on the FVM, results are first compared with the DNS results of Kasagi and Nishimura [4] who used a spectral method. The simulation was started from a coarse grid solution and ran until convergence of the wall shear stresses was reached. From that point on, 101 instantaneous flow fields were extracted after every dimensionless time unit to analyze the temporal evolution of large-scale flow structures in terms of two-point correlation functions and power density spectra. Statistical averaging was performed in the two periodic directions and in time based on every 50th time step for 182 dimensionless time units t_b ($11581 \cdot 50 = 579050$ time steps). The comparison of the first and second order moments shown in Figs. 2, 3, 4 and 5 reveals a relative integral error of 1.288% for the mean streamwise flow profiles, and furthermore lower than 0.171% for the streamwise component of the rms velocity fluctuations. Also, the mean temperature profiles are in good agreement with the reference data. Thus, it is concluded that the DNS with the FVM is well-suited to capture all relevant features of the flow.
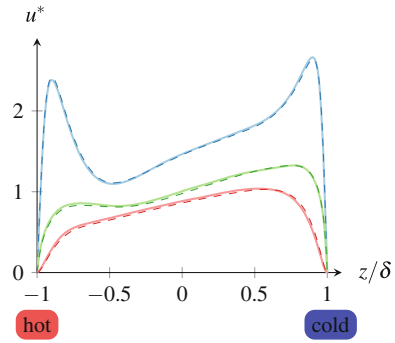

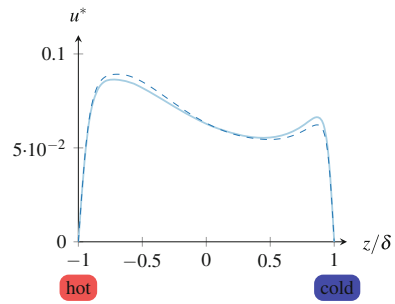**Fig. 2** Mean streamwise velocity profile (*solid line* DNS, *dashed line* Kasagi)
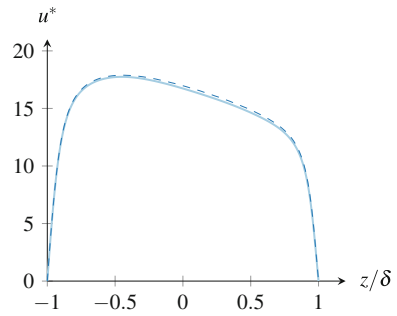
Fig. 3 Mean temperature profile (*solid line* DNS, *dashed line* Kasagi)
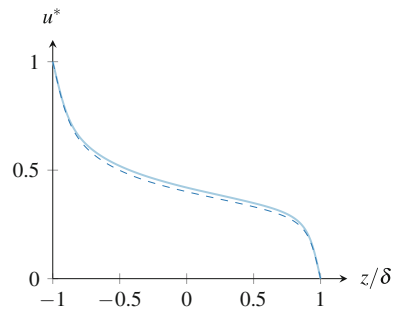
Fig. 4 Velocity rms profiles (*solid lines* DNS, *dashed lines* Kasagi; *top* u_{rms}, *middle* v_{rms}, *bottom* w_{rms})

**Fig. 5** Temperature rms profile (*solid line* DNS, *dashed line* Kasagi)

4 Structure Analysis

In order to assess relaminarization effects in the proximity of the heated wall, the sizes of the coherent structures are determined based on the λ_2-criterion defined in Jeong and Hussain [3]. In Fig. 6, top and bottom, isosurfaces of the values -4 in the λ_2-distributions obtained close to the warmer and colder walls, respectively, are presented together with color contours of the streamwise velocity fluctuations in planes, 14.5 wall units away from each wall. In agreement with Fabregat et al. [1], the structures near the the colder wall are significantly more grainy than those near the warmer wall. For higher Gr, Fabregat et al. [1] also reported that the size of structures close to the warmer wall remains nearly the same while that close to the colder wall becomes even smaller.

In order to assess how the structure size varies over the channel height, the widths and lengths of the streaky structures are determined using two-point correlation functions. They are calculated using the Wiener-Kintchine theorem on the power density spectra. In this respect, a correlation value above 0.15 defines the spatial extension λ^+ of the streaky structure considered here.
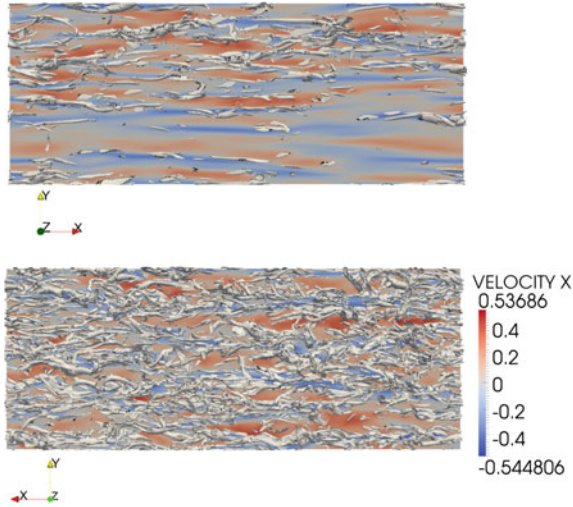
Fig. 6 Streaks of fluctuating streamwise velocity at $z^+ = 14.5$ (*top*) and $z^+ = 276.5$ (*bottom*) with λ_2—isosurfaces for $\lambda_2 = -4$
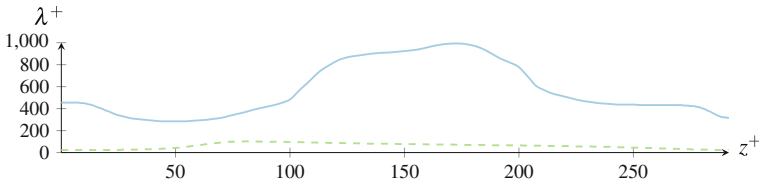
Fig. 7 Size variations of the streaky structures at every wall-parallel plane in the channel (*solid line $\lambda^+_{x,0.15}$, dashed line $\lambda^+_{y,0.15}$*)

In Fig. 7, the length and width distribution calculated for any grid point in wall-normal direction is presented. The variations of the structure widths and lengths, change considerably in wall normal direction. The structure length $\lambda^+_{x,0.15}$ exhibits strong variations near the warmer wall and much less variations near the colder wall while the structure width $\lambda^+_{y,0.15}$ shows less pronounced variations overall. The maximum structure length $\lambda^{+,max}_{x,0.15} = 991.75$ is located between $z^+ = 170.38\ldots174.75$ and the minimum $\lambda^{+,min}_{x,0.15} = 284.32$ at $z^+ = 43.69\ldots54.33$. Near the minimal length, the maximal width $\lambda^{+,max}_{y,0.15} = 102.09$ is found between $z^+ = 80.64\ldots84.37$. These λ^+ variations reflecting the mean structure length and width will serve as one of many criteria for rating the performance of LES subgrid scale models compared to data extracted from the DNS.

5 Summary

Results of a DNS of mixed turbulent convection through an asymmetrically heated channel performed with a fourth-order accurate FVM were presented. The validity of the FVM was demonstrated by comparing first- and second-order moments with those predicted using a spectral method by Kasagi and Nishimura [4]. It was shown that the flow has the tendency to relaminarize near the warmer channel wall as opposed to the colder wall. This behavior is counter-intuitive with regard to the locally higher Reynolds number on the warmer wall, which was supposed to lead to smaller, more dispersed streaky structures. The opposite is true, since the structures prove to be larger with lower turbulence intensities near the warmer wall. The structure sizes obtained from two-point correlation functions further confirmed that the dominating coherent structures near the hot wall show a stronger size variation than those near the colder wall.

References

1. Fabregat A, Pallares J, Vernet A, Cuesta I, Ferré Ja, Grau FX (2010) Identification of near-wall flow structures producing large wall transfer rates in turbulent mixed convection channel flow. Comput Fluids 39(1):15–24. doi:10.1016/j.compfluid.2009.06.010
2. Feldmann D, Wagner C (2012) Direct numerical simulation of fully developed turbulent and oscillatory pipe flows at. J Turbul 13(32):1–28
3. Jeong J, Hussain F (1997) Coherent structures near the wall in a turbulent channel flow. J Fluid 332:185–214
4. Kasagi N, Nishimura M (1997) Direct numerical simulation of combined forced and natural turbulent convection in a vertical plane channel. Int J Heat Fluid Flow 96

Epilogue

Michel O. Deville and Thien-Hiep Lê

In this short epilogue, we would like to draw some conclusions of the TI 2015 conference and give a few hints of possible trails to go along and investigate in the future.

1 Conclusions

The first conclusion is a very strong statement: Avoid second-order schemes in space: doubling the mesh improves the solution by a factor of 4, i.e. 2 bits of precision while the mantissa has 48 bits in a 64-bits word.

We notice with great satisfaction that very complex geometries have been tackled: launcher, aircraft, Koch2, burner, trains, corrugated pipe and more. From the turbulence point of view, taking minute geometrical features into account adds much information on the flow field, as we know that the devil is hidden in the details.

New models have appeared with the LES tensor representation, the δ concept vs grid size, the rotational Smagorinsky model.

Solvers are strained till their last bit and involve direct and iterative methods, preconditioning techniques, etc. As in most cases, linear systems of equations constitute the bottleneck of the computation, major efforts should be devoted to produce solvers with a computational complexity of the order of the number of unknowns.

Periodic problems should be considered as part of a validation procedure.

High-order schemes like 4th-order, DG, wavelet, etc. have been chosen and applied to turbulent flows.

As regards HPC, the complexity of implementation is at the heart of realistic exascale computing.

M.O. Deville
EPFL, Lausanne, Switzerland

T.-H. Lê
ONERA, Châtillon, France

For turbulent results analysis, higher statistics are needed. Some of them presented skewness and kurtosis. What about triple correlation of the velocity field.

2   Roadmap

From now on in this section, we will offer iconoclast propositions.

We should abandon the statistical approach which is the usual treatment when one knows nothing about the physical phenomena at hand. We should envisage to analyze the real time dynamics of the computed flows.

Again, how are we going to incorporate in our line of reasoning the Big Data approach?

For the time integration scheme, we know that the Navier-Stokes equation is a stiff problem. Strongly stable schemes are necessary.

The programming languages like object-oriented languages, Python, Java are among the top 10 languages scientists and engineers use worldwide. Are Fortran practioners a tribe condemned to disappear?

Signal processing algorithms should provide us with toolboxes for the analysis of computed data.

Open vs commercial codes, the endless debate.